# Concept, Modeling and Experimental Characterization of the Modulated Friction Inertial Drive (MFID) Locomotion Principle: Application to Mobile Microrobots

THÈSE N$^{O}$ 4108 (2008)

PRÉSENTÉE LE 27 JUIN 2008

À LA FACULTE SCIENCES ET TECHNIQUES DE L'INGÉNIEUR

Laboratoire de systèmes robotiques 2

SECTION DE MICROTECHNIQUE

ÉCOLE POLYTECHNIQUE FÉDÉRALE DE LAUSANNE

POUR L'OBTENTION DU GRADE DE DOCTEUR ÈS SCIENCES

PAR

Walter DRIESEN

Master in Mechanical-Electrical Engineering, Katholieke Universiteit Leuven, Belgique
et de nationalité belge

acceptée sur proposition du jury:

Prof. Ph. Renaud, président du jury
Dr J.-M. Breguet , directeur de thèse
Prof. N. Chaillet, rapporteur
Prof. B. Nelson, rapporteur
Prof. D. Reynaerts, rapporteur

ÉCOLE POLYTECHNIQUE
FÉDÉRALE DE LAUSANNE

Lausanne, EPFL
2008

*to my wife, Raquel*
*and my son, Alexander*

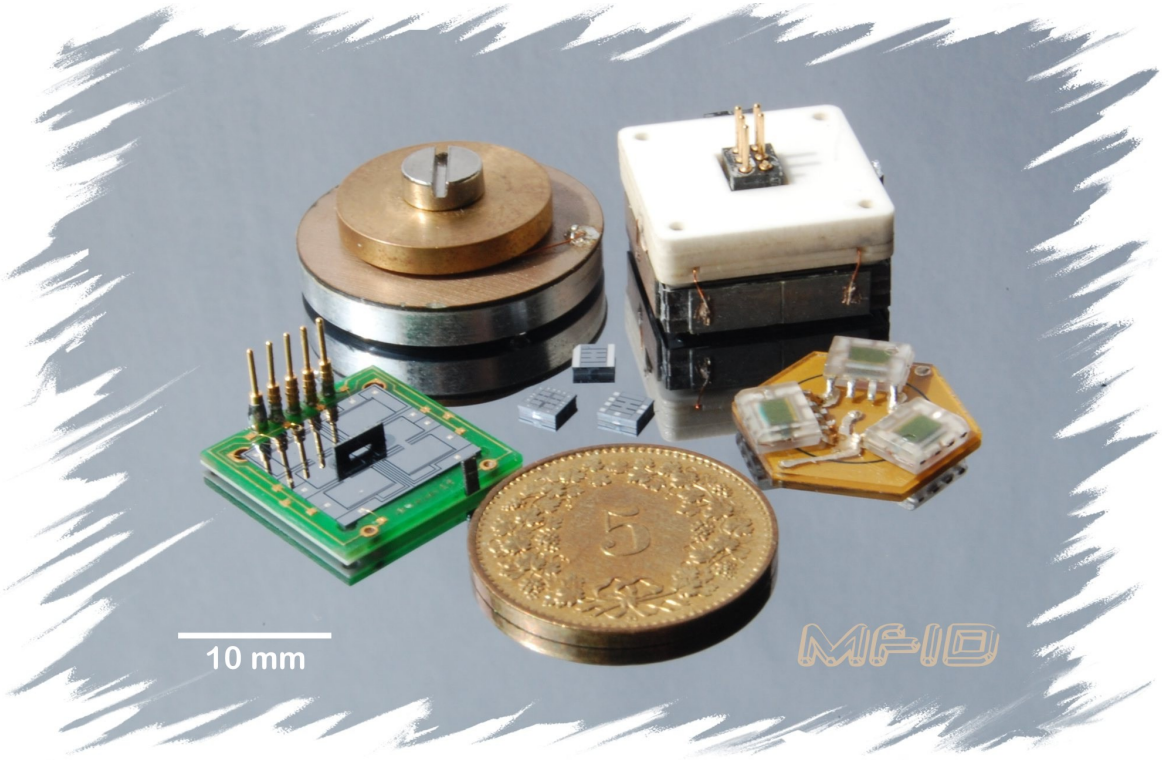

# Contents

# Acknowledgements

*"I can no other answer make,*
*but, thanks, and thanks."*
William Shakespeare (1564-Ű1616)

This work would never have been possible without the help of many people around me.

First of all, I would like to thank Jean-Marc Breguet for giving me the opportunity to work in his group, for supervising my thesis, for believing in me, for his kindness and support, and for the numerous discussions in which he always managed to understand immediately what I wanted to say.

My gratitude also goes to Prof. Reymond Clavel for welcoming me in his lab, for a great management of the lab activities, for our discussions, for his advise and for unveiling to me many secrets of mechanical engineering.

I want to thank the members of the jury, Prof. Nicolas Chaillet (FEMTO-ST, Besançon), Prof. Bradley J. Nelson (ETH Zürich) and Prof. Dominiek Reynaerts (K.U. Leuven), for reading and discussing my work and for their constructive remarks, as well as Prof. Philippe Renaud (EPFL) for chairing the jury.

Many thanks also to Amar Rida for his help on the design and the fabrication of the comb drive actuators, to Thierry and Arvid for our collaboration on the MiCRoN project and to Alexis, Thomas and Vincent for our collaboration on the I-Swarm project. It has also been a great pleasure to collaborate with my other present and past office colleagues, Christophe C., Christophe G., Cédric, Dongfeng, Emanuele, Fabian, Fatma, Florent, Guillaume, Nestor, Robert, Rodolfo and Sébastien and many other colleagues of LSRO. Thanks to you all for the nice atmosphere. Thanks also to Mélanie and Benoit for our collaboration and discussions on micromanipulation and microgrippers and to Jacques for his help on the electronics.

I am also grateful to Blaise Fracheboud and in particular Christophe Groux who have contributed directly to this thesis with their student projects.

The experimental setup and the prototypes developed in this thesis would have never existed without the help of Claude Amendola, Jean-Pierre Rougnon, Jean-Jacques Crausaz, Pascal Zbinden from the mechanical workshop, Giancarlo Corradini and Caroline Jacq from LPM, Philippe Vosseler from ACI and Cyrille Hibert and the rest of the staff of the CMI.

Thanks to Lionel for the informatics support and to the administrative staff of LSRO for their kindness and help.

Endless thanks to my parents for giving me a great education, lots of love and for working very hard for financing my studies, which allowed me to come this far.

And above all, I want to express my deep gratitude to my wife Raquel for finding my job at EPFL in the first place and, more importantly, for her love and passion and her support and patience. Many thanks also to my son Alexander for giving me lots of inspiration, for cheering me up (at any moment of the day ... and night) and for his support by starting to sleep through the night some weeks before the submission of my thesis.

This research was supported financially by the European projects MiCRoN (IST-2001-33567) and I-Swarm (IST-2002-2.3.4.2).

Walter Driesen
Lausanne, June 2008

# Abstract

A *mobile microrobot* is defined as a robot with a size ranging from 1 $in^3$ down to 100 $\mu m^3$ and a motion range of at least several times the robot's length. Mobile microrobots have a great potential for a wide range of mid-term and long-term applications such as minimally invasive surgery, inspection, surveillance, monitoring and interaction with the microscale world. A systematic study of the state of the art of locomotion for mobile microrobots shows that there is a need for efficient locomotion solutions for mobile microrobots featuring several degrees of freedom (DOF).

This thesis proposes and studies a new locomotion concept based on stepping motion considering a decoupling of the two essential functions of a locomotion principle: slip generation and slip variation. The proposed *"Modulated Friction Inertial Drive" (MFID)* principle is defined as a stepping locomotion principle in which slip is generated by the inertial effect of a symmetric, axial vibration, while the slip variation is obtained from an active modulation of the friction force. The decoupling of slip generation and slip variation also has lead to the introduction of the concept of a combination of on-board and off-board actuation. This concept allows for an optimal trade-off between robot simplicity and power consumption on the one hand and on-board motion control on the other hand.

The stepping motion of a MFID actuator is studied in detail by means of simulation of a numeric model and experimental characterization of a linear MFID actuator. The experimental setup is driven by piezoelectric actuators that vibrate in axial direction in order to generate slip and in perpendicular direction in order to vary the contact force. After identification of the friction parameters a good match between simulation and experimental results is achieved. MFID motion velocity has shown to depend sinusoidally on the phase shift between axial and perpendicular vibration. Motion velocity also increases linearly with increasing vibration amplitudes and driving frequency.

Two parameters characterizing the MFID stepping behavior have been introduced. The step efficiency $\eta_{step}$ expresses the efficiency with which the actuator is capable of transforming the axial vibration in net motion. The force ratio $q_F$ evaluates the ease with which slip is generated by comparing the maximum inertial force in axial direction to the minimum friction force.

The suitability of the MFID principle for mobile microrobot locomotion has been demonstrated by the development and characterization of three locomotion modules with between 2 and 3 DOF. The microrobot prototypes are driven by piezoelectric and electrostatic comb drive actuators and feature a characteristic body length between 20 mm and 10 mm. Characterization results include fast locomotion velocities up to 3 mm/s for typical driving voltages of some tens of volts and driving frequencies ranging from some tens of Hz up to some kHz. Moreover, motion resolutions in the nanometer range and very low power consumption of some tens of $\mu$W have been demonstrated. The advantage of the concept of a combination of on-board and off-board actuation has been demonstrated by the on-board simplicity of two of the three prototypes. The prototypes have also demonstrated the major advantage of the MFID principle: resonance operation has shown to reduce the power consumption, reduce the driving voltage and allow for simple driving electronics.

Finally, with the fabrication of $2 \times 2$ $mm^2$ locomotion modules with 2 DOF, a first step towards the development of mm-sized mobile microrobots with on-board motion control is made.

**Keywords:** mobile microrobots, locomotion, resonance operation, low power consumption, piezoelectric actuators, electrostatic actuators

# Version abrégée

Un *microrobot mobile* est défini comme un robot d'une taille allant de 1 $in^3$ à 100 $\mu m^3$ ayant une course de déplacement au moins égale à plusieurs fois sa longueur. Les microrobots mobiles ont un grand potentiel dans de nombreuses applications sur le moyen et le long terme comme la chirurgie mini-invasive, l'inspection, la surveillance, le monitoring et l'interaction avec le monde micrométrique. Une étude systématique de l'état de l'art des solutions de locomotion pour les microrobots mobiles a relevé un manque de solutions efficaces offrant plusieurs degrés de liberté (DDL) avec un encombrement d'environ 1 $cm^3$.

Cette thèse de doctorat propose et étudie un nouveau concept de locomotion basé sur un mouvement pas-à-pas avec un découplage entre les deux fonctions essentielles à un principe de locomotion: la génération du glissement et la variation du glissement. Ce principe appelé MFID ( "Modulated Friction Inertial Drive" ou "actionneur inertiel à modulation de force de contact") est défini comme un principe de locomotion pas-à-pas pour lequel le glissement est généré par l'effet inertiel d'une vibration axiale et symétrique alors que la variation du glissement est obtenue par une modulation de la force de frottement. Le découplage de la génération et de la variation du glissement ont également abouti à l'introduction du concept de la combinaison d'un actionnement embarqué avec un actionnement extérieur au robot. Ce concept permet d'atteindre un compromis optimal entre la simplicité et la consommation du robot d'une part et un contrôle de mouvement intégré sur le robot d'autre part, permettant ainsi une miniaturisation poussée du microrobot.

Le mouvement pas-à-pas d'un actionneur linéaire MFID est étudié en détail à l'aide d'un modèle numérique et d'une caractérisation expérimentale. Le dispositif expérimental est mis en mouvement par des actionneurs piézoélectriques vibrants parallèlement et perpendiculairement au déplacement. Cette combinaison de vibrations permet de générer respectivement le glissement et la variation de la force de contact. Après l'identification des paramètres de frottement, une bonne correspondance entre les simulations et les résultats expérimentaux a pu être atteinte. La vitesse de déplacement d'un actionneur MFID varie de manière sinusoïdale avec le déphasage entre la vibration axiale et perpendiculaire. De plus la vitesse augmente de façon linéaire avec les amplitudes de vibration et la fréquence d'actionnement. Deux paramètres caractéristiques pour le mouvement pas-à-pas d'un actionneur MFID ont été introduits. L'efficacité d'avancement $\eta_{step}$ exprime le rendement de la transformation de la vibration axiale en mouvement d'avancement. Le rapport de forces $q_F$ évalue quant à lui la facilité de la génération du glissement.

L'aptitude du principe MFID pour la locomotion de microrobots mobiles a été démontrée suite au développement et à la caractérisation de trois modules de locomotion avec entre 2 et 3 DDL. Les prototypes ont une taille caractéristique allant de 20 mm à 10 mm et sont entraînés par des actionneurs piézoélectriques et électrostatiques. Les résultats expérimentaux démontrent des vitesses de locomotion allant jusqu'à 3 mm/s pour des tensions d'actionnement typiques de quelques dizaines de volts et des fréquences allant d'une dizaine de Hz à quelques kHz. En outre, des résolutions de positionnement de l'order du nanomètre et une consommation de puissance très basse de quelques dizaines de $\mu$W ont été démontrées. L'avantage du concept de combinaison d'un actionnement embarqué et externe au robot a été illustré par la simplicité de deux des trois prototypes. Les prototypes ont également démontré l'atout majeur du principe MFID qui est le fonctionnement en résonance, ce qui permet une réduction considérable de la consommation d'énergie et des tensions d'actionnement, ainsi qu'une simplification de l'électronique de commande. Finalement, avec la fabrication de modules de locomotion à 2 DDL et d'une taille de $2 \times 2$ $mm^2$, le premier pas vers la réalisation de

microrobots mobiles de taille millimétrique avec un contrôle du mouvement intégré au robot a été réalisé.

**Mots-clés:** microrobots mobiles, locomotion, opération en résonance, basse consommation d'énergie, actionneurs piézoélectriques, actionneurs électrostatiques

# Chapter 1

# Introduction

*"As for the future,*
*your task is not to foresee it,*
*but to enable it."*
Antoine de Saint-Exupery (1900–1944)

## 1.1 Miniaturization

Always wanting more is an intrinsic characteristic of man. Since the beginning of his existence man has always been striving to go bigger, higher, wider, heavier, longer, faster and further. The quest for the smaller, however, has only started with the invention of the optical microscope about 400 years ago [1]. During ages microscopes have been used by physicists, chemicists and biologists for the observation of the small. The quest for the smaller reached the atomic scale in the mids of the $20^{th}$ century. The first time the idea of nanotechnology was introduced was in 1959, when Richard Feynman, a physicist at California Institute of Technology, gave a talk called "There's Plenty of Room at the Bottom" [2]. Though he never explicitly mentioned "nanotechnology", Feynman suggested that it will eventually be possible to precisely manipulate atoms and molecules. His vision became reality in terms of atomic scale observation by the invention of the first Scanning Probe Microscope (SPM) in 1982 and in terms of atomic scale manipulation by the revolutionary stunt of spelling "IBM" with 35 Xenon atoms in 1989 [3].

In his talk Feynman also suggested that it was possible to create "nano-scale" machines, through a cascade of billions of factories. According to the physicist, these factories would be progressively smaller scaled versions of machine hands and tools. He proposed that these tiny "machine shops" would then eventually be able to create billions of tinier factories. History has shown, however, that in the field of batch fabrication of micrometric and submicrometric scale features developed first by the microelectronics industry and later by the Microelectromechanical Systems (MEMS) industry, there is, ironically, rather a tendency of an increasing machine size for decreasing feature sizes. This contradiction of larger machines for smaller feature sizes visible in the microfabrication industry is also present in the field of micromanipulation and microassembly. However, a countermovement has started in the 1990s by the development of the "microfactory" concept. The microfactory concept consists in minimizing production systems to match the size of the parts they produce [4, 5, 6, 7]. The most essential components to be miniaturized in a microfactory are the robots used for manipulation and machining.

The dream of using miniaturized robots for operations at the small scale was also the

inspiration for the 1966 science fiction film "Fantastic Voyage" in which a 5 people and a submarine are miniaturized and injected in the human body in order to cure a disease. Feynman's vision of making micromachines allowing to produce smaller micromachines is revisited by A. Flynn in the late 1980s by developing an autonomous mobile microrobot of a size of 1 cubic inch [8]. From then on many miniaturized mobile robots have been developed for different applications, among which operations at the micro- and the nanoscale. An overview of the mobile microrobots reported in literature and some of their applications will be given in chapter 2.

## 1.2 What is a mobile microrobot?

A clear, generally accepted definition of the field of "microrobotics" or of the term "microrobot" does not exist in literature. Microrobots are either defined on a basis of the task they are performing either on their size [9]. In the case of a task-specific definition the term microrobots refers to robots used to perform specific tasks at the microscale. Such tasks can be actuation (micromanipulation, microassembly, microinjection, etc.) or measurements (force measurements, material characterization, dimensional measurements, etc. ) either of micrometer scale objects either at (sub)-micrometer resolutions. Such microrobots typically have a size ranging from some $cm^3$ to several $dm^3$ or more. The field of microrobotics does not only include the design of such microrobots, but also their operation, control, the required tools, the interacting forces at the microscale, manipulation strategies and so on. Analogously to this task-specific definition of microrobotics, the field of "nanorobotics" has been defined in [10] as "the study of robotics at the nanometer scale."

Apart from this task-specific definition, microrobots can also be defined with respect to their overall size. Miniaturization of the robot size has not only an influence on the robot design and the adopted fabrication techniques, but also on many other parameters such as its motion velocity, the interaction forces and the amount of power that can be dissipated on-board, stored on-board or transferred wirelessly. Scaling effects on microrobots have been studied by several authors [11, 12, 13, 14, 15]. The size limits for such a size-specific definition of microrobots is also subject to discussion. Dario *et al.* [16] proposes a subdivision in three classes: miniature robot, microrobot and nanorobot. They define miniature robots with a size of a few $cm^3$, a microrobot with a size of a few $\mu m^3$ and a nanorobot with a size of a few hundreds of nanometer. Although this definition has the advantage to fit well the SI length scale of micrometer and nanometer, it does not match with the commonly accepted terminology in literature. With such a definition the large majority of robots that were considered as microrobots by their creators would actually be classified as miniature robots. Hayashi [14] adopts a similar size classification. However, in his proposition conflicts with robots that are claimed to be microrobots in literature are avoided by defining the three classes with generic terms: first generation micromechanisms (size larger than 1 mm), second generation micromechanisms (size between 1 mm and several $\mu$m) and third generation micromechanisms (size smaller than several $\mu$m).

Caprari argues in [17] that the complexity of miniaturization scales proportional to the volume and not to the linear dimension. Therefore, Caprari proposes an alternative set of size limits based on a volume scale instead of on a length scale:

| | | | | | |
|---|---|---|---|---|---|
| Robot | : | volume around | 1 | $m^3$ | |
| Minirobot | : | volume around | $10^{-3}$ | $m^3$ | $= 1\ dm^3$ |
| Microrobot | : | volume around | $10^{-6}$ | $m^3$ | $= 1\ cm^3$ |
| Nanorobot | : | volume around | $10^{-9}$ | $m^3$ | $= 1\ mm^3$ |

Remains to define the range of "around". A convenient definition adopted in this dissertation,

which fits well the majority of the robots presented in literature, is to set the upper size limit for microrobots to 1 $in^3$ (=16.4 $cm^3$). The lower size limit to microrobots as defined by Caprari does not match well the generally adopted terminology in literature. Robots with sizes of a few mm aside [18, 19] down to a about a few hundred micrometers aside [20, 266, 22, 23] are still called microrobots and not nanorobots by their authors. Nanorobots are defined in [24] as *"a nanotechnological robot nanomachine, also called a nanite, which is a mechanical or electromechanical device whose dimensions are measured in nanometers ... They will have a diameter of about 0.5-3 microns and will be constructed out of parts with dimensions in the range of 1-100 nm."* Nanorobots are a product of nanotechnology and are most likely to be fabricated by bottom-up approach. Hence, based on a classification implicitly accepted by the majority of the literature on microrobots, a microrobot size limitation ranging from 1 $in^3$ down to 100 $\mu m^3$ is adopted in this work.

In order to differentiate clearly from the task-specific definition of microrobots the term *"mobile microrobots"* will be used in this work. Ideally, the motion range of a "mobile" robot is only limited by its power autonomy. In the reality of mobile *micro*robots often many other limitations exist: physically limited workspace, limited wireless communication range, limited wireless power transfer range, limited actuation range (in the case of external actuation), limited wire length (in the case of tethered operation) or limited position measurement range (in the case of closed loop operation). Therefore, a practical approach defining a motion range of at least several times the robot's body length is adopted. This brings us to the following definition of a mobile microrobot adopted in this work:

> A *mobile microrobot* is defined as a robot with a size of less than 1 $in^3$ and more than 100 $\mu m^3$ and a motion range of at least several times the robot's body length.

## 1.3 Why mobile microrobots?

Man has already achieved to build robots, machines and motorized vehicles that exceed by far the size of the largest animals that can be found in nature. However, we are still very far from outplaying nature at the other end of the length scale. But why would we try to do so? Why mobile microrobots?

In general *mobile* robots feature the advantage of increased motion range and flexibility with respect to stationary robots. Operation of stationary robots is limited to a workspace that is in the best case not much bigger than their own size. Motion ranges of mobile robots are only limited by their autonomy or by their environment. Mobile robots have an increased flexibility as points of interests can be approached under different angles and robots can be easily removed, added or exchanged. On the other hand mobile robots typically feature smaller thrust forces than stationary solutions. Their precision is usually also lower, as high precision sensors with 3 DOF are not commonly available and there is often a trade-off between sensor range and sensor resolution. Moreover, in order to profit fully from the flexibility advantage, mobile robots should ideally be wireless. This requires an on-board energy source and/or wireless energy transmission, wireless communication and integration of the driving electronics (and computational electronics). Mobile robots are nowadays a subject of intensive scientific research and industrial development with applications in inspection, security surveillance, cleaning, assistance of elderly, education, toys, etc.

But why would we want to scale down such mobile robots? Table 1.1 gives a non-exhaustive list of the advantages of miniaturization of mobile robots as well as some applications. Many of the applications listed in table 1.1 are still far from practical realization or immature for competition with performances of stationary mini- and macroscale robots.

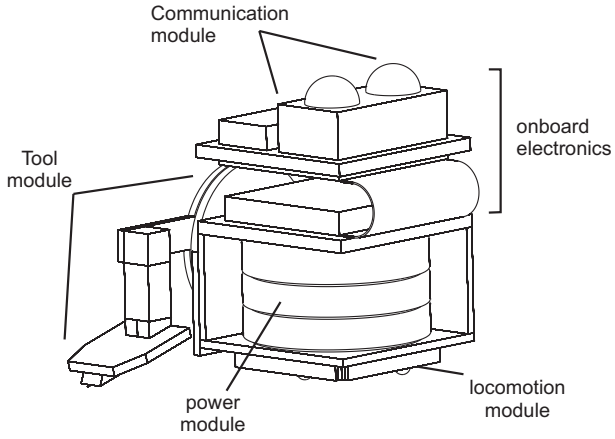


**Figure 1.1:** Structure of a mobile microrobot

Nevertheless, microrobots clearly have a huge potential, which motivates scientific research in that area in order to solve the related technological issues and continuously push further the miniaturization limits. Moreover, solving microrobotic challenges such as micro-actuation, on-board powering, wireless communication, low power electronics, system integration, microfabrication and assembly forces researchers to break down barriers and develop technologies that can find direct applications in the development of other industrial products and processes. For instance the MiCRoN project [25], a European research project on the development of 1 $cm^3$ size untethered mobile robots, has resulted in the application of four patents. For this reason mobile microrobots are an excellent benchmark application for micromechatronic technology. Mobile microrobots have for instance been used as a benchmark for watch technology by Seiko Epson Corp and Citizen Watch Co., Ltd. (see robots in figures 2.2(e) and 2.2(f) on page 24) and as a benchmark for microfabrication technology by Nippondenso Co., Ltd. (see the microcar in figure 2.3(e) on page 26).

## 1.4 Structure of a microrobot

An untethered mobile microrobot developed for a certain application typically consists of the following modules (see figure 1.1):

- Powering module
- Communication module
- Electronics module
- Locomotion module
- Tool module

Each of these module are discussed more into detail below. At the end of this section the problem of position measurement of mobile microrobots is also shortly discussed.

### 1.4.1 Powering module

On-board powering is probably the biggest challenge for mobile microrobots in general[1]. Power can be provided to robot: by on-board energy storage and/or by power transfer from

[1]Unfortunately, compared to locomotion of microrobots, relatively few research effort is explicitly oriented to the development of new powering solutions for mobile microrobots.

| Advantage | Application |
|---|---|
| access to restricted volumes | - operation in pipes: inspection [26, 27], reparations, pulling wires [28]<br>- operation in the human body (inspection [29, 30], drug application [31], surgery [32])<br>- manipulation of several robots under optical microscopes (in chambers with environmental control) [33, 34, 35, 36]<br>- operation in Scanning Electron Microscopes (SEM) and Transmission Electron Microscopes (TEM) [37, 38, 39, 40, 41]<br>- fabrication and assembly tasks in a microfactory [42, 43, 33] |
| low economic cost | - increase system throughput and capability by using a large number of cooperating robots: inspection, surface cleaning, searching, environmental monitoring etc. [44, 17, 45, 46]<br>- increase the robustness of a system by using a large number of error-prone, redundant robots, agents for research on swarm behavior [44, 46]<br>- support for education in the fields as (micro)mechanics, micro-engineering, robotics, control, electronics, embedded software, etc. [47, 17, 48]<br>- disposable robots, advanced toys and gadgets [49] |
| same size as small objects to be interacted with | - positioning of a large number of micro-objects<br>- interaction with small animals and insects [50]<br>- cell operations, cell sorting<br>- attach to small animals and organisms for transportation and tracking purposes [51] |
| imperceptibility | - surveillance for security, espionage (video, sound, vibration, etc.) [52]<br>- observation and tracking of animals |
| easy transportation: small volume and mass | - space applications: inspection, observation, reparations, etc.<br>- pocket robot: gadgets, toys, Personal Assistant (PA) etc. [49, 53, 203] |
| profit from scaling laws | - increased thermal and mechanical stability for precision operations<br>- relative increase in surface forces and friction forces and reduction of gravitational and inertial forces for vertical climbing, operation hanging from a ceiling, flying, walking on water etc. [54, 55] |

**Table 1.1:** Advantages of miniaturization and applications of mobile microrobots

the environment to the robot. Power transfer has the advantage of an unlimited autonomy in time, while on-board storage has the advantage of an unlimited autonomy in space (i.e. the motion range).

### On-board energy storage

The most commonly used means for energy storage are batteries (rechargeable and non-rechargeable), supercaps, springs and fuel [13, 56]. Fuel clearly has the highest energy density, but microscale combustion engines are not available yet[2] and micro fuel cells are still in a research phase. Among the electric energy storages, non-rechargeable batteries have the highest power density, but exchanging exhausted batteries for microscale devices is rather complicated[3]. The energy density of supercaps is very limited, but, compared to rechargeable batteries, they allow for much higher currents for charging and discharging. Batteries and supercaps are available in various sizes in the mm-range: for instance 2 $mm^2$ batteries (11.2 $\mu$Wh) for autonomous MEMS have been reported in literature [59] and $5 \times 5$ $mm^2$ batteries (45.6 $\mu$Wh) can be bought off-the-shelf from Cymbet Corporation [60].

### Power transfer

Power can be transferred to the robot in a tethered or in an untethered way. Tethered power supply is the easiest solution to implement, but it has serious drawbacks. First of all, the motion range is limited by the wire length. Moreover, in the case of obstacles or simultaneous operation of several robots, the motion path of the mobile robots is even more restricted as wires can get tangled up. So, wires decrease the mobility and therefore the flexibility of mobile microrobots, which is just one of the major advantages of mobile microrobots with respect to stationary solutions. As the robot size decreases, their thrust force typically also decreases and their motion gets more and more disturbed by the stiffness and the weight of the wires. Wires can cause parasitic motion, unequal weight distribution or can ever tilt or push over the microrobot. To put it briefly, wires are to be avoided. Unfortunately, wires are often a necessary evil, as either the robot consumes too much for on-board powering, either the investment of developing an on-board powering solution (including on-board signal generation and wireless communication) is too high.

Solutions of wireless power transfer exist, but their performances and applicability are often limited. Power can be transferred to a microrobot by means of sliding electrical contacts, variable electromagnetic or electrostatic fields, mechanical vibrations or by means of electromagnetic waves (microwaves, light, etc.).

While sliding electrical contacts are relatively easy to implement for 1 DOF motion, it gets much more complicated in the case of 3 DOF. Sliding electrical contacts have been demonstrated in the NanoWalker project by transferring 15 W to a set of three-legged mobile microrobots [61].

Electromagnetic coupling is often used for wireless powering of medical implants [62, 63, 64] and the best efficiency is obtained a good alignment and a low distance between the two coils [65]. Again, in the case of 3-DOF motion of one of the coils, things get more complicated. Gao [66] has developed in the MiCRoN project [25, 67] a $180 \times 220$ $cm^2$ "power floor" capable of transmitting 330 mW at 3.1 $V_{dc}$ to $\varnothing$11.5 mm $\times$ 4 mm coils. This power

[2] Peirs *et al.* report on the development of a miniaturized gas turbines with rotor diameters of 10 mm [57] and 20 mm [58], but many technological issues remain for stand-alone operation and miniaturization below 1 $in^3$.

[3] With the mass fabrication capabilities of the microfabrication technologies developed in the last two decades the idea of disposable microrobots becomes close to realistic.

floor was used for powering the $12 \times 12 \times 25$ mm$^3$ untethered MiCRoN robot while performing wireless communication and 3 DOF locomotion driven by the on-board electronics. Wireless powering of mobile robots by electromagnetic coupling has also been reported by Yan *et al.* [68]. They demonstrated a transmission 480 mW of DC power to a ⌀11.5 mm × 0.6 mm coil integrated on an endoscope robot driven by a variation of the inchworm principle. Power transfer with electromagnetic fields have also been demonstrated by Vollmers *et al.* [266] for the excitation of a mechanical resonant vibration on a $0.3 \times 0.3$ mm$^2$ mobile microrobot (see figure 2.13(a) on page 47).

Energy transfer by electrostatic coupling with interdigital external electrodes for inducing an on-board mechanical deformation is proposed by Donald *et al.* [69, 23] for actuation of the untethered scratch drive actuator (see figure 2.14(f) on page 51). Electrostatic coupling can principally also be used to generate on-board energy in the form of electrical charges, which can be used to power for instance on-board electronics. This form of electrostatic induction has, however, up to now not yet been used for powering mobile microrobots.

Yasuda *et al.* [70, 19] has demonstrated energy transmission by a mechanical vibration inducing on-board elastic deformations that, combined with a mechanism of directional friction, result in motion (see figure 2.15(f) on page 55). Mechanical vibration energy can also be harvested and transformed to electrical energy by small inertial masses connected to piezoelectric actuators. However, as for electrostatic induction, this form of mechanical-to-electrical energy conversion has not yet been demonstrated for powering microrobots.

Microwave energy supply has been successfully implemented for an in-pipe micro inspection machine by Nippondenso Co., Ltd. [71, 27]. The pipe serves as a waveguide, which made power transmission of 480 mW possible, while the microwaves were also used for data communication (2.5 Mbit/s). However, it is difficult to apply microwave energy supply for robots not operating in a pipe, but on a flat surface in open air.

Apart from the microwave power link the in-pipe robot from Nippondenso Co., Ltd. was simultaneously also powered by photovoltaic cells [72]. A series connection of 63 tiny, individual solar cells allowed to supply about 100 V for the electrostatic actuators of the on-board camera module. Apart from a series connection of individual cells, different technologies [73, 74, 75] have been developed for fabricating integrated, on-wafer series connections of solar cell segments with generated voltages up to 207 V [75]. Small solar cell modules with output voltages up to 16 V can also be purchased off-the-shelf from Clare, Inc. [76]. An integrated process for fabrication of high voltage solar cells and electrostatic actuators on the same silicon wafer was presented by Bellew *et al.* [77]. The power output of solar cells can be boosted by illuminating with high intensity light. D'Amato *et al.* [78] demonstrated a power output up to 54 W/cm$^2$ by illuminating small solar cells with a laser spot. The autonomous microrobot presented by Hollar *et al.* [79] (see figure 2.6(c) on page 33) is powered by a $3.6 \times 1.8$ mm$^2$ solar cell module providing 100 $\mu$W at different voltages up to 50 V. Thin-film amorphous silicon offers a high efficiency (25%) for indoor applications with visible light [80]. Wyrsch *et al.* (University of Neuchatel, Switzerland) report on the development of $3.9 \times 3.9$ mm$^2$ solar cells for powering the I-Swarm robot [46], based on a concept combining powering, communication and position sensing proposed and tested by EPFL [81]. The I-Swarm robot requires two voltages for operation (1.5 V and 3.3 V), which are generated by a single structured amorphous silicon solar cell with power outputs of 0.41 mW and 0.87 mW for the 1.5 V and 3.3 V outputs respectively. Photovoltaic cells have also been selected by Andre and Martel [51] for powering the on-board electronics of an untethered aqueous microrobots propelled by bacteria.

Energy transfer by light for inducing an asymmetric on-board thermal expansion resulting in locomotion of a mm size microrobot has been demonstrated for 1 DOF motion in [82] and

for 3 DOF motion in [83] (see figure 2.20(c) and 2.20(d) on page 65 respectively). Denninghoff *et al.* [84] also proposes the concept of laser radiation for the untethered actuation of the wings of a flying robot.

### 1.4.2 Communication module

Communication can be required between a robot and a central host (typically in the case of centralized control) and/or between different robots (typically in the case of distributed control). The most common means for wireless communication (both host-robot and robot-robot) is by infrared (IR). IR communication has been implemented on the Alice [13], Jasmine [85, 86], ECO-BE [87], NanoWalker [88] and NanoRunner [89], the I-Swarm robot [90], the LMARC robot [91], and the MiCRoN robot [92, 67] (all these robots are discussed and shown in chapter 2). In the Smart Dust project [52] a power efficient means of communication by on-board variation of the reflection of a laser beam with orientable corner cube mirrors is proposed [93]. The advantages of IR communication are the low power consumption, small size, and the fact that the same modules can also be used for distance sensing. Radio Frequency (RF) communication requires more space, but is omnidirectional (which can also be a drawback in some cases). RF communication has been demonstrated on the Alice microrobot [13] (see figure 2.2(a)), on the Monsieur II microrobot (Seiko Epson Corporation) [53] and on the in-pipe robot from Nippondesno Co., Ltd. [71, 27].

### 1.4.3 Electronics module

The on-board electronics is the heart and the brain of the robot. It includes the peripherals (power and voltage management, drivers for the actuators, interfaces for the sensors and communication module) and possibly some computing power in a Central Processing Unit (CPU). In the case of low voltage operation, the electronics can be very efficient. The CPU of the Alice '99 robot only consumes 4 mW in average (without RF communication), which is similar to the consumption of its motors (3 mW) [13]. In the case of high driving voltage for the actuators (as typically for piezoelectric and electrostatic actuators) the power consumption of the driving electronics increases considerably. The very advanced electronics for the NanoWalker robot [94, 61] features voltage convertors (5 V to 300 V), 12 $\pm 150\ V$ drivers for driving the piezoelectric actuators for locomotion, a 16 bit input for an on-board sensor, a DSP (Digital Signal Processor), and IR communication. This electronics is a major achievement in terms of integration, but the complexity goes with the price of a total power consumption of more than 15 W, which is huge for robot measuring only $32 \times 32 \times 20$ mm$^3$. 15 W is not only a big issue for wireless power transfer (on-board storage at this size is far from feasible), but is also a big problem in terms of heating of the robot due to the dissipated power. In order to avoid overheating of these robots, a cooling chamber working under helium atmosphere had to be developed [95].

In the MINIMAN project [96] an on-board driving electronics consisting of 12 ASICs (Application-Specific Integrated Circuit) was created for driving 48 channels of the 50 V piezoelectric actuators for locomotion and tool actuation of the MINIMAN-V robot (see figure 2.5(a) on page 30) [97]. The on-board electronics was still powered by wires, but allowed to reduce the number of wires from about 50 for actuation of all piezoelectric channels to 6 for powering and communication [98]. An on-board electronics based on several full-custom ICs (Integrated Circuits) capable of driving ten 20 V piezoelectric actuators, sensing and controlling a tool and IR communication was integrated in the untethered $12 \times 12 \times 25$ mm$^3$ MiCRoN robot [99]. The overall power consumption of the robot was about 300 mW during locomotion [100]. Although, this power consumption has proven to be low enough to be

transferred by a power floor based on inductive coupling [66], it is still much higher than the effective power consumption of the locomotion module at maximum velocity (1.0 mW, see figure 2.19(d) on page 64). Another on-board electronics for integration in the $3 \times 3 \times 3$ mm$^2$ I-Swarm microrobot with a power consumption of about 1.5 mW has been presented by Casanova *et al.* [101]. The SoC (System on Chip) consists of a single ASIC of $3 \times 3$ mm$^2$ with integrated power management, 8051 microcontroller, 3.6 V actuator (3 multilayer piezoelectric polymer legs) drivers and IR communication interface.

An analysis of the driving voltages and power consumption of the different electronic modules discussed above illustrate well that in general a reduction of the number of actuation channels and the driving voltage result in a lower power consumption. Nevertheless, ultra low power consumption electronics capable of high voltage operation is possible in the case of square wave actuation of few channels and reduction of the on-board intelligence as illustrated by the autonomous mobile microrobot presented by Hollar *et al.* [79]. The $8.5 \times 4 \times 0.5$ mm$^3$ robot has eight 50 V actuation channels and an overall power consumption of 2.6 $\mu$W (0.1 $\mu$W for the actuators, 2.5 $\mu$W for the voltage translators and 0.022 $\mu$W for the CMOS sequencer).

As powering is the biggest problem of autonomous mobile microrobots and as the power consumption is dominated by its driving electronics it is extremely important to optimize the other on-board modules in terms of complexity and power consumption of the driving electronics. In the case of the locomotion module, the complexity and power consumption of the driving electronics[4] can be minimized by

- reduction of the number of channels
- reduction of the driving voltage
- reduction of the driving current (average and peak)
- avoiding the use of Digital to Analogue Convertors (DAC) and operational amplifiers (op-amp)

The drivers (or amplifiers) of the electronics have to be designed not only in function of the average current drawn by the actuators, but also in function of the maximum peak current. A design allowing for higher peak currents also results in a much larger static (and dynamic) power consumption of the driver[5]. Digital to analogue convertors (DAC) and linear amplifiers can be avoided by implementing a digital switching electronics. A switching electronics typically results in square waves, but saw tooth waves and trapezoidal waves can also be approximated by a switching electronics by charging and discharging capacitances[6]. A reduction of the driving frequency can in some cases also reduce the power consumption, but typically much less than a reduction of the driving voltage or current. Hence, for a constant motion velocity it is favorable in terms of power consumption of the driving electronics to reduce as much as possible the driving voltage (current) and increase the driving frequency[7].

### 1.4.4 Locomotion module

The locomotion module provides the robot with motion, which is for operation on a flat plane typically either 2 DOF either 3 DOF. Depending on the type of application different

[4]The power consumption of the driving electronics does not include the power consumption of the actuator (i.e. $P = IU$ for resistive loads and $P = \frac{1}{2} \cdot fCU^2$ for capacitive loads).

[5]The static power consumption of an electronic circuit is the power consumption when the circuit is not switching, while the dynamic power consumption is the power consumption due to the switching.

[6]Such an switching electronics that charges and discharges capacitances in order to produce a saw tooth signal is implemented in the robot shown in figure 2.17(b) on page 60

[7]Moreover, it has been shown by Driesen *et al.* [102] that a reduction of the driving voltage and corresponding increase in driving frequency also results in a reduction of the power consumption of the actuators in the case of capacitive loads (such as piezoelectric actuators).

requirements in terms of size, DOF, motion velocity, power consumption, step size and motion resolution are imposed. Chapter 2 gives an overview of the different locomotion modules for mobile microrobots reported in literature. when designing the locomotion module for an untethered robot with on-board electronics it is very important to consider also the influence of the design choices for the locomotion on the complexity and power consumption of the electronics.

### 1.4.5 Tool module

Depending on the task the mobile microrobot is designed for, different tools (actuator or sensor) can be integrated. Typically, the tool requires vertical positioning, so an additional actuator has to be integrated on the robot. Some examples of tools integrated on mobile microrobots are: passive needle [34], microgripper [43, 103, 104, 105, 35, 33, 106, 107], scanning probe microscope [88, 108, 109], injection needle [92], pipette [39], machining tools [110], indentation tool [111], light sensors [112, 113], eddy current sensor for crack detection [26] and a camera for inspection [27].

### 1.4.6 Position measurement of mobile microrobots

One of the complications with respect to the control of mobile robots in general is that it is more difficult to obtain an information of the absolute position of the robot. Linear scales and rotary encoders exist with resolution down to the nanometer range. There are, however, few solutions for measuring the 3 DOF $(X, Y, \theta_Z)$ position of a mobile microrobot. Some locomotion modules have better open loop precision than others. Best open loop resolutions are achieved by odometry with wheeled locomotion, as principally no slip occurs between the wheels and the substrate. Odometry requires rotational encoders to be integrated on each wheel, or on the motors driving the wheels. Odometry can have a decent resolution for short distances, but suffers from drift for larger distances. In order to compensate for the drift odometry is usually used in combination with other sensors such as IR distance sensing, light sensors, sound sensors or an on-board camera for obstacle avoidance and navigation in known environments or for map building applications [17]. The open loop positioning is, however, usually insufficient for handling and sensing application on the millimeter scale or below.

The most common way for obtaining absolute 3 DOF information on the robot's position is by optical tracking of the whole robot with a global camera and/or tracking of the objects and end effectors with a local camera (optical microscope or scanning electron microscope) [103, 33, 107, 43, 114, 34, 40]. An alternative solution based on several 2D photosensitive devices (PSD) instead of a camera is proposed in the Nanowalker project [94].

A system with an external position sensor is well suited in the case of centralized control, but in the case of distributed control it would be much more interesting if the robots could measure their own positioning by themselves (EGO-positioning). A concept of EGO-positioning based two on-board photodiodes and an external projector projecting a well-defined digital pattern is proposed and tested for mobile microrobots by Boletis *et al.* [81]. On-board position sensing with the sensor from an optical mouse for coarse positioning and an eddy current sensor for local, fine positioning is proposed by Fuchiwaki *et al.* [111]. Measurement of the relative position of different robots can also be important in the case of cooperative tasks. Aoyama *et al.* [115] reports on inter-robot navigation based on ultrasound. Onboard position sensing has also been demonstrated by Ishihara *et al.* [116] by the development of a microrobot capable of autonomously tracing a line drawn on the floor with the help of onboard photosensors. High resolution, 3 DOF position sensing can be achieved

by the integration of a Scanning Probe Microscope on the robot [108] and scan a surface with a known micropattern.

## 1.5 Motivation and objective of this thesis

Section 1.3 has shown that there is great potential for mobile microrobots. For some applications (for instance in the medical and the inspection field) mobile microrobots have already proven to be effective and commercialization has started. In other fields real applications have already been demonstrated (for instance micro- and nanomanipulation), but the solution with mobile microrobots can still not compete with other, larger scale, stationary solutions. But the capabilities of mobile microrobots are continuously improving and they will soon become the best solution for more and more applications. The motivation of this thesis is to contribute to this development of mobile microrobots, in particular to the locomotion function.

In the microrobotics group at the Laboratoire de Systèmes Robotique at the EPFL a large experience has been achieved with mobile microrobots throughout internal projects and several European projects (MiCRoN [25], I-Swarm [46], Golem [36] and Nanohand [117]). Except for the I-Swarm project these projects are oriented to handling and sensing applications in fields as microassembly, microbiology and nanotechnology. The gained experience does not only concern the development of different actuation solutions for mobile microrobots, but also the understanding of a mobile microrobot as a system, its advantages, drawbacks and its applications. As will be shown in chapter 2 many locomotion solutions, often based on very innovative concepts, have already been proposed in literature. Many of these solutions suffer, however, from either one of two limitations. A first limitation is that many of the proposed solutions are not well suited for untethered operation as either the power consumption is too high, either the required driving electronics is too complex (and therefore consumes too much). Those robots are then operated with wires, which causes one of the major advantages of mobile microrobots, flexibility from mobility, to be partially lost. A second limitation to many of the locomotion solutions proposed in literature is that the systems that have low power consumption often only have a limited number of DOF and/or feature only unidirectional motion (forward, but not backward), which is insufficient for many applications.

The objective of this thesis is to propose a locomotion concept for mobile microrobots that meets the following set of requirements:

- miniaturization to 1 $cm^3$ and below
- motion with up to 3 DOF
- motion velocity of several mm/s
- possibility for motion with nanometric resolution
- possibility for on-board motion control
- limited number of actuation channels
- power consumption less than 5 mW
- driving voltage of some tens of volts
- no high driving current (average and peak)
- simple driving electronics (ideally no DAC, no linear amplifiers)

## 1.6 Actuation principles for mobile microrobots

As the energy source of mobile microrobots is almost always of the electrical type two conversions are required for transforming this energy in motion of the robot [118]. A first conversion, called actuation, is from electrical to mechanical energy based on different actuation principles. This conversion generates a short stroke, too short for motion of a "mobile" microrobot. The second conversion, called locomotion, is a mechanical to mechanical conversion that transform the short stroke displacement of the actuator into a displacement of the mobile robot with virtually infinite stroke.

Chapter 2 gives a systematic and complete literature review of the different locomotion principles (mechanical to mechanical conversion) for mobile microrobots. This thesis does, however, not discuss in detail the different actuation principles (electrical to mechanical conversion), because such reviews have already been reported several times in literature. For instance, a general overview of different actuation principles can be found in [119, 120, 121, 122], a review focussing on microactuators for micromechatronics in [123, 124, 12, 125], while specific reviews for microactuation of mobile microrobots are reported in [16, 126, 9, 118].

The rest of this section discusses shortly piezoelectric and electrostatic actuators as these two actuation principles are used for actuation of the experimental setup and the prototypes developed in this thesis. Other actuator principles such as electromagnetic, thermal, piezoelectric polymers, dielectric polymers, ionic polymer actuators, electrostrictive, magnetostrictive, shape memory alloys (SMA), hydraulic and pneumatic actuation are not discussed here as they are not practically used in this thesis.

### 1.6.1 Piezoelectric actuators

A good review of piezoelectric actuators and piezoelectric motors for micromechatronic application is given by Uchino and Giniewicz [127]. A review on emerging piezoelectric materials, technology, and applications can be found in [128]. A good introduction to piezoelectric actuators for positioning applications with inertial drives has also been presented by Breguet [129] and Bergander [130] in previous PhD dissertations at EPFL. Devos has studied and modeled piezoelectric actuators for application in ultrasonic motors in [131].

The denomination "piezoelectric actuators" generally refers to piezoceramic actuators, which are materials with a specific crystal structure that develop an electric charge when subjected to mechanical stress (direct effect) and that develop a mechanical strain when subjected to an electrical field (converse effect) [132]. The most used group of piezoceramic materials is PZT ($Pb(Zr_xTi_{1-x})O_3$). Within this group a difference can be made between hard PZT (typically high mechanical quality factors) and soft PZT (typically larger strains). Depending on the exploited displacement and the orientation of the polarization field $P$ and actuation field $E$ three different actuation modes of the actuators can be distinguished: axial, transversal and shear mode (see figure 1.2). In the case of axial and transversal mode, the actuation field is applied parallel (either in the same sense or in the opposite sense) to the polarization field, resulting into a simultaneous axial deformation ($\delta_h$) and a transversal deformation ($\delta_l$). When the actuation field is applied perpendicular to the polarization field, a shear strain ($\delta_s$) is induced. Table 1.2 gives an overview of the formula for free strain, blocking force and capacitance of piezoelectric actuators for the different actuation modes. Typical values [130] for coupling coefficients in the case of PZT are $d_{33} = 300 \ldots 800 \cdot 10^{-12}$ m/V, $d_{31} = -150 \ldots -350 \cdot 10^{-12}$ m/V, $d_{15} = 400 \ldots 900 \cdot 10^{-12}$ m/V. Typical values for the elastic constants are $s_{33} = 12 \ldots 23 \cdot 10^{-12}$ m$^2$/N, $s_{11} = 11 \ldots 17 \cdot 10^{-12}$ m$^2$/N and $s_{55} = 38 \ldots 48 \cdot 10^{-12}$ m$^2$/N. Relative permittivity constants are in the range of $\epsilon_{33} = 1500 \ldots 5500$

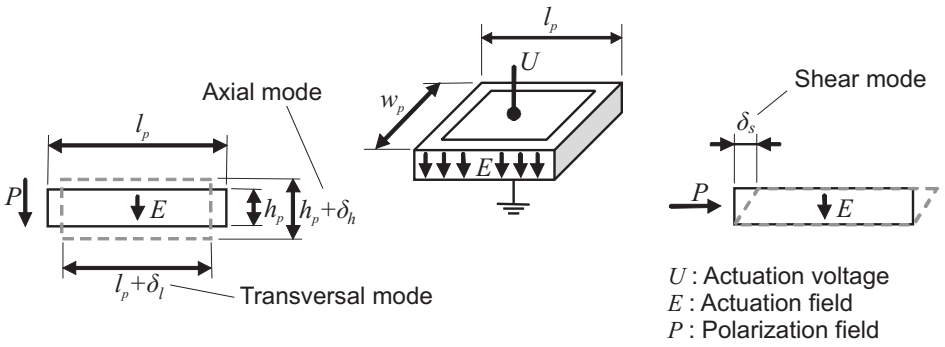


**Figure 1.2:** Actuation modes of piezoelectric actuators

| | Axial | Transversal | Shear |
|---|---|---|---|
| Free strain | $\delta_t = d_{33}U$ | $\delta_t = d_{31}\frac{l_p}{h_p}U$ | $\delta_s = d_{15}U$ |
| Blocking force | $F_b = \frac{d_{33}}{s_{33}}\frac{w_p l_p}{h_p}U$ | $F_b = \frac{d_{31}}{s_{11}}w_p U$ | $F_b = \frac{d_{15}}{s_{55}}\frac{w_p l_p}{h_p}U$ |
| Capacitance | $C = \epsilon_0\epsilon_{33}\frac{w_p l_p}{h_p}$ | $C = \epsilon_0\epsilon_{33}\frac{w_p l_p}{h_p}$ | $C = \epsilon_0\epsilon_{11}\frac{w_p l_p}{h_p}$ |

**Table 1.2:** Free strain, blocking force and capacitance for the 3 piezoelectric actuation mode

and $\epsilon_{11} = 1400 \ldots 4500$. Piezoelectric actuators feature a relatively low strain for high driving voltages, but a relatively high blocking force and bandwidth. The resulting energy density is high and the mechanical strain can be increased by a mechanical amplification. The most commonly used amplification mechanisms are multi layer actuators and bending actuators [132]. Other advantages of piezoelectric actuators are their high resolution, which is mainly limited by the driving electronics. In terms of electrical behavior a piezoelectric actuator can be approximated by a capacitance when actuated sufficiently below its first resonance frequency. Hence, the power consumption of a piezoelectric actuator with capacitance $C$ is given by $P = \frac{1}{2} \cdot fCU^2$, in which $f$ is the actuation frequency and $U$ the maximum voltage. More efficient operation and higher mechanical strains can be obtained when working in resonance mode.

Piezoelectric actuators are commonly used for locomotion and actuation of mobile microrobots. As will be illustrated in the literature review in chapter 2 piezoelectric actuators are integrated in mobile microrobots in the shape of multi layer stack actuators, single or multi layer bending actuators, piezo tubes and monolithic bulk actuators with electrode structuring. However, all most of the designs and the used fabrication techniques are difficult to scale down for robots much smaller than 1 cm$^3$. On the other hand several high resolution microfabrication techniques for thick and thin film printing of piezoelectric layers exist [133], but no piezoelectric microrobot of a size of some mm$^3$ has been reported yet.

### 1.6.2 Electrostatic actuators

When a voltage difference $U$ is applied between two parallel plates in the $XY$ plane and partially shifted along $X$ direction (see figure 1.3(a)) an electrostatic attraction force in $Z$ direction and an alignment force in $X$ direction are generated. The energy stored in a capacitance $C$ charged to a voltage $U$ is given by $W = \frac{1}{2} \cdot CU^2$ with the capacitance $C$ equal

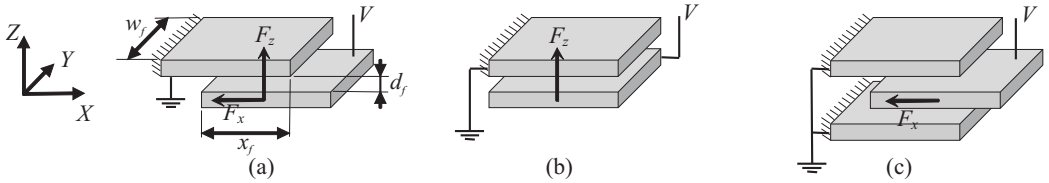


**Figure 1.3:** Perpendicular ($F_Z$) and lateral force ($F_X$) on an electrostatic actuator

to $C = \epsilon_0 \epsilon_r \frac{x_f w_f}{d_f}$. In accordance to the principle of virtual work, the two electrostatic forces can thus be calculated as

$$F_x = \frac{\delta W}{\delta x} = \frac{1}{2}\epsilon_0 \epsilon_r \frac{w_f}{d_f} U^2 \tag{1.1}$$

$$F_z = \frac{\delta W}{\delta z} = \frac{\delta W}{\delta d_f} = -\frac{1}{2}\epsilon_0 \epsilon_r \frac{x_f w_f}{d_f^2} U^2 \tag{1.2}$$

with usually $\epsilon_r = 1$ for air or vacuum environment.

Electrostatic actuators are designed to exploit either the perpendicular force $F_Z$ (figure 1.3(b)) either the lateral force $F_x$ (figure 1.3(c)). In order to increase the actuation force a large number of such elementary actuators are usually arranged in parallel resulting into interdigitated comb structures.

The most commonly used design is a comb structure of equally-spaced fingers, generally known as a comb drive actuator, resulting into a purely lateral force [134, 135, 124]. This design has the advantage of a linear behavior in the actuation direction ($X$), the possibility of large displacements (up to 150 $\mu$m) and a very good mechanical quality factor due to low internal damping of the actuator material (usually silicon) and the low air damping. If the interdigitated comb structures is not equally-spaced, a perpendicular force is generated. Such "offset comb drives" [136] or "gap-closing actuators" (GCA) [137] are less linear than comb drive actuators, feature lower displacements and more damping, but higher forces. Equally spaced and offset comb drive actuators can have resonance frequencies ranging from a few hundreds of Hz to several tens of kHz. Power consumption is typically very low as the involved capacitances are very low as well (max. some tens pF). On the other hand, for sizes of about 1 cm$^2$ the energy density is also relatively low compared to piezoelectric actuators: actuation forces are small and for large displacements high actuation voltages are required. However, one of the major advantages of comb drive electrostatic actuators is their aptitude to miniaturization thanks to well-mastered high-aspect ratio fabrication technologies such as Deep Reactive Ion Etching [138]. It is the latter advantage that makes from electrostatic actuators the most commonly used MEMS actuator for in-plane displacements.

Electrostatic actuators are not only used as displacement actuators but also as clamping actuators. The actuator then corresponds to the configuration depicted in figure 1.3(b), with typically between the two plates a dielectric with a high relative permittivity. MEMS fabrication technologies allow for very small (sub-micrometer) thicknesses of this dielectric layer, resulting into increased clamping forces.

## 1.7 Outline of this work

The current chapter of this dissertation introduced the field of mobile microrobots, stated the motivation of this thesis and discussed shortly the two actuation principles used for the prototypes developed in this thesis.

Chapter 2 gives a literature review and classification of locomotion principles for mobile microrobots and evaluates the suitability of each locomotion class for driving mobile microrobots.

Chapter 3 introduces the proposed Modulated Friction Inertial Drive (MFID) principle as well as the concept of a combination of on-board and off-board actuation.

Chapter 4 investigates the detailed stepping behavior of a MFID actuator through simulation and experiments. A dynamic model is proposed and validated with an experimental setup of a MFID linear actuator.

Chapter 5 demonstrates the MFID principle with three prototypes of mobile microrobots, allowing to illustrate the different configurations and the advantages and drawbacks of the MFID principle.

Chapter 6 restates the contribution of this work to the field of mobile microrobotics, revisits the major results and conclusions and prospects directions of future work.

## 1.8 Reading suggestion

In order to optimize the reading experience, an overview of sections that are essential and less essential for a good understanding of the research carried out in this thesis is given here.

**Chapter 1 Introduction** Section 1.2 describes the definition of the term "mobile microrobot" adopted in this thesis. Sections 1.3, 1.4.3 and 1.5 are important for understanding of the motivation of this thesis.

**Chapter 2 Review and classification of locomotion principles** Section 2.1 and 2.3 are essential for understanding the proposed classification of locomotion principles. A general overview of the suitability of the different locomotion classes for driving mobile microrobots can be achieved by reading for each locomotion class the evaluation (sections 2.4.2, 2.5.3, 2.5.6, 2.6.2, 2.7.2, 2.8.2, 2.9.3) as well as the conclusion (section 2.10).

**Chapter 3 The MFID locomotion principle** A thorough reading of the complete chapter is required for understanding the main concepts proposed in this thesis

**Chapter 4 Modeling and experimental characterization of a MFID actuator** Except for sections 4.3.2, 4.4.6, 4.4.7, 4.4.8 and 4.4.9 a thorough reading of chapter 4 is required for understanding the stepping motion of an MFID actuator.

**Chapter 5 Prototypes of MFID mobile microrobots** The design and the MFID operation of the three prototypes can be understood without the sections on prototype fabrication, calculation and characterization of vibration amplitudes, experimental setup and rotational motion (sections 5.2.2, 5.3.2, 5.3.3, 5.3.4, 5.3.5, 5.3.6, 5.3.9).

**Chapter 6 Conclusion and outlook** It is obvious that this chapter is one of the most important parts of this thesis.

# Chapter 2

# Review and classification of locomotion principles for mobile microrobots

*"Learn the past,*
*watch the present,*
*and create the future."*
Jesse Conrad

## 2.1 Introduction

Several reviews on the field of microrobots in general [9, 15, 139], on actuation of micromotors [140, 141] and on propulsion of mobile microrobots [16, 142, 126, 54, 143, 144, 9, 145] have already been reported in the literature. However, as already discussed in section 1.6, propulsion of mobile microrobots is generally the result of two energy conversions: an electrical to mechanical conversion (actuation) and a mechanical to mechanical conversion (locomotion). All the reviews mentioned above do not explicitly separate actuation principles from locomotion principle. A review on propulsion of mobile microrobots considering separately the actuation and the locomotion function is presented for the first time by Breguet *et al.* in 2006 [118]. In this thesis the same functional separation between actuation and locomotion is adopted. A short discussion of the two actuation principles used in this thesis (piezoelectric and electrostatic) is already given in section 1.6. This chapter gives a detailed literature review of locomotion solutions for mobile microrobots.

Different basis of classification of microrobots have been reported in literature. Two of them (a task-specific and a size-specific) have already been discussed in section 1.2. A third basis of classification based on on-board and off-board functions is first proposed by Hayashi in 1991 [146, 14] and adopted and modified by Dario *et al.* [16], Fatikow and Rembold [142] and Ebefors and Stemme [9]. The functions that can be integrated either on-board either off-board are: control unit (CU), power supply (PS), actuators for positioning (AP), actuators for manipulation (AM). Figure 2.1 shows 4 functional classes defined in [9] for the case of mobile microrobots walking on a substrate. The prototypes developed in this thesis[1] only include locomotion modules (AP) and are therefore part of functional class (a). Most

[1]For two of the three prototypes developed in this thesis the motion is obtained by a combination of on-board and off-board actuation. Hence, to be exact, these prototypes belong to a variant of functional class (a) defined in figure 2.1.

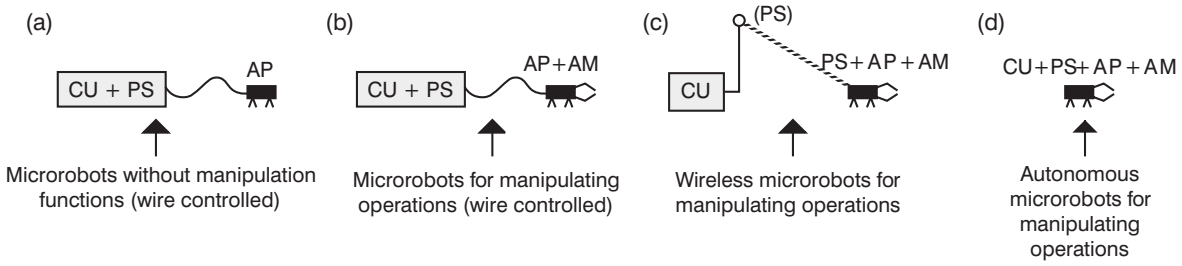


**Figure 2.1:** Functional classes for mobile microrobots moving on a solid substrate as defined in [9]

of the microrobots reported in literature that are used for a practical, robotic application have integrated locomotion (AP) and tools (AM), but are powered externally by means of wires (PS) (functional class (b)). For many applications the ideal would be to integrate also the power supply (PS) on the robot in order to obtain untethered robots that can be controlled by a central unit (CU) (functional class (c)). For other applications it might even be interesting to implement distributed control by integrating also the control unit (CU) on the robot (function class (d) in figure 2.1).

Apart from the size-specific, the task-specific and the function-specific classifications mentioned above, mobile microrobots are often grouped by their type of locomotion systems, such as stick-slip, inchworm, walking, scratch drive, etc. However, no systematic classification of locomotion types has been presented in literature until now. In this chapter the first functional classification of locomotion principles for mobile microrobots is presented. For each locomotion class the mobile microrobots reported in literature will be discussed and each locomotion class will be evaluated qualitatively and quantitatively.

Although it was stated in section 1.2 that in this work the term "mobile microrobot" is restricted to robots of an overall size of 1 cubic inch and below, this review also discusses some locomotion solutions implemented on larger mobile minirobots that are feasible to be scaled down for implementation on mobile microrobots. Furthermore, although very promising work with great potential is being done nowadays on swimming and flying microrobots, this review is restricted to locomotion on and in contact with a flat, solid substrate.

## 2.2 Propulsion of passive parts by external forces

A logical approach for scaling down the size of moving objects is by opting for completely passive parts and a propulsion by external forces.

Devices generating motion of passive parts on a substrate are often referred to as conveyors. Vibratory conveyors are, among other conveyor types, extensively studied in literature as they are widely used in industry for parts feeding in production and assembly lines. The part propulsion on vibratory conveyors is a result of the conveyor substrate vibration, which can be a sinusoidal vibration along an inclined straight line [147, 148], a combination of an out-of-phase longitudinal and perpendicular vibration [149, 150, 151], a non-sinusoidal asymmetric longitudinal vibration on a smooth surface [152] or a symmetric longitudinal vibration on an engineered surface (typically saw tooth shaped) [153]. Vibratory conveyors exist as spiral shaped feeders (vibratory bowl) and as linear conveyors with one or two degrees of freedom and can be used for part sizes down to less than 1 mm [153].

The integration of a large number of micro-actuators on a substrate allowed by MEMS fabrication technologies has lead to the development of MEMS conveyors of which the driving

conditions can be varied locally allowing for so-called distributed manipulation [154]. A review of MEMS based conveyor devices is given by Ebefors *et al.* in [155]. The conveyors can be divided into contact type and contact free type conveyors. Contact-free systems have been realized using pneumatic, electrostatic or electromagnetic forces creating a cushion on which the mover levitates. Contact type systems are based on arrays of movable legs erected from the wafer surface and actuated by thermal, electrostatic, piezoelectric and magnetic means.

Mathieu *et al.* [31] have demonstrated that it is possible to propel and steer a microdevice in a human blood circulatory system using the strong magnetic field of a Magnetic Resonance Imaging (MRI) instrument. Similarly, Yessin *et al.* [156] are investigating the limit and potential of such system for drug delivery, cell separation, protein manipulation or in-situ measurement of chemical and physical properties. Andre *et al.* [51] report on the use of swimming bacteria that swim in the direction of an externally applied magnetic field in order to propel a microrobot in liquid media. An alternative strategy for the propulsion of microparts in liquid media is by means of optical radiation pressure — often called laser tweezers, optical tweezers or laser trap — as for instance discussed by Arai *et al.* in [157]. Untethered propulsion of microscopic objects on a substrate in dry or liquid media by magnetic forces generated by a moving permanent magnet on the other side of the substrate is reported by Dauge *et al.* [158]. There is a great potential for the approach of propulsion by means of external forces, but many challenges still remain. In particular, the absence of any on-board power poses severe constraints on the type of in-situ manipulation or measurement that can be carried out by such a microrobot. Of course the approach of propulsion by external forces does not exclude the integration of on-board powering for only manipulating or sensing purposes. This is demonstrated in 2002 by Khamesee *et al.* [159] who developed a microrobot (length 50 mm, body diameter ∅12 mm) that is magnetically levitated with the help of external coils and contains an on-board SMA actuated gripper powered by on-board batteries and remotely controlled with the help of LEDs and a photosensitive IC.

The rest of this review, however, does not treat the propulsion of completely passive parts by external forces such as in the conveyor and propulsion systems discussed above.

## 2.3 Classification of locomotion principles

As mentioned in the introduction of this chapter, this literature review only considers locomotion on and in contact with a flat, solid substrate. Relative motion between two solid bodies that are in contact with each other can only happen if either rolling either slipping occurs at the interface between both media.

Rolling motion with wheels can be implemented either by using the wheels only for guiding and apply an additional thrust force, either by driving the rotation of the wheels. Such an additional thrust force could be a jet or an air flow that is generated on-board as used for large high speed vehicles. Such jet propulsion will not be considered in this review. Wheel driven locomotion, on the other hand, is widely used and very efficient for macro- and miniscale robots. However, as the literature review will point out scaling down wheeled locomotion to a size of 1 $cm^3$ and below is possible, but goes with a gradual loss in efficiency of the actuation and guiding of the rotational motion.

As for rolling motion, slip motion can be driven by an additional thrust force (not considered here) or by an actuation of the contact points at which the slip occurs. As such an actuation of the contact points is — rolling excluded — of limited stroke some kind of repetitive stepping motion is required in order to allow for the long motion range required for mobile robots.

One of the contributions of this thesis, and in particular of this literature review, is the

identification of two essential functions of a stepping mechanism: *slip generation* and *slip variation*[2]. It is obvious that without *slip generation* the motion range of the robot would be limited to the displacement range of its actuators. Besides slip generation, a second requirement for successful locomotion is that the forward slip is not equal to the backward slip (*slip variation*), as otherwise the robot would be sliding in place and no net motion would be generated.

In this thesis a classification of stepping principles based on the two functions *slip generation* and *slip variation* is proposed [160]. As illustrated in table 2.1 slip can be generated either by a *differential* displacement between contact points either by the *inertial* effect of a dynamic displacement of the robot's feet with respect to the robot's body. In order to identify the possibilities for *slip variation* the theoretical slip distance $\Delta x_{slip}$ is expressed as the double integration over the slip time $\Delta t$ of its acceleration $a$

$$\Delta x_{slip} = \int_{\Delta t} \int_{\Delta t} a \, dt^2. \tag{2.1}$$

The acceleration can be expressed as $a = \frac{F_t}{M}$ with $M$ the mass of the robot and $F_t$ the friction force, which depends on friction coefficient $\mu$ and contact force $F_c$

$$\Delta x_{slip} = \int_{\Delta t} \int_{\Delta t} \frac{\mu F_c}{M} \, dt^2. \tag{2.2}$$

Equation 2.2 shows that the (forward and backward) slip distance can be varied by varying three parameters: contact force $F_c$, friction coefficient $\mu$ and slip time $\Delta t$. In other words the 3 solutions for *slip variation* are respectively: contact force variation, directional friction and asymmetric actuation. Based on the two solutions for slip generation and the three solutions for slip variation 6 different classes of stepping mechanisms are defined in table 2.1: $DF_c$, $IF_c$, $D\mu$, $I\mu$, $D\Delta t$ and $I\Delta t$.

Based on this classification a review of locomotion modules used for mobile and microrobots reported in literature is given in the rest of this section. For each robot the size, motion velocity and power consumption[3] is analyzed. Based on the data gathered from this literature review, each class of locomotion principles is evaluated in terms of their suitability for driving mobile microrobots. The evaluation is based on the following criteria:

- $v_s$ specific motion velocity, expressed in body lengths per second[4] (L/s), where the body length L is defined as the geometric mean of the footprint dimensions[5]
- $P_s$ specific power consumption expressed as the consumed power (in mW) per unit of motion velocity (in mm/s): $\frac{\text{mW}}{\text{mm/s}}$
- DOF the number of DOF with unidirectional motion only counting as half a DOF
- Elec Suitability for driving with an on-board driving electronics, mainly depending on the number of actuation channels per DOF, actuation voltages and driving currents
- 1 cm$^3$ Ease of fabrication and assembly for a size of 1 cm$^3$ and below
- Res motion resolution (i.e. the smallest repeatable step size), which is an important parameter in the case of precision applications

[2]It should be noted that the concept of *slip* is interpreted here in a generalized way, also including the relative motion without contact, which is considered as slip with zero friction force.

[3]Unfortunately, although on-board powering is a major issue for mobile and microrobots, the power consumption is not specified for many of the robots presented in literature. Where possible the power consumption was approximately calculated. For resistive loads the power consumption of the actuator is calculated as $P = UI$. For capacitive loads the power is calculated as $P = \frac{1}{2} \cdot fCU^2$ (with $U$ the driving voltage, $I$ the driving current, $f$ the driving frequency and $C$ the electrical capacitance). In the case of bipolar actuation ($[-U, +U]$))of capacitive loads a factor 2 is added $P = \frac{1}{2} \cdot fC \cdot 2U^2$.

| | | Slip generation | |
|---|---|---|---|
| | | Differential ($D$) | Inertial ($I$) |
| **Slip variation** | Contact force variation ($F_C$) | $DF_c$ 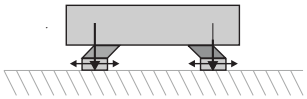 | $IF_c$ 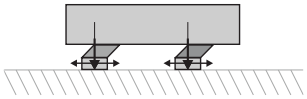 |
| | Directional friction ($\mu$) | $D\mu$ 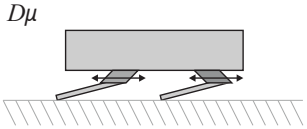 | $I\mu$ 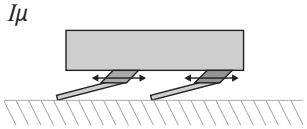 |
| | Asymmetric actuation ($\Delta t$) | $D\Delta t$ 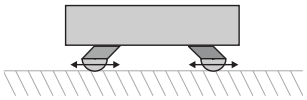 | $I\Delta t$ 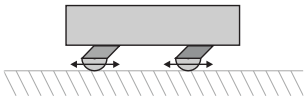 |

**Table 2.1:** Classification of locomotion principles based on stepping motion

For all of the criteria listed above an evaluation is done with the following scale:


The literature review in the rest of this chapter discusses first robots with wheeled locomotion. Then, the six classes of stepping motion are treated successively. For each locomotion class first the literature on mini and microrobots is reviewed and consequently the suitability of the locomotion class for driving mobile microrobots is evaluated with the criteria mentioned above. At the end of this chapter a comparison of the discussed locomotion classes is made.

## 2.4 Wheeled locomotion

Wheeled locomotion is definitely the most efficient way in terms of motion velocity and power consumption for driving macroscale robots. Wheeled locomotion has the advantage of low friction with the substrate, allows for low friction ball bearings and can be directly driven by electromagnetic rotary motors, which feature — at that scale — a high efficiency. However, for microrobots in the 1 cm$^3$ range and below the integration of efficient rotary bearings is very complicated and the efficiency of electromagnetic motors decreases considerably[6].

[4] A study reported by T. Hayashi [14] has shown that the motion of animals and machines generally scales linearly with their size, so the velocity in terms of body lengths per second should be size independent.

[5] For in-pipe robots the body length is defined as the geometric mean of the robot diameter and the robot length.

[6] An analysis of scaling laws for different actuation technologies can be found in [11, 12, 14]

Another drawback of wheeled locomotion is that — except for some designs — it typically results in nonholonomic locomotion[7] with 2 DOF $(X, \theta_Z)$. Nonholonomic locomotion can be a problem for certain applications, specifically handling applications.

### 2.4.1 Literature review

In 1989 a wheeled mobile robot of about 1 in$^3$ developed at MIT is presented by Flynn *et al.* [161, 8]. The robot called *Squirt* is actuated by one motor, which drives one of the rear wheels, while the other rear wheel slips through an unidirectional clutch. The front is supported by castors. This arrangement causes the robot to go straight when moving forward and to pivot about a rear wheel when backing. The robot has on-board powering and control circuitry.

Probably one of the most intelligent autonomous microrobots ($< 1$ in$^3$) is the *Alice* robot developed at EPFL by Caprari *et al.* [162, 13]. The Alice 99 version (see figure 2.2(a)) features an overall size of $21 \times 21 \times 12$ mm$^3$ with integrated powering (autonomy 10 hours), overall power consumption 4-10 mW depending on the operation, on-board proximity sensors, IR and radio communication. It is driven by two watch movement motors from ETA (Swatch Group), featuring a maximum velocity of 40 mm/s and a power consumption of 3 mW (total for two motors). A comparison in [13, 17] with other electromagnetic motors of similar size shows the superior characteristics of this motor in terms of power consumption and torque. Different robot versions and extensions have been developed for the Alice robot in order to be able to meet the demands of a large range of applications [163]. The features and performances of the Alice robot make it an interesting robot for education and research on collective multi robot (swarm) behavior. Another robot for research on swarm behavior has been developed jointly by the University of Stuttgart and the University of Karlsruhe within the scope of the European project *I-Swarm* [46, 164]. The *Jasmine* robot [85, 86] (see figure 2.2(b)) has an overall size of $26 \times 26 \times 26$ mm$^3$ and one of its design criteria was an overall component cost of less than 100 €. Apart from the lower cost *Jasmine* features increased functionality in terms of on-board electronics and a higher maximum motion velocity compared to *Alice*. It is driven by two DC motors, which are cheaper than the watch motors of *Alice*, but also consume much more. The overall consumption (at maximum velocity and maximum communication activity) is about 200 mA at 3.7 V or 740 mW, which is much higher than that of *Alice*. Fortunately, it is powered by a lithium-ion polymer battery with a large capacitance (250 mA/h), which still results in a autonomy of 1-2 hours. Several other autonomous microrobots of a size of about 1 in$^3$ and driven by DC motors have been reported in literature. They are not discussed here because their construction is similar to the *Alice* and *Jasmine* robot, a design that is difficult to scale down below 1 cm$^3$. An overview of these robots can be found in [17].

In the framework of a DARPA-funded plume tracing project, a 0.25 in$^3$ (i.e. about 4 cm$^3$) autonomous robot (see figure 2.2(c)) was developed at Sandia National Laboratories in 2001 [113]. The chassis of the Mini Autonomous Robot Vehicle (MARV) is fabricated by stereolithography and the two track belts are driven by two ∅3 mm Smoovy gear motors (RMB SA) with a two-stage planetary gear system for a 1:25 speed reduction. It consumes about 220 mW of power, and will run about 10 min on new batteries. In order to meet the constraints in terms of size, the on-board electronics is a hybrid assembly of unpackaged IC components and passive SMD components.

*Pico* (see figure 2.2(d)) is a home-brew robot of an overall size of $12.5 \times 12.5 \times 12.5$ mm$^3$. It is driven by two ∅4 mm × 8 mm DC motors. Powered by a 10mAh Li-Poly battery

[7] Nonholonomic locomotion (as a car) allows for all in-plane positions $(X, Y, \theta_Z)$ to be reached, but only by approaching along specific paths.

(approx 3.7V), it features an autonomy of 15 minutes corresponding to an overall average power consumption of about 140 mW.

In 1993 Seiko Epson Corporation presented *Monsieur*: an autonomous robot of a size of $11 \times 12.4 \times 10.8$ mm$^3$ (see figure 2.2(e)) [49]. It is driven by two small stepping motors yielding a maximum velocity of 14.7 mm/s. It was commercialized for the Japanese market in 1993. In 1994, *Monsieur* entered the Guinness Book of World Records as the world's smallest robot. In the 1994 and 1995 the EMRoS (Epson Micro Robot System) family was expanded with three other microrobots: Niño (0.5 cm$^3$), Ricordo (1 cm$^3$, equipped with a recording and playback function) and Rubie (1 cm$^3$, equipped with capricious wandering function). Later, in 2003, they presented *Monsieur II-P*, which is a bit larger (7.8 cm$^3$), but with integrated bluetooth module for wireless communication, longer autonomy (5 hours) and driven by two ultra thin ultrasonic motors up to a maximum controlled velocity of 70 mm/s [53].

The example of the *Monsieur* robot was followed by Citizen Watch Co., Ltd., another Japanese watch maker that presented *Eco-Be* in 1995. The improved version presented in 2001 (see figure 2.2(f)) features an overall size of $18 \times 18 \times 25$ mm$^3$ and is remotely controlled by IR [87]. The robot is powered by a CR1616 coin-shaped lithium battery (3 V, 50 mAh) and driven by two step motors (size $7 \times 8.5 \times 1.9$ mm$^3$) that consume 4-12 mA (12-36 mW) each and drive the robot up to a maximum velocity of 25 mm/s. *Eco-Be* made its appearance to the public at RoboCup 2006 (an international robotics football competition held annually), where the RoboCup Citizen Eco-Be League was introduced.

A 1 cm$^3$ robot called *Jemmy* has been developed at EPFL (see figure 2.3(a)) [166]. It is driven by two electromagnetic ∅3 mm RMB Smoovy motors, it has an on-board driving electronics, but is powered by wires. It was the winner of the International Microrobot Maze Contest '97, Nagoya (Japan) in the 1 cm$^3$ category. The same lab also developed another 1 cm$^3$ robot driven by rotating piezomotors with an efficiency of 30% yielding a maximum robot velocity of 250 mm/s [167, 166].

In 1998 Dario *et al.* presents the *Pollicino* (Tom Thumb) a teleoperated mobile microrobot (see figure 2.3(b)) of $10 \times 10 \times 10$ mm$^3$ actuated by two electromagnetic wobble micromotors [168]. The developed wobble micromotors are based on the variable reluctance principle and are integrated directly into the wheels of the robot. Each motor consists of three coils of which two are actuated at the same time with a current of 140 mA, which corresponds to an overall power consumption of 165 mW (resistance of two coils 4.2 Ω). The robot has a maximum velocity of 100 mm/s and can climb a slope of 15°. The robot won the 1995 and 1996 "International Micro Robot Maze Contests" in Nagoya. The power of this 1 cm$^3$ robot is supplied through wires. In 1999 a 1 inch$^3$ autonomous adaptation with batteries and sensors was also built [17]. A smaller, 4 mm diameter version of the wobble micromotor has also been developed [168].

All the robots presented above are driven by two wheels and feature two degrees of freedom $(X, \theta_Z)$. Such non-holonomic locomotion can be a serious drawback for certain applications such as handling and manipulation. Li *et al.* propose a solution by developing two omnidirectional wheel-driven robots. A first omnidirectional mobile microrobot (OMMR-I, see figure 2.3(c)) consists of two castors that can be oriented simultaneously by one motor to any in-plane direction [169]. Each castor consists of two coaxial wheels of which one is driven by a custom developed electromagnetic micromotor. The $2.1 \times 2.1 \times 1.3$ mm$^3$ motor consists of six planar coils in the microfabricated stator and a multipolar rotor, which is the wheel. These micromotors can drive the robot, which has an overall size of $8 \times 6 \times 6$ mm$^3$ up to a maximum velocity of 100 mm/s. A second design (OMMR-II, see figure 2.3(c)) consists of three orientable castors with one wheel and one motor each [170]. The motor is slightly larger than for the previous robot ($3.1 \times 3.1 \times 1.4$ mm$^3$), but are based on the same principle

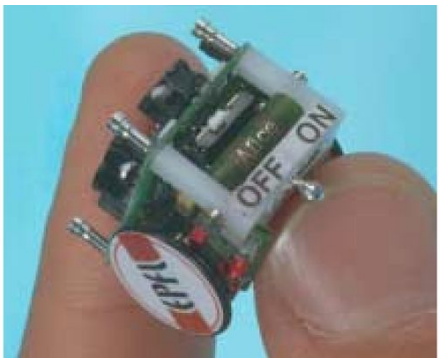


**(a)** Alice 99, EPFL, CH [13]
$21 \times 21 \times 12$ mm$^3$, 40 mm/s, 4-10 mW

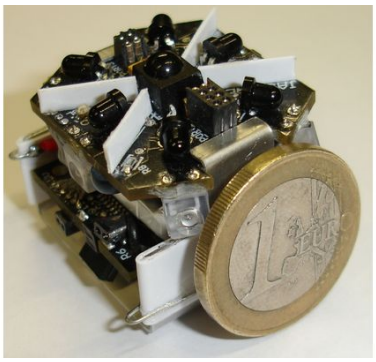

**(b)** Jasmin, I-SWARM [85]
$26 \times 26 \times 26$ mm$^3$, 200 mm/s, 740 mW

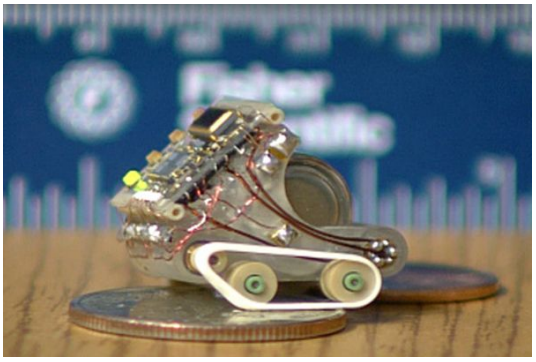

**(c)** MARV, Sandia Nat. Labs, US [113]
4 cm$^3$, 17 mm/s, 220 mW

**(d)** Pico, Tezuka, O. [165]
$12.5 \times 12.5 \times 12.5$ mm$^3$, 150 mm/s, $\sim$ 140 mW

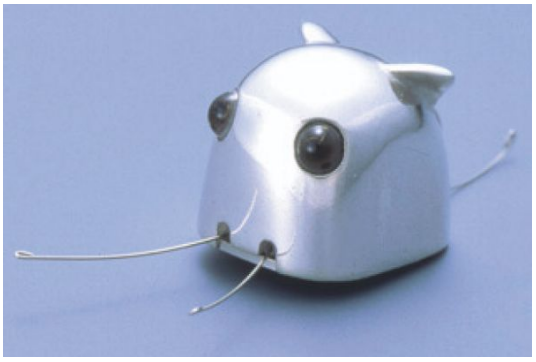

**(e)** Monsieur I, Seiko Epson Corp, JP [49]
$11 \times 12.4 \times 10.8$ mm$^3$, 15 mm/s


**(f)** ECO-BE, Citizen Watch Co., Ltd., JP [87]
$18 \times 18 \times 25$ mm$^3$, 25 mm/s, 24-72 mW (motors)

**Figure 2.2:** Wheeled microrobots of a size $> 1$ cm$^3$

| | $v_s$ [L/s] | $P_s$ [$\frac{\text{mW}}{\text{mm/s}}$] | DOF | Elec | 1 cm$^3$ | Res |
|---|---|---|---|---|---|---|
| Wheels | $1 \cdots 10$ | $10^{-1} \cdots 10$ | 2 | | | |

**Table 2.2:** Evaluation of wheeled locomotion for mobile microrobots

of planar coils in the stator and a multipolar rotor (the wheel). The smallest step size of the motors is 70 $\mu$m. The robot is equipped with a piezoelectric gripper and the robot has been used for a manipulation experiment controlled by optical tracking.

In 1995 Nippondenso Co., Ltd. (now DENSO Corporation) presented a $1/1000^{th}$ scale replication of Toyota's first passenger car, the 1936 Model AA sedan (see figure 2.3(e)) [18, 171]. The microcar has an overall size of $4.8 \times 1.8 \times 1.8$ mm$^3$ and consists of 24 parts including body, tires, spare tire, wheels, axle, bearings, headlights, rear lights, front bumper, rear bumper, step, number plate and emblem. It is driven up to a maximum velocity of 100 mm/s by one custom developed electromagnetic motor, which consumes 20 mA of alternating current at 3V (i.e. a power consumption of 60 mW) supplied by two electrical wires. In 1995, the microcar was awarded by the Guinness Book of Records as the world's smallest motorized car.

### 2.4.2 Evaluation

Wheeled locomotion features excellent motion velocities ranging from 1 L/s (body length per second) up to 30 L/s. It should be noted that for an average passenger car with a length of 4.5 m a velocity of 30 L/s corresponds to 135 m/s = 486 km/h! Wheeled locomotion also features very good power efficiency with specific power consumptions ranging from 13 $\frac{\text{mW}}{\text{mm/s}}$ for the robot from Sandia Nat. Labs, mainly because of friction in the caterpillar tracks, down to only 0.1 $\frac{\text{mW}}{\text{mm/s}}$ for the ALICE robot, because of the low power consumption of the used watch motors. One of the major drawbacks of wheeled locomotion is that at this scale it only allows for nonholonomic motion. At the macroscale real 3 DOF wheeled motion can be obtained with the use of omnidirectional wheels. However, omnidirectional wheels are to complicated for implementation at the cm$^3$ scale. The solution implemented on the omnidirectional robots in figures 2.3(c) and 2.3(d) allows to change the direction of the translational DOF, but does not provide real 3 DOF as preferred for robotic manipulation. The driving electronics for wheeled robots is very simple: low driving voltage without peak currents. The state of the art shows that miniaturization of wheeled robots to a size well below 1 cm$^3$ is possible. However, at that scale the efficiency of the electromagnetic motors and rotary bearings considerably decreases and sophisticated 3D fabrication and assembly techniques are necessary. Micrometer resolution can be obtained with rotary motors if encoders and a large reduction without play can be used. Moreover, wheeled locomotion allows for a relative, open loop precision (by odometry) that is typically better than the stepping principles presented below as principally no slip occurs between the wheels and the substrate. However, at a size of in$^3$ performance of encoders and reduction are rather limited, while at a size below 1 cm$^3$ they become unfeasible (except if they integrated directly in the motor operating principle as for the wobble motor of the robot in figure 2.3(b)). Table 2.2 summarizes the evaluation of the suitability of wheeled locomotion for driving mobile microrobots.

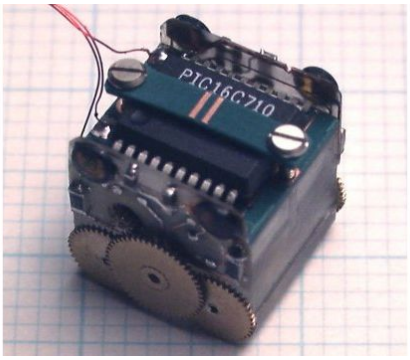


**(a)** Jemmy, EPFL, CH [166]
1 $cm^3$

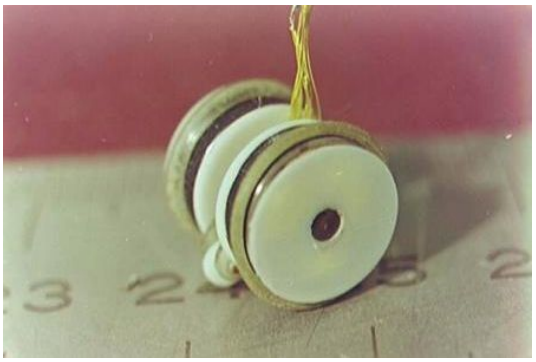

**(b)** Pollicino II, SSSA, IT [168]
$10 \times 10 \times 10$ $mm^3$, 100 mm/s, 165 mW

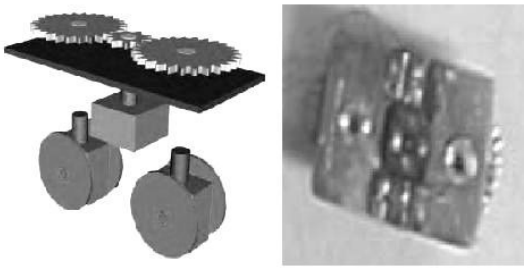

**(c)** OMMR-I, Shanghai Jiao Tong U., CN [169]
$8 \times 6 \times 6$ $mm^3$, 100 mm/s

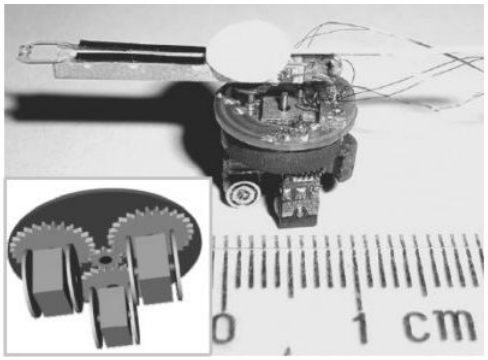


**(d)** OMMR-II, Shanghai Jiao Tong U., CN [170]
$9 \times 9 \times 6$ $mm^3$, 50 mm/s

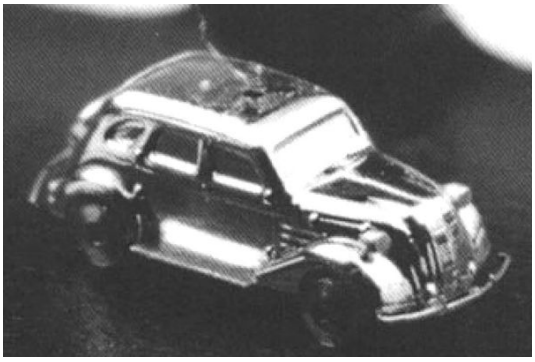

**(e)** Nippondenso Co., Ltd., JP [18]
$4.8 \times 1.8 \times 1.8$ $mm^3$, 100 mm/s, 60 mW

**Figure 2.3:** Wheeled microrobots of a size $\leq 1$ $cm^3$

## 2.5 Differential slip generation with contact force variation (class $DF_c$)

The two most used locomotion principles based on differential slip generation and contact force variation are the walking principle and the inchworm principle. The difference between both principles lies in the way the contact force is varied. For walking the contact force is varied by transferring the weight completely from one set of contact points (feet) to another. For the inchworm principle the contact force is varied by adding an additional contact force typically generated by mechanical, electromagnetic or electrostatic clamps at each contact point. The rest of this section discusses the state of the art of mobile microrobots (and some minirobots) based on the walking and the inchworm principle as well as some variants of these locomotion principles.

### 2.5.1 Literature review on walking locomotion

Just as wheels are the most straightforward choice for locomotion of microrobots when being inspired by macroscale robots, locomotion by walking is definitely the most obvious choice if one is inspired by nature. During walking motion the weight of the robot is alternately supported by two sets of contact points or feet (typically two sets of three), which is the result of a differential vertical displacement. This differential vertical displacement is superposed with a differential, horizontal back and forth displacement between each transfer of the robot weight. Both differential displacements (vertical and horizontal) can be obtained either by moving only one set of feet either by moving both sets of feet in opposite direction. Walking is essentially a quasistatic locomotion principle. High frequency walking is possible, but can result in dynamic effects such as bouncing of the feet on the substrate, which can cause motion instabilities.

Rembold and Fatikow present in 1997 [172] a piezoelectric walking robot called *SPIDER-II*. It is actuated by 9 piezoelectric bimorph actuators. Three feet can be actuated independently in $X$ and $Y$ direction by two bimorph actuators per foot, while the three other feet can be actuated vertically by one bimorph actuator per foot. The robot has an overall size of 105 cm$^3$ (so according to the definition stated in section 1.2 this is a minirobot and not a microrobot) and is actuated with $\pm 60V$ signals. The driving electronics is integrated on the robot, while power and control is supplied by six wires. A piezoelectrically actuated microgripper is integrated on the robot for micromanipulation applications.

Within the scope of the MINIMAN project [96] another piezoelectrically actuated microrobot based on the walking principle is presented by Simu *et al.* from Uppsala University (see figure 2.5(a)) [173, 174]. The monolithic fabrication process of multilayer piezoelectric actuators allowed for an overall size of the robot of only $10 \times 10 \times 22$ mm$^3$. The *MINIMAN V* robot features 3 DOF for locomotion as well as 3 DOF for the manipulator that is mounted on top of the robot. The same actuation module ($10 \times 10 \times 6$ mm$^3$) used for locomotion is also used for the rotation of the sphere on which the tool can be attached. Each actuation module consists of 6 legs with 3 DOF (two bending modes and one axial mode) and 4 actuation channels each. Apart from quasistatic walking, the robot can also be actuated in stick-slip mode and inertial stepping mode [175]. The robot features a maximum velocity of 5 mm/s for a driving voltage of $U = 50$ V and a driving frequency of $f = 1$ kHz [176]. Each actuation channel has a capacitance of $C = 24$ nF, which results in a total power consumption of $P = 6 \cdot 4 \cdot \frac{1}{2} \cdot fCU^2 = 720$ mW. The robot is equipped with an on-board electronics for generation of the 24 signals and is powered and controlled by means of 6 wires.

MEMS fabrication technology has a great potential for the fabrication of insect inspired

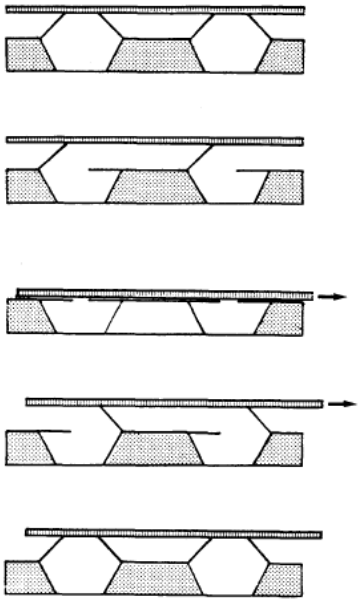

**Figure 2.4:** Walking motion with ciliary motion fabricated by MEMS technologies as proposed in 1989 by Benecke and Riethmuller [177]

locomotion modules. The concept of walking motion by means of MEMS fabricated ciliary actuators (see figure 2.4) was already proposed by Benecke and Riethmuller in 1992 [177]. Based on this concept Ebefors *et al.* (Royal Institute of Technology, Stockholm) presented the first MEMS mobile robot in 1999 (see figure 2.5(b)) [178]. The robot is actuated by thermal polyimide joint actuators that bend out of the plane of the silicon robot. The robot has a size of $15 \times 5$ mm$^2$ (silicon substrate thickness 0.5 mm) in which two rows of four legs are integrated. The robot features 2 DOF with a maximum translational velocity of 6 mm/s and can carry a load of 30 times its body weight. The maximum velocity is reached at a driving frequency of 100 Hz and a driving voltage of 18 V. The biggest drawback of this robot is that it suffers from a high power consumption (about 1.1 W), which makes untethered operation difficult with the current state of powering technology.

Kladitis *et al.* [179] (University of Colorado at Boulder) presented two MEMS robot prototypes based on walking motion in 2000. The robots are actuated by thermal actuators that are erected manually from the silicon substrate. The first prototype (size $10 \times 10 \times 0.75$ mm$^3$) has 96 legs that can bend in 2 DOF. A second prototype (chip size $5 \times 5 \times 0.5$ mm$^3$, see figure 2.5(c)) has 90 legs with 1 DOF each. No mobile robot locomotion could be demonstrated, possibly due to the wire stiffness. However, both designs have been demonstrated as microconveyors (i.e. upside down operation). The 2-DOF prototype was capable of transporting a mass of 3.06 mg at 7.55 $\mu$m/s for a driving frequency of 2 Hz and a driving voltage of 5 V, which corresponds to a power consumption of 714 mW (resistance R=35 $\Omega$).

Mohebbi *et al.* [180] present another walking MEMS microrobot in 2001. The robot has an overall size $30 \times 10 \times 1$ mm$^3$ and consists of two actuator chips ($10 \times 10$ mm$^2$) assembled at each end. Each actuator chip is composed of 256 cilia in an $8 \times 8$ array of cilia motion pixels where each motion pixel contains four orthogonally oriented cilia actuators, resulting in a robot with 3 DOF. The robot reaches a maximum translational velocity in diagonal direction of 635 $\mu$m/s and a maximum rotational velocity of 0.037 rad/s for a driving frequency of

110 Hz. The robot has a high power consumption of 1600 mW, which causes the robot to heat up after a certain time of operation causing a decrease in motion velocity [181].

Another thermally actuated walking MEMS robot is presented by Bonvilain and Chaillet in 2003 [182]. The robot has an overall size of $6 \times 3.5 \times 0.5$ mm$^3$ and has six legs. Each leg is actuated by two thermal silicon-SU8 bimorph actuators. Simultaneous bending of both actuators causes the contact point (foot) to bend upwards (i.e. out-of-plane), while differential actuation results in a local rotation which causes the foot move horizontally [183]. Locomotion has, however, not yet been demonstrated. Theoretically, a velocity of 0.1 mm/s should be reached. The robot is expected to be able to run for about 3 hours with an energy of 2750 J, which corresponds to a theoretical power consumption of about 250 mW.

A comparison of the performances of the thermally actuated with the piezoelectrically actuated walking robots clearly shows the major drawback of thermal actuators: the high power consumption. As on-board powering is probably the biggest challenge in mobile microrobotics, this is very important obstacle for thermally actuated autonomous mobile microrobots. Remotely powering of thermal actuators could, however, be a solution as suggested for walking motion by Baglio *et al.* in [184] and illustrated for impact drive locomotion by Ohmichi *et al.* [82] and Sul *et al.* [83]. Piezoelectric actuators, on the other hand, suffer from low strains resulting in small displacements of the robot's feet. Mechanical amplification can result into displacement amplitudes that are sufficiently large. A promising design of a MEMS array of piezoelectrically actuated 3-DOF legs is proposed by Ruffieux *et al.* [185]. Each actuator has a triangular shape with sides of 400 $\mu$m and consists of three piezoelectric out-of-plane bimorph actuators and a vertical leg of 300 $\mu$m length. The actuator has shown horizontal and vertical displacement amplitudes of 10 $\mu$m and 3 $\mu$m respectively for quasistatic operation with a driving voltage of only $\pm$10 V. Moreover a quality factor of 14 has been measured for the vertical resonance mode. Unfortunately, no locomotion has been reported with this design.

An interesting trade-off between low power consumption and large strain can be obtained with electroactive polymer (EAP) actuators. In 1997 Tadokoro *et al.* [186] demonstrated walking motion with Ionic Conducting Polymer gel Film (ICPF) actuators for driving a rotational actuator. By combining the ICPF actuators in pairs elliptic motion of the contact point can be generated resulting in a tangential velocity of about 2.5 mm/s for a driving frequency of 5 Hz and a driving voltage of only $\pm$1.5 V. In 2002 Kim *et al.* (Korea Institute of Science and Technology, South Korea) [187] presented a walking minirobot based on Ionic Polymer Metal Composite (IPMC) actuators. The robot (see figure 2.5(f)) has an overall size of $65 \times 42 \times 15$ mm$^3$ and is actuated by two rows of 4 IPMC actuators of a length of 20 mm. The robot has shown a maximum velocity of 0.28 mm/s for a driving frequency of 0.8 Hz and driving voltage of $\pm$4 V. A miniaturized design and control of a microrobot with six legs each consisting of two microfabricated IPMC actuators is proposed by Otis *et al.* [188]. It should be noted, however, that these ICPF and IPMC actuators have to be actuated in aqueous environment, which limits the applications to underwater operation. New technological developments, for instance the one proposed by Gursel *et al.* [189], allow for actuation of conducting polymer actuators in air. Development of microfabrication technologies for these polymer actuators is also required for the integration of these promising actuators in cm$^3$ size microrobots.

Electrostatic actuators feature low power consumption and are well suited for miniaturization by MEMS fabrication technologies, but large displacements can only be reached with high actuation voltages. Two techniques for the amplification of the displacement have been used for the locomotion of mobile microrobots: operation in resonance mode or by stepping mode operation. The solution of electrostatic resonance mode actuation of microrobots is

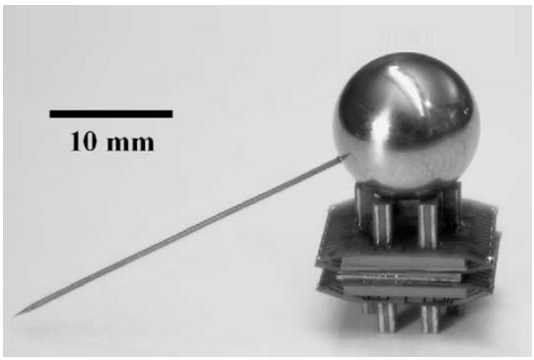


**(a)** MINIMAN V, Uppsala U., SE [173, 174]
$10 \times 10 \times 22$ mm$^3$, 5 mm/s, 720 mW

**(b)** KTH, Royal Inst. of Technology, SE [190]
$15 \times 5 \times 0.5$ mm$^3$, 6 mm/s, 1100 mW

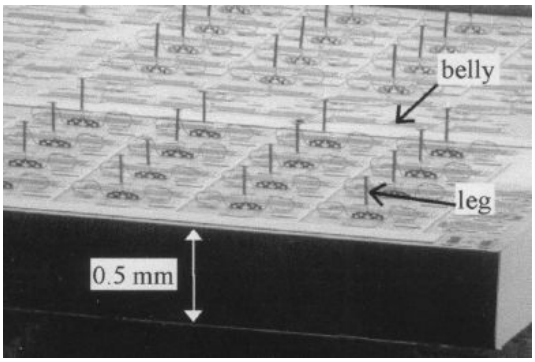


**(c)** U. of Colorado at Boulder, US [179]
$10 \times 10 \times 0.5$ mm$^3$, 0.076 mm/s, 714 mW

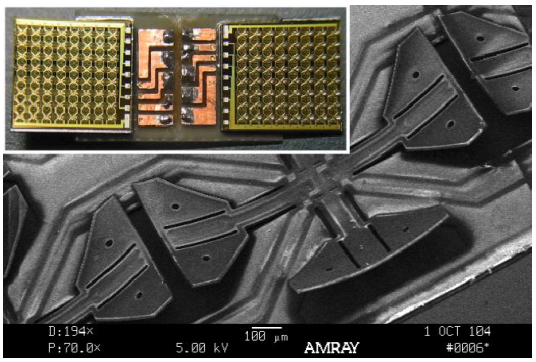


**(d)** University of Washington, US [180, 181]
$30 \times 10 \times 1$ mm$^3$, 0.25 mm/s, 1600 mW

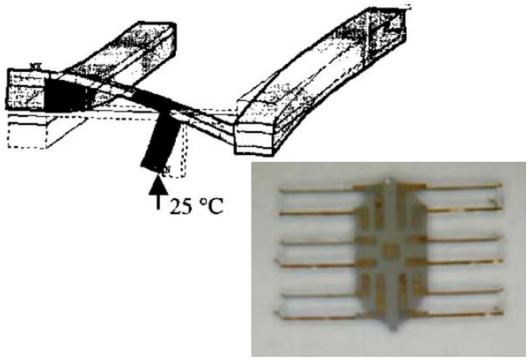


**(e)** LAB, CNRS, FR [182, 191]
$6 \times 3.5 \times 0.5$ mm$^3$, 0.1 mm/s, 250 mW

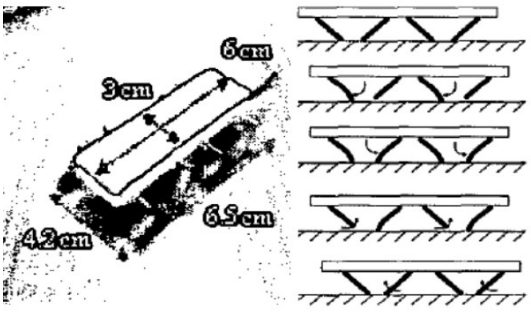


**(f)** KIST, KR [187]
$65 \times 42 \times 15$ mm$^3$, 0.28 mm/s

**Figure 2.5:** Walking microrobots

demonstrated in the third prototype presented in this thesis in section 5.3. Displacement amplification by stepping mode operation for the actuation of walking microrobots has been proposed by Yeh *et al.* in 1996 [192] (University of California, Los Angeles). Four gap-closing electrostatic actuators are used for creating an inchworm motor (see section 2.5.4) that drives a shuttle with large displacement. The in-plane motion of the shuttle is transformed to an out-of-plane motion by a mechanism of links, hinges and three dimensional, folded silicon structures. Based on this technology Yeh *et al.* [193] (by then in Berkeley Sensor and Actuator Center (BSAC), USA) propose a design of an articulated walking silicon microrobot with a bio-inspired exoskeleton structure[8]. The proposed design features a robot size of $10 \times 10$ mm$^2$, 6 articulated 2-DOF legs, a theoretical motion velocity of 7 mm/s, a driving voltage of 12-30 V for an overall power consumption of only 0.40 mW.

Six legged insects walk by moving their legs in two sets of three legs each. In each set the three legs are arranged like a tripod containing the robot's center of gravity. Consequently, the robot has a stable support on every moment of the gait cycle, allowing for quasistatic motion. In nature all of the six legs can be moved vertically and horizontally. This is, however, not completely necessary for obtaining locomotion. The robot can be, for instance, simplified by using only 1 DOF legs. The robots based on cilia actuators shown in figures 2.5(b), 2.5(c), 2.5(d) and 2.5(f) illustrated already one possible walking gait with 1 DOF legs (see also figure 2.4).

Another gait for walking with 1 DOF legs was demonstrated by the Walker-3 robot presented by Zhang *et al.* in 2007 [195] (see figure 2.6(a)). The robot features 2 DOF motion obtained with 6 ICPF actuators. Each ICPF actuator has 1 DOF: three of them used for thrusting the robot forward, while the three other legs are used to lift the robot while retracting the thrusting legs. The robot has a size $55 \times 30 \times 8$ mm$^3$ and achieves a maximum velocity of 6 mm/s in translation and 7.1 deg/s in rotation for an actuation with 10 V signals at 0.5 Hz.

Another possible simplification of the walking gait is demonstrated by Snis *et al.* (Uppsala University, Sweden) [196] within the MiCRoN project [25, 67]. Motion is obtained with one set of active feet with 2 DOF and one set of passive feet. The active feet lift the robot and thrust it forward, while the passive feet support the robot while the active feet are retracted. With this variation of the walking principle they realized a 3 DOF locomotion module (see figure 2.6(b)) of a size of $10 \times 10 \times 0.5$ mm$^3$. The module consists of four passive feet and four feet actuated by multilayer piezoelectric benders. Each active foot has two degrees of freedom (one bending mode and one axial mode). Translation in $X$ ($Y$) direction is obtained by actuating the two feet with the benders oriented in $X$ ($Y$) direction, while $\theta_Z$ rotation is obtained by actuating all four benders. The module is fabricated with the same monolithic, multilayer fabrication technology as their MINIMAN V robot discussed earlier (see figure 2.5(a)), with the difference that for this locomotion module the piezoelectric benders are not arranged vertically, but inside the horizontal plane. It has a maximum translational velocity with stable motion of 0.075 mm/s for a driving frequency of 80 Hz and a driving voltage of 28 V. This corresponds to a power consumption of $P = \frac{1}{2} f C U^2 = 1.6$ mW for a capacitance of $C = 4 \cdot 12.5$ nF. The same authors presented a rotational actuator with a similar design for the vertical displacement of a tool on the MiCRoN robot [197].

Another simplification of the walking gait based on only 2 legs with 1 DOF is proposed by the Berkeley Sensors and Actuators Center (BSAC). One leg at the front of the robot is trusting the robot forward, while the other leg is lifting the robot's front allowing the thrusting leg to retract. The passive rear of the robot is supposed to be dragged forward by

[8]The creation of an insect-based microrobot with an external skeleton and elastic joints was already proposed by Suzuki *et al.* in 1992 [194].

the trusting leg at the front. Based on this simplified walking gait BSAC presents in 2003 a mobile microrobot (size $8.5 \times 4 \times 0.5$ mm$^3$) with integrated actuators, driving electronics and powering by solar cells [79] (see figure 2.6(c)). It is actuated by electrostatic inchworm actuators [193], which drive two shuttles of which the motion is transformed by means of links and hinges to an out-of-plane rotation of the two legs. The electrostatic actuators are operated at 50 V, which is supplied by a series connection of 90 solar cells integrated on the robot. The robot has an overall power consumption of only 2.6 $\mu$W, including the power consumption of the legs of 0.1 $\mu$W, while the solar cells power source can provide up to a maximum power of 100 $\mu$W. The operation of the powering, electronics and leg motion has been demonstrated by lifting the robot's front end more than 300 $\mu$m above the surface, but forward locomotion has not been demonstrated yet. An operation during 8 minutes caused the robot to rotate for about 20°. Apparently, the drag force of the sliding rear of the robot is too large to be overcome by the thrust force of the driving legs. Another design of a low power consumption, electrostatically actuated, walking silicon microrobot is also proposed by the same group at BSAC in [198], but this design has never been realized.

### 2.5.2 Literature review on variants to the walking locomotion

Walking with more than 6 legs is also possible as demonstrated by the robots shown in figures 2.5(b), 2.5(c) and 2.5(d). Walking motion with an infinite number of feet with an infinitesimally small spacing is also know as the traveling wave principle often used for ultrasonic motors. In Traveling Wave Ultrasonic Motors (TWUM) a wave is generated in an elastic medium (usually a bending wave), which causes all the points on the surface of that elastic medium to perform an elliptical motion that drives the slider that is brought into contact with it (see figure 2.7). The resulting motion direction of the slider is opposite to direction the wave travels. The TWUM principle was invented by Sashida, T. in 1982 [199] and is particularly interesting for rotary motors [200, 201, 202, 203], because they can reach good efficiencies due to resonance operation with a circulating wave energy. In order to obtain the same efficiency for a linear actuator the elastic body should be a closed structure allowing for a circulation of the wave energy. This is the case for the ring type linear ultrasonic traveling wave motor proposed by Seemann [204]. Another possibility is to generated the wave at one end of a linear stator and absorb it at the other end [205]. Absorption is necessary in order to avoid reflection, but reduces considerably the efficiency of the actuator. Another solution for linear TWUM is not to operate in resonance, but to impose a wave shape deformation to a flexible structure. A linear actuator based on this *forced traveling wave* principle is presented by Houben *et al.* in [206] and a 2 DOF design is presented by Devos *et al.* in [207]. TWUMs can be very simple, thin and low cost as illustrated by the miniature motors for integration in LEGO$^{\text{TM}}$ bricks presented by Bansevicius *et al.* in [203]. Miniaturization of TWUMs has also been studied by Minotti *et al.* [208] and rotary TWUMs with a diameter down to ∅2 mm have been fabricated.

A mobile microrobot based on TWUM has been developed by Volkov *et al.* (Northumbria University, UK) [211]. The robot (see figure 2.8(a)) has a size of approximately ∅20 mm × 30 mm and features locomotion with 3 DOF $(X, Y, \theta_Z)$ as well as a tool actuator with 3 rotational DOF. The active structure of the robot consists of a large diameter piezotube with structured electrodes. At both ends the electrodes of the piezotube are radially divided in 12 sections that can be actuated individually. Applying the right sequence of actuation signals to these electrode sections allows to generate different traveling waves on the border of each end of the tube. The interaction of the traveling waves on the lower end with the substrate causes the robot to move, while the interaction of the traveling waves on the upper end with

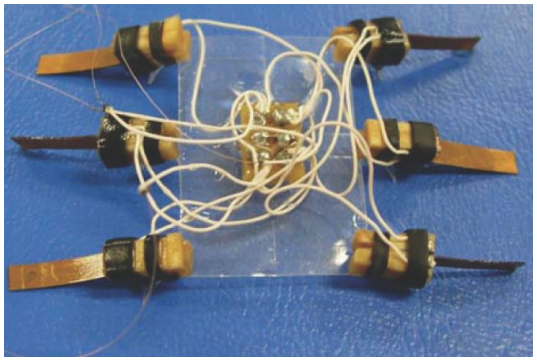

**(a)** Kagawa University, JP [195]
$55 \times 30 \times 8$ mm$^3$, 6 mm/s

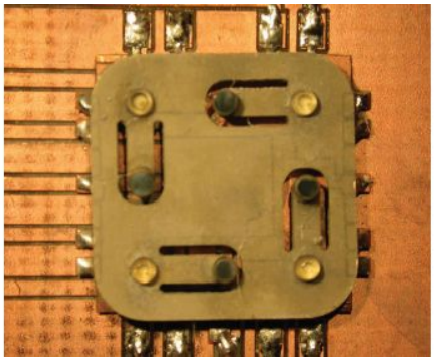

**(b)** Uppsala University, SE [196]
$10 \times 10 \times 0.5$ mm$^3$, 0.075 mm/s, 1.6 mW

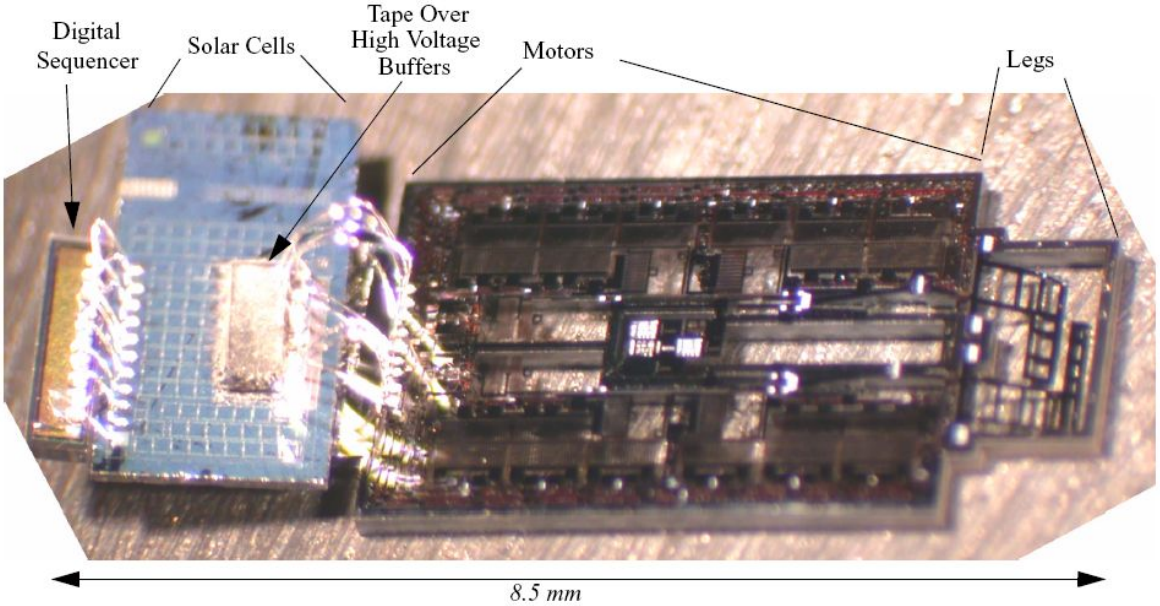


**(c)** BSAC, University of California, Berkeley, US [79]
$8.5 \times 4 \times 0.5$ mm$^3$, 2.6 $\mu$W

**Figure 2.6:** Walking microrobots

a ball carrying a tool causes the ball to rotate. The middle part of the piezotube can possibly be used for a high resolution, quasistatic scanning mode displacement of the tool in $X, Y$ and $Z$ direction. The technology of this robot has been patented by Northumbria University [209] and they are aiming to commercialize it.

Surface Acoustic Wave (SAW) motors are a special case of traveling wave motors. In SAW a Rayleigh wave is excited by interdigital electrodes on the surface of a piezoelectric (typically lithium niobate) substrate [213]. The advantages of SAW motors are their high energy density and small size. The major drawback is that high driving frequencies (10 MHz or higher) are required. SAW motors are generally applied as linear motors and require therefore an absorption of the excited wave at the end of the stator. To improve the power efficiency, a method of power circulation is proposed in [213] allowing for a driving voltage of less than 10 V and a driving power in the order of 100 mW. High driving velocities (up to 1 m/s) and high driving forces (several N) have been reported [213]. SAW motors are well suited for miniaturization as slider sizes down to $2 \times 2$ mm$^2$ [214] and stator sizes down to

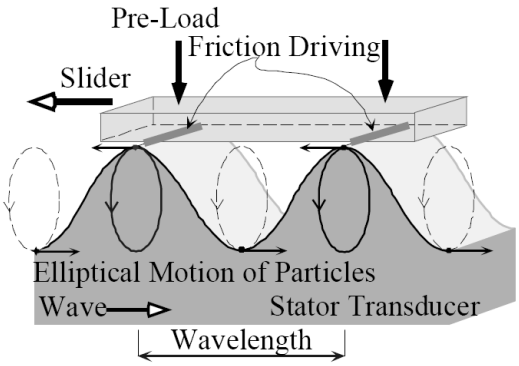


**Figure 2.7:** The traveling wave driving principle (from [210])

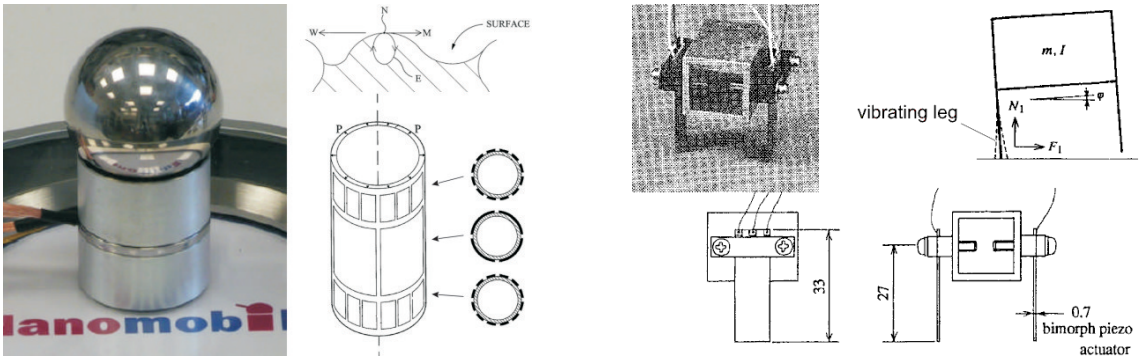


**(a)** Nanomobile, Northumbria U., GB [211, 209]
$\varnothing \sim 20$ mm $\times \sim 30$ mm

**(b)** Mechanical Engineering Laboratory, JP [212]
$38 \times 27 \times 28$ mm$^3$, 60 mm/s, 18 mW

**Figure 2.8:** The traveling wave driving principle and a miniature robot based on dynamic walking

$3 \times 12 \times 0.5$ mm$^3$ [215] have been reported as well as 2 DOF $XY$ motion [216]. Application of SAW motors for driving mobile microrobots requires the surface acoustic wave to be generated on the slider (robot) as suggested in [213]. Unfortunately, no such SAW mobile robots have been reported so far.

As already mentioned before, walking is essentially a quasistatic locomotion principle. Dynamic walking is, however, possible and it can result in faster velocities (cf. running vs. walking), but instabilities can easily occur due to small changes in mass, friction parameters, stiffnesses, driving frequency and actuation amplitude. A very interesting robot based on dynamic walking is presented by Tani [212] (Mechanical Engineering Laboratory, Tsukuba, Japan) in 1996. The robot (see figure 2.8(b)) has an overall size of $38 \times 27 \times 28$ mm$^3$ and consists of two vertically oriented piezoelectric bimorph actuators serving as legs. Vibrating one of the legs in its bending mode causes the robot to rock back and forth during each vibration cycle, thereby changing its body weight from the active to the passive leg and back[9]. The superposition of this variation in contact force with the slip generated by the vibrating leg causes the robot to move forward in the direction of the passive leg. Experiments have shown a robot velocity of about 60 mm/s for a driving voltage of 60 V and a driving frequency of 250 Hz. The capacitance of the piezos is estimated to about 20 nF per channel (2

[9]For this robot the slip generation is in fact based on a combination of the differential motion between the feet and the inertial effect of the vibration. This robot cannot operate in quasistatic mode. However, the robot belongs to the walking class, as the body weight is repeatedly transferred from one foot to the other.

| | $v_s$ [L/s] | $P_s$ [$\frac{\text{mW}}{\text{mm/s}}$] | DOF | Elec | 1 cm$^3$ | Res |
|---|---|---|---|---|---|---|
| Walking | $10^{-2}\cdots1$ | $10\cdots10^4$ | 2-3 | | | |

**Table 2.3:** Evaluation of walking locomotion for mobile microrobots

channels per piezo), resulting in a total power consumption of only $P = 2\cdot\frac{1}{2}\cdot fCU^2 = 18$ mW. A design with 2 bidirectional DOF is also presented [212].

### 2.5.3 Evaluation of walking locomotion

The walking microrobots reported in literature feature motion velocities from 0.0075 L/s up to 0.7 L/s, which is moderate compared to other locomotion principles. The specific power consumption of piezoelectrically actuated quasistatically walking robots is in the range of $20\cdots150$ $\frac{\text{mW}}{\text{mm/s}}$, while for thermally actuated walking robots it is $200\cdots10000$ $\frac{\text{mW}}{\text{mm/s}}$, which illustrates clearly the major drawback of thermal actuators for mobile microrobots. Ionic polymer actuators are expected to feature both low power consumption than thermal actuators and large deflections than piezoelectric actuators. However, due to technological limitations, up till now only robots capable of underwater motion have been developed. The electrostatic inchworm actuation of the BSAC autonomous microrobot shown in figure 2.6(c) also features very low power consumption. However, its implementation is rather complex and fragile and no successful locomotion has been demonstrated so far. Good motion velocity (2 L/s) and low power consumption 0.3 $\frac{\text{mW}}{\text{mm/s}}$ can be achieved, however, for dynamic walking[10]. Most walking robots feature nonholonomic 2 DOF motion. 3 DOF walking robots have been demonstrated, but with a minimum of 8 actuation channels, which is rather complex for an on-board driving electronics. The thermally actuated robots allow for electronics with low driving voltage and 2 channels per DOF. The two multilayer piezoelectric robots require average driving voltages, but 2.7 and 8 channels per DOF. Except for robots based on ionic polymers, all presented walking locomotion modules are realized by integrated fabrication process without any assembly, allowing for batch fabrication and further miniaturization. Specially thermal actuators featuring small sizes and large deflections can be fabricated with processes that are well established. In fact, most of thermally actuated robots have arose from a technology push from MEMS engineers, rather than from a application pull from robotics engineers. The motion resolution of walking actuators mainly depends on their step size. The piezoelectric walkers allow for resolutions of some tens of nm, while the resolution of the thermal walkers is rather in the range of some tens of micrometer. The parasitic vertical motion during each step cycle of a walking robot could be an problem for certain precision applications. Table 2.3 summarizes the evaluation of the suitability of walking motion for driving mobile microrobots.

### 2.5.4 Literature review of the inchworm principle

The Inchworm® motor is a registered trademark from Burleigh Instruments, Inc. (now EXFO Electro-Optical Engineering Inc.) and its first design was patented in 1975 [217]. As

[10] In terms of locomotion principle, dynamic walking definitely belongs to the walking class. In terms of performances such as velocity and power consumption, dynamic walking is, however, closer to the $IF_c$ class.

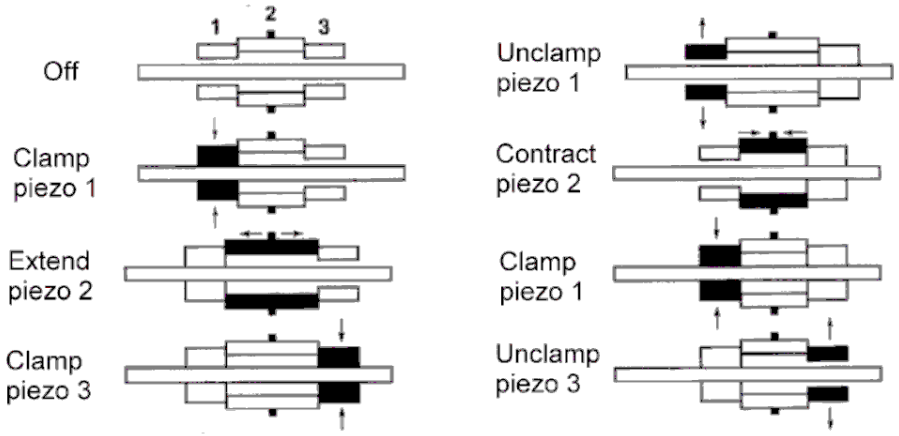


**Figure 2.9:** Inchworm operation principle [217]

shown in figure 2.9 this first inchworm® motor is based on three piezoelectric actuators. The two outer actuators (1 and 3) alternately clamp the slider, while the distance between both clamps is adjusted by the middle piezoelectric actuator (2). In the rest of this work the inchworm principle will be used to refer to the generalized motion principle of two active clamping units between which the distance can be adjusted. The major advantages of the inchworm principle are its high force capabilities and higher resolution motion. The major drawback is that the design becomes rather complex for motion with three DOF $(X, Y, \theta_Z)$.

Since 1992 Aoyama *et al.* (University of Electro-Communications, Tokyo) have been developing mobile mini- and microrobots with inchworm locomotion driven by piezoelectric actuators and electromagnetic clamps. They developed many robots and demonstrated how several of such cooperating robots can be used for applications such as machining, indentation, measuring, surface cleaning, biological manipulation under optical microscopes and operation in Scanning Electron Microscopes (SEM). They developed many robot designs with different tools and sensors, but generally for the robots based on the inchworm principle 2 configurations can be distinguished. In a first configuration electromagnets allow to clamp either the two front feet either the two rear feet, while the distance and relative orientation between both sets of feet can be adjusted by means of two piezoelectric stack actuators. The smallest robot realized with this 2 DOF $(X, \theta_Z)$ configuration measures $20 \times 20 \times 18$ mm$^3$ (see figure 2.10(a)) [38]. The robot features a maximum velocity of 1.16 mm/s for a stepping frequency of 162 Hz. The clamping by electromagnets allows the robots to climb vertical walls and to walk upside down. The second robot configuration based on the inchworm principle used by Aoyama *et al.* is shown in figure 2.10(b) [218]. It consists of four piezoelectric actuators arranged in a square between the four feet and two electromagnetic clamps connecting two diagonally opposed feet. Based on this configuration with 3 DOF a robot of a size of $32 \times 32 \times 15$ mm$^3$ with a motion velocity of 0.7 mm/s has been reported. No data about the power consumption of these robots is provided, but driving currents for the electromagnets up to 2.6 A have been reported [38], which are very difficult to provide by an on-board power source. The high force capabilities of these robots, however, limit the disturbance of electrical wires to the robot's motion. Another drawback of clamping by electromagnets is the generated stray magnetic field, which have shown to disturb the image in a scanning electron microscope [38]. Magnetic shielding has shown to reduce this effect.

Codourey *et al.* (ETHZ, CH) [219] presented in 1995 another 3 DOF design for a mobile minirobot based on the inchworm principle. The robot (see figure 2.10(c)) has an overall

footprint size of $60 \times 60$ mm$^2$ and consists of an inner and an outer structure interconnected by three, triangularly arranged piezoelectric stack actuators. Application of the right voltages to these three piezo stacks allows to generate a relative displacement of the inner structure with respect to the outer structure in any arbitrary, in-plane direction $(X, Y, \theta_Z)$. Electromagnetic clamps integrated in the inner and the outer structure allow for alternately clamping both units. Hence, 3 DOF inchworm locomotion with 3 + 2 actuation channels is obtained. No data on motion velocity has been reported.

Koyanagi *et al.* (Aichi Institute of Technology) [220] presented in 2000 a similar design with a triangularly arranged piezoelectric actuators, but with three feet that can be moved individually. The robot has a diameter ∅28 mm and a maximum velocity of 0.027 mm/s. In 2001 Torii *et al.* [221] from the same research group proposed another similar design with the piezo actuators arranged in a Y-shape instead of a triangular shape. The ∅32 mm robot (see figure 2.10(d)) features a maximum motion velocity of 0.19 mm/s and 2.0 mrad/s for a stepping frequency of 100 Hz. The electromagnets have a resistance $R = 450\ \Omega$ and where actuated with $I = 10$ mA, which results in a power consumption of $P = 2RI^2 = 90$ mW. The piezoelectric actuators have a capacitance of $C = 1.5\ \mu$F and are actuated at $U = 30$ V for a driving frequency of $f = 100$ Hz, which corresponds to a power consumption of $P = 3 \cdot \frac{1}{2} fCU^2 = 189$ mW. Hence, the total power consumption of the robot is 90 + 189 = 279 mW.

Another design of a minirobot based on inchworm locomotion is proposed by Yan *et al.* [222]. The 3 DOF robot (see figure 2.10(e)) has a size of $55 \times 35 \times 20$ mm$^3$ and consists of one piezoelectric stack actuator that deforms a flexible structure with four electromagnetic clamps serving as feet. A maximum velocity of 0.4 mm/s for a stepping frequency of $f = 40$ Hz was reported. The piezoelectric actuator has a capacitance of $C = 1.4\ \mu$F and is driven at $U = 100$ V, which corresponds to a power consumption of $P = \frac{1}{2} fCU^2 = 280$ mW. Each electromagnetic clamp has a resistance of $R = 25\ \Omega$ and is driven with $U = 5$ V, resulting in a current of $I = 200$ mA. During translation in $X$ and $Y$ direction, two electromagnets are used with a duty cycle of 50%. The power consumption of the clamping is thus $P = 2 \cdot 0.5 \cdot UI = 1000$ mW, resulting in a total power consumption 1280 mW.

All robots based on the inchworm locomotion principle realized by stack piezo actuators and electromagnetic clamps discussed above (and shown in figure 2.10) suffer from low velocities and high power consumption, which shows that this locomotion solution is less interesting for driving untethered mobile microrobots. An interesting solution to the velocity problem is proposed by Chen *et al.* [223] and Song *et al.* [107] (Harbin Institute of Technology, China). They propose a hybrid locomotion solution, which allows to switch between efficient and fast wheeled 2 DOF (nonholonomic) locomotion and high resolution 3 DOF (holonomic) by the inchworm principle[11]. The inchworm locomotion module is based on a configuration similar to the robot shown in figure 2.10(b): four piezoelectric stack actuators are arranged in a square and four independent electromagnetic clamps in the four corners. Switching between both locomotion modules is done by a vertical displacement of the wheels driven by an electromagnetic motor. The robot has an overall size of $90 \times 70 \times 70$ mm$^3$ and has a maximum velocity of 50 mm/s when driven by the wheels and 0.19 mm/s when driven by the inchworm principle. At a maximum driving frequency of 30 Hz the piezoelectric actuators consume an average current of 6 mA for a driving voltage of 120 V, corresponding to a power consumption of 720 mW. The electromagnets have a resistance of $R = 80\ \Omega$ and are driven with $I = 100$ mA. During translation all four electromagnets are used with a duty cycle of 50% resulting in a power consumption $P = 4 \cdot \frac{1}{2} \cdot RI^2 = 1600$ mW. Hence, in total the inchworm

[11] The major drawback for such a hybrid solution is the complexity, which makes miniaturization to the cm$^3$ range difficult.

locomotion consumes 2320 mW. The robot is equipped with on-board driving and control electronics and batteries yielding an autonomy of about 3 hours. Moreover, a microgripper that can be positioned with 3 DOF is integrated on the robot and a micromanipulation operation has been demonstrated in closed loop with global and local optical tracking.

As mentioned before electromagnetic clamping devices suffer from high power consumption and miniaturization typically leads to fabrication and efficiency problems. An interesting alternative for electromagnetic clamping is electrostatic clamping. Electrostatic clamps have low power consumption, do not consume any power in static mode and are well suited for miniaturization by MEMS technologies. On the other hand, they have the drawback of smaller forces, high actuation voltages and sensitivity to dust and surface roughness. Cusin *et al.* [224] present a linear inchworm actuator (size $18 \times 18$ mm$^2$) with electrostatic clamping and piezoelectric actuation. The same group also presented a linear actuator with one piezoelectric actuator and multiple sliders that can be driven individually by controlling the voltage applied to each slider [225]. Apart from the clamping function electrostatic actuators can also be applied for the driving force as demonstrated in [226]. However, in order to achieve an acceptable level of the electrostatic driving force amplification is necessary. An interesting design with force amplification is the shuffle motor presented in [227, 228]. It consists of two electrostatic clamps interconnected by a flexible plate that is bent under influence of an out-of-plane electrostatic force resulting into an amplified force that shortens the distance between two electrostatic clamps. The shuffle motor can be fabricated by silicon surface micromachining, which allows for actuator sizes below 1 mm$^2$. Even at this small size forces can go up to the 1 mN range for a driving voltage of 55 V with velocities of several mm/s for a driving frequencies of almost 100 kHz. A 2 DOF shuffle motor has also been presented in [229]. However, up to now shuffle motors have only been developed for applications such as mass data storage and in-situ material characterization and not for microrobotic locomotion. The force of electrostatic actuators can also be multiplied by arranging a large amount of electrostatic actuators in parallel as in equally spaced comb drive actuators [230, 135] and offset comb drive actors or gap-closing actuators [136, 231]. Such actuators can be used both for the clamping as for the driving force of in-plane MEMS inchworm motors [232]. Forces can be amplified further by mechanical leveraging [233]. Gear teeth on the shuttle and the clamping units can be used in order to avoid slippage and allow for repeatable step sizes as demonstrated by Yeh *et al.* [137] for the electrostatic inchworm motors used to actuate the autonomous MEMS robot shown in figure 2.6(c). Mechanical clamping with electrostatic comb drive actuators has also been combined with a driving force provided by an assembled piezo stack actuator [234]. Finally, apart from electrostatic actuators also thermal MEMS actuators have been reported for the actuation of a linear inchworm motor with mechanical clamping [235]. The advantage of mechanical clamping is that, if it is realized by piezoelectric or electrostatic actuators as usually is the case, there is no static power consumption. The disadvantage is that due to the small stroke of these actuators (specially for piezoelectric actuators) the system can be sensitive to wear between the clamps and the shuttle.

Mechanical clamping inchworm robots have been reported mainly for locomotion inside a tubular structure. Anthierens *et al.* [236] present two SMA actuated inchworm robots developed for small diameter canalization exploration. The largest robot (University of Poitiers, France) consists of 5 actuation modules connected in series. Each actuation module ($30 \times 30 \times 3$ mm$^3$) consists of a bistable, SMA actuated structure that fulfills both the clamping and the axial displacement function. The smallest robot (Laboratoire d'Automatique de Besançon, France) consists of two clamping units actuated by SMA wires interconnected by another SMA actuator. The robot has a size of $\varnothing$10 mm $\times$ 22 mm and a maximum velocity of 0.5 mm/s has been reported. Maximum actuation currents of 700 mA have been reported,

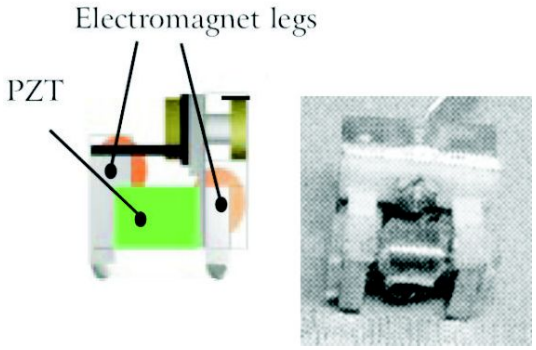


**(a)** U. of Electro-Communications, JP
$20 \times 20 \times 10$ mm$^3$, 1.16 mm/s [38]

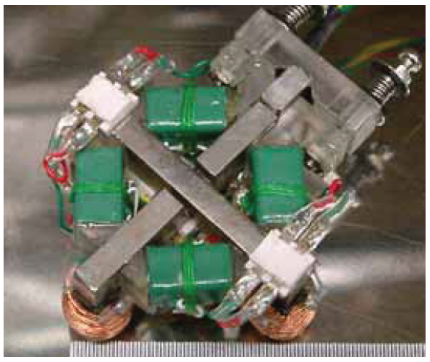

**(b)** U. of Electro-Communications, JP
$32 \times 32 \times 15$ mm$^3$, 0.7 mm/s [218]

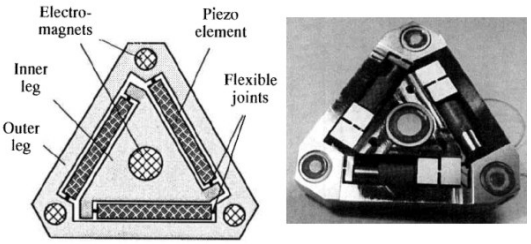


**(c)** ETHZ, CH [219]
$60 \times 60$ mm$^2$

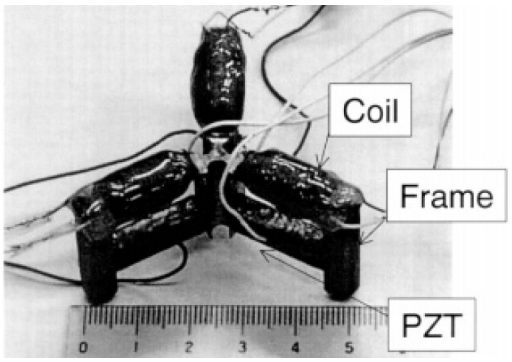


**(d)** Aichi Institute of Technology, JP [221]
∅32 mm, 0.19 mm/s, 279 mW

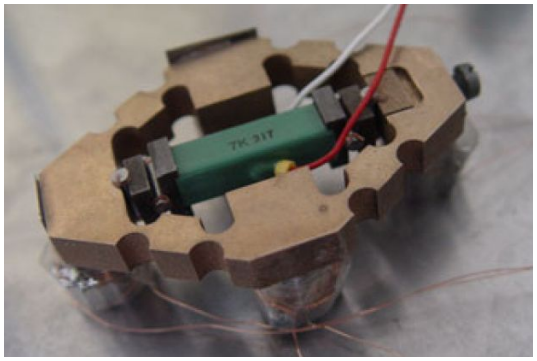

**(e)** Tsinghua University, CN [222]
$55 \times 35 \times 20$ mm$^3$, 0.4 mm/s, 1280 mW

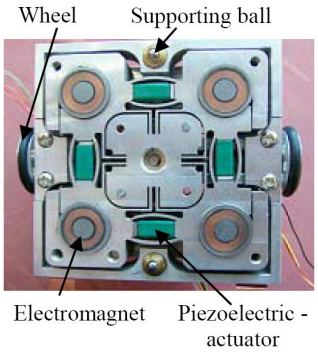


**(f)** Harbin Institute of Technology, CN [107]
$90 \times 70 \times 70$ mm$^3$, 0.19 mm/s, 2320 mW

**Figure 2.10:** Mini and microrobots based on the inchworm locomotion principle

which is the major drawback of SMA actuation. Pneumatic actuators have also been reported for the actuation of inchworm robots [237, 238, 54, 236, 143]. Pneumatic actuators can lead to large strokes and the number of pneumatic connections can be limited to one if the valves are integrated on the robot. However, on-board generation of pressured air is required for untethered operation, which is not really feasible yet for robot sizes of 1 $cm^3$. Inchworm motion with mechanical clamping could principally also be used for the 3 DOF locomotion of mobile robots that clamp between two flat substrates (one on which the robot is walking and one just above the robot). However, no such 3 DOF microrobots have been reported in literature, probably because the constraint imposed by the additional substrate just above the robot in terms of accessability for manipulation, wiring, optical tracking and so on.

In this dissertation an inchworm configuration with another, innovative way of contact variation is discussed under the name *inertial inchworm* principle. In the inertial inchworm principle the contact force between the "clamping" units and the substrate is varied by means of the inertial effect of a vertical vibration of an additional inertial mass. The advantage of this way of contact force variation is that it does not suffer from high power consumption and stray magnetic fields as for electromagnetic clamping, nor from sensitivity to dust such as for electrostatic clamping, nor from sensitivity to wear as for mechanical clamping. The major drawback is that it does not allow to increase the force in a quasistatic manner, reducing the capabilities of high resolution quasistatic scanning mode operation. In the framework of a student project a first inertial inchworm actuator was developed and tested by Christophe Groux [239]. In this thesis the *inertial inchworm* principal has been experimentally characterized and compared to the stick-slip and the Modulated Friction Inertial Drive (MFID) principle in section 4.4.9.

### 2.5.5 Literature review on variants for the inchworm principle

As shown in figure 2.9 a linear inchworm consists of two clamping units and one actuator allowing to vary the distance between both. Just as for the walking motion the number of legs (clamping units) can be increased. The advantage of for instance three "clamping units" for a linear actuator is that it is not necessary anymore to vary the clamping force in the three units: if each unit is moved individually, the two other units will not slide because their joint friction force is the double of that of the sliding unit.

This driving principle was patented by Pan *et al.* in 1993 [240] for 1 and 2 DOF linear and rotational motion. In 1997 Guangyi *et al.* present a linear actuator based on this principle. It has a total size of $54 \times 12 \times 12$ $mm^3$ and consists of three clamping units with permanent magnets interconnected by two piezoelectric stack actuators. Actuated at 30 V it features step sizes of 700 nm, which result in a motion velocity of 0.14 mm/s for a maximum driving frequency of 200 Hz. Yan *et al.* [68] present a wireless endoscope robot based on the same principle but with four modules. The robot has a size of $\varnothing$12.1 mm $\times$ 120 mm and is actuated by electromagnetic motors without any clamping mechanism. The principle is also applied by Brown *et al.* in 2007 for the locomotion of their untethered frictional microcrawler [241]. It has an overall size of only $1.4 \times 0.5 \times 0.01$ $mm^3$ and consists of three sliding units interconnected by two thermal chevron actuators [242]. The current for driving the thermal actuator is provided to the microcrawler by individual sliding contacts between the substrate and the sliding units. A maximum velocity of 0.72 mm/s was reported, which is reached at a driving voltage of 2.75 V and a total average power consumption of 127 mW. Minimum repeatable step size is reached at a voltage of 1.25 V and a power consumption of 26 mW. The same group presents in 2008 two actuator designs capable of moving a passive slider in 2 DOF ($XY$ and $X\theta_Z$) [243]. The actuators are based on the same principle of a redundant number

| | $v_s$ [L/s] | $P_s$ [$\frac{\text{mW}}{\text{mm/s}}$] | DOF | Elec | 1 cm$^3$ | Res |
|---|---|---|---|---|---|---|
| Inchworm | $10^{-3} \cdots 10^{-2}$ | $10^{3} \cdots 10^{4}$ | 2-3 | | | |

**Table 2.4:** Evaluation of inchworm locomotion for mobile microrobots

of sliding contacts driven by external, thermal chevron actuators. The number of sliding units can also be increase to more than three. Jung *et al.* [244] presents a locomotion device driven by Dielectric Elastomer Actuators (DEA). It has an overall size of ∅20 mm× 45 mm and consists of 8 modules with each 6 DEA actuators (3 on every side), which gives each unit 3 DOF motion with respect to the neighboring units. A linear locomotion velocity of 2.5 mm/s was reported by individually moving the module back and forth in axial direction. Other bio-inspired worm- or snake-like locomotion principles such as the ones reported in [245, 246] are not studied here because they are difficult to scale down to a robot size of 1 cm$^3$ or below.

### 2.5.6 Evaluation of inchworm locomotion

Robots based on inchworm motors reported in literature feature motion velocities from 0.0025 L/s up to 0.02 L/s, which is slow compared to other principles, but still enough for the precision manipulation applications these robots are developed for. Power consumptions are very high, with specific power consumptions ranging from 1500 $\frac{\text{mW}}{\text{mm/s}}$ up to 12'000 $\frac{\text{mW}}{\text{mm/s}}$. Most robots feature 3 DOF and the electromagnetic clamping allows for vertical and upside-down motion. Inchworm robots are unsuitable for driving with on-board electronics, because of the combination of large current, low voltage operation for the electromagnets with high voltage operation for the piezoelectric stack actuators. An average of 2 channels per DOF are required. Inchworm motors with electromagnetic clamps are unsuitable for miniaturization below 1 cm$^3$ because of the required 3D integration, the combination of two different actuation technologies and poor scaling of electromagnetic forces. Electrostatic shuffle motors feature low power consumption, high power densities and are very well suited for miniaturization. However, no electrostatic inchworm mobile microrobots have been reported so far. Another drawback of inchworm motors is that electromagnetic clamps generate stray magnetic fields and require for a ferromagnetic surface, electrostatic clamping is sensitive to dust and surface roughness, while mechanical clamping with piezoelectric actuators is sensitive to mechanical tolerances and wear. Finally, the reported inchworm robots feature large thrust forces and good resolution in the range of some nm. Table 2.4 summarizes the evaluation of the suitability of inchworm locomotion for driving mobile microrobots.

## 2.6 Inertial slip generation with contact force variation (class $IF_c$)

Apart from the differential displacement of contact points slip can also be generated by the inertial effect of a horizontal vibration (see table 2.1). When the feet of a robot are vibrated very slowly in horizontal direction, no slip between feet and substrate will occur and the body of the robot will move back and forth. However, when the frequency of this horizontal vibration is increased, slip between feet and substrate will occur above a certain

threshold frequency, as the inertial force generated by the back-and-forth motion of the robot's body will be larger than the maximum friction force between feet and substrate. As for the differential slip generation the contact force variation can either result from a direct force such as a mechanical, magnetic or electrostatic clamping force either from the inertial effect of a vertical vibration. Apart from one robot presented at the end, the contact force of all the other robots for this locomotion class results from the inertial effect of a vertical vibration.

### 2.6.1 Literature review

De Ambroggi *et al.* [112] present a robot with two feet vibrating in vertical and horizontal direction, while the third foot is passive[12]. The 2 DOF actuation of the feet is realized by a series connection of two piezoelectric benders resulting in a 2 DOF robot with a footprint size of $20 \times 20$ mm$^2$. High motion velocities up to 180 mm/s were reported, but with great instability problems. These instabilities resulted from an undesired excitation of resonance frequencies of the actuating structures, while the robot was not designed for resonance operation.

Varma and Dixon (Oak Ridge National Laboratory, USA) [247] report on a design of a minirobot with two passive wheels and driven by the vibration of two piezoelectric actuators. Compared to the previous robot this design uses passive wheels instead of a passive sliding leg and uses only one actuator per active leg. The design has a size of $35 \times 35 \times 6$ mm$^3$ and features 2 DOF. The stroke of the piezoelectric actuators is amplified 107 times by a two stage compliant lever mechanism. The vibration as well as the vibrating legs are inclined with respect to the substrate resulting in an unidirectional motion. Experiments with a 1 DOF prototype have shown a motion velocity up to 650 mm/s for an actuation voltage of 200 $V_{p2p}$ and a frequency of 575 Hz.

Although resonance mode excitation can sometimes result in instable operation (as for the first robot discussed in this section), a carefully design of the resonance behavior of the actuating structure can result in very efficient and stable locomotion. Snis *et al.* (Uppsala University, Sweden) [248] propose an efficient and simple design of a three legged locomotion module. The two front legs touch the substrate with an angle of 60°, while the rear leg is reversed (angle –60°). Each of the legs is operated in its bending resonance mode. Actuation of the two front legs moves the robot forward, while actuation of the rear leg moves the robot backwards. Forward motion with a rotation is obtained by actuation of only one of the front legs. Because of the inclination angle between the vibration direction and the substrate the function of contact variation and inertial slip generation are both fulfilled by legs with only 1 DOF. Based on this design a robot actuated by multilayer piezoceramic legs (see figure 2.12(a)) is developed by Snis *et al.* (Uppsala University, Sweden) [249]. The robot has a footprint size of $34 \times 22$ mm$^2$ and features a maximum forward velocity of 14 mm/s and a power consumption at resonance of 2 mW, when actuated at 5.5 kHz with a 10 V signal. With one front leg actuated the robot moves with a turning radius of 12 mm.

Based on the same configuration of inclined vibrating legs the same group at Uppsala University also developed a miniaturized locomotion module [250] for the I-Swarm robot (see figure 2.12(b)) [46]. The body of the module has a size of $3 \times 3$ mm$^2$, while the legs have a length of 2.15 mm. The module is a monolithic structure of piezoelectric polymer (P(VDF-TrFE)) and electrodes fabricated by a dry etching process. The legs are excited at their second flexural resonance mode. The module is actuated with a 3.6 V square wave signal

[12] In fact, for this robot the slip generation results from a combination of differential motion between active and passive feet and the inertial effect of the vibration of the active feet with respect to the robot's body. At the frequency at which the maximum velocity is obtained (i.e. 1 kHz) the slip generation is dominated by the inertial effect, which is the reason why the locomotion of this robot is classified under inertial slip generation.

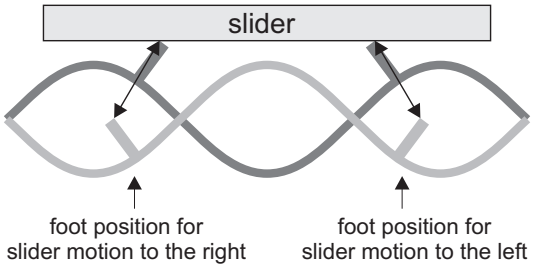


**Figure 2.11:** Standing Wave Ultrasonic Motor (SWUM) operating principle

generated by an on-board ASIC that is powered by the solar cells on top of the robot. The robot has an integrated IR module for communication with other robots, in order to obtain an intelligent swarm behavior. All these components are assembled on and interconnected by a flexible printed circuit board that is folded twice [251]. First locomotion test in upside down operation have shown that the module is be able to move a 75 mg (i.e. the weight of the robot) glass slider a velocity of 100 $\mu$m/s at $U = 3.6$ V and $f = 25$ kHz [252]. The legs have a total capacitance of $C = 350$ pF, resulting in a power consumption of $P = \frac{1}{2} \cdot fCU^2 = 0.057$ mW.

Motion modules actuated by a resonance vibration of the contact points that is inclined with respect to the motion substrate are generally referred to as *Standing Wave Motors*, in particular *Standing Wave Ultrasonic Motors* (SWUM) if the excitation frequency is in the ultrasonic region as usually is the case. As for the traveling wave ultrasonic motors (TWUM) discussed in section 2.5.2 standing wave motors are based on the deformation of an elastic structure. The difference is that the nodes and peaks of the wave shaped vibration stay at a fixed position for the SWUM and do not move in a direction opposite to the motion of the slider as for the TWUM. Moreover, for SWUM there is no continuum of contact points as for TWUM, but rather a limited number of feet that are arranged at well-chosen positions of the vibrating structure. For instance, as illustrated in figure 2.11, the arrangement of the foot on the right (left) side of the peaks of a bending wave causes the contact point to describe a motion path that thrusts the slider to the right during the upward motion during while the foot is in contact with the slider. Bidirectional (forward and backward) motion is obtained by exciting different resonance modes of the flexible structure. 2 DOF bidirectional $XY$ motion can be obtained by exciting different vibration modes in $X$ and $Y$ direction.

The design of a bidirectional SWUM with 2 DOF ($XY$) is presented by Ferreira *et al.* in 1995 [253]. In 1997 the integration of the SWUM on a 2 DOF mobile minirobot is presented by the same authors [91]. The SWUM consists of a piezoelectric plate assembled to the metallic resonator (size $64 \times 38$ mm$^2$). The electrodes of the piezoelectric actuator are structured in order to allow to excite four (two in $X$ direction and two in $Y$ direction) out-of-plane bending modes of the piezo-resonator structure. The motor is typically excited with 20 V signals with a driving frequency ranging from 37 kHz to 113 kHz for the different resonance modes. Motion velocities up to 300 mm/s and a thrust force of 1 N were reported. The SWUM has been integrated in an autonomous mobile minirobot (see figure 2.12(c)) with on-board powering by battery, on-board driving electronics and infrared communication. The robot has a size of $64 \times 38 \times 20$ mm$^3$ and an autonomy of about 1 hour. Miniaturization of the 2 DOF SWUM by MEMS fabrication technologies to a footprint size of $47 \times 29$ $mm^2$ is presented by Ferreira and Fontaine in [254].

A similar SWUM, but now with 3 DOF ($X, Y, \theta_Z$) is presented by Dembele *et al.* [255]. This robot is driven with a typical voltage of 15 V (minimum voltage 4 V) and frequencies ranging form 15 kHz to 63 kHz. Velocities of 20 mm/s in positive $X$ and $Y$ direction and

about 8 mm/s in negative $X$ and $Y$ direction were reported. The authors also present a autonomous robot with on-board powering, driving electronics and wireless communication.

Simplified and miniaturized (⌀10 mm and less than 1 mm thick) SWUMs with 3 DOF have also been presented by Bansevicius *et al.* in [203]. A disk shaped piezoelectric bimorph actuator with sectioned electrodes ($3 \times 120°$) is excited with voltages ranging from 30 to 80 V and frequencies between 65 and 80 kHz. Unfortunately, no data on motion velocity and power consumption is provided so far.

Another way to obtain a multi DOF mobile robot driven by SWUM is by combining two linear bidirectional SWUMs as proposed by Son *et al.* (Carnegie Mellon University, USA) in 2006 [256]. They developed a mobile minirobot (size $53 \times 45 \times 19$ mm$^3$) based on two piezoelectric-metal composite beams vibrating in resonance mode (see figure 2.12(d)). The robot has 2 DOF $(X, \theta_Z)$ and features a maximum velocity of 58.6 mm/s and 33.7 mm/s in positive and negative direction for a driving voltage of ±10 V and frequency of 14.2 kHz and 24.7 kHz respectively.

The previously discussed robots show that resonance operation of standing wave ultrasonic motors yields large motion velocities with large driving forces and low driving voltages for robots of several cm a side. Scaling down to robot sizes of 1 cm$^3$ results in higher resonance frequencies and low vibration amplitudes. This is probably the reason why no 1 cm$^3$ size robots driven by SWUMs have been reported in literature so far.

Although resonance operation can increase the efficiency of the actuator, ultrasonic operation below the resonance frequency is possible. This is demonstrated by the mobile minirobot (size $30 \times 30 \times 15$ mm$^3$) developed at EPFL (see figure 2.12(e)) [257]. The 3 DOF robot is based on three monolithic piezoelectric push-pull actuators operated in ultrasonic mode as presented by Cimprich *et al.* in [258]. These ultrasonic actuators feature a maximum velocity of 25 mm/s for a driving frequency of $f = 65$ kHz. The price of non-resonance operation is the high driving voltage of $U = \pm 150$ V. Each push-pull actuator has 4 actuation channels with an electrical capacitance of $C = 280$ pF, resulting in an overall power consumption of $P = 3 \cdot 4 \cdot \frac{1}{2} \cdot Cf \cdot 2U^2 = 4'914$ mW. This very high power consumption shows that it is not efficient to drive piezoelectric actuators at high frequencies and high voltages without resonance mode operation.

Jumping motion is also based on inertial slip generation and a variation of the contact force by the inertial effect of a vertical vibration. Jumping motion allows for locomotion on rough surfaces and even climbing small steps. A promising design of an autonomous jumping microrobot is presented by Bergbreiter and Pister (Berkeley Sensor and Actuator Center, University of California, Berkeley) [259]. It is driven by an on-board inchworm motor actuated by electrostatic gap-closing actuators that stores deformation energy in an elastomer, which is suddenly released in order to make the robot jump. On-board powering by solar cells and control by a commercial microcontroller is included in the design. The robot development is at current date still work in progress and no locomotion has been demonstrated yet.

Inertial slip generation and inertial contact force variation can be realized simultaneously by a rotation of an eccentric mass about a horizontal axis. Locomotion by vibration of an eccentric mass was studied by Gaberson and Stone in 1974 [260]. Vartholomeos *et al.* (National Technical University of Athens, Greece) [261] propose a ⌀36.5 mm robot driven by two eccentric motors. The robot has 2 DOF, is powered by a battery and a maximum velocity of 1.5 mm/s was reported. The same authors also presented a 3 DOF design with three eccentric motors [262]. As for wheeled locomotion the advantage of locomotion by eccentric motors is efficiency and simplicity of the driving electronics. Moreover, locomotion with eccentric motors allows for smaller step sizes than wheeled locomotion.

In all the robots presented above in this section the slip generation and contact force

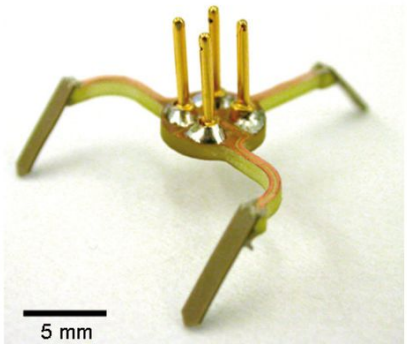


**(a)** Uppsala University, SE [249]
$34 \times 22$ mm$^2$, 14 mm/s, 2 mW

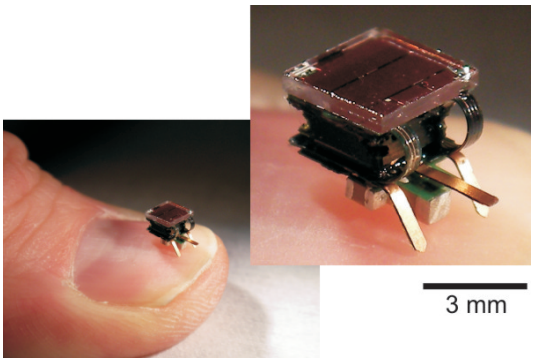


**(b)** I-Swarm robot, Uppsala U., SE [251, 46]
$3 \times 3 \times 3$ mm$^3$, 0.1 mm/s, 0.057 mW

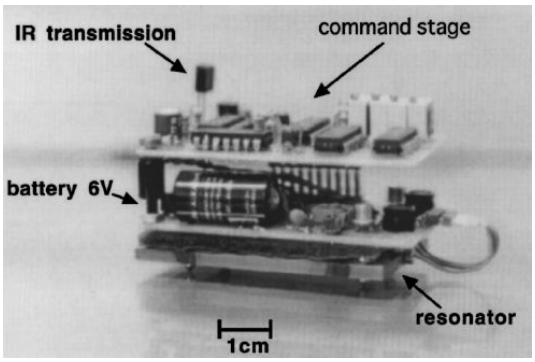


**(c)** LMARC, Besançon, FR [91]
$64 \times 38 \times 20$ mm$^3$, 300 mm/s

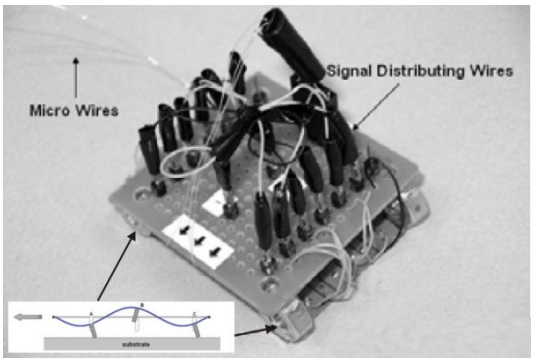


**(d)** Carnegie Mellon University, US [256]
$53 \times 45 \times 19$ mm$^3$, 58.6 mm/s

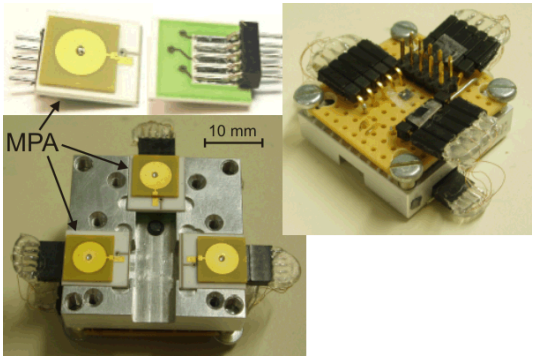


**(e)** EPFL, CH [263]
$30 \times 30 \times 15$ mm$^3$, 25 mm/s, 4'914 mW


**(f)** NTUA, GR [261]
∅36.5 mm, 1.5 mm/s

**Figure 2.12:** Mini- and microrobots driven by a locomotion principle based on inertial slip generation and contact force variation

variation is realized by the same actuator. One of the contributions of this dissertation is to decouple slip generation and contact force variation. Such decoupling is also the basis of the classification of locomotion principles presented in table 2.1. Such decoupling can help for the understanding of a locomotion principle and allows for independent optimization of the actuation solution for slip generation and contact force variation. Decoupling also allows for a combination of on-board and off-board actuation, which can result in a interesting trade-off between on-board simplicity and power consumption on the one hand and autonomy and on-board controllability on the other hand as illustrated by the first and the third prototype presented in chapter 5 of this dissertation.

Locomotion by decoupling of horizontal and vertical inertial vibration has also been discussed and simulated by Bolotnik *et al.* in 2006 [264]. Locomotion based on a combination of on-board and off-board actuation with the objective of simplification of the robot has also been proposed by Nguyen and Martel in 2006 [265]. Probably the most impressive demonstration of locomotion by a combination of on-board vibration and off-board contact force variation is a microrobot developed in the group of Brad Nelson (ETHZ, Switzerland) [266]. The microfabricated robot has a size of $0.3 \times 0.3 \times 0.07$ mm$^3$ and consists of two magnetic bodies connected by a spring. Application of an external magnetic field creates an attractive force between both magnetic bodies. Hence, by a variation of the external magnetic field a vibration on the robot can be excited, causing the robot to slip back and forth on the substrate. A simultaneous variation of the contact force by electrostatic clamping with interdigital electrodes integrated on the surface of the substrate allows the robot to move forward and backward. The orientation of the robot can be controlled by the direction of the external magnetic field[13]. The robot is also capable of locomotion by the impact drive principle. If the amplitude of the variation of the magnetic field is sufficiently large, collision between the two vibrating masses will occur, which will cause the robot to move forward without the variation of the contact force. When driven by a magnetic field of 2.2 mT the device starts moving from rest at $2500 \pm 100$ Hz, while, once moving, motion can be maintained for a frequency range from 2000 to 3000 Hz with a variation of the motion velocity from 0.75 to 1.5 mm/s. At higher magnetic fields motion velocities up to 12.5 mm/s (i.e. 42 body lengths per second!) have been reported. Such high motion velocities for relatively low magnetic fields are possible due to the resonance operation with a quality factor of about 150. The robot participated to the nanogram league (robots size $< 300$ $\mu$m) of the international Robocup championship in Atlanta, USA, July 2007 and won in all three categories (videos can be found in [21]).

Another sub-millimeter size microrobot driven by an external magnetic field is presented by Floyd *et al.* (Carnegie Mellon University, USA) [267]. The robot (see figure 2.13(b)) consists of a piece of NdFeB of size of $0.25 \times 0.13 \times 0.1$ mm$^3$ that is magnetized in the direction of the longest axis. Application of a magnetic field causes the robot to rotate and align to the field lines. Two locomotion modes have been tested. In a first mode a horizontal, pulsed field is applied. At each pulse the robot moves a small step forward. In the second locomotion mode an inclined magnetic field is implied, which causes the back of the robot to be lifted in order to align to field line (see figure 2.13(b) on the right). A variation of the inclination angle of the magnetic field causes the inclination angle of the robot to vary as well. This varying inclination causes slip as well as a variation of the contact force between robot and substrate. The superposition of this slip and contact force variation results in a linear motion. For a maximum field of 3.4 mT and a driving frequency of 70 Hz a motion velocity of almost 0.7 mm/s was obtained with the first locomotion mode and more than

[13]The actuation of the orientation of the robot is the result of a pure externally applied force in which the robot remains passive. The translational motion, however, is the result of a real *on-board* vibration between two masses, for which the energy is supplied wirelessly.

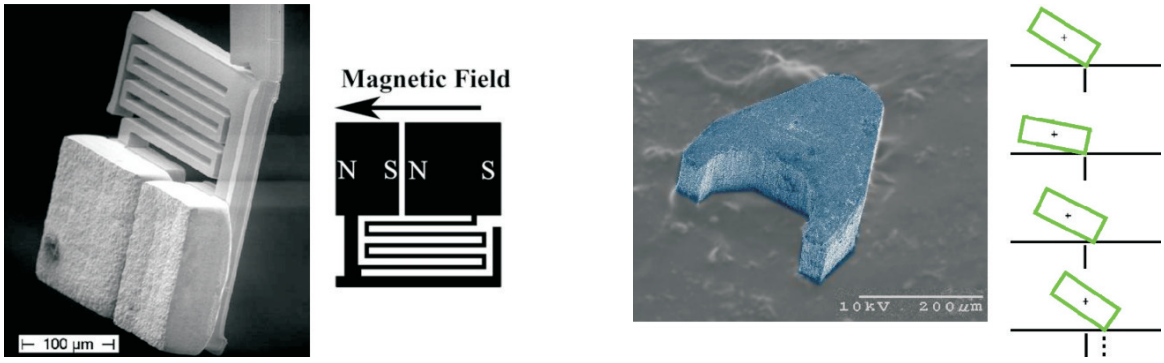


**(a)** ETHZ, CH [266]
$0.3 \times 0.3 \times 0.07$ mm$^3$, 12.5 mm/s

**(b)** Carnegie Mellon University, US [267]
$0.25 \times 0.13 \times 0.1$ mm$^3$, 2.8 mm/s

**Figure 2.13:** Sub-millimeter size microrobots driven by a locomotion principle based on inertial slip generation and contact force variation

| | $v_s$ [L/s] | $P_s$ [$\frac{\text{mW}}{\text{mm/s}}$] | DOF | Elec | 1 cm$^3$ | Res |
|---|---|---|---|---|---|---|
| $IF_c$ | $1 \cdots 10$ | $10^{-1} \cdots 10^2$ | 2-3 | | | |

**Table 2.5:** Evaluation of locomotion class $IF_c$ for mobile microrobots

2.8 mm/s with the second mode (i.e. 15 body lengths[14] per second).

### 2.6.2 Evaluation

Motion velocities of robots in the $IF_c$ class[15] range from 0.5 L/s up to 40 L/s, which is as high as for wheeled robots. This high velocity is obtained form resonance operation. Resonance operation also allows for very low specific power consumptions such as 0.14 $\frac{\text{mW}}{\text{mm/s}}$ for the three legged robot from figure 2.12(a). Non resonant operation of piezoelectric actuators at high frequencies, on the contrary, results in high power consumption such as 200 $\frac{\text{mW}}{\text{mm/s}}$ for the robot in figure 2.12(e). However, at these frequencies, power consumption of the electronics could be reduced by operation at electrical resonance. Moreover, resonance operation allows for driving with a digital electronics without any power greedy Digital to Analogue Convertor (DAC) and operational amplifiers. Robots in the $IF_c$ locomotion class typically feature 2 or 3 DOF with 1-4 channels per DOF. The locomotion principle can result in very simple designs that are well suited for miniaturization as illustrated by the sub-millimeter size robot shown in figure 2.13(a) and the 3 legged polymer robot developed in the I-Swarm project [248, 250]. Step sizes are typically in the range of some micron for fast motion, which can be reduced to about 100 nm for resonance operation [91] and even some nm for non resonance operation [258]. Table 2.5 summarizes the evaluation of the suitability of the $IF_c$ locomotion class for driving mobile microrobots.

[14]The body length of this robot is $\sqrt{0.25 \cdot 0.13} = 0.18$ mm.

[15]The lower velocity of the robot driven by eccentric motors shown in figure 2.12(f) is ignored as this robot design could be optimized for large step sizes by increasing the ratio between the mass of the eccentric and the mass of the robot's body.

## 2.7 Differential slip generation with directional friction (class $D\mu$)

Besides the contact force variation, a second way for obtaining a net displacement from a symmetric back and forth slip is by an (apparent) change of the friction coefficient. With the exception of some designs proposed in [264] all the robots based on directional friction presented in this literature review obtain directional friction from a non-perpendicular contact angle between robot's feet and substrate[16]. The literature shows that very simple and efficient robot designs can be obtained for locomotion based on directional friction. Some of the robots feature both translational and rotational motion, but only a few of them feature bidirectional (reversible) motion.

### 2.7.1 Literature review

One of the first mobile robots based on differential slip generation and directional friction is reported by Aoshima *et al.* (NTT Transmission Systems Laboratories, Japan) in 1993 [28]. The robot (see figure 2.14(a)) is developed for unidirectional motion in ∅20 mm pipes. The robot consists of piezoelectric bimorph actuator ($38 \times 16 \times 0.5$ mm$^3$) with four flexible fins attached to it. Excitation of the bending resonance mode of the piezoelectric actuator causes relative slip between the fin tips and the tube walls. Because of the inclination angle between the fin tips and the tube wall, the friction is lower for forward relative slip than for backward slip, which causes the symmetric vibration to result in a net forward motion. A maximum velocity of 332 mm/s and thrust force of 0.12 N was measured for an excitation at ±60 V at 600 Hz. A similar design, but with an axially expanding stack piezoelectric actuator instead of a bimorph actuator is discussed by Gmiterko *et al.* [268].

Kim *et al.* (Korea Institute of Science and Technology, KIST, South Korea) [269] present a mobile robot inspired by earthworm locomotion. The robot (see figure 2.14(b)) consists of two units equipped with small hooks interconnected by an SMA actuator preloaded by a bellow. The robot has a size of ∅9.5 mm× 50 mm and is powered by an on-board battery and can be remotely controlled by an inductive coupling. A maximum velocity of 0.17 mm/s was reported as well as an autonomous operating time of 8 minutes on 3 alkaline batteries (1.55 V, 33 mAh) corresponding to a power consumption of approximately 1150 mW. A similar endoscope robot was already presented by the same author in 2004 [270]. For that previous robot (∅13 mm× 33 mm) the differential motion was not generated between the two robot ends but rather between the passive body and four individual slider driven by SMA actuators and equipped with small hooks. Experiments have shown velocities up to about 0.4 mm/s for a power consumption of about 600 mW (300 mA and 2 V). These robot clearly show the advantages of easy integration and simple driving electronics for SMA actuators, but also the drawback of their high power consumption. Because of this simplicity, SMA actuators were chosen for *Stiquito*, a simple, but successful mobile robot used for education in electronics [47, 271]. A driving principle with tiny hooks actuated by two electromagnetic motors is also proposed by Quirini *et al.* [30] for the locomotion of a ∅11 mm × 25 mm endoscopic capsule robot in the lower gastrointestinal tract (large bowel).

A similar design of an in-pipe robot is presented by Sun *et al.* (Shanghai University, China) in 1998 [272]. The robot has an overall size of ∅15 mm × 30 mm and consists of two units between which the distance can be varied by an on-board electromagnetic actuator.

[16] It should be noted that non-perpendicular contact angle does not really change the friction coefficient. It causes an intrinsic, automatic change in contact force when changing the slip direction. The effect on the friction force can, however, be represented by a virtual change in friction coefficient.

Each of the units is equipped with inclined fins touching the walls of the pipe. Experiments have shown that for driving frequencies of 30–70 Hz, AC driving voltages of 14–20 V, and an AC driving current of about 60 mA a motion velocity of 5.3–8.4 mm/s and a peak power consumption of 840–1200 mW were obtained. The robot is also capable of vertical motion with slightly lower velocities.

In 1990 a microrobot (see figure 2.14(c)) capable of upsidedown locomotion was developed by T. Hayashi (Tokyo Institute of Technology, Japan) [54]. The microrobot (size $13 \times 5 \times 5$ mm$^3$) consists of an arc shaped PVDF actuator interconnecting two strips of cloth with inclined bristles. The strips of cloth are drenched with water, resulting in an attractive, capillary force between the strips of cloth and the walking substrate allowing the robot to walk upside-down hanging from the ceiling. An eccentric mass is attached to the rear leg. A maximum velocity of 1.8 mm/s for an actuation frequency of 1 kHz was reported. T. Hayashi presents in 2000 [143] an alternative design allowing for bidirectional 2 DOF motion. The actuator is still an arc shaped PVDF actuator, but the cloth strips are replaced by sharp tips. Excitation of the right resonance mode makes the robot move forward or backward. Moreover, one of the arc ends is split in two, allowing for turning motion. The author reports that motion was achieved for robot sizes down to 3 mm.

A six legged robot design based on directional friction is proposed by Sahai *et al.* [273] (University of California, Berkeley) in 2006. The robot has a length of 35 mm and is actuated by two piezoelectric bender actuators. The motion of the piezoelectric benders is distributed to the legs and amplified by a kinematic of three slider cranks in series. Polyurethane strips with inclined microfibers are attached to the feet for directional friction. The robot is equipped with on-board battery and driving electronics. Three prototypes have been fabricated and leg motion (40° angular stroke) has been demonstrated, but no locomotion has been reported so far.

As demonstrated by the robots discussed above, locomotion based on direction friction can be obtained with only one on-board actuator. Moreover, differential slip generation allows for slow, quasistatic actuation. Because of these two reasons, such locomotion principle is well suited for wireless actuation. Uchino *et al.* [274, 275] presented in 1989 a two legged robot of a size of $21 \times 12 \times 9$ mm$^3$ (see figure 2.14(d)) actuated by photostrictive actuators[17]. The photostrictive legs bend by $\pm 150$ $\mu$m with a response time of about 10 s under the influence of incident light. Inclined sharp tips are attached to the leg ends in order to obtain directional friction. A motion velocity of about 0.017 mm/s is reported, which could still be improved by improving the efficiency of the directional friction units. The velocity of such a wireless robot can also be increased by using other photoactive materials such as the Photo-Induced Phase Transition (PIPT) material presented in [277] exhibiting a response time of only 2 ms.

Maeda *et al.* (Waseda University, Tokyo) [278] present an untethered, autonomous walking device actuated by an self-oscillating chemical reaction. The chemical reaction in an artificial gel causes autonomous swelling-shrinking behavior, which causes a bending oscillation in the arc shaped gel device. The two ends of the arc slip on a saw tooth shaped surface, resulting in a net forward motion. The oscillation cycle time and amplitude are about 112 s and 410 $\mu$m respectively, resulting in a velocity of about 2.8 $\mu$m/s.

One of the most well known locomotion solutions based on directional friction applied in the field of microrobotics is probably the scratch drive principle. The scratch drive principle was first presented by Akiyama *et al.* [22] (Sophia University, Tokyo) in 1993. A scratch drive actuator has an L-shaped structure fabricated by surface micromachining (see figure 2.14(e)). Electrostatic attraction resulting from an applied voltage difference between device and sub-

[17] Photostriction in ferroelectrics arises from a superposition of photovoltaic and inverse piezoelectric effects [276].

strate causes the device to bend. During this bending the tail is stuck to the substrate, which forces the head to slide forward. When the voltage difference is removed the elastic energy is released and the device is trusted forward due to directional friction between the head and the substrate[18]. The voltage potential is applied to the device by means of sliding electric contacts (see figure 2.14(e)). Akiyama *et al.* demonstrated linear and a rotary scratch drive actuators with different sizes. The devices with dimensions $0.080 \times 0.080$ mm$^2$ and bushing height ($h$) of 2 $\mu$m have shown a motion velocity of 0.080 mm/s when actuated with a voltage of 150 V and a driving frequency of 1 kHz.

Donald *et al.* [69] (Dartmouth College, Hanover, USA) proposes an untethered version of the scratch drive actuator by applying a voltage difference between interdigital electrodes structured on the substrate. With this technology velocities up to 1.9 mm/s were reported for actuation at 100 kHz with 60 V. Based on the same technology the same authors [23] presented in 2006 a scratch drive actuator capable of forward motion and turning motion to one side (see figure 2.14(f)). An arm that is slightly bent upwards is added to the design. By adjusting the voltage wave form the arm can be lowered to the substrate during scratch drive locomotion, which causes the robot to turn around the small dimple (see figure 2.14(f)) beneath the end of the arm. The robot has an overall size of $0.250 \times 0.060 \times 0.010$ mm$^3$ and maximum velocities of 200 $\mu$m/s have been reported. The authors claim this robot to be the world's smallest [279]. Although these results are very impressive and promising, it should noted that these robots only allow for forward motion and turning to one side, which still limits considerably the possible applications as a mobile robot.

A solution for bidirectional motion could principally be obtained by fabricating several scratch drive actuators with different orientations and with the bushing facing upwards on a substrate and flip this substrate upside down in order to walk on top of another substrate. This concept is demonstrated for unidirectional motion by Kanamori and Hane [280]. They fabricated a micro translation stage of $2.3 \times 2.0$ mm$^2$ with 300 upward facing scratch drive actuators on top. Flipping the micro translation stage on top of a conductive substrate and applying a voltage between the stage and the substrate resulted in a motion velocity of 0.045 mm/s for an actuation voltage and frequency of 120 V and 500 Hz. With the same technology one could imagine to have scratch drive actuators oriented in all four orthogonal directions and actuated them individually in order to obtain bidirectional $XY$ motion.

Locomotion based on differential slip and directional friction is also used in MEMS for obtaining large strokes with actuators featuring small displacements. Lateral electrostatic clamping similar to that of the scratch drive mechanism is proposed by Tas *et al.* [233] for driving a linear MEMS actuator. Electrothermal actuators have also been used for linear actuators based on differential slip and directional friction [281, 282]. A compliant ratchet mechanism driven by electrostatic comb drive actuators is presented in [283] and [284].

### 2.7.2 Evaluation

Directional friction allows to obtain motion with a very simple robot design: one actuator, which can be operated in resonance mode, is sufficient. If not considering the two robots with SMA actuators and photostrictive actuators, for which the motion velocity is limited because of the limited bandwidth of the actuator, the $D\mu$ class features motion velocities in the range of 0.2 to 12 L/s, which is rather fast. Almost no data is available on power consumption for the robots reported in literature, but this locomotion class should allow for power efficient robots because of the simplicity and the possibility for resonance mode

[18] In fact, the scratch drive is a mixture between clamping of the tail as in the inchworm principle and directional friction at the head.

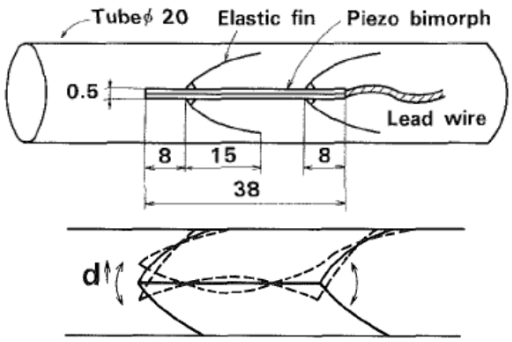


**(a)** NTT Transmission Systems Lab., JP [28]
⌀20 mm× 38 mm, 332 mm/s

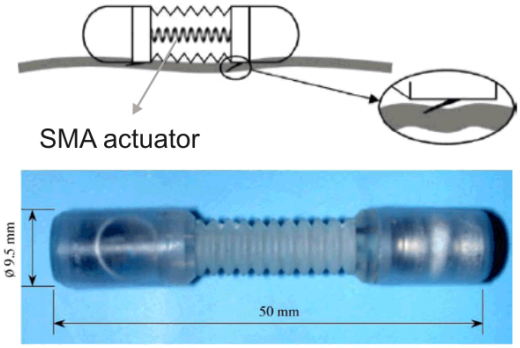


**(b)** KIST, KR [269]
⌀9.5 mm× 50 mm, 0.17 mm/s, 1150 mW

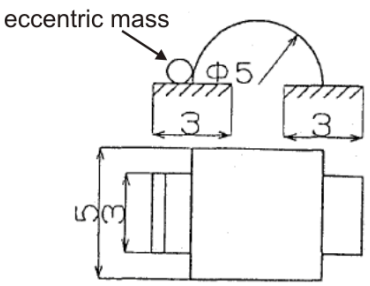


**(c)** Tokyo Institute of Technology, JP [54]
$13 \times 5 \times 5$ mm$^3$, 1.8 mm/s

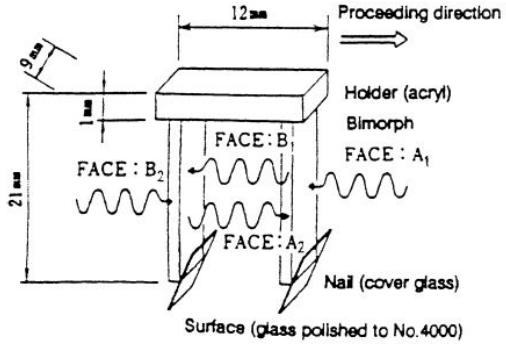


**(d)** Pennsylvania State University, US [275]
$21 \times 12 \times 9$ mm$^3$, 0.017 mm/s

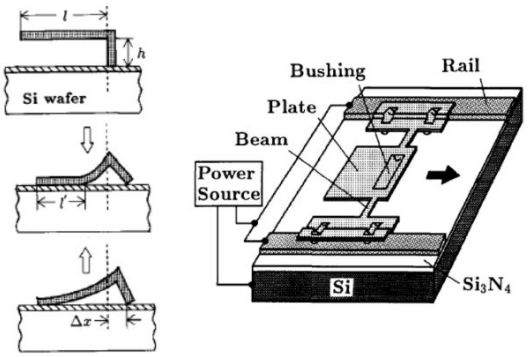


**(e)** Sophia University, JP [22]
$0.080 \times 0.080$ mm$^3$, 0.08 mm/s

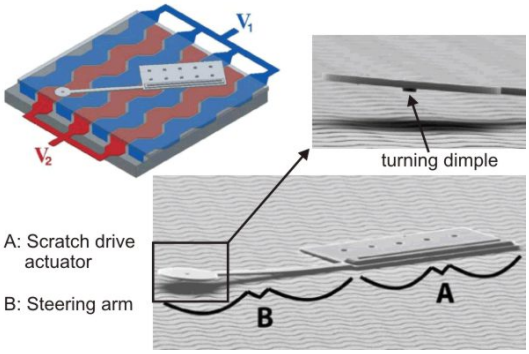


**(f)** Dartmouth College, US [23]
$0.250 \times 0.060 \times 0.010$ mm$^3$, 0.017 mm/s

**Figure 2.14:** Mini and microrobots based on differential slip and directional friction

| | $v_s$ [L/s] | $P_s$ [$\frac{\text{mW}}{\text{mm/s}}$] | DOF | Elec | 1 cm$^3$ | Res |
|---|---|---|---|---|---|---|
| $D\mu$ | $10^{-1} \cdots 10$ | | 0.5-1 | | | |

**Table 2.6:** Evaluation of locomotion class $D\mu$ for mobile microrobots

operation. The major drawback of locomotion with directional friction is that it generally results in unidirectional motion. Bidirectional motion is possible by orienting the feet of the robot, but this complicates the robot design considerably. The scratch drive actuator shown in figure 2.14(f) features 2 times half a DOF (forward motion and right turning motion), but still, when such a robot runs into an obstacle, it can not back off by itself, which is a severe restriction for practical mobile robot applications. The in-pipe robot shown in figure 2.14(a) is developed for feeding electrical wires through small diameter pipes, which is an example of an industrial application where unidirectional motion is not an issue. Because of the limited number of actuation channels and because of the possibility for resonance operation, on-board electronics can be very simple. Again because of simplicity, this locomotion class is very well suited for miniaturization as well as for wireless actuation. Because of the elasticity of the directional fins and typically relatively large steps motion resolution is usually not very good. Logically, the step size decreases when the robot decreases in size, as illustrated by the scratch drive actuator. But due to the limited DOF also the scratch drive robots are not well suited for precision applications. Table 2.6 summarizes the evaluation of the suitability of the $D\mu$ locomotion class for driving mobile microrobots.

## 2.8 Inertial slip with directional friction (class $I\mu$)

This section discusses robots with locomotion based on directional friction and a slip generation that results not from a differential displacement as for the robots in the previous section, but rather from the inertial effect of a vibration. This type of locomotion has been studied by Mansour *et al.* [285] in 1975 and Okabe *et al.* [286] in 1988 for the conveyance of passive parts with bristled, vibrating tracks. The principle has also been used for driving rotary motors as patented by Sashida *et al.* [287] in 1982. The development of MEMS fabrication technologies allowed for smaller integration of inclined, elastic fins on vibrating actuators. Used actuating principles are piezoelectric bimorph disks for rotary motors with applications in the watch industry [288, 289], or electrostatic [290] and electrothermal [291] actuators driving linear, high stroke motors for optical bench applications.

### 2.8.1 Literature review

Fukuda *et al.* (Nagoya University, Japan) [292, 293] reported in 1992 on a mobile microrobot based on directional friction and inertial vibration. The robot has a size of $8 \times 7 \times 9$ mm$^3$ and has 0.5 DOF (forward linear motion, no backward). The bottom of the robot is covered with nylon bristles that are inclined with an angle of 45° to the floor. The robot is actuated by a horizontally oriented electromagnetic actuator of which the displacement is limited in each direction by a mechanical stops. Impact between the stops during vibration of the actuator causes the robot to slip back and forth on the floor. Because of the bristle inclination, the forward slip is larger than the backward slip, resulting in a net forward motion. Motion

velocities of about 0.4 mm/s have been reported.

Two similar designs of mobile robots with locomotion based on directional friction are presented by Ishihara *et al.* [116] from the same research group at Nagoya University. In a first design two spring-guided, magnetic cores are vibrated inside two coils. Again the vibration is transformed into motion by the inclination of bristles attached to the bottom of the robot. The locomotion module (see figure 2.15(a)) has a size of $10 \times 10 \times 6$ mm$^3$ and is driven with a current of 70 mA and a frequency of 120 Hz. No data on the motion velocity has been reported. Two photosensors and a Programmable Logic Device (PLD) have been added to the locomotion module (total robot size $16 \times 10 \times 13$ mm$^3$) for a line tracing experiment. The second design presented by Ishihara *et al.* [116] is driven by piezoelectric actuators instead of electromagnetic. It has an overall size of $10 \times 10 \times 10$ mm$^3$ and a velocity of 2 mm/s has been reported. It is powered by three on-board button cell batteries and equipped with four on-board photosensors and a PLD, allowing for autonomous light searching behavior.

Matsuoka *et al.* (Meitec Corporation, Nagoya, Japan) [294] reported in 1993 on two similar mobile microrobots. The smallest of the two robots (see figure 2.15(b)) has an overall size of $10 \times 10 \times 5$ mm$^3$ and features forward motion with left and right turning. It is actuated by two piezoelectric unimorph disk actuators that excite the resonance frequencies of the two interconnected frames. Velvety brushes with an inclined orientation are glued to the bottom of the frame resulting in directional friction. A maximum locomotion velocity of 100 mm/s was reported for square wave actuation with $U = 80$ V at around $f = 3$ kHz. The piezoelectric actuators have an average electrical capacitance of $C = 212$ pF, resulting into a power consumption of only $P = 2 \cdot \frac{1}{2} \cdot fCU^2 = 4.1$ mW. The authors also report on an alternative design with a closed frame and two piezoelectric stack actuators instead of two unimorph actuators. The same maximum velocity was reached with this design, but the power consumption is more than 1000 times higher because of the much larger electrical capacitance of the stack actuators and higher driving voltages and frequency. The stack piezo design was, without the inclined bristles, also capable of bidirectional motion by exciting different resonance modes of the frame as for standing wave ultrasonic motors (see section 2.6).

Ioi *et al.* (Kinki University, Higashihiroshima, Japan) [295] present a minirobot with inclined brushes and a vibration generated by the centrifugal forces of two eccentric motors. The robot (see figure 2.15(c)) has an overall size of $28 \times 10.7 \times 4.5$ mm$^3$ and has an on-board button cell battery . The motors are operated at a maximum velocity of 9400 rpm and motion velocities up to 200 mm/s were reported.

Isaki *et al.* (Tohoku University, Sendai, Japan) [296] propose to use inclined brushes and eccentric motors for active driving of the flexible cable of a scope camera. As a proof of concept they first developed a $38.8 \times 19.7 \times 15.1$ mm$^3$ mobile minirobot with inclined cilia and one eccentric vibration motor. A maximum velocity of almost 80 mm/s is reported for a motor frequency of 140 Hz.

As for differential slip and directional friction, locomotion based on inertial slip and directional friction can lead to very simple robot designs with only one on-board actuation in the case of 1 DOF motion. Fukuda *et al.* (Nagoya University, Japan) [297] reports in 1991 on two in-pipe robots actuated by an external magnetic field. The first robot (see figure 2.15(d)) has a size of $\varnothing 6$ mm $\times$ 4 mm and consists of a Giant Magnetostrictive Alloy (GMA) actuator and 16 inclined legs touching the tube wall. External generation of an alternating magnetic field generates a strain in the GMA actuator. The resulting vibration causes slip between the robot's feet and the tube wall, which is converted into a forward trust motion due to the directional friction of the inclined feet. A maximum unidirectional motion velocity of about 0.8 mm/s was reported for an actuation frequency of 80 Hz.

| | $v_s$ [L/s] | $P_s$ [$\frac{\text{mW}}{\text{mm/s}}$] | DOF | Elec | 1 cm$^3$ | Res |
|---|---|---|---|---|---|---|
| $I\mu$ | $10^{-1} \cdots 10$ | | 1-1.5 | | | |

**Table 2.7:** Evaluation of locomotion class $I\mu$ for mobile microrobots

The second in-pipe robot presented by Fukuda *et al.* in [297] is larger (⌀21 mm × 71 mm), but allows for bidirectional motion. The robot (see figure 2.15(e)) consists of one GMA actuator and four sets of legs that can be inclined by means of an amplifying lever mechanism. A DC component in the external magnetic field allows to choose the inclination of the legs, while an AC component generates a vibration in the legs trusting the robot forward or backward. A maximum motion velocity of 1.5 mm/s was reported for a driving frequency of 180 Hz.

Yasuda *et al.* (University of Tokyo) [70, 19] report on an untethered microrobot actuated by a mechanical vibration field (see figure 2.15(f)). The microfabricated robot has a size of 1.5 × 0.7 mm$^2$ and features 1.5 DOF motion. The main structural material is polysilicon, but polyimide has been used for the two soft springs and folding joints. The robot has 4 supporting legs in the outer corners, and two kicking legs generating the driving force. The feet of the kicking legs are inclined with respect to the substrate, allowing for directional friction. The two kicking legs have been designed to have a different resonance frequency (390 Hz and 460 Hz). Selective excitation of one or both of the resonance frequencies by the external vibration of the substrate allows to drive the robot forward (0.5 DOF) and turn left or right (1 DOF). Motion velocities of 4.5 mm/s and more were reported for a substrate vibration amplitude of 8 $\mu$m.

### 2.8.2 Evaluation

Locomotion based on directional friction with inertial slip generation (class $I\mu$) features the same advantages and drawbacks as in the case of differential slip (class $D\mu$). Motion velocity ranges from 0.16 L/s up to 12 L/s. A very low specific power consumption of 0.04$\frac{\text{mW}}{\text{mm/s}}$ could be calculated for one robot (see figure 2.15(b)), but also for the other robots power efficiency is expected to be good. As for the $D\mu$ class, the major drawback is the DOF. Three of the presented robots feature forward motion as well as left and right turning. But as the turning is coupled to a forward motion (like a car), these robots cannot recover from a situation after running into a wall. Bidirectional motion is demonstrated for the robot in figure 2.15(e), but then the advantage of simplicity is partially lost. Again, simplicity allows for a high level of miniaturization through microfabrication and wireless actuation. Motion resolution, however, is even worse than for the $D\mu$ class. Table 2.7 summarizes the evaluation of the suitability of the $I\mu$ locomotion class for driving mobile microrobots.

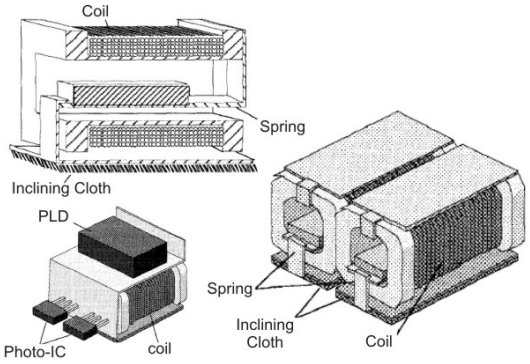


**(a)** Nagoya University, JP [116]
$10 \times 10 \times 6$ mm$^3$

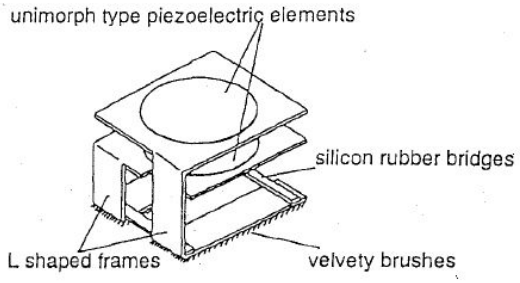


**(b)** Meitec Corporation, JP [294]
$10 \times 10 \times 5$ mm$^3$, 100 mm/s, 4.1 mW

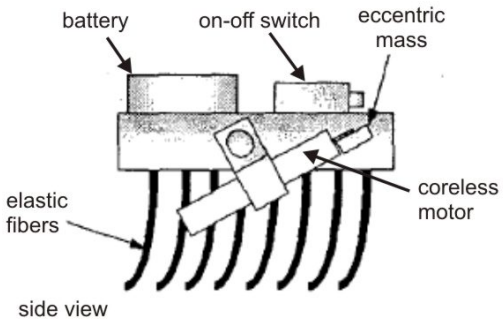


**(c)** Kinki University, JP [295]
$28 \times 10.7 \times 4.5$ mm$^3$, 200 mm/s

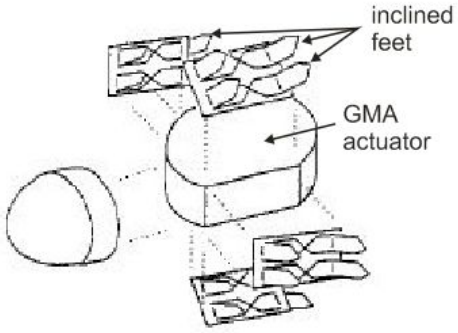


**(d)** Nagoya University, JP [297]
∅6 mm × 4 mm, 0.8 mm/s

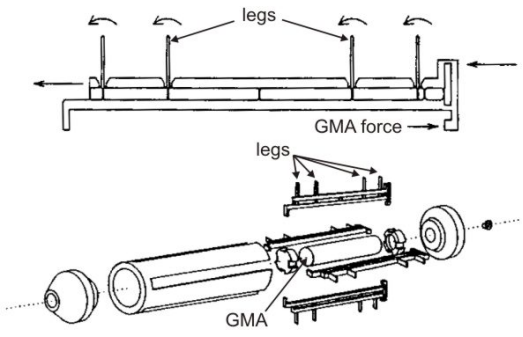


**(e)** Nagoya University, JP [297]
∅21 mm × 71 mm, 1.5 mm/s

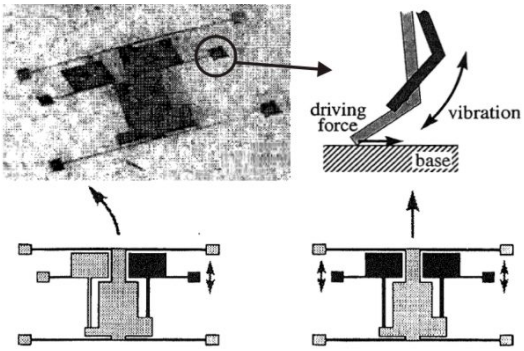


**(f)** University of Tokyo, JP [19, 298]
$1.5 \times 0.7$ mm$^2$, 4.5 mm/s

**Figure 2.15:** Mini and microrobots based on inertial slip and directional friction


**(a)** The *stick-slip* principle **(b)** The *impact drive* principle

**Figure 2.16:** Two types of *inertial drive* principles

## 2.9 Inertial slip with asymmetric vibration (classes $D\Delta t$ and $I\Delta t$)

### 2.9.1 Inertial drives: stick-slip and impact drive principle

Besides contact force variation and directional friction a third way to obtain net motion from a repetitive slip is by inducing an asymmetric slip behavior. As expressed by equation 2.2 on page 20 the slip distance $\Delta X_{slip}$ depends on the slip time $\Delta t$. Hence, net motion can be obtained by inducing a different slip time for forward and backward slip. In literature, locomotion based on asymmetric slip is generally referred to as the *inertial drive* principle. Two types of *inertial drive* principles can be distinguished: the *stick-slip* principle and the *impact drive* principle. In fact there is no essential, qualitative difference between these two types of inertial drives. The quantitative difference can, however, be expressed by dividing the robot in two parts that are interconnected by the actuator that is generating the vibration for slip generation (see figure 2.16). Let's consider $M_f$ the mass of the part of the robot that is in contact with the floor (feet) and $M_i$ the mass of the rest of the robot (inertial mass). Hence, the condition for the stick-slip principle is $M_f \ll M_i$, while the impact drive principle is characterized by $M_f \geq M_i$. In the stick-slip principle slip is generated by rapidly retracting the feet ($M_f$) with respect to the robot's body ($M_i$). Stick-slip actuators are optimized by trying to minimize the mass of the feet ($M_f \ll M_i$). For the impact drive principle slip of the robot's body ($M_f$) on the floor is caused by a rapid extension (or contraction) of an actuator with an additional inertial mass ($M_i$) attached to it with typically $M_f \geq M_i$. Inertial drive locomotion with an external, actuator and a passive slider is generally also categorized under the stick-slip principle.

Apart from a few exceptions, inertial drive actuators are actuated by piezoelectric actuators, because of their high bandwidth. A typical voltage waveform for a stick-slip actuator is a sawtooth signal with a *linear* ramp: during the ramp phase of the saw tooth signal the body of the robot moves forward at a constant velocity, while during the edge, a small backlash typically occurs. Impact drives, on the other hand, are typically driven with a saw tooth signal with a *quadratic* ramp phase: the body of the robot does not move during the ramp phase, while a sudden forward step occurs during the edge. The quadratic shape of the ramp phase allows to store a maximum amount of kinetic energy in the motion of the inertial mass, resulting in the maximum step displacement of the body of the robot.

Prof. Toshiro Higuchi (University of Tokyo) is the first to report on the impact drive principle in 1984 [299]. He proposes to move an object by mechanical impacts of a inertial mass against the object. In this first configuration an electromagnetic actuator is used to store potential energy in a spring, which is than transformed in kinetic energy that is absorbed by the mechanical impact causing the object to move. In 1987 Higuchi *et al.* [300] propose the use of a piezoelectric actuator for generation of the impact. In 1991 an in-pipe impact drive actuator with an additional mechanical clamping unit (30 mm × 15 mm, 6.5 mm/s,

100 Hz, 100 V) is presented by Ikuta *et al.* (Kyushu Institute of Technology, Japan) [301] as a cybernetic actuator featuring the same 4 states as a human muscle: free, decreasing, increasing and locked. In 1992 an enhancement of the impact drive principle by increasing the friction force during the stiction phase by an electromagnet is proposed by Higuchi *et al.* [302] and Ikuta *et al.* [303]. In the same year Higuchi *et al.* also proposes an impact drive with friction force variation by the vertical acceleration of an additional inertial mass [304].

The stick-slip principle has been proposed for the first time by Besocke (Kernforschungsanlage Jülich GmbH, Germany) [305] in 1987 for positioning of a sample for a Scanning Tunneling Microscope (STM). Besocke proposes three piezo tubes for positioning of the sample and a fourth tube for positioning of the tip. In the same year a linear stick-slip actuator driven by the axial deformation of a piezo tube is presented by Pohl (IBM Zürich Research Laboratory, Switzerland) [306]. In 1991 a variant of the stick-slip principle is proposed by Matsuda and Kaneko (NTT Applied Electronics Laboratories, Tokyo, Japan) [307]. They drive a passive slider with the bending mode of piezo tube by applying a fast, 1-period sine wave. The direction in which the sine wave starts determines the direction of the generated step. Two variants of the stick-slip principle with electrostatic clamping and mechanical clamping are presented by Peichel *et al.* [308] in 2002 and Lee *et al.* [309] in 2007.

As expressed in table 2.1 the inertial slip generation of the stick-slip principle can also be combined with a differential slip generation. This idea has been patented by CSEM (Centre Suisse d'Électronique et de Microtechnique SA) in 1995 [310]. Breguet *et al.* in [129] has tested this idea for a linear stick-slip actuator by exciting the slip phase of the three feet with a slight delay. The advantage of this is that the backlash per foot retraction is lower and that the excitation of the resonance frequencies of the actuator (robot) is lower. However, on the other hand the backlash and the resonance excitation occurs three times per stepping cycle, which causes that at the end the gain in performance of differential actuation of the feet is limited. Moreover, the major drawback of differential stick-slip actuation is that it requires independent actuation signals for the different feet, which requires a more complicated driving electronics. Therefore, no robot actuated by differential stick-slip is reported in literature.

The advantage of the inertial drive principle is that it allows for high resolution, bidirectional motion with only one actuator. Stick-slip features a smoother motion of the robot's body than the impact drive principle and is typically more efficient as it results normally in larger step sizes for the same actuator amplitude. Impact drive has the advantage that it can easily be added to a passive object (robot) and it can result in a better robustness of the robot as the weight of the robot does not have to be carried by the actuator and the actuator can be encapsulated in order to protect it from external forces and environmental conditions (dust, humidity, etc.).

### 2.9.2 Literature review

One of the first mobile microrobots based on the inertial drive principle is the one proposed by Ikuta *et al.* (Kyushu Institute of Technology, Japan) [301] (already discussed in section 2.9.1) They presented a cybernetic in-pipe impact drive actuator based on an impact drive principle with friction force control by means of a mechanical clamping unit. The 1 DOF device is actuated by 2 piezo stacks and features a size of 30 mm $\times$ 15 mm and a maximum velocity of 6.5 mm/s ($U = \pm 100$ V, $f = 100$ Hz. The authors' next prototype (see figure 2.17(a)) is based on the impact drive principle with electromagnetic contact force variations [303] and is quite a bit smaller ($20 \times 5 \times 5$ mm$^3$). It features a velocity of about 35 mm/s for a driving frequency of 37 kHz. Several of these actuators have been combined for creating a hyper redundant active endoscope [311].

Another 1 DOF robot is presented in 1995 by Idogaki *et al.* (Nippondenso Co., Ltd.) [26] for pipe inspection applications. The robot has a size of ∅5.5 mm × 20 mm and is driven with one piezoelectric stack actuator. A maximum velocity of 10 mm/s was reported ($U$ = 100 V, $f$ = 4 kHz) as well as vertical upward motion. Nishikawa *et al.* from the same company (by then Denso Corporation) present in 1999 [312, 313] a completely wireless in-pipe microrobot. The robot has a size of ∅9.5 mm × 66 mm and features an on-board CCD camera (with integrated focus module and tilting mirror) for pipe inspection and on-board driving electronics with wireless energy transmission and communication by microwaves (RF). It is driven by a set of piezoelectric bimorph disk actuators connected in parallel (see figure 2.17(b)) and features a maximum velocity of 10 mm/s ($U$ = 12 V, $f$ = 1000 Hz). A first prototype [27] of the robot had an overall power consumption of 480 mW, while a later prototype [313] consumed in total 200 mW, of which 56 mW is consumed by the locomotion module.

In the previous two 1-DOF robots the low piezoelectric strain is amplified by using a stack and a bimorph configuration respectively. Rembold and Fatikow (at that date in University of Karlsruhe, Germany) [172] propose the use of the same amplification mechanisms for two different robot designs with 3 DOF. In a first robot the strain from three stack piezos is further amplified by a tilting lever mechanism. The robot has a size of 30 × 30 × 35 mm$^3$ and 3 DOF actuated by only 3 independent channels. A maximum step size of 36 $\mu$m and a maximum velocity of 0.9 mm/s for a driving voltage of ±20 V were reported. The second robot, called *SPIDER-I*, has a diameter of ∅60 mm and consists of 3 times 2 piezoelectric bimorph actuators connected in series (see figure 2.17(d)). It is actuated with 6 independent, bipolar voltage signals with amplitude ±20 V and a velocity of 0.33 mm/s was reported.

The previous two robots feature large amplification and therefore large step sizes at low driving voltage, but the motion velocity is quite limited, specially when compared to the size of the robots. The reason for this is the low bandwidth of the amplifying mechanical structure, which limits the stepping frequency. Moreover, the two previous designs are not well suited for miniaturization down to the 1 cm$^3$ size. A more integrated approach for obtaining 2 DOF actuation of the robot's feet with mechanical amplification is by using the two bending modes of a piezo tube. One of the first 3-DOF mobile robots based on stick-slip motion with piezo tubes is presented in 1995 by Magnussen *et al.* [314] (University of Karlsruhe, Germany). Their "Piezoelectric RObot for HAndling of Microobjects" (PROHAM) has a size of 80×80×50 mm$^3$, on-board driving electronics and features a motion velocity up to 30 mm/s ($U$ = ±150 V, $f$ = 5 kHz) [315, 142]. Within the MINIMAN project [96] several robots were developed with 3 DOF locomotion actuated by piezo tubes. Moreover, the locomotion module can also be flipped upside down in order to drive the three rotative DOF of a ball in which a manipulator can be integrated. The robots *MINIMAN*, *MINIMAN II*, *MINIMAN III* (see figure 2.17(e)) and *MINIMAN IV* all feature locomotion based on piezo tubes with a maximum velocity of about 30 mm/s ($U$ = ±150 V, $f$ = 5 kHz) [103, 33, 106]. One of the disadvantages of this robot design is that 4 channels per leg are needed, so 12 channels for locomotion (plus 12 channels for manipulator). This number of channels could be reduced by a factor of two by a reverse polarization of the opposite electrodes on the piezo tubes as proposed by Bergander *et al.* [316] for monolithic push-pull piezo actuators (MPA). The last robot developed in the MINIMAN project, the *MINIMAN V* robot, (already presented in the section on walking robots, see figure 2.5(a) on page 30) does not only feature walking motion, but also stick-slip motion as discussed in [175]. This robot design is, however, not optimized for stick-slip motion as it has 6 legs (while 3 would be sufficient), 24 driving channels and actuators with large electrical capacitance resulting in large peak driving currents during the slip phase.

Another mobile minirobot based on stick-slip actuation with piezo tubes is presented by Juhas *et al.* [317]. Their robot has a size of $54 \times 49 \times 57$ mm$^3$ and has on-board driving electronics. The velocity of the robot is limited to 0.06 mm/s, because of the limited driving frequency (20 Hz) of the on-board electronics.

Another configuration of the piezo tube legs for a stick-slip robot is proposed by Martel *et al.* (Massachusetts Institute of Technology, USA) [88]. The NanoWalker [88] and the NanoRunner [89] robots are both based on a arrangement of the piezo tubes in the shape of a pyramid with the apex pointing upwards. This arrangement allows for a smaller overall size of the robot, but requires the piezo tubes to operated in a combination of the bending and the axial mode in order to allow for a motion of the legs parallel to the substrate. Both robots are equipped with an on-board driving electronics with DC-DC convertors, wireless communication, signal generation and 12 power amplifiers for driving the 3 piezo tubes. The NanoWalker is also equipped with a Scanning Probe Microscope (SPM) tool with readout electronics for nanoscale operations. The NanoWalker has an overall size of $32 \times 32 \times 20$ mm$^3$ (mass 32 g) and is actuated by three piezo tubes of 19 mm long, while the smaller NanoRunner (see figure 2.17(f)) is based on piezo tubes of 12.7 mm long [89]. Because of its advanced, but complex electronics the robot has an overall power consumption of 15 W. With an experimental, wired version that is slightly larger (leg length 19 mm, mass 88 g) a maximum velocity obtained with a sawtooth signal was 3.9 mm/s ($U = \pm 40$ V, $f = 571$ Hz), while with a triangular signal (2/3 rise time, 1/3 fall time) a velocity of 26.3 mm/s ($U = \pm 50$ V, $f = 1316$ kHz) was recorded [89]. Driving with 2/3-1/3 triangular signal (called the *push-slip* method by the author) allows for higher motion velocities as higher driving frequencies and driving voltages can be applied due to the lower harmonic content in the driving signal. Higher velocities of 200 mm/s were reported for resonant mode operation ($U = \pm 40$ V, $f = 4000$ Hz) [318] for another, wired 8 g prototype with 12.5 mm long piezo legs. However, at this velocity the motion was rather unstable [94].

Piezoelectric shear mode actuators are well suited for actuation of stick-slip drives as they are small, easy to integrate and have high resonance frequencies. The relatively low displacement of some hundreds of nm is compensated by the high bandwidth, which allows for high frequency operation. The use of shear mode piezo actuators for driving linear and rotary stick-slip actuators has been patented by the company Omicron in 1992 [322]. A very straightforward way to obtain robots with 3 DOF stick-slip motion is by stacking three times two perpendicularly oriented shear mode actuators on top of each other as illustrated by Breguet *et al.* (EPFL) in [323]. They present a mobile minirobot with 3 DOF locomotion (see figure 2.18(a)) actuated by 6 independent channels. The robot has a size of ∅50 mm × 34 mm, is actuated by 6 independent actuation channels and maximum velocities of 4 mm/s were reported ($U = \pm 150$ V, $f = 10$ kHz). During translation 3 piezoelectric actuators with a capacitance of about $C = 100\ pF$ (estimated from [129]) are actuated with a bipolar voltage resulting in a power consumption of $P = 3 \cdot \frac{1}{2} \cdot f \cdot 2CU^2 = 68$ mW. An alternative way to combine the motion of two shear piezos into the $XY$ motion of a foot is by using a flexible $L$ shaped structure as shown in the inset in figure 2.18(b) [324]. Three of such structures can be combined in order to obtain 3 DOF locomotion with 6 actuation channels. The resulting robot (see figure 2.18(b)) has a size of ∅32 mm × 19.8 mm and is equipped with an integrated vertical stick-slip axis with a microgripper for micromanipulation purposes [43]. The robot features a maximum locomotion velocity of 4 mm/s ($U = \pm 133$ V, $f = 10$ kHz). The robot is driven by the same piezoelectric actuators as the robot shown in figure 2.18(a) featuring a capacitance of about $C = 100$ pF resulting in a power consumption of $P = 3 \cdot \frac{1}{2} \cdot fC \cdot 2U^2 = 53$ mW. In order to reduce the number of assembly steps and to allow for a further miniaturization a monolithic approach is to be preferred. Based on the concept

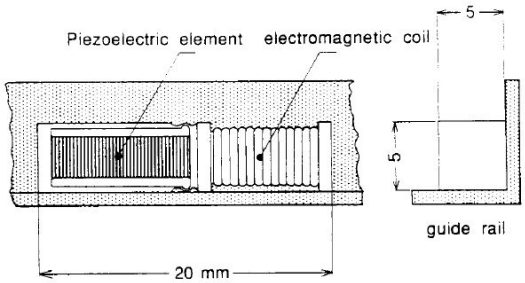


**(a)** Kyushu Institute of Technology, JP [303]
$20 \times 5 \times 5$ mm$^3$, 35 mm/s

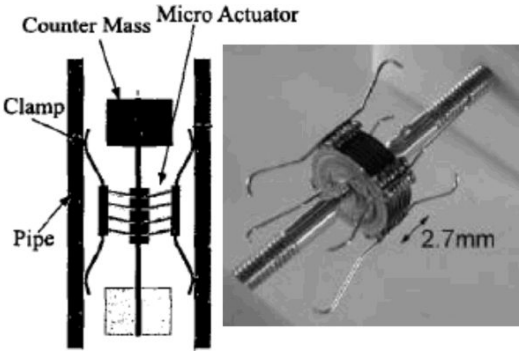


**(b)** DENSO Corporation, JP [312, 319]
∅9.5 mm, 10 mm/s, 56 mW

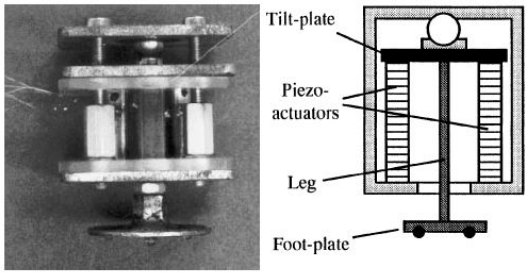


**(c)** University of Karlsruhe, DE [172]
$30 \times 30 \times 35$ mm$^3$, 0.9 mm/s

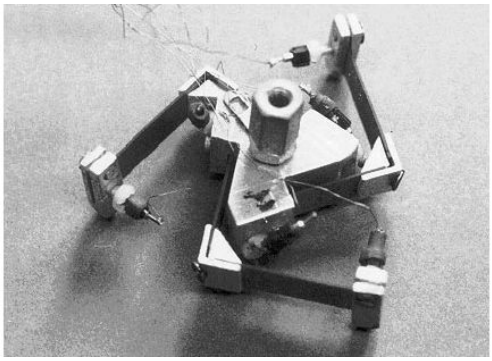

**(d)** SPIDER-I, U. of Karlsruhe, DE [172]
∅60 mm, 0.33 mm/s

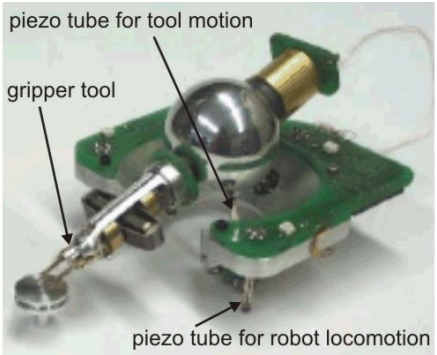


**(e)** MINIMAN III-2, U. of Karlsruhe, DE [320]
$\sim 65\times \sim 65$ mm$^2$, 30 mm/s

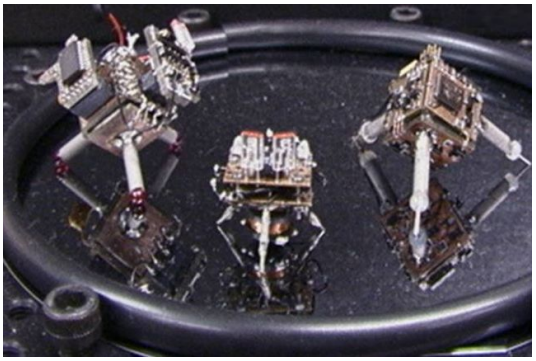

**(f)** NanoRunner, MIT, US [321]
legs 12.7 mm , 26.3 mm/s (with larger proto.)

**Figure 2.17:** minirobots driven by the stick-slip principle

of Monolithic Piezo Actuators (MPA) [325] a monolithic locomotion module based on the transversal piezoelectric effect is developed. In the MPA concept guiding flexures are cut directed in the piezoceramic material by laser, while active and passive piezoelectric material is delimited by structuring the actuating electrodes. The 3 DOF robot (see figure 2.18(c)) based on this locomotion module has a diameter of ∅42 mm and features a maximum velocity of 5 mm/s ($U = \pm 150$ V, $f = 10$ kHz). The six active piezoelectric zones have a capacitance of $C = 335$ pF each[19]. Three actuators are actuated simultaneously for translational motion along the natural axes, resulting in a total power consumption of $P = 3 \cdot \frac{1}{2} \cdot fC \cdot 2U^2 = 226$ mW. From a mechanical point of view the robot is very simple as it consists only of 6 mechanical parts (3 feet, piezoelectric actuation module, spacer and body). From an electrical point of view it requires 6 independent channels, which is already a major improvement compared to the 12 channels for the robots actuated by piezo tubes discussed above, but this is still the double of the optimum of 1 channel per DOF as for the robot design shown in figure 2.17(c).

An inertial drive locomotion module design that is well suited for integration and that requires only 3 actuation channels for 3 DOF is proposed by Zesch *et al.* (Swiss Federal Institute of Technology Zürich, ETHZ) [326]. The *Abalone* locomotion module[20] (size $38 \times 32 \times 9$ mm$^3$) consists of a monolithic steel structure with an inner and an outer ring interconnected by elastic joints and three integrated piezoelectric stacks (see figure 2.18(d)). Actuation of the stacks results in a 3 DOF displacement of the inner ring with respect to the outer ring. The inner ring is touching the ground at three contact points, while the outer ring is to be connected to the robot's body. Actuation with a saw tooth signal allows for 3 DOF inertial drive motion. A maximum velocity of 1 mm/s was reported for a driving voltage of 80 $V_{p2p}$ and frequency of 400 Hz. Breguet *et al.* realized a robot with a design similar to the Abalone robot, but instead of individual piezo stacks the concept of Monolithic Piezo Actuators (MPA) was used. The 3 DOF robot has an overall size of ∅20 mm × 5 mm with only 3 actuation channels (see figure 2.18(e)) [327]. The robot features a maximum motion velocity of about 3 mm/s ($U = \pm 140$ V, $f = 7750$ Hz). The three active piezoelectric zones have a capacitance of $C = 335$ pF, resulting in a power consumption of $P = 3 \cdot \frac{1}{2} \cdot fC \cdot 2U^2 = 153$ mW. Another design similar to the Abalone robot, but than with 4 stack piezos in stead of 3 is proposed by Nomura and Aoyama (University of Electro Communications, Tokyo) [328]. The robot (see figure 2.18(f)) has a size of $28 \times 28 \times 16.5$ mm$^3$, 4 actuation channels and a maximum velocity of 1 mm/s ($U = 150$ V, $f = 100$ Hz). The stack piezos have a capacitance of $C = 750$ nF and 2 piezos are used simultaneously for translational motion. The power consumption can thus be calculated as $P = 2 \cdot \frac{1}{2} \cdot CFU^2 = 1688$ mW, which is rather high for such a small robot.

One of the drawbacks of the concept of Monolithic Piezo Actuators with flexible joints in the piezoelectric material as used for the robots in figures 2.18(c) and 2.18(e) is the fragility of the piezoelectric material after the laser cut. This is especially an issue when further miniaturization and therefore smaller hinges is required. In order to solve this problem the concept of monolithic piezoelectric push-pull actuators is proposed by Bergander *et al.* (EPFL) [316]. This concept is only based on structuring of the electrodes on a sheet of piezoelectric material and does not require any laser cut of flexible hinges. Electrodes in the shape of two adjacent half-circles are deposited directly on the piezoceramics by screen printing. Actuation of both half-circular electrodes with an opposite voltage allows for an in-plane displacement of the center of the circle. Reverse polarization [316] of both electrode halves gives the same result with only one voltage signal. Dividing the circle in 4 quarter-circles instead of 2 half-

[19] This capacitance has been calculated for an actuator length of 7 mm, width of 3 mm, thickness of 1 mm and relative permittivity of $\epsilon_r = 1800$ (piezo material PXE5, Morgan Electro Ceramics) as reported in [129].

[20] An earlier version of the Abalone robot was based on the same design but on inchworm locomotion [219]. Electromagnetic clamps were integrated in the inner and outer ring for individual clamping.

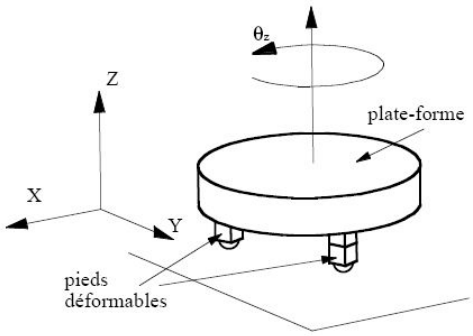


**(a)** EPFL, CH [323, 129]
⌀50 mm × 34 mm, 4 mm/s, 68 mW

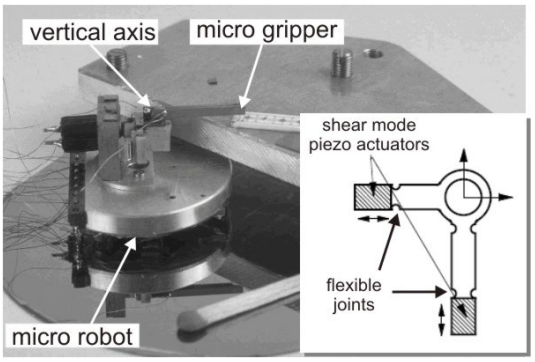


**(b)** EPFL, CH [129, 324]
⌀32 mm × 19.8 mm, 4 mm/s, 53 mW

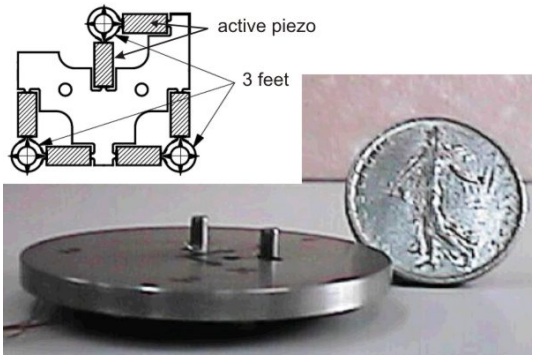


**(c)** EPFL, CH [129, 327]
⌀42 mm, 5 mm/s, 226 mW

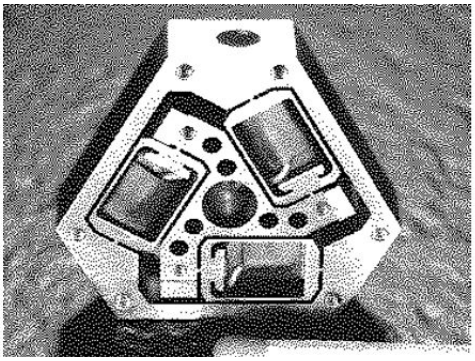

**(d)** Abalone, ETHZ, CH [326]
$38 \times 32 \times 9$ mm$^3$, 1 mm/s

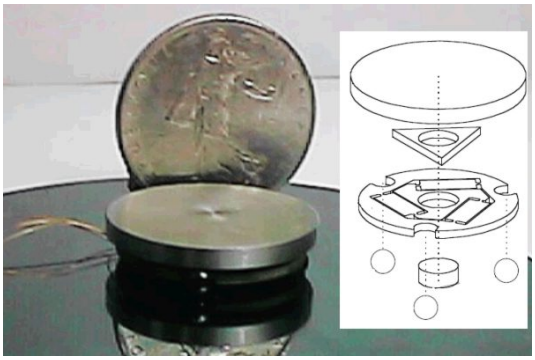

**(e)** EPFL, CH [129, 327]
⌀20 mm, 3 mm/s, 153 mW

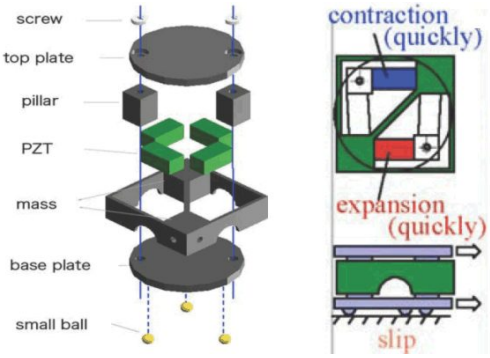


**(f)** U. of Electro Communications, JP [328]
$28 \times 28 \times 16.5$ mm$^3$, 1 mm/s, 1688 mW

**Figure 2.18:** Mini and microrobots driven by the stick-slip principle

circles allows for 2 DOF of a robot foot with 2 actuation signals. A combination of 3 such modules yields a locomotion module with 3 DOF. The major advantages of the monolithic piezoelectric push-pull actuators are high robustness, high bandwidth, miniaturization and batch fabrication techniques. Based on this concept three different mobile microrobots were developed within the scope of the Nanohand [117] and the Golem [36] project. The three different designs [41, 329] have an overall robot size of $20 \times 18.5 \times 12$ mm$^3$, $15 \times 15 \times 12$ mm$^3$ and $13.5 \times 12 \times 12$ mm$^3$. The $15 \times 15 \times 12$ mm$^3$ robot (see figure 2.19(a)) has a maximum velocity of about 3 mm/s ($U = \pm 200$ V, $f = 9$ kHz). The locomotion module consists of 12 quarter circle electrodes with a capacitance of $C = 250$ pF each, resulting in a power consumption at maximum velocity of $P = 12 \cdot \frac{1}{2} \cdot fC \cdot 2U^2 = 1080$ mW. The 12 electrodes are interconnected in order to allow for actuation with only 4 voltage signals.

Another monolithic design of a locomotion module is presented by Kortschack *et al.* (University of Oldenburg, Germany) [39]. They use the out-of-plane deformation of a piezoelectric bimorph disk actuator with structured electrodes to drive a sphere in two degrees of freedom on which the robot is rolling. Based on this concept they present two mobile robots. The largest design is driven by three individual piezoelectric disk actuators, while for the smallest robot (see figure 2.19(b)) the actuation of the three spheres is integrated on the same, structured piezoceramic sheet. Both robots consist of a locomotion module with a manipulator unit on top. The locomotion module of the smallest robot has a size of approximately ∅30 mm $\times$ 13 mm and is driven by 6 independent channels. A maximum velocity of about 0.17 mm/s and a power consumption of 800 mW are reported ($U = \pm 40$ V, $f = 1$ kHz). The locomotion with rolling spheres makes the robot much less sensitive to roughness and scratches on the walking substrate. The drawbacks of this design, however, are that it is difficult to scale this design further down and that the generated vertical motion of the piezoelectric disk actuators might disturb high precision operation.

The monolithic designs discussed above suffer either from high driving voltages, either from miniaturization limits and parasitic vertical motion. As already mentioned before, the driving voltage can be lowered by integrating some kind of mechanical amplification. A 1 cm$^2$ size locomotion module with mechanical amplification is proposed by Driesen *et al.* (EFPL) in [102]. The locomotion module (size $10 \times 10 \times 1$ mm$^3$) consists of a flexible steel frame to which four piezoelectric bars are assembled from the side (see the inset in figure 2.19(d)). The steel-piezo sandwich results in four piezoelectric bimorph actuators of which the deformation is combined in a 3 DOF displacement of the inner structure to which the feet are assembled (illustrated for $Y$ motion in the inset in figure 2.19(c)). Based on this locomotion module different tethered and untethered robots have been developed in the scope of the MiCRoN project [25, 67]. Driesen *et al.* present in [35] a tethered microrobot (size $12 \times 12 \times 12$ mm$^3$) with integrated arm actuator and microgripper (see figure 2.19(c)). The robot features a maximum velocity of 2 mm/s ($U = \pm 200$ V, $f = 1500$ Hz) with a power consumption of 171 mW. This robot and variants of this design have been used for applications such as microhandling [35] and AFM surface measurements [108] in open loop operation and close loop operation with optical tracking [34]. The same locomotion module has also been used for driving the untethered mobile microrobot developed in the MiCRoN project (see figure 2.19(d)). This robot features 3 DOF motion with a resolution of 3 nm, arm actuator [197] with tool, on-board powering by inductive energy transfer from a power floor [66], on-board driving electronics [99], wireless IR communication [92] and targets for high accuracy optical tracking [114]. The tools that have been integrated on the robot are a microgripper [105], an AFM scanner [109] and micro-injection chip [92]. In order to allow for a reduction of the on-board driving voltage the locomotion module was adapted with thinner piezoelectric actuators than the robot shown in figure 2.19(c)). The maximum velocity of

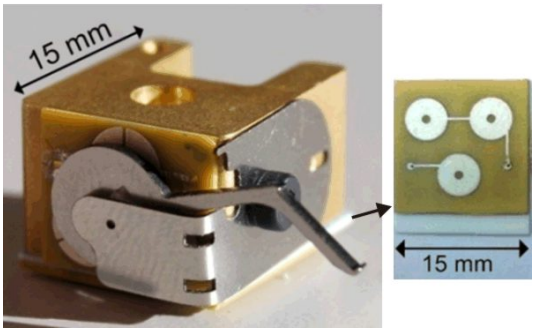


**(a)** EPFL, CH [41]
$15 \times 15 \times 12$ mm$^3$, 3 mm/s, 1080 mW

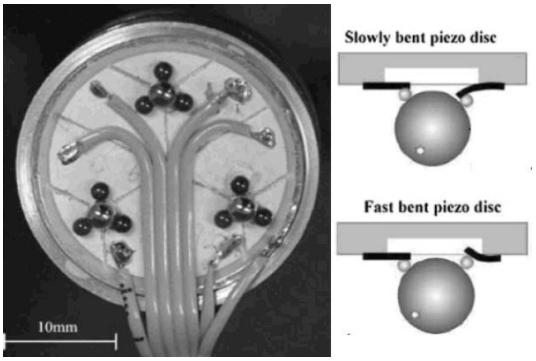


**(b)** University of Oldenburg, DE [39]
$\varnothing$30 mm $\times$ 13 mm, 0.17 mm/s, 800 mW

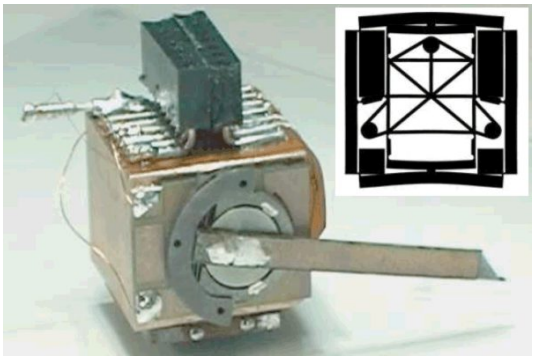

**(c)** EPFL, CH [35]
$12 \times 12 \times 12$ mm$^3$, 2 mm/s, 171 mW

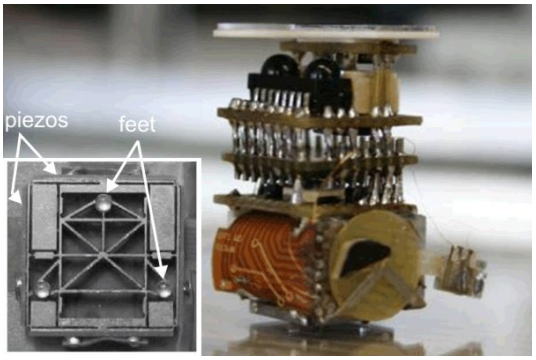


**(d)** MiCRoN, EPFL, CH [330]
$12 \times 12 \times 25$ mm$^3$, 0.75 mm/s, 1.0 mW

**Figure 2.19:** Micro robots driven by the stick-slip principle

the robot with signal generation with the on-board electronics was 0.7 mm/s in diagonal direction for a driving voltage[21] of $U = 14$ V and a driving frequency of $f = 3500$ Hz. The capacitive load for $X$ and $Y$ translation motion is $C = 1.43$ nF, while for diagonal $XY$ motion both translation modes are excited simultaneously, resulting in a power consumption of only $P = 2 \cdot \frac{1}{2} \cdot fCU^2 = 1.0$ mW.

Until now, all mobile robots discussed in this section have been actuated by piezoelectric actuators. Piezoelectric actuators feature the advantage of high bandwidth, which is essential for the inertial drive principle, and high motion resolution, which is important if micromanipulation applications are aimed for. When miniaturizing down to the mm-scale, other actuation technologies, such as electrostatic and thermal, also become interesting.

Mita *et al.* (University of Tokyo) [331] presents in 2003 a MEMS fabricated 1 DOF impact drive with an electrostatic actuator (see figure 2.20(a)). The device has a size of only $3 \times 3 \times 0.6$ mm$^3$ and consists of a frame with a movable mass that enters in collision with two driving electrodes. The maximum velocity of 2.7 $\mu$m/s ($U = 100$ V, $f = 200$ Hz) is, however, rather limited. The same authors presented in 2005 [332] a 2 DOF version with a size of $5 \times 5 \times 0.525$ mm$^3$ and a maximum velocity of 10 $\mu$m/s ($U = 200$ V, $f = 440$ Hz). Although no data was reported, power consumption of both devices is probably low.

[21] At lower frequencies the on-board electronics generates saw tooth signals with a peak-to-peak voltage of 20 V. However, at a frequency of 3500 Hz the amplitude of the saw tooth signal drops to 14 V.

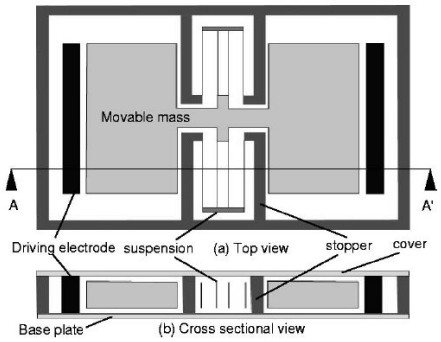


**(a)** University of Tokyo, JP [331]
$3 \times 3 \times 0.6$ mm$^3$, 0.003 mm/s

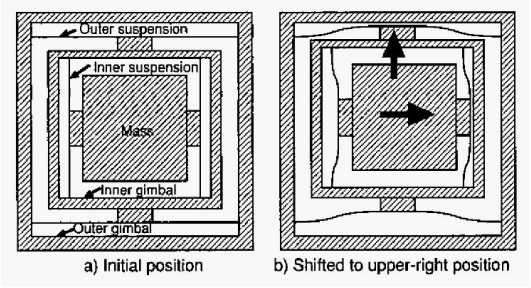


**(b)** University of Tokyo, JP [332]
$5 \times 5 \times 0.525$ mm$^3$, 0.010 mm/s

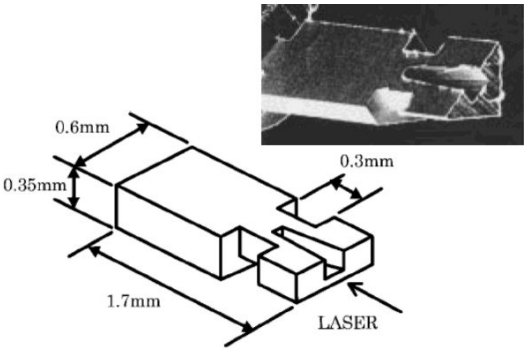


**(c)** University of Tokyo, JP [82]
$1.7 \times 0.6 \times 0.4$ mm$^3$, 31 mm/s

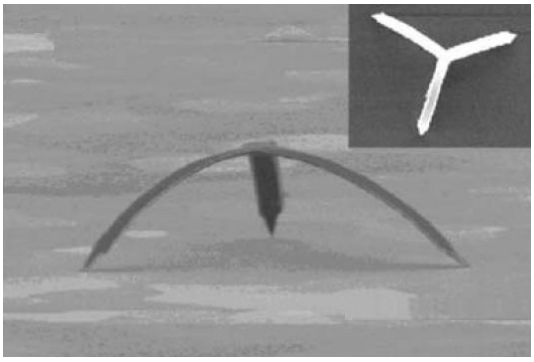

**(d)** U. of North Carolina at Chapel Hill, US [83]
0.030 mm, 0.1 mm/s

**Figure 2.20:** Micro robots driven by the impact drive principle

Ohmichi *et al.* (University of Tokyo) [82] present a wirelessly actuated microrobot driven by the impact drive principle (see figure 2.20(c)). The 1 DOF device has a size of $1.7 \times 0.6 \times 0.4$ mm$^3$ and is fabricated by precision cutting techniques with an end mill of ∅0.2 mm in diameter. The device is actuated by the sudden thermal expansion of one part of the monolithic device induced by a pulsed laser radiation. A maximum motion velocity of 31 mm/s was reported for a pulse rate of 5 kHz with an energy of 0.7 mJ/pulse, corresponding to an average irradiation power of 3500 mW.

Another thermally actuated impact drive microdevice is reported by Sul *et al.* (University of North Carolina at Chapel Hill, USA) [83]. The microfabricated device has a tripod structure with a size down to 30 $\mu$m that is bend out-of-plane because of the intrinsic stress in a Al:Cr layer (see figure 2.20(d)). 3 DOF motion by irradiating the feet with a pulsed laser (maximum power 18 mW) and a maximum velocity of 0.1 mm/s was reported.

### 2.9.3 Evaluation

Mobile robots based on the inertial drive principle with piezoelectric actuators typically feature a motion velocity of about 0.1 L/s. Velocities around 1 L/s are possible in the case of mechanical amplification of the actuator strain and driving at a frequency close to, but still below, the resonance frequency. Piezoelectric stack actuators result in slightly lower

velocities of around 0.03 L/s, probably because the actuation frequency is limited by the electronics because of the high driving current during the slip phase. Electrostatic impact drive devices feature even lower velocities of around 0.001 L/s. External, optical actuation of sub-millimetric impact drive devices has demonstrated velocities of 3 L/s (see figure 2.20(d)) and 30 L/s (see figure 2.20(c)) , although in the latter case we can hardly speak of a mobile robot.

Most inertial drive robots are not very power efficient with specific power consumptions ranging from 100 $\frac{\text{mW}}{\text{mm/s}}$ to 5000 $\frac{\text{mW}}{\text{mm/s}}$. As discussed by Driesen *et al.* in [102] the power consumption of a stick-slip actuator can not be reduced by reducing the driving voltage by means of multilayer piezoactuators, as the power consumption scales quadratically with both the driving voltage and the number of layers. However, an amplification of the piezoelectric strain with a bending structure coupled to a mechanical design optimized in terms of resonance frequency and low voltage operation has shown to result in a specific power consumption of 5 $\frac{\text{mW}}{\text{mm/s}}$ and 1.3 $\frac{\text{mW}}{\text{mm/s}}$ for the robots in figures 2.17(b) and 2.19(d) respectively. Almost all reported inertial drive robots feature 3 DOF locomotion, with the exception of the designs for in-pipe locomotion and those with a size below 1 $\text{cm}^2$. The robots typically feature between 1 and 2 channels per DOF. Robots actuated with piezo tubes have 4 channels per DOF, but in most cases this can be reduced to 2 by reverse polarization of opposite electrodes. Inertial drive robots generally require a complex electronics featuring high driving voltage and high peak currents. Moreover, in the case of high precision applications, which is the major field of interest for inertial drive mobile microrobots, DACs and operational amplifiers are required. The complexity of the on-board electronics for inertial drives is very well demonstrated in the NanoWalker project (robot in figure 2.17(f)), yielding an overall power consumption of 15-20 W. However, in the case of lower driving voltages obtained by mechanical amplification and a low number of channels per DOF resulting from an integrated design of the locomotion module, an on-board electronic with a power consumption of some hundreds of mW can be achieved (as demonstrated for the MiCRoN robot in figure 2.19(d)). If no scanning mode operation with nanometric resolution is required a simpler switching electronics can be implemented (as demonstrated for the robot in figure 2.17(b)). Finally, one of the major advantages of the inertial drive principle — and in particular the stick-slip principle — is its high resolution. Apart from their small locomotion step sizes ranging from some $\mu$m to a few hundreds of nm, stick-slip robots can be actuated in scanning mode[22] allowing for sub-nanometric resolution (determined by step size and resolution of the DAC of the electronics). Table 2.2 summarizes the evaluation of the suitability of the inertial drive principle for driving mobile microrobots.

## 2.10 Conclusion

Table 2.9 gives an overview of the evaluations of the different locomotion classes discussed in this chapter. Before drawing any further conclusions it should be noted that these evaluation results are each time an average for the whole locomotion class. The performances of a robot are not only dependent on the type of locomotion, but also on the actuator technology and the design. Therefore, within the same locomotion class performances can differ quite a lot (for instance between piezoelectric and thermal actuation for walking locomotion). In

[22]During scanning mode operation the voltage applied to the actuators (typically piezoelectric) is varied very slowly in order to avoid slip of the robot's feet. The results is a quasistatic motion of the robot with a range corresponding to the quasistatic displacement of the actuators and typically a resolution equal to the scanning range divided by the number of increments of the DAC of the driving electronics (for instance 4096 for a 12 bit electronics).

| | $v_s$ [L/s] | $P_s$ [$\frac{\text{mW}}{\text{mm/s}}$] | DOF | Elec | 1 cm$^3$ | Res |
|---|---|---|---|---|---|---|
| Inertial drive | $10^{-2}\cdots1$ | $1\cdots10^3$ | 3 | | | |

**Table 2.8:** Evaluation of the inertial drive principle (class $D\Delta t$ and $I\Delta t$) for mobile microrobots

some cases the evaluation is based on a limited amount of data (specially power data is often lacking), which means that adjustments to this evaluation are likely to be made as more mobile microrobots are presented in the future. Nevertheless, this evaluation allows to compare the suitability of the different locomotion classes for different applications with different requirements in a systematic and objective manner.

Throughout this chapter table 2.9 was constructed row by row by considering consecutively each locomotion class. It is now interesting to analyze the table column-wise, i.e. from an application point of view based on a certain set of requirements. Three microrobot requirement sets have been defined:

**Autonomous microrobot**
: overall size below 1 in$^3$, untethered, 2 DOF, velocity in the range of 1 L/s, good power autonomy

**Smallest microrobot**
: footprint size well below 1 cm$^2$, with 2 DOF

**Precision microrobot**
: overall size below 1 in$^3$, 3 DOF motion with a resolution of 10 nm

**Autonomous microrobot** The locomotion classes that fit well the requirements of such an autonomous microrobot are wheeled locomotion, the $IF_c$ locomotion class (in the case of resonance operation) and the two classes with directional friction. If motion velocity and power autonomy are to be favored, wheeled locomotion is the best choice for overall sizes of 1 cm$^3$ and above. For smaller sizes locomotion based on directional friction is a good solution, if unidirectional motion is acceptable. If, on the other hand, motion resolution and 3 DOF motion are to be favored the locomotion class $IF_c$ is a good option.

**Smallest microrobot** The three locomotion classes that are well suited for miniaturization are the $IF_c$, $D\mu$ and $I\mu$ classes. Several walking robots have been fabricated by MEMS technologies, allowing for a high level of miniaturization. However, almost all of these robots suffer from high power consumption, while tethered operation becomes unfeasible for robot sizes below 1 cm$^3$. The walking robot based on electrostatic inchworm motors shown in figure 2.6(c) on page 33 features very low power consumption and autonomous operation has been demonstrated. However, the design is very complex and features only two legs, with which no efficient walking motion can be achieved. The $IF_c$ class is to be preferred if bidirectional motion is required, while locomotion based on directional friction typically leads to very simple, efficient designs.

**Precision microrobot** In general, the best solution for precision microrobots is stick-slip operation (class $I\Delta t$). Walking with piezoelectric actuators can be an option, but typically features lower resolution and a higher number of actuation channels as well as a vertical

| | $v_s$ [L/s] | $P_s$ $[\frac{\text{mW}}{\text{mm/s}}]$ | DOF | Elec | 1 cm$^3$ | Res |
|---|---|---|---|---|---|---|
| Wheels | $1 \cdots 10$ | $10^{-1} \cdots 10$ | 2 | | | |
| Walking | $10^{-2} \cdots 1$ | $10 \cdots 10^4$ | 2-3 | | | |
| Inchworm | $10^{-3} \cdots 10^{-2}$ | $10^3 \cdots 10^4$ | 2-3 | | | |
| $IF_c$ | $1 \cdots 10$ | $10^{-1} \cdots 10^2$ | 2-3 | | | |
| $D\mu$ | $10^{-1} \cdots 10$ | | 0.5-1 | | | |
| $I\mu$ | $10^{-1} \cdots 10$ | | 1-1.5 | | | |
| Inertial drive | $10^{-2} \cdots 1$ | $1 \cdots 10^3$ | 3 | | | |

**Table 2.9:** Comparison of locomotion principles for mobile microrobots

motion during the stepping. Inchworm actuation can be preferred if high force capabilities and motion on inclined or vertical planes are required. However, inchworm robots are only a good choice if stray magnetic fields are not an issue and if the constraint on the size is not very strict. The $IF_c$ locomotion class can finally also be an option, if untethered operation is important and a resolution of some tens of nanometer is sufficient.

### Contribution of this thesis to the state of the art

This thesis contributes to the state of the art of locomotion for mobile microrobots by proposing the concept and a model of the *Modulated Friction Inertial Drive (MFID)* principle and discussion three designs of mobile microrobots based on this principle. The MFID principle is to be situated in the $IF_c$ locomotion class and allows for:

**Good locomotion velocities** up to 3 L/s has been demonstrated in this thesis

**Very good power efficiency** as resonance operation is possible. A specific power consumption of 0.0083 $\frac{\text{mW}}{\text{mm/s}}$ has been demonstrated, which is lower than any value that could be calculated for the robots discussed in this literature review.

**3 DOF** with bidirectional motion

**Simple driving electronics** because of a reduction in driving voltages and a compatibility to square wave operation due to the resonance operation and because of the limited number of actuation channels (around 1 channel per DOF)

**Miniaturization below 1 cm$^3$** a size of 1 cm$^2$ has been demonstrated, and smaller modules

have been fabricated. A high degree of miniaturization is allowed due to the simplicity, resonance operation and the combination of on-board and off-board actuation.

**High resolution motion** a design with 3 DOF actuated by piezoelectric actuators and capable of scanning mode operation has been demonstrated

Apart from the MFID principle in particular the concept of a combination of on-board and off-board actuation has also been studied and demonstrated. The mobile robots reported in this literature review feature either only on-board actuation either only off-board actuation. On-board actuation has the advantage of individual, on-board control of each robot and allows for a large number of robots to operate in parallel. Off-board actuation has the advantage to simplify considerably the robot design allowing for untethered operation of very small robots. However, off-board actuation does not allow for on-board control of the robot motion, the DOF are limited as well as simultaneous, independent actuation of several robots. Often, an interesting trade-off between robot simplicity and on-board motion control can be found by combining on-board and off-board actuation. The concept of a combination of on-board and off-board control can be applied in a much wider area than only MFID operation of mobile microrobots.

The next chapters respectively present the proposed MFID principle more in detail (chapter 3), study the stepping motion of a linear MFID actuator (chapter 4) and illustrate the advantages of the MFID principle with the description of the design and characterization results of three prototypes of MFID mobile microrobots (chapter 5).

# Chapter 3

# The MFID locomotion principle

*"Everything should be made*
*as simple as possible,*
*but not simpler."*
Albert Einstein (1879–1955)

## 3.1 Definition

The major contribution of this thesis is the definition, the study and the demonstration of a new locomotion principle for mobile microrobots. The locomotion principle has been called the "Modulated Friction Inertial Drive" (MFID) principle and is based on stepping motion. As for the classification of stepping locomotion principles shown in table 2.1 on page 21 the definition of the MFID principle is based on the two functions of a locomotion principle: *slip generation* and *slip variation*.

> The **"Modulated Friction Inertial Drive" (MFID)** principle is a locomotion principle based on stepping motion in which the *slip is generated* by the *inertial* effect of a symmetric, axial vibration and the *slip variation* is obtained from an active *variation of the friction force*.

The axial vibration causes the robot's feet to slip back and forth on the substrate. As this vibration is symmetric, no net motion would be generated if no synchronized variation of the contact force would be present. If the contact force is increased during the time the robot (or the robot's feet) is slipping backward and decreased during the time the robot is slipping forward, the repetitively resulting difference between the large forward thrust force and the small backward thrust force will cause the robot to move forward (see figure 3.1).

The friction force can either be varied by a variation of the contact force either by a variation of the friction coefficient. As illustrated by the microrobots discussed in sections 2.7 and 2.8 a variation of the apparent friction coefficient in function of the slip direction can be obtained by inclined flexible legs. However, such directional friction is a passive variation of the friction force, while the MFID principle is defined for *active* variation of the friction force. Such active variation of the friction coefficient could be obtained by a variation of the inclination of the legs during each locomotion step. Such a solution would result in bidirectional motion, but would be rather complicated to implement. The friction coefficient can also be reduced actively by a fast vibration perpendicular to the substrate, causing the robot to bounce. In the case a fast vertical vibration with a large surface having a small gap to the substrate, a squeeze film effect could be generated, resulting in a levitation of

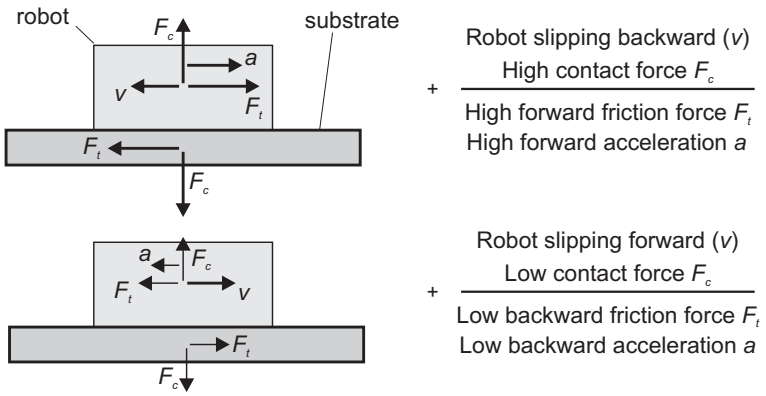


**Figure 3.1:** Working principle of the "Modulated Friction Inertial Drive" (MFID) principle ($v$: velocity, $F_c$: contact force, $F_t$: friction force $a$: acceleration)

the robot and a complete absence of dry friction. In the case of viscous friction, an active variation of the friction coefficient could also be realized by means of magnetorheological or electrorheological fluids[1]. This could be an interesting solution for locomotion in liquid media. This thesis focuses, however, on locomotion on a dry, solid, flat substrate (so no liquid and no air). As a variation of the contact force is much easier to implement than an active variation of the friction coefficient, this thesis focusses on MFID locomotion with slip variation by contact force variation.

MFID locomotion by contact force variation corresponds to the $IF_c$ locomotion class defined in section 2.3 (page 19). As discussed in section 2.6 several mini- and microrobots with locomotion in the $IF_c$ class have already been presented in literature. Hence, the implementation of MFID locomotion is not new for driving mobile microrobots. What is new is to subject this locomotion class to a systematic study considering a decoupling of slip generation and contact force variation, which is the major contribution of this thesis.

## 3.2 Comparison with other locomotion principles

Ultrasonic motors (except for the traveling wave type) are part of the $IF_c$ locomotion class and are therefore a special case of the MFID principle. Some ultrasonic motors (such as the ones used to drive the mobile robots shown in figures 2.12(a) [2], 2.12(c), 2.12(d) and 2.12(e) on page 45) are based on intermittent contact between the vibrating feet and the substrate, while for other ultrasonic motors [131] a permanent contact is maintained. The bouncing of the feet caused by such a hopping motion can result in instable motion as concluded by Devos in [131]. This is also observed in the case of mobile microrobots [112, 94, 175]. The experimental with a linear MFID actuator discussed in chapter 4 have confirmed that for vertical accelerations that are just sufficient for making the robot jump unstable motion is obtained. For higher accelerations the motion stability becomes better again, but there is no gain in velocity with respect to operation with permanent mechanical contact. Moreover, in general the lower the applied vertical acceleration, the lower the required power consumption. For these reasons this thesis studies only MFID operation for the case of permanent contact between stator and rotor.

[1] Magnetorheological and electrorheological fluids are fluids of which the viscosity can be varied by application of respectively a magnetic and a electric field.

[2] The robot in figure 2.12(a) is in fact not really driven by an ultrasonic motor as the operation frequency is 5.5 kHz, but its operation principle is similar to that of standing wave ultrasonic motors.

| | | Slip generation | |
|---|---|---|---|
| | | off-board | on-board |
| Contact force variation | off-board | 1 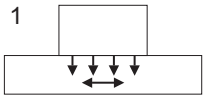 | 2 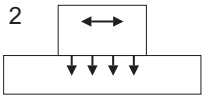 |
| | on-board | 3 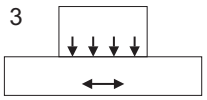 | 4 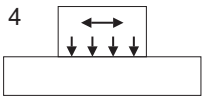 |

**Table 3.1:** Configurations of the MFID principle

The MFID principle could also be seen as some kind of mix of the inertial drive principle (stick-slip or impact drive) and the walking or inchworm principle. The inertial aspect is fundamental for the generation of slip of an MFID actuator as is the case for the inertial drive principle. However, as in the MFID principle this inertial vibration is symmetric, motion can only be obtained if also a variation of the contact force (or friction coefficient) is present. The symmetrical nature of the vibration features the advantage that it can be generated by an actuator working in resonance mode, resulting in higher vibration amplitudes, lower power consumption and simpler driving electronics. Moreover, in the case of a sinusoidal vibration no higher harmonics are excited, which is not the case for a saw tooth signal as often used for inertial drives. On the other hand, the integration of a variation of the contact force typically complicates the mechanical design.

As for the walking and the inchworm principle (class $DF_c$) the MFID principle is based on contact force variation. The difference is that slip for the MFID principle is not generated from a differential displacement, but from the inertial effect of an axial vibration. This has the advantage of increased simplicity, certainly in the case of several DOF. Inchworm locomotion has, on the other hand, the advantage of larger driving forces.

## 3.3 Configurations

One of the particularities of the proposed MFID concept is that the decoupling of the slip generation and the contact force variation allows for a combination of on-board and off-board actuation. Such a combination of on-board and off-board actuation can lead to a lower on-board power consumption and a simpler robot design. Four different configurations of the MFID principle can be distinguished (see table 3.1). In configuration 4 both the variation of the contact force and the slip generation are generated on the robot. This approach is the most commonly used in mobile microrobotics. It results in robots that are independent of their environment, but typically also leads to robots with rather complicated designs and high power consumption that are therefore difficult to miniaturize. Configuration 1 is the other extreme where all actuation happens off-board. This configuration gives a completely passive robot, which is easy to miniaturize, but no on-board control of the robot's motion is possible and individual control of several robots is rather complicated. An interesting trade-off between robot simplicity and power consumption on the one hand and on-board controllability of several robots is given by configurations 2 and 3 by combining on-board and off-board actuation. These configurations require, however, a synchronization between on-board and off-board actuation, which can be an issue in the case of untethered operation.

Decoupling of slip generation and contact force variation is very well illustrated by the

| Slip generation | Slip variation | |
|---|---|---|
| Inertial | Inertial | Direct force |
| 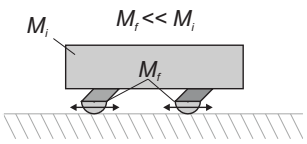  Vibrating feet | 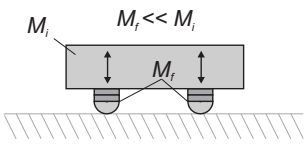  Vibrating feet | 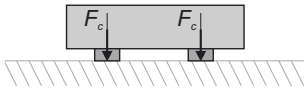  |
| 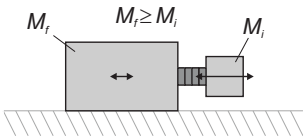  Vibrating Mass | 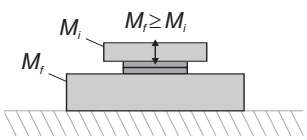  Vibrating Mass | |

**Table 3.2:** Variants for on-board slip generation and slip variation

sub-millimeter size microrobot developed at ETHZ [266] (see figure 2.13(a) on page 47). For their microrobot the slip is generated from the inertial effect of an on-board vibration excited by the attraction between two tiny permanent magnets under a variable magnetic field that is generated off-board. The contact force variation is realized by electrostatic clamping with interdigital electrodes in the substrate. While the contact force variation is definitely an off-board actuation, the slip is in fact generated on-board, but actuated off-board. If we consider the magnetic field as a way for wireless energy supply for an on-board actuation, this locomotion of this robot is an illustration of MFID configuration 2.

Apart from the microrobot from ETHZ mentioned above and the robots developed in this thesis, no other microrobots are reported in literature with locomotion based on inertial slip and contact force variation (class $IF_c$) and a combination of on-board and off-board actuation.

## 3.4 Variants for slip generation

In the MFID principle the slip is generated by the inertial effect of a symmetrical, mechanical vibration. This mechanical vibration can be either the feet of the robot that are vibrating with respect to the body of the robot or an inertial mass (not in contact with the work floor) that is vibrating with respect to the rest of the robot's body (see figure 3.2). The difference between slip generation by vibrating feet and by a vibrating inertial mass is exactly the same as the difference between the stick-slip principle and the impact drive principle as discussed in section 2.9.1.

For both variants the resulting excitation of the robot's body is only a fraction of excitation of the actuator ($M_i/(M_f + M_i)$). For the variant with vibrating feet the value of $M_f$ is very small compared to $M_i$ and the fraction is very close to 1. However, for the variant with vibrating mass $M_i$ is typically smaller than $M_f$, so the robot's body ($M_f$) is vibrating with a smaller amplitude than the inertial mass $M_i$. On the other hand, the solution with the vibrating mass can lead to a simpler design of the robot. For instance, several degrees of freedom motion can be obtained by adding extra inertial masses with each an individual linear actuator, which can be simpler than actuating the robot's feet in several degrees of

freedom. Moreover, the inertial mass and its actuator can be encapsulated inside the robot which could be interesting in the case of a fragile actuator in order to increase the robustness of the robot or in the case special environments such as vacuum can improve the actuator performances (for instance higher quality factor in resonance due to lower air damping).

## 3.5 Variants for contact force variation

As discussed for the classification of locomotion principles in section 2.3 the variation of the contact force can be realized by a direct, quasistatic force (such as a mechanical, magnetic or electrostatic clamping mechanism), or by the inertial effect of a mechanical vibration as for the slip generation (see figure 3.2).

A variation of the contact force by vibration of an inertial mass has the advantage that the same kind of actuators could be used as for the vibration that is generating the slip, which could simplify the robot's design and the driving electronics. However, the resulting (out-of-plane) vibrations could be an issue for certain applications such as micromanipulation. A contact force variation by vibration allows not only to increase the contact force, but also to reduce the contact force. This reduction of contact force results in a reduced power dissipation when the robot is sliding and therefore typically a better power efficiency. However, in the case of a symmetrical vertical vibration (which is usually the case) the addition of contact force is equal to the reduction of contact force. So, if a zero contact force is to be avoided (in order to avoid uncontrolled bouncing) the maximum contact force is limited to the double of the static contact force that is present when the robot is at rest. This static contact force is normally equal to the weight of the robot, but can also be increased by a constant mechanical or magnetic preload. A combination of increase and decrease of the contact force can also be generated by a magnetic actuator consisting of a coil and a permanent magnet (or a second coil). Moreover, such magnetic actuators allow to apply a DC offset force, which allows for higher amplitudes of the force variation. On the other hand, in some environments (such as Scanning Electron Microscopes) the generation of magnetic fields is to be avoided as it disturbs the image of the microscope. Mechanical clamping and electrostatic clamping do typically not allow for a reduction of the contact force, but the increase of the contact force is not limited to the double of the static force. The drawback to mechanical clamping is that it is sensitive to wear as it is typically executed with short stroke piezoelectric actuators. Moreover, mechanical clamping can also become more complicated in the case of multi-DOF motion. Electrostatic clamping features the advantage of low power consumption, simplicity and suitability for miniaturization. However, they typically require high actuation voltages and/or a high sensitivity to dust particles, surface roughness and accumulation of electrical charges.

Finally, as for the slip generation the variation of the contact force through the inertial effect of a vibration perpendicular to the actuation direction can be generated either by vibrating the robot's feet either by vibrating an inertial mass (see figure 3.2). Also here, the solution with vibrating feet features the advantage of an efficient use of the vibration amplitude, but also causes the whole robot to move up and down, which can be a problem for applications where high precision is required. The vibrating mass solution can sometimes also lead to a simpler design.

## 3.6 Conclusion

The "Modulated Friction Inertial Drive" (MFID) principle has been proposed as a locomotion solution for mobile microrobots. A first major advantage of this locomotion principle is that it can be operated by sinusoidal vibration, allowing for resonance mode operation. Resonance mode operation allows to reduce power consumption, reduce driving voltage and allows to drive with a square wave generated by a digital electronics. The second major advantage of the MFID principle is that the decoupling of slip generation and slip variation allows for a combination of on-board and off-board actuation. Such a combination can result in very simple, small robot designs with low on-board power consumption featuring on-board motion control.

Four configurations are identified based on whether the slip generation and the contact force variation are generated on-board or off-board. For every configuration different variants have been defined based on the way the contact force is varied and the way the horizontal or vertical inertial force is generated. The next chapters study into detail the stepping behavior of a MFID actuator and illustrate its suitability for microrobotic locomotion by the discussion of the design and performances of three MFID microrobot prototypes. The advantages and drawbacks of the MFID principle will be revisited by a quantitative comparison of the developed MFID microrobot prototypes and the microrobots reported in literature.

# Chapter 4

# Modeling and experimental characterization of a MFID actuator

*"In theory, there is no difference*
*between theory and practice.*
*But in practice, there is.*
Jan L. A. van de Snepscheut (1953-1994)

## 4.1 Introduction

In order to be able to study the behavior of the MFID principle in detail a dynamic model and an experimental setup have been developed. In order to simplify the experimental setup and to allow for high resolution, long range measurements by interferometer, simulations and experiments have been carried out for a 1 DOF linear actuator. The configuration with off-board slip generation and off-board contact force variation (i.e. configuration 1 in table 3.1 on page 73) has been selected as it allows for an actuator without any wires or on-board electronics on the mobile part. Concerning the contact force variation the inertial effect of a vibration perpendicular to the actuation axis has been selected, because of its simplicity as it allows to choose for the same actuator technology as chosen for the mechanical vibration for slip generation.

The next two sections present the developed dynamic model (section 4.2) as well as the developed experimental setup together with the identification of the most important parameters of the setup (section 4.3). In section 4.4 the results obtained by simulation and experiments are presented and compared.

## 4.2 MFID model

### 4.2.1 The dynamic model

Figure 4.1 shows the dynamic model used for the simulation of a 1 DOF linear MFID actuator. The actuation consists of an axial vibration of the base , which causes slip between slider and base combined with a variation of the contact force between slider and base. The axial vibration is considered sinusoidal with an amplitude $X$ and a pulsation $\omega$

$$x = X \sin(\omega t) \tag{4.1}$$

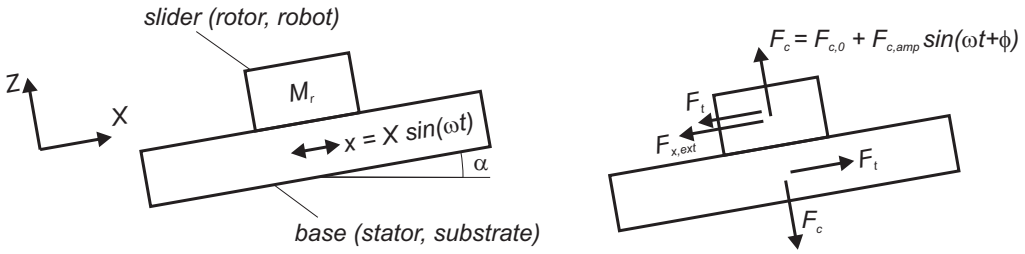


**Figure 4.1:** Dynamic model of MFID actuator

The variation of the contact force $F_c$ between the slider $M_r$ (rotor) and the base (stator) is also considered sinusoidal with an amplitude $F_{c,amp}$, an offset $F_{c,0}$ and a phase shift $\phi$ with respect to the slip generation:

$$F_c = F_{c,0} + F_{c,amp} \sin(\omega t + \phi) \tag{4.2}$$

In the case of a mobile robot walking on a surface with inclination $\alpha$ the offset $F_{c,0}$ typically corresponds to the projected weight of the robot ($F_{c,0,g} = M_r g \cos(\alpha)$) either with or without an additional preload ($F_{c,0,add}$). The model is independent of the way the variation of the contact force is generated: either on-board or off-board and either by a direct force or by the vibration of an inertial mass (see chapter 3). In the experimental setup presented later in this chapter, the variation of the contact force is generated off-board through the inertial effect of a vibration of the base with amplitude $Z$

$$z = Z \sin(\omega t + \phi), \tag{4.3}$$

resulting in the following variation of the contact force

$$F_c = F_{c,0,add} + M_r(g \cos(\alpha) - A_Z \sin(\omega t + \phi)), \tag{4.4}$$

where $A_Z = Z\omega^2$.

The differential equation of the position $x_r$ of the mass $M_r$ is obtained by simply applying Newton's second law:

$$-F_{x,ext} - F_t = M_r \frac{d^2 x_r}{dt^2}. \tag{4.5}$$

The external force $F_{x,ext}$ is the sum of the projection of the weight of the slider ($M_r g \sin(\alpha)$) and any additional external force in the axial ($X$) direction of the actuator. The complexity in solving this differential equation lies in the fact that the friction force $F_t$ is non-linear and that an adequate model should be chosen for modeling this force.

### 4.2.2 The friction force model

Altpeter [333] presents in his PhD dissertation a survey of friction modeling for simulation and control purposes. He concludes that, basically, friction models can be classified into kinetic friction models and dynamic friction models. The kinetic friction models are based on the experimental observations of Coulomb [334] and describe friction force as a static relation between velocity and applied external forces. However, the kinetic friction models provide only a rough accuracy at the presence of the dynamic effects caused by the repetitive, small back-and-forth motion as generated by a MFID actuator. Altpeter concentrates his study of dynamic friction models on the LuGre model [335]. This model has also been used previously in other works dealing with the modeling of stick-slip actuators [129, 130, 336].

In the LuGre model the friction force $F_t$ at an interface with relative velocity $\dot{x}$ is described as

$$F_t = \sigma_0 z_c + \sigma_1 \dot{z_c} + \sigma_2 \dot{x}. \tag{4.6}$$

This model considers a local deformation $z_c$ of the contact interface and models it as a spring damper system with stiffness $\sigma_0$ and viscous damping coefficient $\sigma_1$. The energy dissipated in slip at the sliding interface is modeled by the viscous friction coefficient $\sigma_2$.

The local contact deformation $z_c$ is as follows

$$\dot{z_c} = \dot{x} - \frac{|\dot{x}|}{g(\dot{x})} z_c, \tag{4.7}$$

where $g(\dot{x})$ denotes the Gaussian model describing the non-linear part of the relation between velocity and friction force

$$g(\dot{x}) = \frac{F_{t,coul} + (F_{t,stat} - F_{t,coul}) e^{-(\dot{x}/v_s)^2}}{\sigma_0}. \tag{4.8}$$

This equation models the Stribeck effect and allows for a smooth transition from maximum static friction force $F_{t,stat}$ and dynamic friction force $F_{t,coul}$, which depend on the respective friction coefficient: $F_{t,stat} = \mu_s F_c$ and $F_{t,coul} = \mu_d F_c$.

In quasistatic conditions an external tangential force can be applied leading to a local deformation of the contact without any sliding motion. The maximum presliding deformation $x_s$ is given by

$$x_s = \frac{F_{t,stat}}{\sigma_0} = \frac{\mu_s F_c}{\sigma_0}. \tag{4.9}$$

Back and forth motion is subject to a hysteresis effect described by the Dahl's curve shown in figure 4.2(b).

It can be easily deduced that in steady state ($\dot{x} = c^{st}$, $\dot{z_c} = 0$) the expression for the contact deformation $z_c$ (equation 4.7) is reduced to $z_c = \text{sign}(\dot{x}) g(\dot{x})$. The resulting steady state friction force $F_{t,ss}$ is then equal to

$$F_{t,ss} = \text{sign}(\dot{x})(F_{t,coul} + (F_{t,stat} - F_{t,coul}) e^{-(\dot{x}/v_s)^2}) + \sigma_2 \dot{x}. \tag{4.10}$$

The behavior of the steady state friction force in function of the slip velocity is depicted in figure 4.2(a) for the case that $F_{t,stat} > F_{t,coul}$ (as is the case for the dry friction on the experimental setup used for the experiments in this chapter).

### Discussion of the friction force model

Figure 4.3(a) shows a plot of the friction force resulting from an imposed relative velocity pattern in the shape of a square wave[1]. The friction parameters used in this simulation correspond to those obtained from the experimental setup in the case of a maximum axial vibration amplitude, a driving frequency of 2000 Hz, a maximum contact force of $F_c = 140$ mN (see table 4.1 on page 96). At these parameter settings the experimental setup features a tangential contact stiffness of $\sigma_0 = 10.9$ N/$\mu$m and the following values for the friction parameters $\sigma_1 = 1$ Ns/m, $\sigma_2 = 0.1$ Ns/m, $\nu_s = 5$ mm/s, $\mu_s = 0.15$ and $\mu_d = 0.1$. The amplitude of the square wave is set to 3.67 mm/s, which corresponds to the maximum velocity of the axial sinusoidal vibration on the experimental setup at maximum axial driving voltage

[1]The square wave pattern has only been chosen for theoretical understanding of the friction model and cannot correspond to a physical experiment as it involves infinite accelerations.

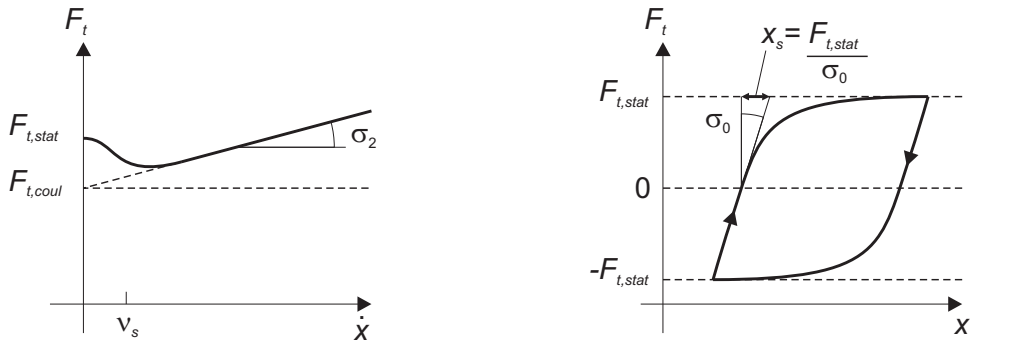


**(a)** Steady state friction force

**(b)** Hysteresis of the contact deformation (Dahl's curve)

**Figure 4.2:** Influence of slip velocity and contact deformation on the friction force

and a driving frequency of 2000 Hz (as deduced from the measurement shown in figure 4.11 on page 91).

The decomposition of the simulated friction force into the different terms of equation (4.6) is depicted in figure 4.3(b). This graph illustrates that the damping of the contact deformation $\sigma_1 \dot{z}_c$ is a transient effect that occurs at the change of velocity and that the friction force is dominated by the term $\sigma_0 z_c$.

### 4.2.3 Implementation in Simulink

The dynamic model presented above has been implemented in MATLAB/Simulink in order to be able to perform numeric simulation, which are presented in section 4.4. A variable step size algorithm with the ODE 23tb solver (an implementation of TR-BDF2, an implicit Runge-Kutta formula) and a maximum step size of 1 $\mu$s has been selected. The simulation time is typically 25 ms or 50 ms depending on the driving frequency. In order to minimize the influence of transient effects on the calculated steady state motion velocity, the average motion velocity is calculated by the distance traveled in the last 10 actuation periods of the simulation time. The simulation is repeated in two nested loops, which allow to vary automatically the driving frequency $f$ and the phase shift $\phi$. In order to include the influence of the hysteresis of the piezoelectric actuators used on the experimental setup, an harmonic fit (see figure 4.11 on page 91) of the measured axial vibration is used as an input for the simulation.

## 4.3 Experimental setup

### 4.3.1 Description

A characterization setup has been developed in order to be able to experimentally study the behavior of a real MFID actuator and compare the experimental results with the simulation results. The design of this experimental setup is focused on the capability to explore a wide range of input parameters (driving amplitudes, driving frequency, phase shift and preloading force) and not on the actuator's performance and efficiency.

Figure 4.4 shows the developed experimental setup. The actuation of the mobile shaft (the slider) consists of the combination of an axial ($X$) vibration and a vibration perpendicular

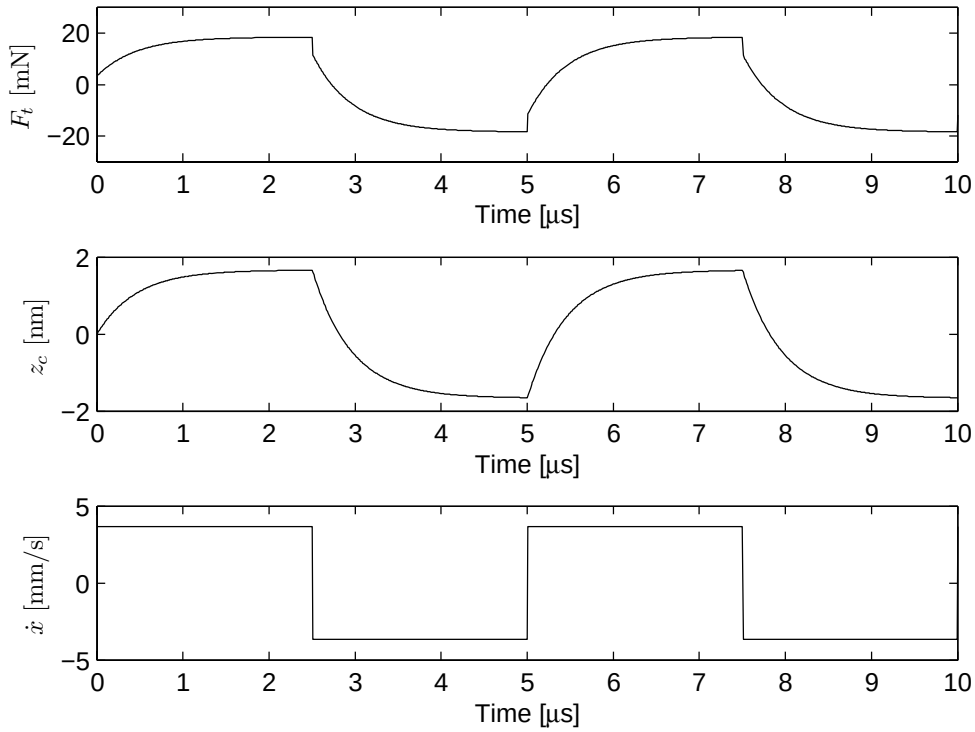


**(a)**

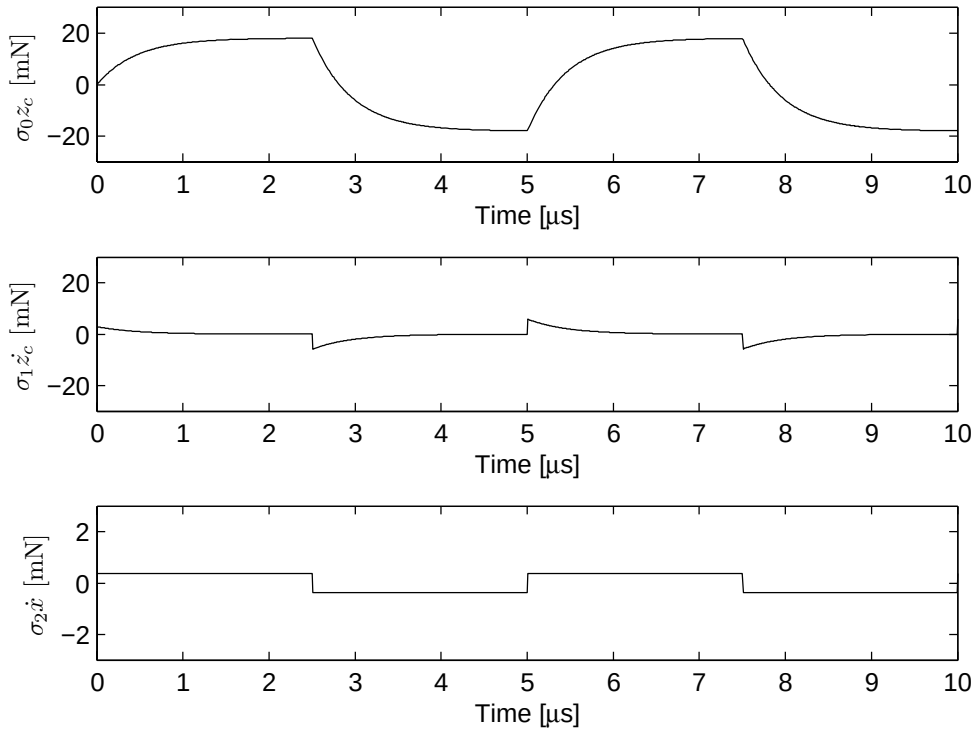


**(b)**

**Figure 4.3:** Response of the friction model to a square wave relative velocity pattern at 2000 Hz with an amplitude of 3.43 mm/s

($Z$) to the axis of the shaft. The perpendicular ($Z$) vibration is generated with two stack piezoelectric actuators (size $5 \times 5 \times 3$ mm$^3$, see also appendix F.1), on top of which two shear mode piezoelectric actuators (size $4 \times 3 \times 1$ mm$^3$, see also appendix F.1) are glued for generation of the axial ($X$) vibration. On top of each shear mode piezo two sapphire half spheres (size ∅1 mm × height 0.6 mm, see also appendix F.2) are glued for guiding the mobile shaft (size ∅2.5 mm × 35 mm, first resonance frequency 9040 Hz, see also appendix F.2). These four half spheres generate four contact points, leaving the shaft free for translation along its axis and for rotation about its axis[2]. The linear position of the shaft is measured by an interferometer (see appendix F.4), of which the laser beam is reflecting on the shaft's end[3].

The setup includes a set of permanent magnets that apply a downward preloading force to the shaft (see detail in upper left of figure 4.4). The cylindrical magnets (size ∅2 mm × 3 mm, material: NdFeB, BBA AG) are arranged with opposite orientation and are glued on top of a steel (St 37-2) yoke that allows to close the magnetic circuit[4]. The gap between the magnets and the shaft can be varied in order to vary the applied magnetic force. The vertical position of the yoke is fixed by clamping it from the side with a set of screws.

The complete setup (i.e. actuator and interferometer) is fixed on block of aluminium, which can be inclined in order to study the influence of the inclination angle $\alpha$ on the motion velocity. Because of this possible inclination the terms "horizontal" and "vertical" vibration are generalized to "axial" and "perpendicular" vibration.

### Implementation in LabVIEW

The sinusoidal actuation signals for the piezoelectric actuators are created in LabVIEW 7.1 and generated by a NI 6713 analogue output board featuring ±10 V, 12 bit output with a sampling rate up to 1 MS/s (see appendix F.3 for detailed specifications). These ±10 V signals are amplified to a ±200 V range by a lab-made high voltage amplifier. The shaft's position measured by an interferometer is communicated to LabVIEW by a by USB connection. The measurement algorithm implemented in the LabVIEW program starts the signal generation, waits 20 ms for transition effects to disappear and takes two position measurements with a time interval of 0.5 s or 1 s [5]. At the end of each measurement sequence the shaft is moved back to its initial position. This measurement sequence is repeated in several nested loops, allowing to change automatically the driving frequency $f$ and the phase shift $\phi$ and/or to repeat the same measurement several times for statistical analysis. For the experiments on open loop repeatability and motion resolution discussed in section 4.4.8 the measurement

[2] In an earlier version two sapphire V-grooves were used as guiding elements. V-grooves result theoretically in four contact lines instead of contact points resulting into lower contact pressure for a given contact force. However, experience has proven that aligning the V-grooves with a shaft during the gluing process is not sufficient to remove completely the hyperstaticity that is intrinsic to this contact configuration. This small misalignment results into four contact points at the border of the V-grooves resulting into very high contact pressures due to the small contact radius. For this reason four well-defined contact points with four half spheres was preferred.

[3] The fact that the shaft is free for rotation about its axis implies that it was needed to machine the edge of the shaft with a very good perpendicularity to the axis of the shaft. An error on this perpendicularity results in a deviation of the reflected laster beam when the shaft is rotated about its axis, which can cause the interferometer to loose the signal (tolerance on angle about 2' of arc).

[4] Experience has proven that it is important to close the magnetic circuit as an excess of parasitic magnetic flux exerts a non-negligible lateral force to the shaft that tends to bring it back to its central position.

[5] As the experiments have not been carried out on a real-time system, the time interval is not constant. Therefore, at every position measurement, the exact time is also recorded in order to calculated by substraction a more accurate measurement of the elapsed time

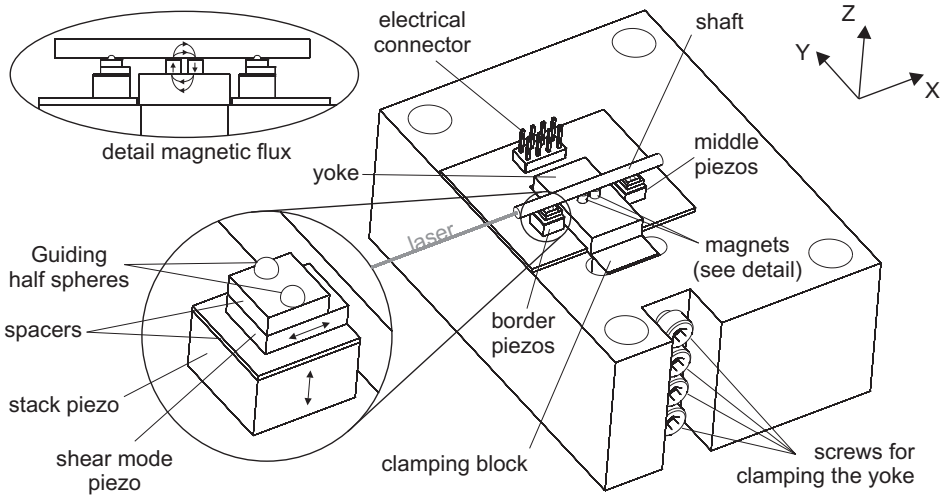


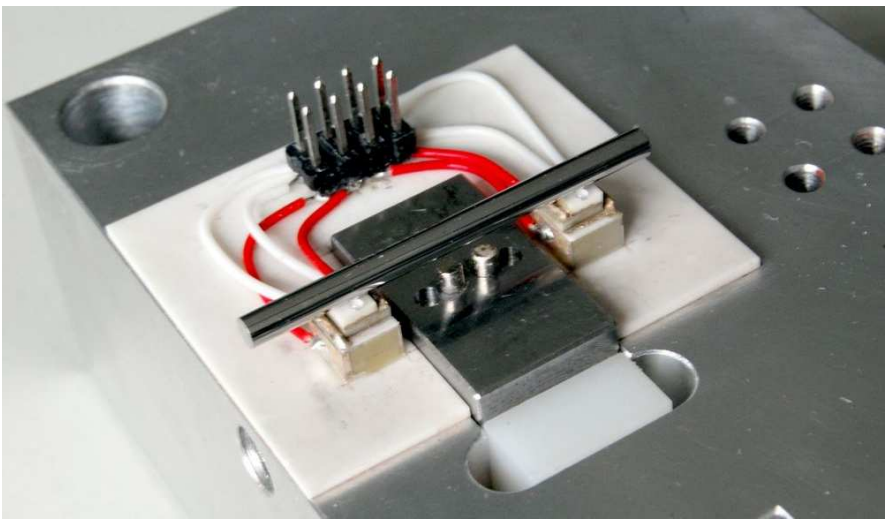

**Figure 4.4:** Experimental setup

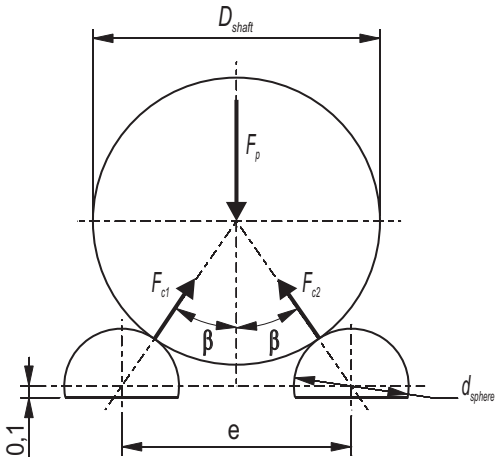


**Figure 4.5:** Drawing of the geometrical contact configuration between the mobile shaft and the guiding half spheres

algorithm consists of measuring the position, launching the motion for a limited number of locomotion periods and measuring the position again.

### 4.3.2 Parameter identification

#### Geometrical contact configuration

The preload force $F_p$ (i.e. the sum of the weight of the shaft and the magnetic preload force) causes contact forces $F_{c1}$, $F_{c2}$, $F_{c3}$ and $F_{c4}$ at the four contact points between the shaft and the four half spheres. The relation between $F_p$ and $F_{ci}$ depends on the contact angle $\beta$ which is given by (see figure 4.5)

$$\beta = \arcsin\left(\frac{e/2}{d_{sphere}/2 + D_{shaft}/2}\right) = 34.85^\circ \tag{4.11}$$

where $e$ is the spacing between the centers of the two half-spheres ($e = 2$ mm), $d_{sphere}$ is the diameter of one of the half-spheres ($d_{sphere} = 1$ mm) and $D_{shaft}$ is the diameter of the shaft ($D_{shaft} = 2.5$ mm).

Let's consider $F_c$ the algebraic sum of all four contact forces ($F_c = \sum_{i=1}^{4} F_{ci}$). The ratio between $F_c$ and $F_p$ is called the contact geometry coefficient $c_g$ and is given by

$$c_g = \frac{F_c}{F_p} = \frac{1}{\cos(\beta)} = 1.22 \tag{4.12}$$

#### Maximum contact pressure

According to the Hertz theory [337] the maximum contact pressure $p_m$ between two smooth, non-conforming surfaces[6] with relative curvatures in two orthogonal directions $1/R'$ and $1/R''$

[6]Non-conforming surfaces are surfaces that can be adequately approximated in the contact region by a second order polynomial. These surfaces can therefore be characterized completely by their radii of curvature at the point of contact. This is the case if the relative curvatures $1/R'$ and $1/R''$ are sufficiently large with respect to the size of the area of contact deformation.

is given by

$$p_m = \sqrt[3]{\frac{6F_{ci}E_Y'^2}{\pi^3 R_e^2}} \cdot (F_1(e))^{-2}, \tag{4.13}$$

with $R_e$ the equivalent radius defined by $R_e = \sqrt{R'R''}$. The relative curvature in a given direction is the algebraic sum of the curvatures of the two bodies in that direction. Hence, for the case of a contact between a sphere with radius $r$ and a cylinder with radius $R$ the relative curvature in the direction of the axis of the cylinder is given by

$$\frac{1}{R'} = \frac{1}{r} + \frac{1}{\infty} = \frac{1}{r}, \tag{4.14}$$

while the relative curvature in the direction perpendicular to the cylinder axis is equal to

$$\frac{1}{R''} = \frac{1}{r} + \frac{1}{R}. \tag{4.15}$$

For the case of a cylinder radius $R = 1$ mm and a sphere radius $r = 0.5$ mm the equivalent radius is then

$$R_e = \sqrt{\frac{r^2 R}{r+R}} = 0.41 \text{ mm}. \tag{4.16}$$

In the case of a sphere-plane contact the equivalent radius $R_e$ would be equal to the radius of the sphere.

The equivalent Young's modulus $E_Y'$ in equation (4.13) is given by

$$E_Y' = \frac{1}{\frac{1-\nu_1^2}{E_{Y,1}} + \frac{1-\nu_2^2}{E_{Y,2}}}. \tag{4.17}$$

with $E_{Y,1}$, $E_{Y,2}$, $\nu_1$ and $\nu_2$ respectively the Young's modulus and the Poisson coefficients of the two contacting materials. For the combination of the steel and sapphire (see appendix F for the material properties) the equivalent Young's modulus becomes $E_Y' = 154.7$ GPa.

The factor $(F_1(e))^{-2}$ in equation (4.13) is a factor that corrects for the fact that the contact area is elliptical and not cylindrical as is the case for a sphere-plane contact. This correction factor depends on the ratio between the two relative curvatures $R'/R''$ and is to be extracted from a graph in [337]. In the case of this experimental setup a ratio of $R'/R'' = 0.5/0.33 = 1.5$ results in $F_1(e) = 0.995$.

It can now be calculated that the approximation of the sphere-cylinder contact by a sphere-plane contact would — for these values — have resulted in a pressure that is $(R_e/r)^{2/3} \cdot (F_1(e))^2 = 0.87$ times lower than calculated with the sphere-cylinder contact model.

According to [338] the maximum contact pressure should not surpass 75–90% of the tensile strength (for the shaft $R_m = 1995$ N/m$^2$). As in this case also friction is involved we will take the lower limit $0.75 \cdot 1995 = 1496$ N/mm$^2$. With equation (4.13) it can be calculated that such a contact pressure results in a contact force per half sphere of $F_{ci,max} = 118$ mN, which results in a total preload force $F_p = 387$ mN.

Bergander presents in [130] a study of the wear formation for stick-slip actuators. These wear tests have shown that for a contact between ruby half spheres on a stainless steel (AISI 301, 1.4310, X12 CrNi17 7, tensile strength $R_m \approx 1600$ N/mm$^2$) flat substrate velocity variations of up to 200% can occur during an initial stabilization phase of about 250 cycles (back and forth movements), after which velocity variations are limited to about 20%. These tests were carried out at a contact pressure of about 550 MPa leading to a wear profile width of 240 $\mu$m and a depth of about 1 $\mu$m after 4680 cycles. Much lower velocity variations were

obtained by the application of special coatings such as TiN or $MoS_2$ or by working on a silicon substrate coated with 500 nm of $SiO_2$. However, it is difficult to apply these results to the case of the experimental setup presented in this chapter, as the mobile shaft in this setup is free to rotate about its longitudinal axis, which could impede the accumulation of wear in the form of a scratch.

**Tangential contact stiffness**

The tangential stiffness of the contact between a sphere and a cylinder is given by [339]

$$\sigma_0 = 4 \cdot \frac{1}{\frac{1}{8R_{c,e}}\left(\frac{2-\nu_1}{E_{Y,1}} + \frac{2-\nu_2}{E_{Y,2}}\right)} \tag{4.18}$$

where $\nu_1$, $\nu_2$, $E_{Y,1}$ and $E_{Y,2}$ are the poisson ratio and the Young's modulus for the material of the sphere and plane respectively. The factor 4 comes from the total number of contact points of which the stiffness should be added up. The variable $R_{c,e}$ in equation (4.18) is the equivalent contact radius of the elliptical contact area and is calculated by [337]

$$R_{c,e} = \sqrt[3]{\frac{3F_{ci}R_e}{4E'_Y}} \cdot F_1(e) \tag{4.19}$$

with $E'_Y$ the equivalent Young's Modulus (see equation (4.17)), $R_e$ the equivalent radius (see equation (4.16)) and $F_1(e)$ a correction factor taking into account the elliptical shape of the contact (for this experimental setup $F_1(e) = 0.995$ [337]).

As $\sigma_0$ depends on the contact force $F_{ci}$, which is not a constant value for the MFID principle, the tangential contact stiffness should be recalculated at every simulation step. The dependence of $\sigma_0$ and $F_{ci}$ can be calculated with

$$\sigma_0 = 2.088 \cdot 10^7 \sqrt[3]{F_c} \qquad [\mathrm{N/m}], \tag{4.20}$$

which results in $\sigma_0 = 5.21$ N/$\mu$m for a contact force of $F_c = 15.6$ mN, corresponding to the weight of the shaft ($M_r = 1.301$ g) and $\sigma_0 = 10.9$ N/$\mu$m for a contact force of $F_c = 140.5$ mN, achieved at a maximum preload corresponding to $M_r 9.02g$ (with $g$ the acceleration of gravity) as illustrated in figure 4.15 on page 95.

For these values of the tangential contact stiffness and for a static friction coefficient of $\mu_s = 0.15$ (see table 4.1) the maximum presliding deformation $x_s$ can now be calculated with equation (4.9) on page 79 as $x_s = 0.45$ nm in the case of only gravitational preload and $x_s = 1.9$ nm in the case of maximum preload of $M_r 9.02g$.

**Vibration amplitude of the piezoelectric actuators**

In order to be able to test the MFID principle with a preload of up to about ten times the weight of the shaft, the stack piezo actuators must be able to generate an acceleration of up to $10g$. Such an acceleration at a frequency of some hundreds of Hz requires a vibration amplitude of several micrometer. Therefore, stack piezo actuators with a rated displacement of 4.8 $\mu m_{p2p}$ have been chosen (see appendix section F.1). These piezo stacks require a driving voltage between 0 and 150 V. As these stack actuators have an unloaded resonance frequency of >300 kHz, testing at a driving frequency of several kHz should not be a problem in terms of mechanical resonance. However, at these higher frequencies vibration amplitudes of only some tens of nanometers, and thus voltage swings of some volts, are required for generating accelerations[7] in the order of $1g$.

[7] For a constant acceleration, the vibration amplitude decreases quadratically with increasing frequency.

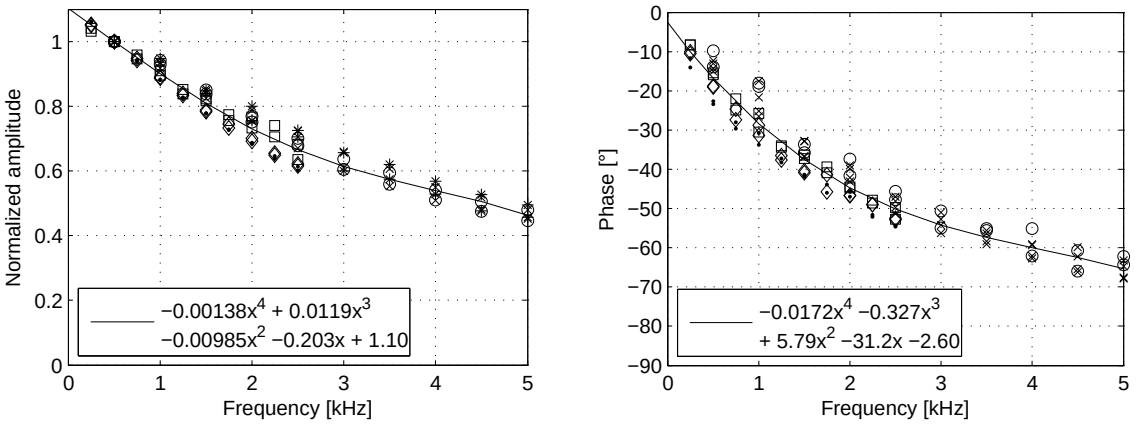


**Figure 4.6:** Amplitude and phase shift response of the complete system of amplifier and stack piezo actuator

In order to comply with the required driving voltage up to 150 V for low frequency operation, a lab-made high voltage (±200 V) amplifier (see appendix section F.3) was selected for amplifying the signal generated by an analogue output board (see appendix section F.3). This amplifier was developed earlier for stick-slip applications based on shear mode piezo actuators. Hence, they were optimized for driving capacitive loads of some nF with a sawtooth signal ranging between −200 V and +200 V with a peak current of about 200 mA, resulting in a voltage slew rate of several hundreds of V/$\mu$s. This peak current should theoretically be sufficient for driving the stack piezos (electrical capacitance of about 220 nF) with sinusoidal vibrations with frequencies up to 5 kHz and an acceleration of some tens of $g$. However, it has been experimentally observed that the selected amplifier is not able to deliver the same peak current of 200 mA when driving higher capacitances at low voltage amplitudes. The initial amplification factor of 20 is reduced to about 9 at 5 kHz with a phase lag of about 60° when driving the stack piezos, while no significant phase lag or reduction in amplification factor was observed when driving the shear mode piezos. Hence, this amplifier appears not to be optimized for such kind of driving conditions. However, the lack of availability of another high voltage amplifier didn't leave any choice but using this amplifier and compensating for the loss in amplification fact and the phase lag. An overview of the amplifier specifications as well as the measured behavior when driving one of the stack piezos can be found in appendix section F.3.

The compensation of the limited bandwidth of the amplifier is combined with the compensation for the phase lag introduced by the hysteresis of the stack piezos. Figure 4.6 shows the amplitude and phase shift response of the complete electromechanical system consisting of amplifier and stack piezo actuator. The vibration amplitude of the stack piezos has been measured by interferometer (resolution 1 nm, more specs in appendix F.4). The amplitude response has been normalized to the amplitude measured at a frequency of 500 Hz and the response has been measured for an input voltage amplitude of 0.025, 0.050 and 0.10 $V_{\text{amp}}$. These graphs show that at a frequency of 5 kHz the amplitude response drops to about 60% of its value at 500 Hz, while a negative phase lag of more than 60° is present. Two $4^{\text{th}}$ degree polynomials have been fitted trough the measured amplitude and phase lag response. Figure 4.7 shows the measured amplitude and phase lag response when compensating the voltage amplitude and phase shift of the input signal of the amplifier by means of these polynomials. These measurements were carried out individually for each stack piezo: the one on border and the one in the middle of the setup (see figure 4.4). The compensated amplitude

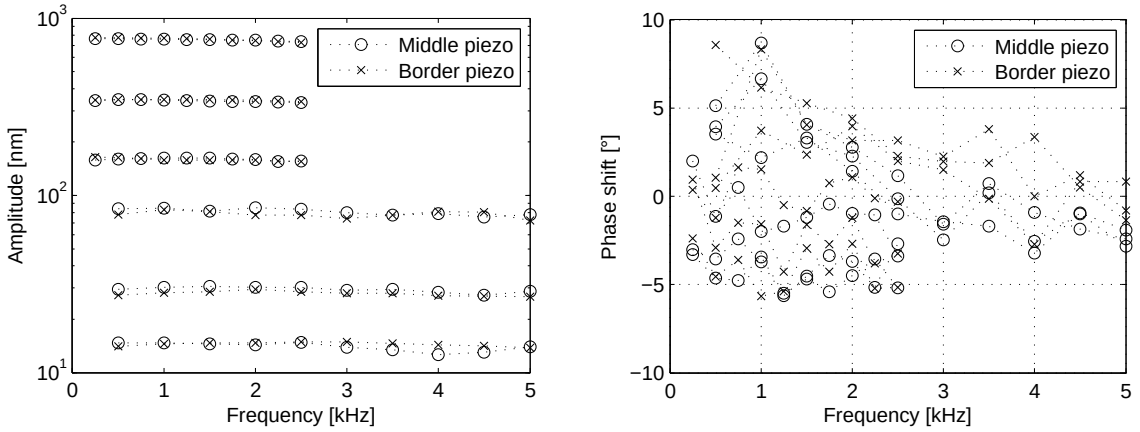


**Figure 4.7:** Response of the complete system of amplifier and stack piezo actuators after compensation based on calibration curves in figure 4.6

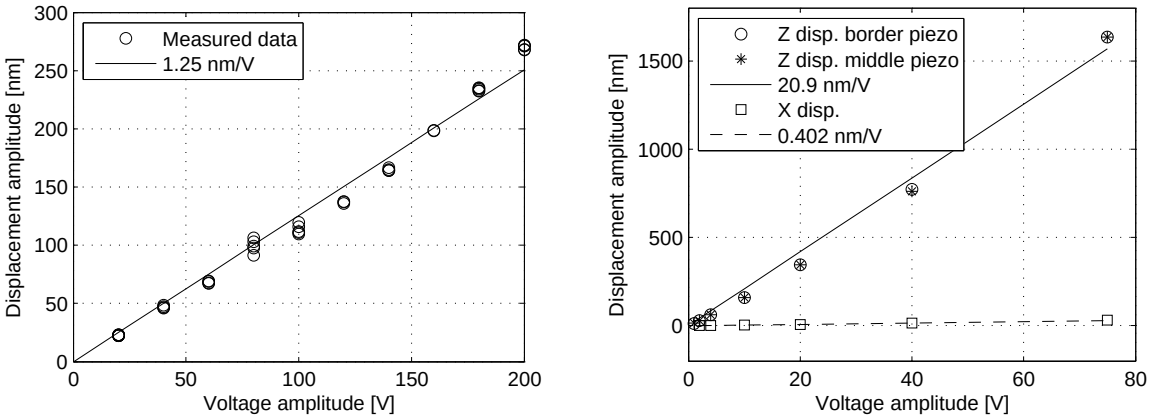


**(a)** Shear mode piezos

**(b)** Stack piezos

**Figure 4.8:** Displacement vs. voltage characteristic of the piezoelectric actuators at a frequency of 500 Hz

shows a relative difference between maximum and minimum value of maximum 10%, while the compensated phase shift error is generally below 5°.

Figure 4.8 shows the measured *displacement vs. voltage* profile of the shear mode and the stack piezoelectric actuators for a driving frequency of 500 Hz. The displacement of the shear mode piezos has been obtained by measuring by interferometer the axial displacement of the shaft positioned on the four contact feet while the shaft is preloaded by a magnetic force in order to prevent it from slipping. For the displacement of the stack actuators a small, flat silicon mirror is glued to the side of the shaft, which allows to measure by interferometer the vertical displacement of the shaft. The stack piezo amplitude has been measured twice, once for the border piezo and once for the middle piezo (see figure 4.4). Both for the shear mode as for the stack piezos the displacement profile can be well approximated by a straight line with slopes 1.25 nm/V and 20.9 nm/V respectively.

Also the parasitic displacement has been measured and plotted in figure 4.8(b). When actuating the shear mode piezos, no significant vertical displacement is observed. However, when actuating the stack piezos an axial motion of the shaft of 0.40 nm/V has been measured. This parasitic motion is relatively small compared to the vertical motion of the stack piezos

(about 2%), but is not negligible (32 nm at 75 V) compared to the motion of the shear mode piezos (272 nm at 200 V).[8] The parasitic motion of the stack piezos is probably due to imperfections in fabrication of the stack and assembly of the stack on the experimental setup.

As illustrated in figures 4.9 and 4.10 the shear mode and the stack piezo actuators suffer from typical piezoelectric effects such as creep and hysteresis. These effects should be taken into account when using the actuators for high precision applications. Another consequence of the hysteresis is that a sinusoidal voltage signal does not result in a perfect sinusoidal displacement profile. Figure 4.11 shows the measured position and the velocity profile of the shear mode piezos while actuated with a sinusoidal voltage signal. In order to reduce the noise on the measurement, the position is measured during 7 periods and an average over these periods is taken. The velocity profile is calculated by derivation of this average position profile. No further filtering of the measured data is applied. As clearly visible in the figure, the deviation from a perfect sinusoidal signal is particularly visible when looking at the velocity profile. For the MFID principle the velocity profile of the motion of the stator is quite important as the shift from acceleration to deceleration (or vice versa) occurs at the moments of equal velocity between stator and rotor. Hence, in order to improve the match between observed and measured behavior, a harmonic fit of the measured displacement is used as the input for the simulations. A harmonic analysis of the signal has shown dominant harmonics at 2, 3 and 5 times the driving frequency. Hence, using the MATLAB Curve Fitting Tool with the trust-region algorithm the following curve fit (coefficient of determination: $R^2 = 0.999965$) has been obtained

$$\begin{aligned} x(t) &= 0.268\sin(\omega t - 0.246) + 0.000347\sin(2\omega t - 1.78) \\ &\quad +0.00882\sin(3\omega t - 2.20) - 0.00556\sin(5\omega t + 2.61) \quad [\mu\text{m}] \end{aligned} \tag{4.21}$$

where $\omega = 2\pi f$ and $f = 2000$ Hz. Equation 4.21 shows that there is a phase lag of $-0.268$ rad $= -15.4°$ on the sine with the fundamental frequency (i.e. 2000 Hz). This phase lag is due to the hysteresis in the shear mode piezos. It should also be noted that although the amplitude of the fifth harmonic is only 5 nm, it has an important influence on the velocity and acceleration of the axial vibration as velocity and acceleration amplitude is multiplied by $5\omega$ and $(5\omega)^2$ respectively. For the acceleration this results in an amplitude of $0.00556 \cdot 5^2\omega^2 = 0.139\omega^2$, which is half of the vibration amplitude of the sinusoidal vibration at the fundamental frequency. It must be noted that this vibration shape was measured by measuring by interferometer the position of the shaft and that a high magnetic preload was applied in order to prevent the shaft from slipping on the feet. The fact that the shaft is vibrating together with the feet might result in a vibration behavior that is slightly different from the one of the feet without the shaft. However, it is difficult to know the real vibration shape of the feet as the experimental setup does not allow to measure their displacement during MFID locomotion.

As for the shear mode actuators the displacement of the stack actuators has also been measured while exciting them with a sinusoidal signal. While for the shear mode piezos the important characteristic is the velocity profile, for the stack actuators it is the acceleration profile that will determine the variation of the contact force. The acceleration profile could be obtained by a double derivation of the position measured by interferometer. However, such a

[8] Theoretically, it is possible to use the shear mode piezos to compensate for this parasitic motion. However, this would limit the useable amplitude of the shear mode piezos and moreover, as the parasitic motion depends on the amplitude of the perpendicular vibration, this amplitude limit would be variable. Hence, it has been preferred not to do any compensation. However, it should be taken in account that this parasitic motion could cause a preferential motion direction and this specially at high perpendicular vibration amplitudes.

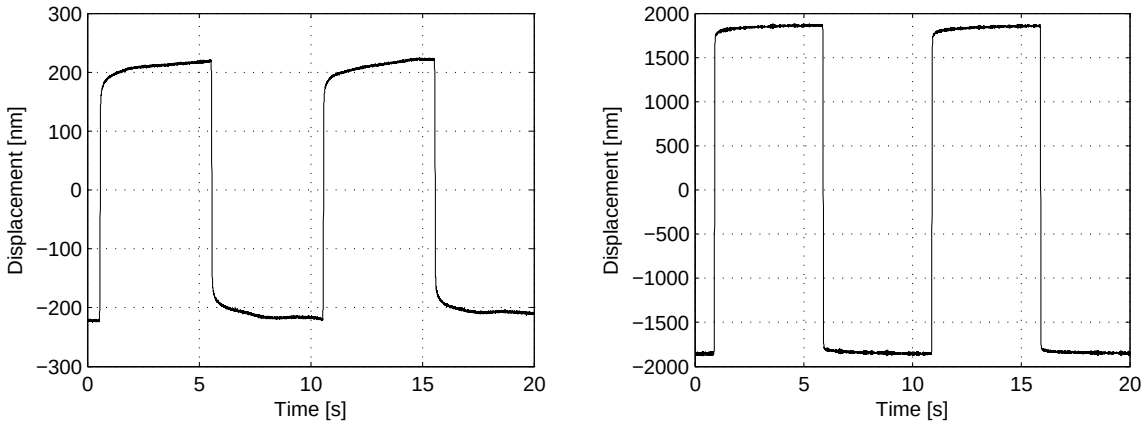


**(a)** Shear mode piezos **(b)** Stack piezos

**Figure 4.9:** Creep characteristic of the piezoelectric actuators

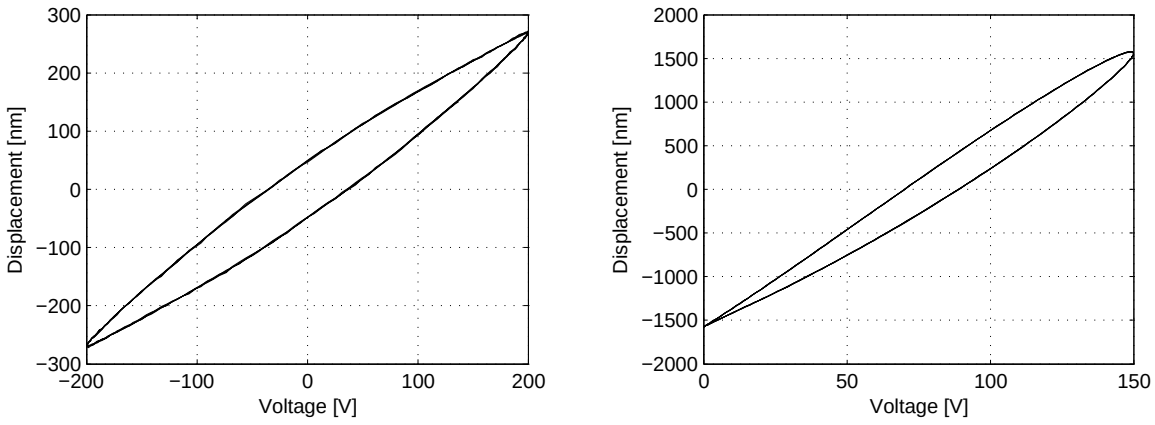


**(a)** Shear mode piezos **(b)** Stack piezos

**Figure 4.10:** Hysteresis characteristic at a frequency of 500 Hz of the piezoelectric actuators

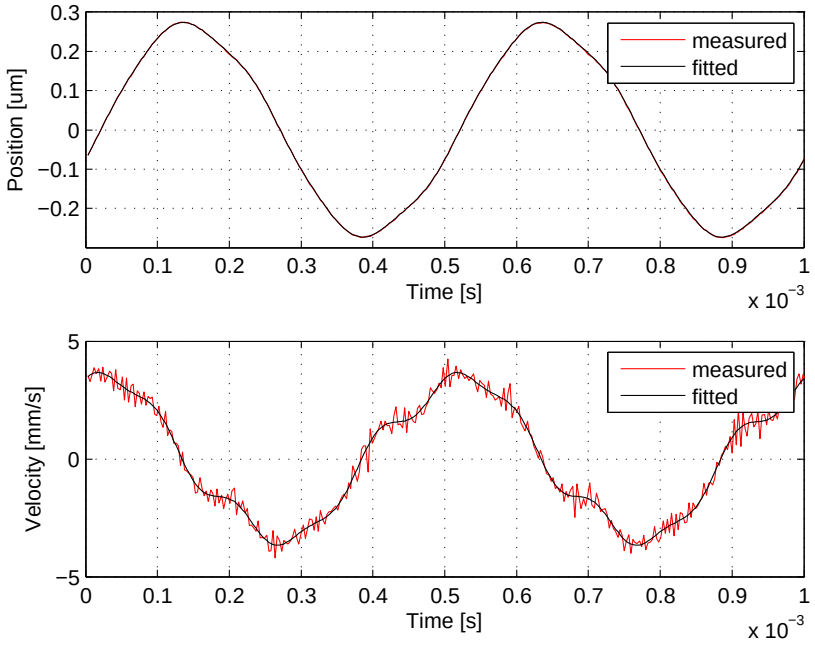


**Figure 4.11:** Harmonic fit on the measured displacement of the shear mode piezos when excited with a 2000 Hz sinusoidal signal

double derivation would cause a large amplification of the noise on the measured position. As the harmonics on the vibration of the stack piezos has shown to have a large impact on the optimal MFID motion characteristics, the harmonics in the vibration of the stack piezos has been measured by a vibrometer (specifications in appendix F.4) coupled to a lock-in amplifier (specifications in appendix F.4). The vibrometer outputs a analogue voltage signal that is proportional to the measured velocity (factor 5 mm(sV)$^{-1}$). This analogue signal is filtered by the lock-in amplifier, which is feeded with the sinusoidal excitation signal. The lock-in amplifier allows to measure the amplitude and phase of the fundamental frequency (i.e. 2000 Hz) and its higher harmonics. In order to allow for a reliable measurement of the higher harmonics the experiment was carried out at a driving voltage that is 7 times higher than the one used for the locomotion experiments described later in this chapter. The measured amplitudes have been scaled down by the same factor in order to correspond to the conditions of the locomotion experiments. The velocity is measured on a small silicon mirror glued to the middle of the shaft, which is clamped on the stack piezos by the magnetic preload. This experiment resulted in the following harmonic fit for the perpendicular vibration:

$$\begin{aligned} z(t) \;=\; & 21.6\sin(\omega t - 2.57) + 0.270\sin(2\omega t + 2.61) \\ & +0.437\sin(3\omega t + 2.32) - 0.160\sin(4\omega t - 1.13) \\ & +0.0735\sin(5\omega t - 0.227) - 0.0401\sin(6\omega t + 0.873) \\ & +0.0490\sin(7\omega t + 0.820) - 0.0045\sin(8\omega t + 0.873) \quad [\text{nm}]. \end{aligned} \tag{4.22}$$

Figure 4.12 plots the position, velocity and acceleration of the fundamental sine wave and the complete harmonic fit. The graph shows that for the position profile the deviation from a sinusoidal waveform is almost not visible, while in the acceleration profile the harmonic fit shows a maximum negative acceleration of $-0.51g$, instead of only $-0.35g$ for the fundamental sine wave. Hence, it can be concluded that the harmonics introduced by the hysteresis of the stack piezos has a large influence on the acceleration profile. Moreover, with this experimental

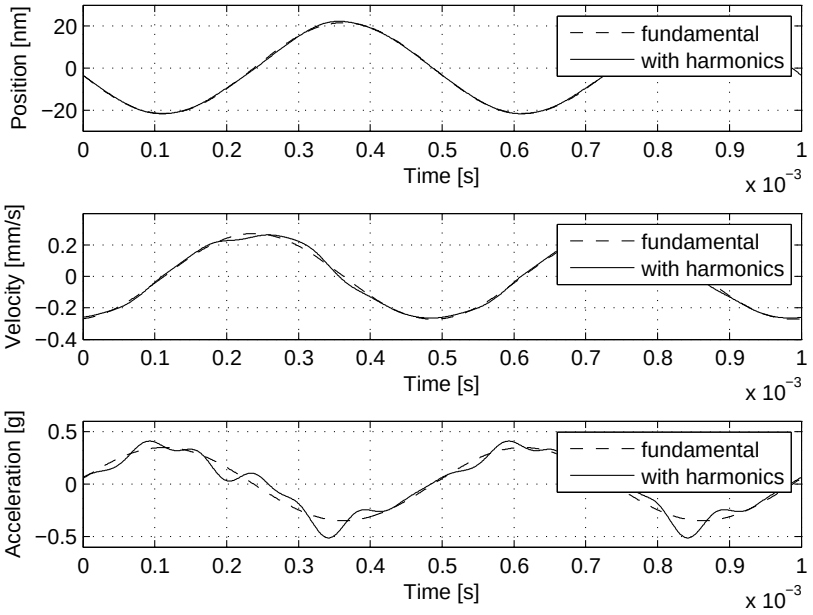


**Figure 4.12:** Displacement, velocity and acceleration of the perpendicular vibration of the shaft with and without higher harmonics measured by vibrometer

setup the limited band width of the electrical amplifier does not allow to compensate for these harmonics by input shaping of the waveform of the voltage excitation of the stack piezos.

With the same measurement setup used for the harmonic analysis of the vibration of the stack piezos the frequency response of the cylindrical shaft has been measured (see figure 4.13). The position (velocity) of the shaft is measured in its middle point, while being excited by the stack piezos. The shaft has a resonance frequency of 9450 Hz and a quality factor (ratio between amplitude at resonance and quasistatic amplitude) of about 10. If this resonance would be excited by one of the harmonics in the perpendicular vibration, the resulting acceleration of the shaft could increase a lot. Even though the measured resonance frequency of the shaft (9450 Hz) is not really close to any of the harmonics of the excitation (2000 Hz), resonance excitation could still occur after an axial displacement. Simulation in ProMechanica has shown that an axial displacement of the shaft of 2.5 mm causes a shift in resonance frequency of 1074 Hz. Moreover, higher harmonics on excitation vibration could also excite higher resonance mode of the shaft. Hence, it can be concluded that the harmonics resulting from the hysteresis in the stack piezos can have a large influence on the generated perpendicular acceleration profile of the shaft, particularly at certain specific frequencies. This parasitic acceleration is a considerable limitation to the measurement setup and one of the consequences is that without any preload the motion starts to become unstable when actuated with perpendicular accelerations of the fundamental sine wave above 0.35 m/s$^2$.

### The static friction coefficient

In order to be able to determine the friction coefficient experimentally an asymmetric signal with a well-defined maximum acceleration has been applied to the shear mode piezos and the minimum frequency at which net motion occurs is measured. In the first part of the signal (1/5 of the period) a constant positive acceleration $A_X$ is applied, while in the second part

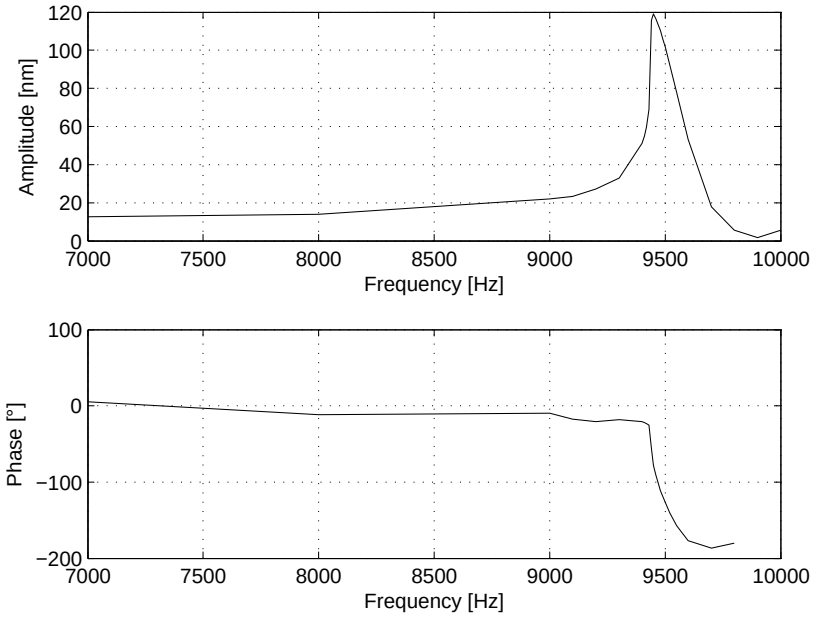


**Figure 4.13:** Resonance response of the shaft measured by vibrometer

(4/5 of the period) a constant negative acceleration of $-A_X/4$ is applied[9]. Such a signal is more practical in use than a sinusoidal signal as the occurrence of slip during the period of maximum acceleration is easily detected as the shaft will start to move in one direction. Compared to a saw-tooth signal as typically used for stick-slip actuators it is easier to model as the maximum acceleration is better defined and much less dynamic effects occur.

It has been observed that starting with no motion of the shaft and steadily increasing the driving frequency until motion occurs does not lead to a good estimation of the friction coefficient as a large variation (more than 10%) is observed between the threshold frequency measured at different trials. However, a very good repeatability (below 1 Hz) has been observed when searching for the highest frequency at which an initial motion (generated by shortly pushing the shaft manually) is slown down steadily until no more slip occurs[10]. This experiment resulted in a threshold frequency of 250 Hz for motion in positive direction and 249 Hz for motion in negative direction (i.e. with an inverted signal).

Figure 4.14 shows the applied and measured displacement and acceleration for a signal of 250 Hz. The measured acceleration is obtained by a double derivation of the measured displacement, which resulted in a very noisy signal. Therefore, the measured acceleration has been filtered with a second order Butterworth low pass filter at 2000 Hz. It is observed that the shape of the measured and applied displacement do not match exactly and that the measured acceleration peak is somewhat higher than the applied one. This is probably due to the hysteresis of the shear mode piezos (see figure 4.10(a)). Hence, a maximum acceleration of $a_{X,\max} = 1.8$ m/s$^2$ is measured. The inertial force $M_r a_{X,\max}$ resulting from this acceleration must be generated by static friction between the feet and the shaft. As the experiment is carried out without any magnetic preload the maximum static friction force is

[9] As the signal shape is kept constant, i.e. independent of the frequency, the acceleration $A_X$ varies proportionally to the square of the frequency.

[10] One could mistakenly think that such a procedure can only be used to identify the dynamic friction coefficient as the procedure starts from motion, i.e. a dynamic state. However, this is definitely not the case as during the period of low acceleration sticking occurs.

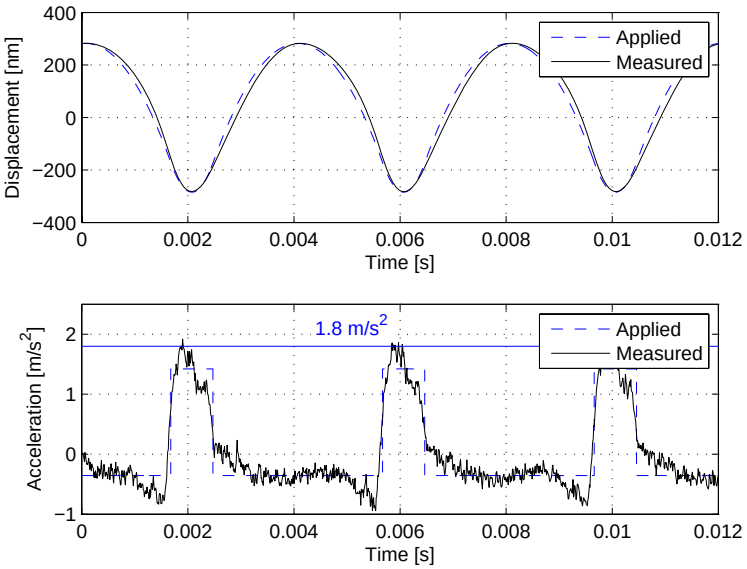


**Figure 4.14:** Applied and measured acceleration signal

given by $\mu_s c_g M_r g$. Hence the static friction coefficient $\mu_s$ can be calculated as

$$\mu_s = \frac{a_{X,\max}}{c_g g} = 0.15 \tag{4.23}$$

with $c_g = 1.22$ the contact geometry coefficient (see section 4.3.2). Also in literature [340] a value of $\mu_s = 0.15$ can be found for the static friction coefficient of sapphire on steel.

### Other friction coefficients: $\mu_d, \sigma_1, \sigma_2$ and $v_s$

Both the dynamic friction coefficient $\mu_d$ and the viscous friction coefficient $\sigma_2$ characterize the friction force when slip occurs. While the dynamic friction coefficient is a measure for the influence of the contact force on the friction force, the viscous friction coefficient expresses the influence of the slip velocity on the friction force. The Stribeck velocity $v_s$ determines around which sliding velocity the friction coefficient $\mu$ reduces from the static value $\mu_s$ to the dynamic value $\mu_d$. It is difficult to design a reliable experiment compatible with the presented measurement setup that would allow to decouple these three coefficients and determine their values independently. Therefore, these coefficients have been determined by fitting the results from the simulated locomotion velocities on the measured locomotion velocities (see figure 4.30 on page 112).

As already concluded in section 4.2.2 (on page 78) the viscous damping coefficient $\sigma_1$ has only a small transient influence on the friction force on the moment of sudden change in motion direction. This has been confirmed during simulation of the MFID locomotion, which showed that a variation of the viscous damping coefficient $\sigma_1$ has a negligible influence on the simulated motion velocity. According to Altpeter [333], experimental results have shown that independent of the system the ratio $\sigma_1/\sigma_2$ is always close to 10. Hence, the viscous damping coefficient $\sigma_1$ will be calculated in function of the viscous friction coefficient $\sigma_2$.

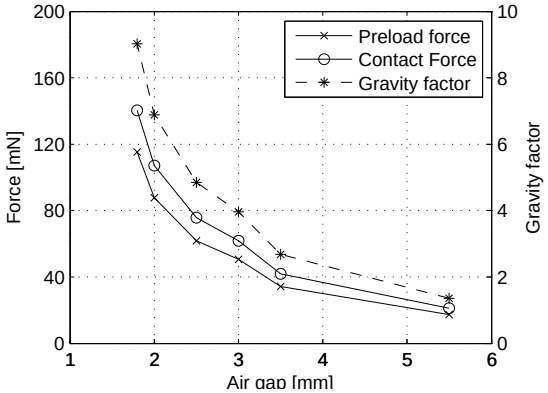


**Figure 4.15:** Measured magnetic preload and resulting contact force in function of the air gap. The graph also shows the gravity factor: i.e. the ratio between the preload force and the weight of the shaft.

### Calibration of the magnetic force

The setup is equipped with a yoke with two permanent magnets that can be fixed at a variable height in order to vary the air gap between the magnets and the shaft and consequently vary the magnetic preload. The same technique as used for measuring the static friction coefficient discussed above has been applied here for calibration of the value of the preload force in function of the air gap. The procedure consists of finding for different values of this air gap, the highest driving frequency at which the shaft does not move under excitation of the asymmetric signal shown in figure 4.14. Comparison of the maximum axial acceleration that can be calculated from the signal shape and the driving frequency with the maximum axial acceleration measured without magnetic preload allows to find the ratio between the total preload force $F_p$ and the weight of the shaft $M_r g = 12.8$ mN (this ratio is called here the gravity factor). Figure 4.15 shows the total preload force $F_p$ and the contact force $F_c$ ($F_c/F_p = c_g = 1.22$, see figure 4.5 and equation (4.12)) as well as the gravity factor. The value of the gravity factor also expresses the amount of perpendicular acceleration that has to be applied by the stack piezos in order to make the shaft jump on its guiding feet. The air gap has not been reduced below 1.8 mm in order to keep the maximum contact force $F_c = 140.5$ mN well below the maximum contact force allowed ($F_{c,max} = 472$ mN) as calculated in section 4.3.2. Moreover, at these values for the air gap, a remanent magnetization of the steel shaft has already been observed, which has shown to have some kind of hysteresis effect on the motion velocity.

### Overview of identification results

Table 4.1 gives an overview of the most important physical and mechanical parameters of the experimental setup as obtained from the identification procedures described in this section.

## 4.4 Simulation and experimental results

This section discusses and compares the results obtained by simulation of the dynamic model presented in section 4.2 and by measurements on the experimental setup presented in section 4.3. First the stepping locomotion is studied in detail. Consequently, the average motion velocity is considered and the influence of respectively the phase shift, perpendicular accel-

| Parameter | Symbol | Unit | Value |
|---|---|---|---|
| Mobile shaft mass | $M_r$ | g | 1.301 |
| Mobile shaft diameter | $D_{shaft}$ | mm | 2.5 |
| Mobile shaft length | $l$ | mm | 35 |
| First resonance frequency | $f_r$ | Hz | 9040 |
| Contact angle | $\beta$ | ° | 34.85 |
| Contact geometry coefficient | $c_g$ | | 1.22 |
| Contact force at $1g$ preload | $F_c$ | mN | 15.6 |
| Contact force at $9.02g$ preload | $F_c$ | mN | 140.5 |
| Static friction coefficient | $\mu_s$ | | 0.15 |
| Dynamic friction coefficient | $\mu_d$ | | 0.1 |
| Tangential contact stiffness at $1g$ preload | $\sigma_0$ | N/$\mu$m | 5.22 |
| Tangential contact stiffness at $9.02g$ preload | $\sigma_0$ | N/$\mu$m | 10.9 |
| Viscous damping coefficient | $\sigma_1$ | Ns/m | 1 |
| Viscous friction coefficient | $\sigma_2$ | Ns/m | 0.1 |
| Stribeck velocity | $v_s$ | mm/s | 5 |

**Table 4.1:** Overview of physical and mechanical parameters of the experimental setup

eration, axial vibration amplitude, driving frequency, angle of inclination and the preload is discussed. Then, the suitability of the MFID principle for precision application is discussed by studying the open loop repeatability and the motion resolution. Finally, the performance of the MFID principle is experimentally compared to that of the inertial inchworm and the stick-slip principle.

Table 4.2 presents the default parameter settings that (except if explicitly mentioned otherwise) have been used for the experiments and the simulations presented in this section. The default driving frequency of 2000 Hz corresponds to the maximum frequency were no hopping of the shaft occurs. A phase shift of 90° is where we would intuitively expect the maximum velocity: a synchronization of the moment of maximum contact force with the moment of maximum base velocity. The perpendicular (vertical) acceleration amplitude of $0.35g$ (with $g = 9.81$ m/s$^2$) is the maximum acceleration at which stable motion is obtained. The horizontal vibration amplitude is the measured sinusoidal vibration amplitude of the shear mode piezos when driven at their maximal voltage [-200 V, 200 V]. By default the experimental setup is not inclined, so the axis of the shaft lies within the horizontal plane. By default no additional magnetic preload is applied, so the only preload is due to the weight of the shaft. The preload is expressed as a factor of the acceleration of gravity $g$ the value of the force is thus obtained by multiplying this factor with $M_r g$.

### 4.4.1 Stepping motion

Figure 4.16 shows the simulated behavior of a MFID actuator at default parameter settings (see table 4.2). The upper graph depicts the position of the base and the stepping motion of the slider. The position of the base is the harmonic fit on the measured vibration shape as shown in figure 4.11. The middle graph depicts the instantaneous velocity of slider and base as well as the average velocity of the slider. It can be clearly seen that the slider is accelerated (decelerated) when the velocity of the base is larger (smaller) than that of the slider. It can also be seen that the acceleration is larger (larger slope) than the deceleration, which is intrinsic to the MFID principle as it is caused by the variation of the friction force. The graph also shows that the acceleration phase is shorter than the deceleration phase,

| Parameter | Symbol | Unit | Value |
|---|---|---|---|
| Driving frequency | $f$ | Hz | 2000 |
| Phase shift | $\phi$ | $^\circ$ | 90 |
| Perpendicular vibration amp. | $Z$ | $\mathrm{nm}_{amp}$ | 21.6 |
| Perpendicular acceleration amp. | $A_Z$ | $g$ | 0.35 |
| Axial vibration amp. | $X$ | $\mathrm{nm}_{amp}$ | 270 |
| | $X$ | $\mathrm{nm}_{p2p}$ | 540 |
| Inclination | $\alpha$ | $^\circ$ | 0 |
| Perpendicular preload | $F_{p,0}$ | $g$ | 1 |

**Table 4.2:** Default parameter settings for the simulations and experiments for the characterization setup

which is due to the shape of the base position curve. At default parameter settings as for the simulation shown in this graph the velocity of the slider never becomes negative. However, for other values of the input parameters (for instance in the case of a lower variation of the contact force) the velocity of the slider becomes negative at the end of each deceleration phase, resulting in a small backward motion.

The lower graph in figure 4.16 depicts the friction force $F_t$ and the contact force $F_c$ between base and slider. The contact force is varied sinusoidally around a certain offset value, but never becomes negative. The friction force switches to a positive value when the base is moving faster than the slider and switches back to a negative value when the base is moving slower than the slider. The absolute value of the friction force is the sum of the dry friction term $\sigma_0 z_c$ and the viscous damping term $\sigma_2 \dot{x}$ in equation (4.6). The small increase in friction force that can be observed just after each polarity switch of the $F_t$ is caused by the Stribeck effect (i.e. the smooth transition from the dynamic friction coefficient to the larger static coefficient at very low velocities).

Figure 4.17 shows the measured position and velocity of the shaft at default parameter settings, but with a perpendicular acceleration amplitude $A_Z = 0.072g$ on the graph on the left-hand side and $A_Z = 0.35g$ (i.e. the default value) on the graph on the right-hand side. The position has been measured by interferometer (resolution 1 nm, sampling rate of 1 MHz) and the velocity is obtained by derivation of the position. In order to limit the noise on the velocity, a $4^{\text{th}}$ order low pass Butterworth filter with a cutoff frequency of 40 kHz has been applied to the position data before derivation. These graphs clearly show that at low perpendicular acceleration, the position profile shows a small backward motion at every step, while for higher accelerations the position profile is very smooth and only a slight variation of the velocity can be observed. Figure 4.18 shows that there is a good match between the measured and the simulated velocity profile.

The measured and simulated stepping behavior shown in figure 4.18 features an average slider velocity of 1.38 mm/s. This average velocity depends on a large number of parameters. The next subsections study the influence of these parameters on the average slider velocity.

### 4.4.2 Influence of the phase shift

Figure 4.19 shows the simulated and measured influence of the phase shift $\phi$ between slip generation (i.e. axial vibration) and contact force variation (i.e. perpendicular vibration) on the motion velocity. The phase shift has been varied from 0° to 360° with steps of 20° and at each value five repetitive measurements of the motion velocity are taken. The simulated behavior represented by the solid line in figure 4.19 shows a good match with the experimental

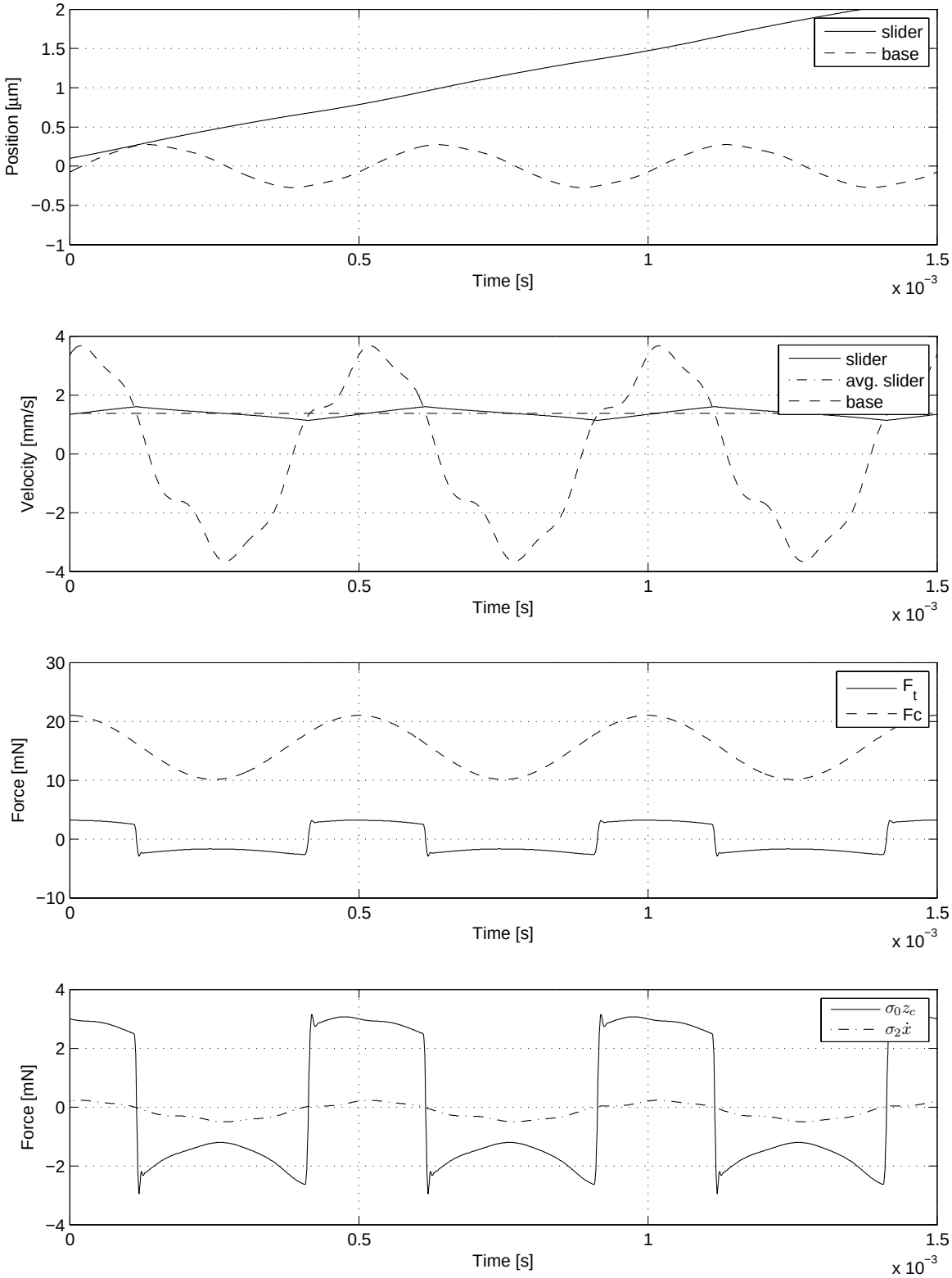


**Figure 4.16:** Simulated stepping motion at default parameter settings

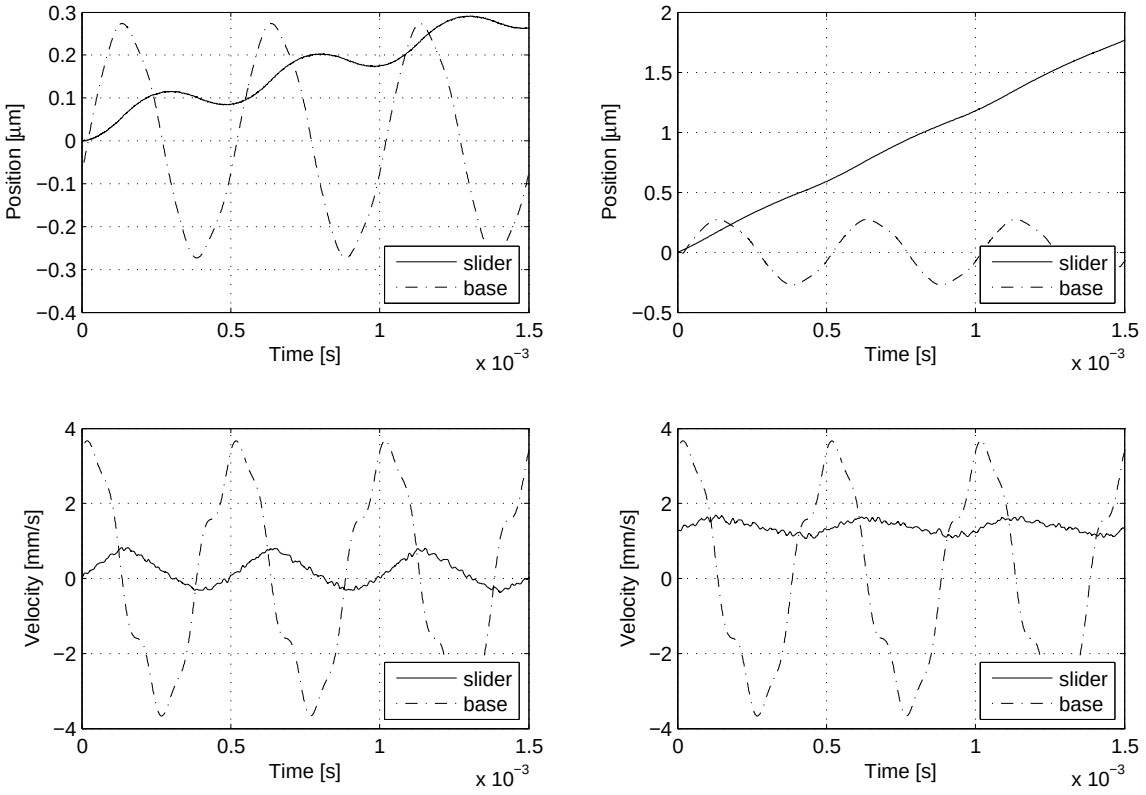


**(a)** Perpendicular acceleration $A_Z = 0.072g$ **(b)** Perpendicular acceleration $A_Z = 0.35g$

**Figure 4.17:** Measured stepping behavior at default parameter settings for two different perpendicular acceleration amplitudes

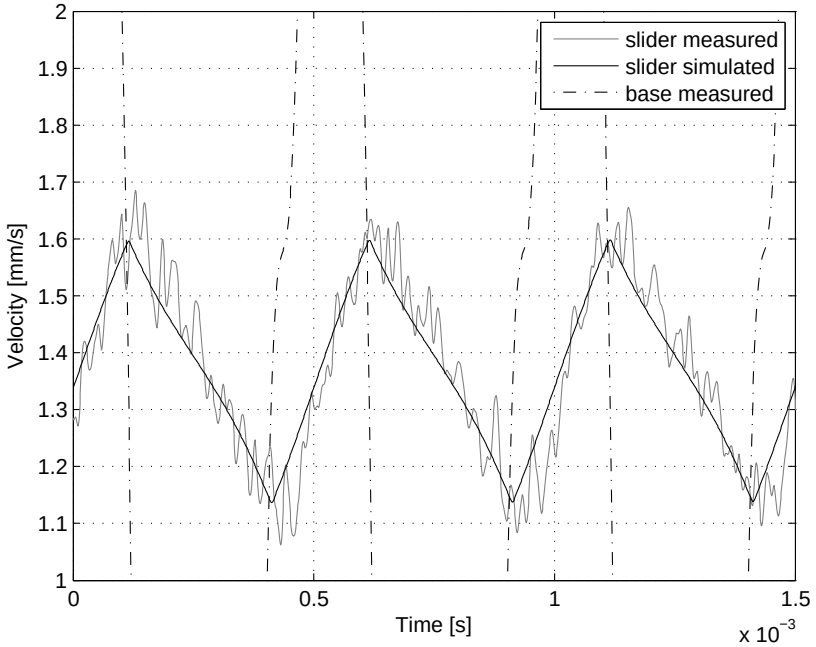


**Figure 4.18:** Comparison of the measured and the simulated velocity profile at default parameter settings

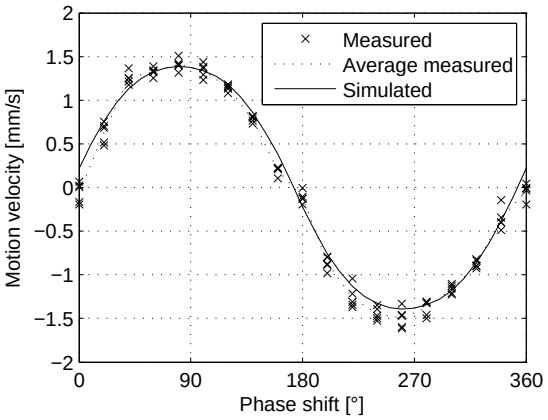


**Figure 4.19:** Measured and simulated motion velocity in function of phase shift

data. The maximum velocity is achieved at a phase shift of 80° and 260°, while the curve reaches zero velocity around 0° and 180°.

It is intuitively easy to understand that the optimal phase shifts are around 90° and 270°. A phase shift of 90° between axial and perpendicular vibration means that the moment of maximum velocity (positive or negative) of the axial vibration and the moment of maximum contact force coincide (i.e maximum perpendicular acceleration). Hence, the shaft is accelerated the most on the moment of maximum velocity of the base. The fact that the maximum velocity is reached at 80° and not at 90° as one would intuitively expect, is due to the hysteresis in the piezo actuators which causes an additional phase lag and a vibration that is not completely sinusoidal (see figure 4.11).

The graph in figure 4.19 also shows that the dispersion between the five velocity measurements lies within 10% at the maximum velocity in positive and negative direction and that a good symmetry between motion in positive and negative direction is observed. The repeatability of the motion will be discussed more into detail in section 4.4.8.

### 4.4.3 Influence of the perpendicular acceleration

Figures 4.20 and 4.21 show the influence of the perpendicular acceleration amplitude on the *velocity vs. phase shift* profile. Up to an acceleration amplitude of $A_Z = 0.35g$ the maximum velocity increases with increasing perpendicular acceleration and the dispersion between the different measurements is low. Starting from a perpendicular acceleration of $A_Z = 0.43g$ the maximum velocity still increases but the dispersion also increases considerably and the symmetry of motion in positive and negative direction detoriates. For a perpendicular acceleration amplitude of $A_Z = 0.43g$ and above, a small noise caused by the shaft that is bouncing on the feet can be heard. As discussed in section 4.3.2 the hysteresis of the stack piezos introduces higher harmonics which cause a non-negligible parasitic acceleration resulting in a peak acceleration of $0.63g$[11] in stead of $0.43g$. Moreover, as discussed in the same section, the resonance frequency of the shaft can be excited at certain axial positions, resulting into an amplification of certain harmonics and therefore a larger parasitic acceleration. When the sum of the ideally sinusoidal acceleration and the parasitic acceleration introduced by the hysteresis and possibly amplified by the resonance of the shaft becomes larger than $1g$ the shaft will start to hop. Such hopping results in an intermittent contact between the guiding

[11] This value is extrapolated from the measured peak acceleration of $0.51g$ for an acceleration of the fundamental size wave of $0.35g$.

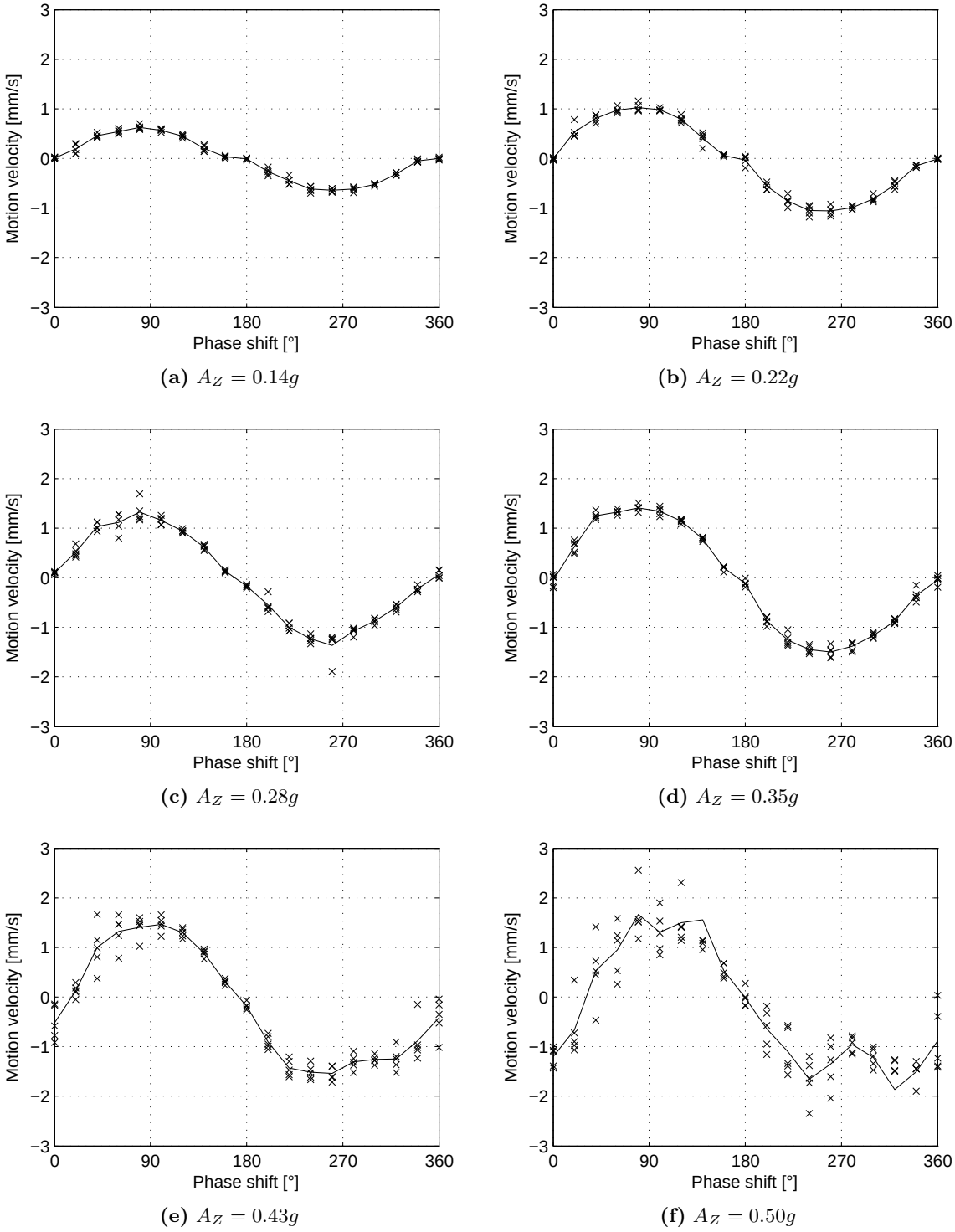


**(a)** $A_Z = 0.14g$ **(b)** $A_Z = 0.22g$

**(c)** $A_Z = 0.28g$ **(d)** $A_Z = 0.35g$

**(e)** $A_Z = 0.43g$ **(f)** $A_Z = 0.50g$

**Figure 4.20:** Measured motion velocity in function of the phase shift for a perpendicular acceleration amplitude $A_Z$ ranging from $0.14g$ to $0.5g$

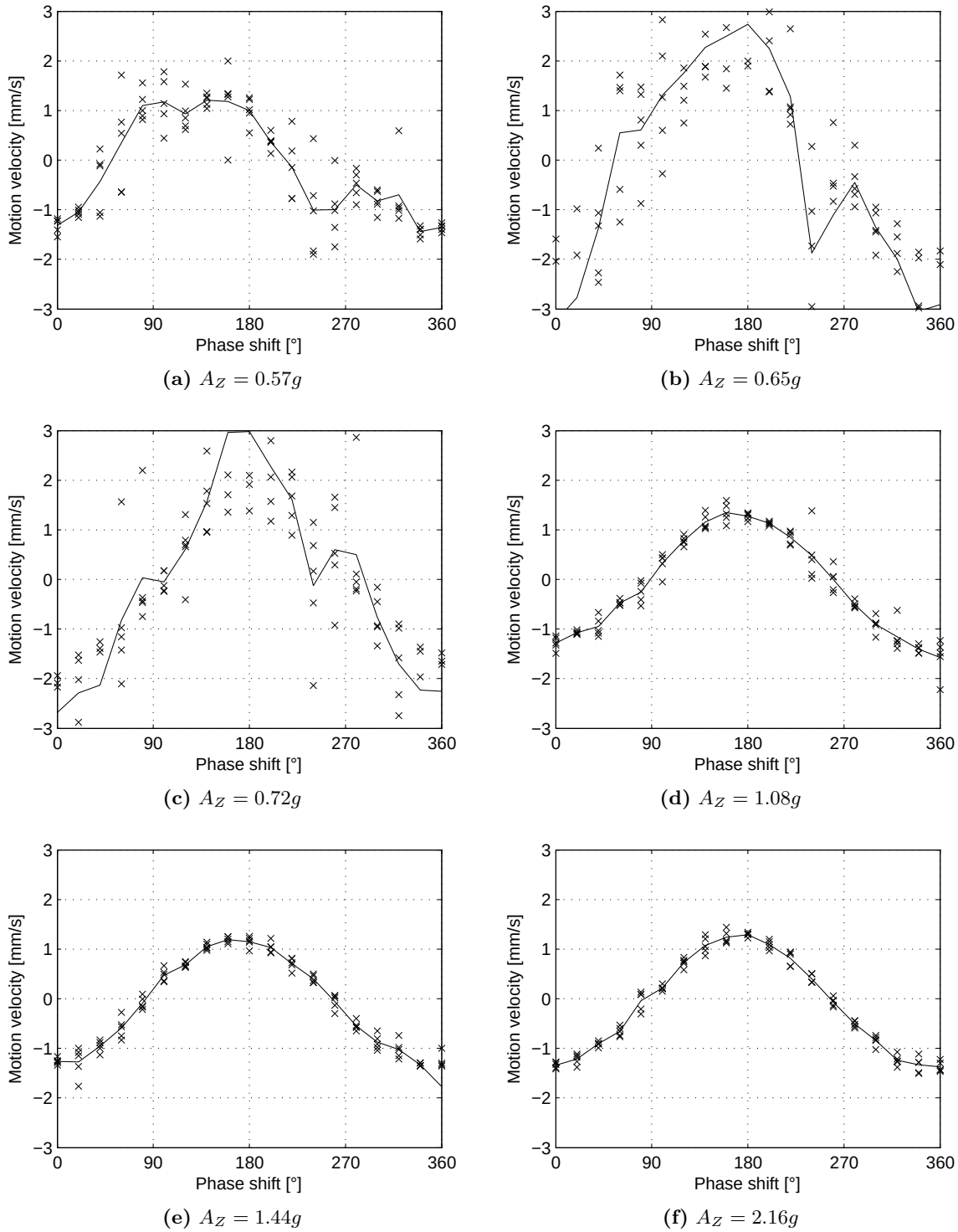


**(a)** $A_Z = 0.57g$ **(b)** $A_Z = 0.65g$

**(c)** $A_Z = 0.72g$ **(d)** $A_Z = 1.08g$

**(e)** $A_Z = 1.44g$ **(f)** $A_Z = 2.16g$

**Figure 4.21:** Measured motion velocity in function of the phase shift for a perpendicular acceleration amplitude $A_Z$ ranging from $0.57g$ to $2.16g$

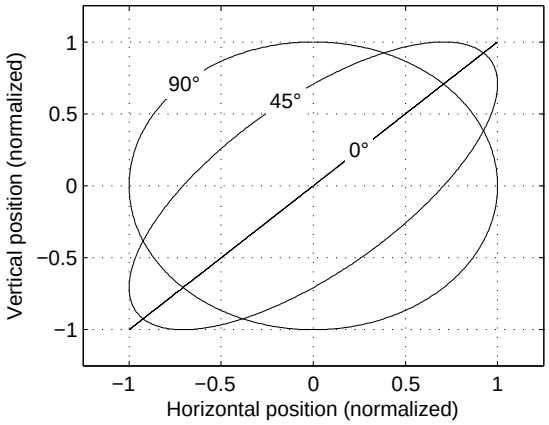


**Figure 4.22:** Vibration shapes of the contact points in function of the phase shift

feet and the shaft. The hopping height and the flight time depend on the driving frequency, the vertical vibration amplitude, the contact stiffness and damping and the axial position of the shaft. Moreover, uncontrolled bouncing can occur when the shaft comes back into contact with the guiding spheres. Hopping motion is rather complex to model and easily results in motion instabilities. These instabilities are clearly visible in figures 4.20 and 4.21 by the large dispersion on the measured motion velocity for perpendicular acceleration amplitudes of $A_Z = 0.5g$ and above. However, the graphs also show that for acceleration amplitudes of $A_Z = 0.5g$ and above considerably higher motion velocities can be reached. This is because the bouncing can result in a lower apparent friction coefficient, reducing the backlash during the deceleration phase and therefore increasing the average motion velocity.

It is interesting to observe that for a perpendicular acceleration amplitude above $A_Z = 1g$ the dispersion again decreases and a good repeatability and motion symmetry comparable to the one at $A_Z = 0.35g$ is reached. Also a comparable maximum velocity in positive and negative direction is obtained, but this maximum velocity is, however, not reached at a phase shift of 80° and 260° as is the case at $A_Z = 0.35g$ but rather around 0° and 180°. This shift in phase shift (which is already gradually visible for acceleration amplitudes between $A_Z = 0.35g$ and $A_Z = 1g$) is explained by the shift from the MFID locomotion principle to a kicking locomotion principle. In fact at a phase shift of 0° or 180° the contact points of the feet are not moving along an elliptical path as is the case for a phase shift of 80° and 260°, but rather along a straight line with a diagonal orientation (see figure 4.22).

This tendency of maximum velocity, dispersion and phase shift is also clearly visible in figures 4.23(a) and 4.23(b), which represent respectively the maximum velocity in positive direction and the phase shift at which this maximum velocity occurs in function of the perpendicular acceleration amplitude. The error bars in the upper graph represent the standard deviation of the five measurements taken for every acceleration value. Figure 4.23(a) also shows the simulated *velocity vs. perpendicular acceleration* profile, which shows a good match with the experimental data up to $0.5g$. Above this value the shaft starts to jump in the experiments, which causes the deviation between simulated and measured data. As the hopping motion of the shaft (take off, flying and landing) is not included in the dynamic model, no simulation can be carried out for perpendicular acceleration amplitudes larger than $1g$.

Ultrasonic motors are based on the vibration of the contact points along an elliptical path or along a (more or less) straight, inclined line. Such a vibration is in fact a combination of an axial and a perpendicular vibration with a phase shift of 90° for the elliptical path and 0° for the straight line path. This is why ultrasonic motors (except for the traveling wave

ultrasonic motors) are a special case of MFID locomotion. The standing wave ultrasonic motors used to drive the mobile robots shown in figures 2.12(a) [12], 2.12(c) and 2.12(d) on page 45 generate a vibration of the contact point along a straight line. These robots are characterized by an intermittent contact between the robot's feet and the substrate. The ultrasonic motors discussed by Devos in [131] are based on a permanent contact between the vibrating feet and the substrate. He reports an optimal velocity for a phase shift between horizontal and vertical vibration of 90°, resulting in a motion of the feet along an elliptical path. This corresponds to the *optimal phase shift vs. perpendicular acceleration* profile for MFID locomotion in figure 4.23(b), which shows an optimal phase shift of 90° if no hopping occurs and 0° for accelerations above $1g$ [13].

The *velocity vs. perpendicular acceleration* profile shows a good linear behavior up to an acceleration amplitude of $A_Z = 0.28g$. Above this value a saturation occurs (specially visible in simulated profile). This saturation is due to the non sinusoidal shape of the vibration of the shear mode piezos due to hysteresis. As clearly visible in the velocity profile of figure 4.16, a further increase of the slider velocity results in an important reduction of the duration of the acceleration phase (and consequently an increase of the duration of the deceleration phase), which limits the resulting increase in average motion velocity. Despite of the linear behavior for acceleration amplitudes up to $A_Z = 0.28g$, the perpendicular acceleration is not a very good parameter for velocity control if smooth motion at low velocity is required, because at low perpendicular acceleration the shaft is constantly moving back and forth (see figure 4.17(a)).

Figure 4.23(a) has shown that a reduction of the perpendicular acceleration amplitude results into a reduction of the motion velocity. However the amplitude of the axial vibration still remains the same. So, the efficiency with which the axial vibration is transformed into an average motion velocity decreases with decreasing perpendicular acceleration. In order to quantify this efficiency the step efficiency $\eta_{step}$ is introduced. The step efficiency $\eta_{step}$ is defined as the ratio between the average motion velocity of the slider $v_{r,avg}$ and the maximum instantaneous velocity $v_{x,max}$ (corresponds to the amplitude $V_X$ of the velocity variation in case of a sinusoidal vibration) of the axial vibration.

$$\eta_{step} = \frac{v_{r,avg}}{v_{x,max}} \tag{4.24}$$

A step efficiency of $\eta_{step} = 1$ would thus mean that the average motion velocity is equal to the maximum instantaneous velocity of the axial vibration. This would theoretically only be possible if an infinite contact force would be applied on the exact moment of maximum axial vibration velocity and a zero contact force at any other moment. This is the theoretical upper limit to the motion velocity of the MFID principle.

In the case of a sinusoidal axial vibration with amplitude $X$ and frequency $f$, the maximum instantaneous axial velocity is equal to $v_{X,max} = 2\pi f X$. In the case of this experimental setup, an axial vibration amplitude of $X = 270$ $\text{nm}_{amp}$ and a driving frequency of at $f = 2000$ Hz, would result in a maximum instantaneous axial velocity of $v_{X,max} = 3.39$ mm/s. However, as depicted in figure 4.11 the axial vibration is not purely sinusoidal due to the hysteresis of the shear mode piezos, which results in a slightly higher maximum instantaneous velocity of 3.67 mm/s. Figure 4.23(c) shows the measured and simulated step efficiency

[12] The robot in figure 2.12(a) is in fact not really driven by an ultrasonic motor as the operation frequency is 5.5 kHz, but its operation principle is similar to that of standing wave ultrasonic motors.

[13] Hopping motion does not always result in an optimal phase shift of 0°. For instance, the ultrasonic robot shown in figure 2.12(e) (page 45) reaches an optimal velocity for a phase shift of 90°, while electrical measurements have shown that there is an intermittent contact between feet and substrate.

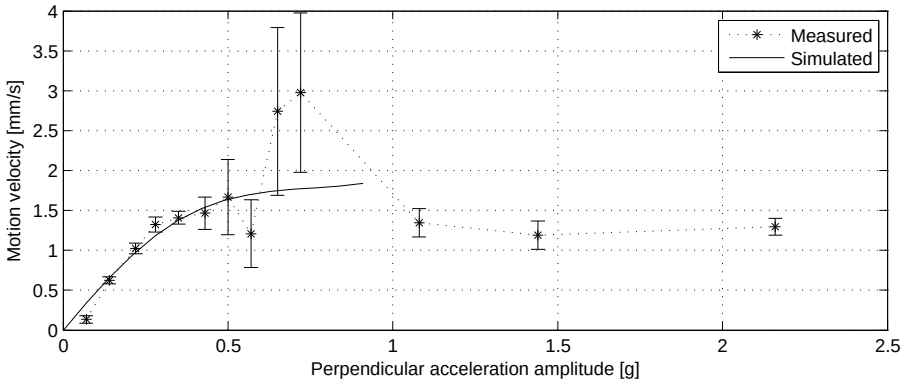


**(a)** Maximum velocity

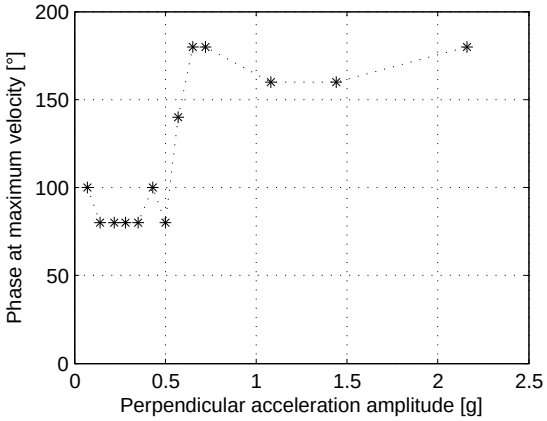


**(b)** Optimal phase shift

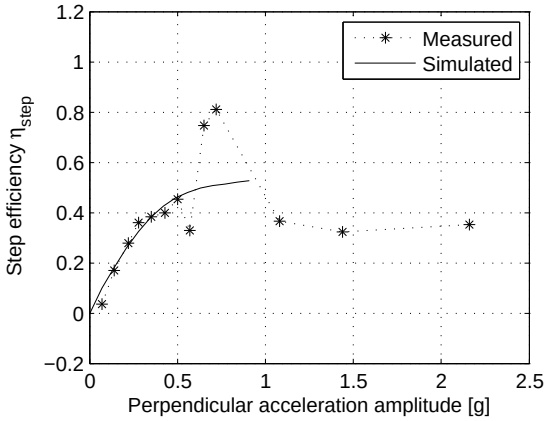


**(c)** Step efficiency

**Figure 4.23:** Influence of the perpendicular acceleration on maximum velocity, optimal phase shift and step efficiency

$\eta_{step}$ obtained by dividing the measured and simulated motion velocity by this maximum instantaneous velocity of 3.67 mm/s. It should be noted that a step efficiency above $1/\pi = 0.32$ results in a motion velocity that is higher as the one that could have been obtained with an ideal[14] stick-slip actuator with the same axial vibration amplitude $X$ and driving frequency $f$ ($v_{max,stick-slip} = 2fX$). For $X = 270$ nm$_{amp}$ and $f = 2000$ Hz such an ideal stick-slip actuator would feature a motion velocity of 1.08 mm/s, which is lower than the 1.38 mm/s obtained with this MFID actuator at default parameter settings.

### 4.4.4 Influence of the axial vibration amplitude

Figure 4.24(a) shows the measured and simulated motion velocity in function of the axial vibration amplitude. The figure shows a good linear behavior with low dispersion even at low velocities, which makes from the axial vibration amplitude the best parameter for velocity control of the MFID actuator. Moreover at low axial vibration amplitudes, the step size also becomes smaller, which allows for motion with high resolution. The curve crosses zero at an axial vibration amplitude of around $X = 23$ nm and not at $X = 0$ nm, which is due to fact that the generated axial acceleration is not high enough anymore to overcome the friction

[14] An "ideal stick-slip actuator" is considered here as a stick-slip actuator without any backlash during the slip phase.

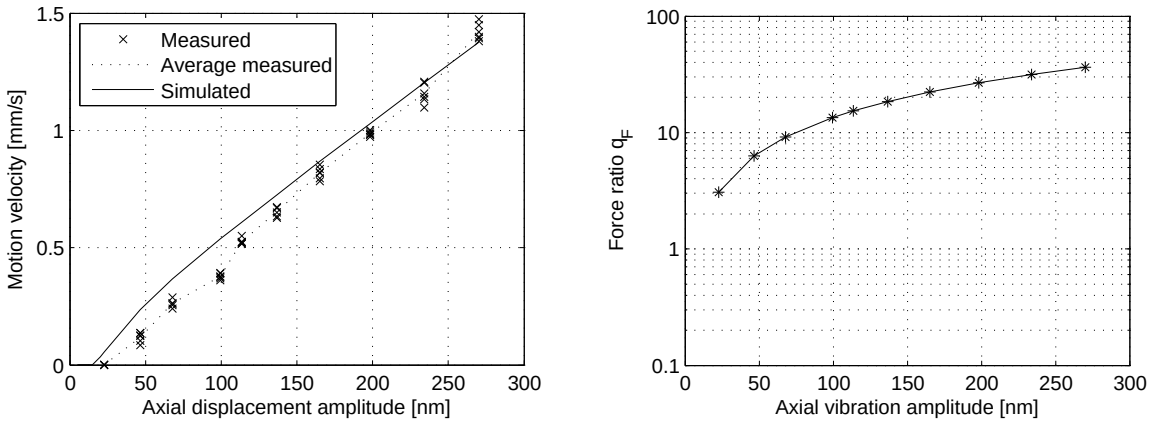


**(a)** Velocity **(b)** Force ratio

**Figure 4.24:** Measured and simulated motion velocity and force ratio in function of the axial displacement amplitude

force. In order to be able to quantify the "ease" with which slip is generated the force ratio $q_F$ is introduced.

The force ratio $q_F$ is defined as the ratio between the maximum inertial force $F_{i,X,max}$ generated by the axial vibration and the minimum instantaneous static friction force $F_{t,s,min}$

$$q_F = \frac{F_{i,X,max}}{F_{t,s,min}}. \tag{4.25}$$

One of the conditions for MFID locomotion is that $q_F > 1$, because a force ratio smaller than 1 would mean that the static friction force is large enough to compensate for the maximum inertial force. Hence, no slip would be generated and the slider would keep on vibrating back and forth with the base.

In order for a slider with mass $M_r$ to follow a sinusoidal vibration of the base with amplitude $X$ and pulsation $\omega$ an inertial force equal to

$$F_{i,X} = -M_r X \omega^2 \sin(\omega t) \tag{4.26}$$

would have to transmitted by the friction force between slider and base. The maximum inertial force is thus $F_{i,X,max} = M_r X \omega^2$.

The varying contact force $F_c$ between slider and base can be expressed as

$$F_c = F_{c,0} + F_{c,amp} \sin(\omega t + \phi). \tag{4.27}$$

In the case of only gravitational preload and horizontal motion (inclination angle $\alpha = 0°$) the static contact force corresponds to $F_{c,0} = M_r g$. If the variation of the contact force is generated by a perpendicular vibration of the base with amplitude $Z$ and pulsation $\omega$, the amplitude of the contact force variation is given by $F_{c,amp} = M_r Z \omega^2$. The minimum contact force then becomes

$$F_{c,min} = M_r g - M_r Z \omega^2 = M_r g (1 - \frac{Z\omega^2}{g}). \tag{4.28}$$

If defining $A_{X,g} = \frac{X\omega^2}{g}$ and $A_{Z,g} = \frac{Z\omega^2}{g}$, which expresses the axial and the perpendicular acceleration amplitude as a fraction of $g$, the minimum static friction force becomes

$$F_{t,s,min} = \mu_s c_g M_r g (1 - A_{Z,g}) \tag{4.29}$$

and the force ratio $q_F$ is given by

$$q_F = \frac{A_{X,g}}{\mu_s c_g (1 - A_{Z,g})} \tag{4.30}$$

with $\mu_s$ the static friction coefficient and $c_g$ the contact geometry coefficient (see figure 4.5).

At default parameter settings ($f = 2000$ Hz, $X = 270$ nm, $A_{X,g} = 4.35$, $A_{Z,g} = 0.35$, $\mu_s = 0.15$ and $c_g = 1.22$) a force ratio of $q_F = 36.6$ is obtained, which is sufficiently above 1 in order to allow for stable motion. Figure 4.24(b) plots the force ratio $q_F$ in function of the axial vibration amplitude. At the minimum vibration amplitude of $X = 23$ nm a force ratio of $q_F = 3.1$ is still reached. However, according to the experimental results shown in figure 4.24(a) no motion is generated at $X = 23$ nm. A first reason for this mismatch, is the fact that the calculation of the force ratio assumes a synchronization of the moment of maximum axial acceleration and the moment of minimum contact force, which implies a phase shift between axial and perpendicular vibration of $\phi = 0°$. Indeed, as observed in the next section, when slip generation becomes critical (i.e. a force ratio close to 1), the optimal phase shift tend to shift to 0° and 180°. The experiment shown in figure 4.24(a), however, was carried out at the default phase shift of $\phi = 90°$. For a phase shift of 90° the moment of maximum axial acceleration coincides with a contact force that is equal to the static contact force $F_{c,0}$, which is $\frac{1}{1-A_{Z,g}}$ times higher than the minimum contact force. If calculated for a phase shift of 90° the force ratio would then become $3.1 \cdot (1 - A_{Z,g}) = 2.0$. The remaining mismatch of a factor 2 would imply that the static friction coefficient is in reality higher than $\mu_s = 0.15$, which is confirmed by the fact that in figure 4.24(a) the simulated motion velocity reaches zero velocity for lower vibration amplitudes than the measured velocity. However, increasing the static friction coefficient detoriates the fit goodness between simulated and measured data in other graphs (in particular the graph in figure 4.31(a) showing the influence of the inclination on the motion velocity). Despite of this mismatch, it can still be concluded that the force ratio gives an estimation of the minimum vibration amplitude for locomotion at a given driving frequency and contact force variation. Hence, as the calculation of the force ratio does not require any simulations or experiments it can be used as an indicator during the design process of an MFID actuator in order to choose the required vibration amplitudes and driving frequencies.

### 4.4.5 Influence of the driving frequency

Figure 4.25(a) shows the influence of the driving frequency on the measured and simulated motion velocity at default parameter settings. The experiment has been carried out at constant perpendicular acceleration ($A_Z = 0.35g$) over the whole frequency range, which means that for every frequency the perpendicular vibration amplitude is adapted accordingly. A fairly good fit between measured and simulated data is observed. At default parameter settings there is a threshold at about 500 Hz below which no locomotion is possible. Above this threshold frequency, the motion velocity increases with increasing driving frequency, but the increase is not really linear[15]. The non-linearity of the *velocity vs. frequency* profile makes from the frequency a bad parameter for velocity control. Moreover, a frequency control is more complicated to implement than an axial vibration amplitude control as, if the perpendicular acceleration is kept constant as in this experiment, the amplitude of perpendicular vibration must be adapted according to the frequency change.

[15]The reasons for the dips in measured motion velocity from 800 Hz to 1000 Hz and from 1400 Hz to 1600 Hz are not clear.

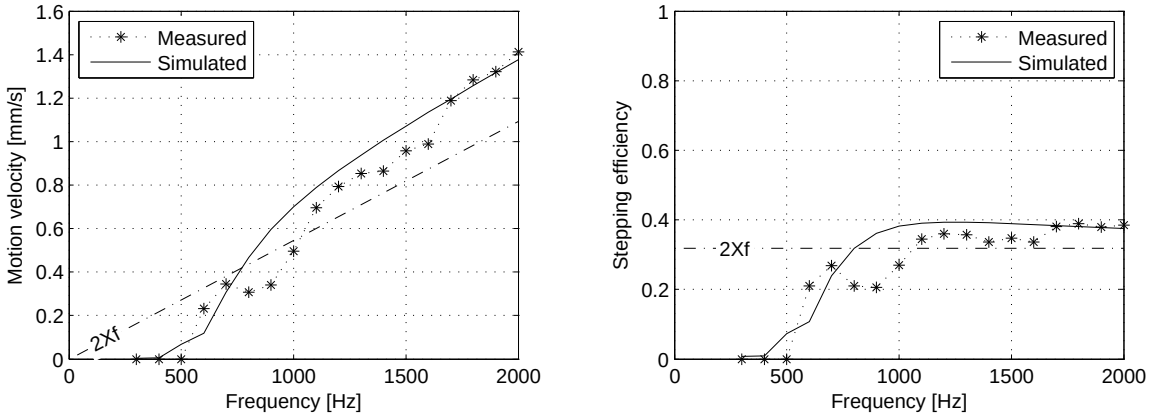


**(a)** Motion velocity

**(b)** Step efficiency $\eta_{step}$

**Figure 4.25:** Measured and simulated velocity and step efficiency in function of the driving frequency for a phase shift of 90°

The dash-dotted line in figure 4.25(a) traces the motion velocity ($v_{r,avg} = 2Xf$) that would be obtained with an ideal stick-slip actuator or an ideal quasistatic walking actuator that is actuated with the same amplitude and frequency. Above 1000 Hz the measured MFID velocity is higher than this line, from which can be concluded that above that frequency the MFID principle is more efficient than the other locomotion principles in transforming the axial vibration into a motion velocity. Figure 4.25(b) shows the step efficiency in function of the driving frequency obtained by dividing the measured and simulated motion velocity by the maximum instantaneous velocity of the axial vibration (i.e. 3.67 mm/s at 2000 Hz). The graph shows that the step efficiency starts at zero at around 500 Hz and saturates at a maximum value of about $\eta_{step} = 0.4$. The dash-dotted line indicates the step efficiency of $\eta_{step} = 1/\pi = 0.32$ that would be obtained with a velocity $v_{r,avg} = 2Xf$ (i.e. the velocity of an ideal stick-slip actuator or quasistatic inchworm or stepping actuator).

For the *velocity vs. phase* profile studied in section 4.4.2 it was observed that at default operation conditions (driving frequency 2000 Hz) the maximum velocity in positive and negative direction is reached at a phase shift of 80° and 260° respectively. However, this is not the case at lower driving frequency. Figures 4.26(a) and 4.26(b) show respectively the maximum velocity in positive and negative direction in function of the driving frequency and the phase shift at which this maximum velocity is reached[16]. A good match between measured and simulated optimal velocity and optimal phase shift is observed. Both the measured and the simulated velocity reach zero at a frequency of 300 Hz, which is lower than the 500 Hz in the case of a constant phase shift of 90° as in figure 4.25(a). The reason for this threshold frequency is that below this frequency the axial acceleration is not sufficient for causing the slider to slip on the base. Figure 4.27 shows the force ratio in function of the driving frequency. As defined in the previous section a force ratio of $q_F = 1$ is the lower limit at which locomotion is still possible. The force ratio in figure 4.27 reaches 1 between 300 and 400 Hz, which matches well the measured and simulated behavior shown in figure 4.26(a).

Figure 4.26(b) shows that the optimal phase shift of 80° and 260° at 2000 Hz increases with decreasing frequency up to 160° and 360° at 300 Hz. This is caused by the fact that

[16]The difference between figure 4.26(a) and figure 4.25(a) is that the experiment in figure 4.25(a) is carried out at a constant phase shift of 90°, while in figure 4.26(a) the phase shift is adapted to the optimal phase shift (see figure 4.26(b)) at every frequency.

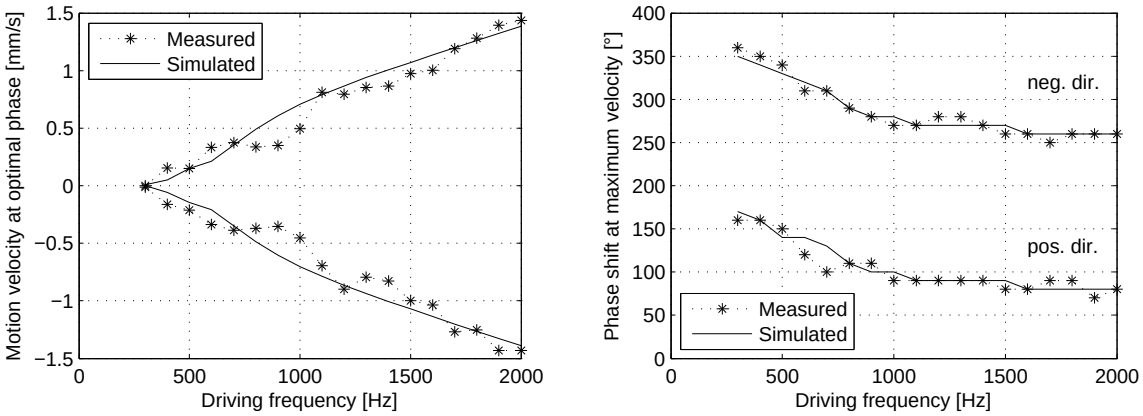


**(a)** Maximum velocity **(b)** Phase at maximum velocity

**Figure 4.26:** Measured and simulated optimal velocity and optimal phase shift in function of the driving frequency up to 2000 Hz

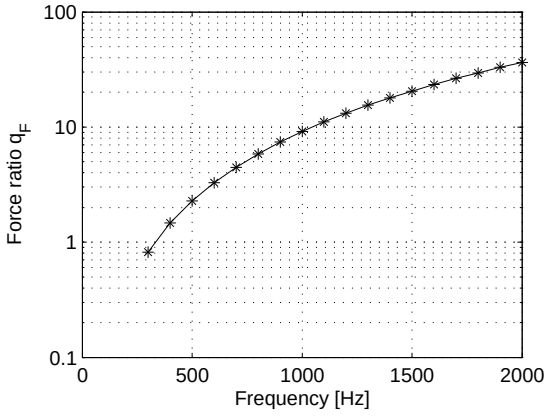


**Figure 4.27:** Force ratio $q_F$ in function of the driving frequency

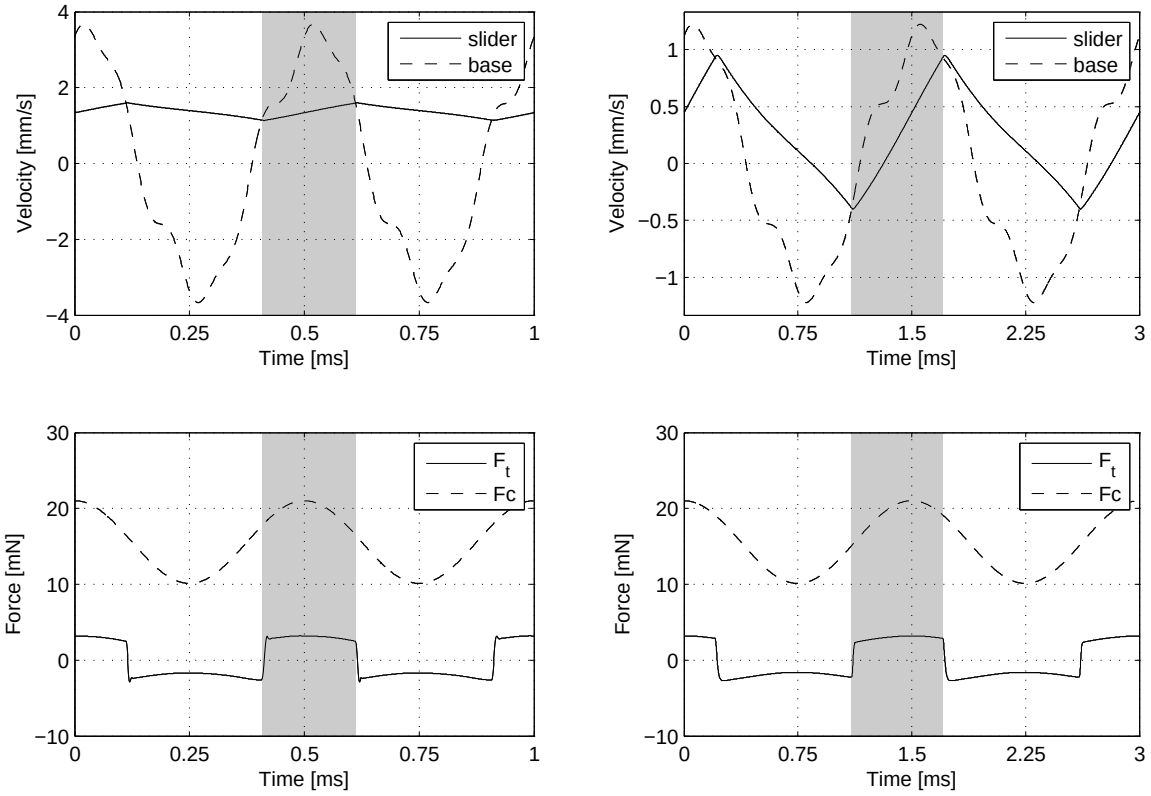


**(a)** $f = 2000$ Hz **(b)** $f = 667$ Hz

**Figure 4.28:** Simulated velocity and force profile at a driving frequency of 2000 Hz and 667 Hz (the gray patch delimits de acceleration phase)

the acceleration phase starts and ends earlier at lower frequencies. Figure 4.28 shows the simulated velocity and force profile at default parameter settings for a driving frequency of 2000 Hz and 667 Hz[17]. The scales of the $X$ and $Y$ axes of these figures are adjusted in order to allow for an easy comparison of both graphs. The slope of the velocity — which corresponds to the acceleration — during the acceleration phase depends on the contact force and the friction coefficients, which are the same for both graphs. However, it is due to the adjustment of the scales that the velocity slope on the 667 Hz graph appears higher than on the 2000 Hz graph. This apparently higher velocity slope causes the acceleration phase (delimited by the gray patch in figure 4.28) to start and end earlier on the 667 Hz graph than on the 2000 Hz graph. One can intuitively expect that the highest average velocity is obtained when the maximum of the contact force is well aligned with the middle of the acceleration phase. This explains why there is a shift in optimal phase shift when the driving frequency decreases. Moreover, as shown in figure 4.27, at low driving frequencies the force ratio becomes close to 1 and the slip generation becomes critical. Therefore, it becomes more and more important at decreasing frequency to synchronize the moment of the lowest contact force (maximum negative perpendicular acceleration) with the moment of maximum axial acceleration, which corresponds to a phase shift of 0° or 180°.

Figure 4.29 shows the measured optimal motion velocity and the optimal phase shift at which this velocity occurs as in figure 4.26, but for frequencies up to 6500 Hz. Below 2000

[17]The frequency of 667 Hz was chosen because the shift of the acceleration phase is well visible at this frequency and the period corresponding to this frequency allows for convenient values on the $X$ scale.

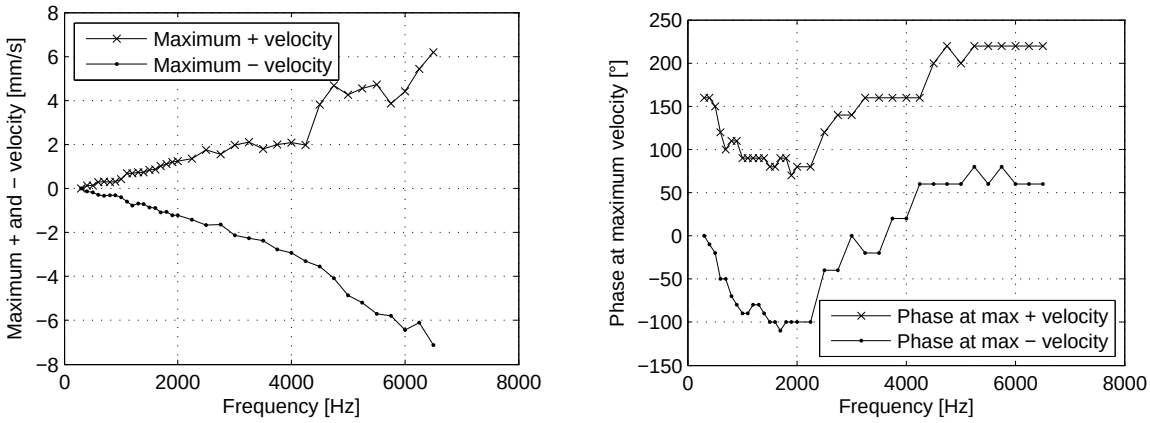


**(a)** Maximum velocity

**(b)** Phase at maximum velocity

**Figure 4.29:** Measured optimal velocity and optimal phase shift in function of the driving frequency

Hz there is a good symmetry between motion in positive and negative direction. Above 2000 Hz, the velocity keeps on increasing with increasing frequency but the linearity and the symmetry gets worse. Moreover, figure 4.29(b) also shows that for frequencies above 2000 Hz the optimal phase shift tends to increase again. A possible explanation for this would be that the shaft starts bouncing on the feet, which has proven to cause a phase shift as observed in the *optimal phase vs. perpendicular acceleration* profile shown in figure 4.23 on page 105. The first resonance frequency of the steel shaft of 9040 Hz should, however, not yet be excited by frequencies of 6500 Hz and below. But it could be the higher harmonics of this frequency resulting from the hysteresis of the stack piezos that excite this resonance frequency.

As mentioned in section 4.3.2 on page 94 the values for the dynamic friction coefficient $\mu_d$, the viscous friction coefficient $\sigma_2$ and the Stribeck velocity $v_s$ are determined by fitting the simulation results on the experimental results. Figure 4.30 shows the influence of these three friction parameters on the *velocity vs. frequency* profile at default parameter settings. For each friction parameter the simulated velocity profile is plotted for the fitted[18] value and one value above and one below that fitted value. As mentioned in section 4.3.2 the ratio $\sigma_1/\sigma_2$ is always close to 10. The identified value of $\sigma_2 = 0.1$ Ns/m yields a value of $\sigma_1 = 1$ Ns/m for the viscous damping coefficient.

### 4.4.6 Influence of the inclination

An easy way to characterize the behavior of the MFID actuator under an external axial force is by inclining the whole measurement setup. Figure 4.31(a) shows the measured and simulated influence of the inclination angle ($\alpha = 0°, 0.5°, 1°, 1.5°$) on the *velocity vs. phase* profile. An inclination angle of $\alpha = 1.5°$ corresponds to a external axial force[19] of $F_{x,ext} = M_r g \sin(\alpha) = 0.33$ mN. As expected, with increasing inclination angle the uphill motion velocity decreases while the downhill motion velocity increases. The graph also shows that the optimal phase shift remains at around 80° and 260°. In fact, an increasing inclination appears to shift the

[18] During the fit a more important weight is given to the frequency range around the default driving frequency of 2000 Hz, because most of the experiments are carried out at that frequency.

[19] An inclination of the axis of the shaft does not only result in an external axial force, but also lowers the perpendicular preload on the shaft due to gravitation by a factor $\cos(\alpha)$. This effect is included in the dynamic model, but has practically no influence for low inclination angles of some degrees.

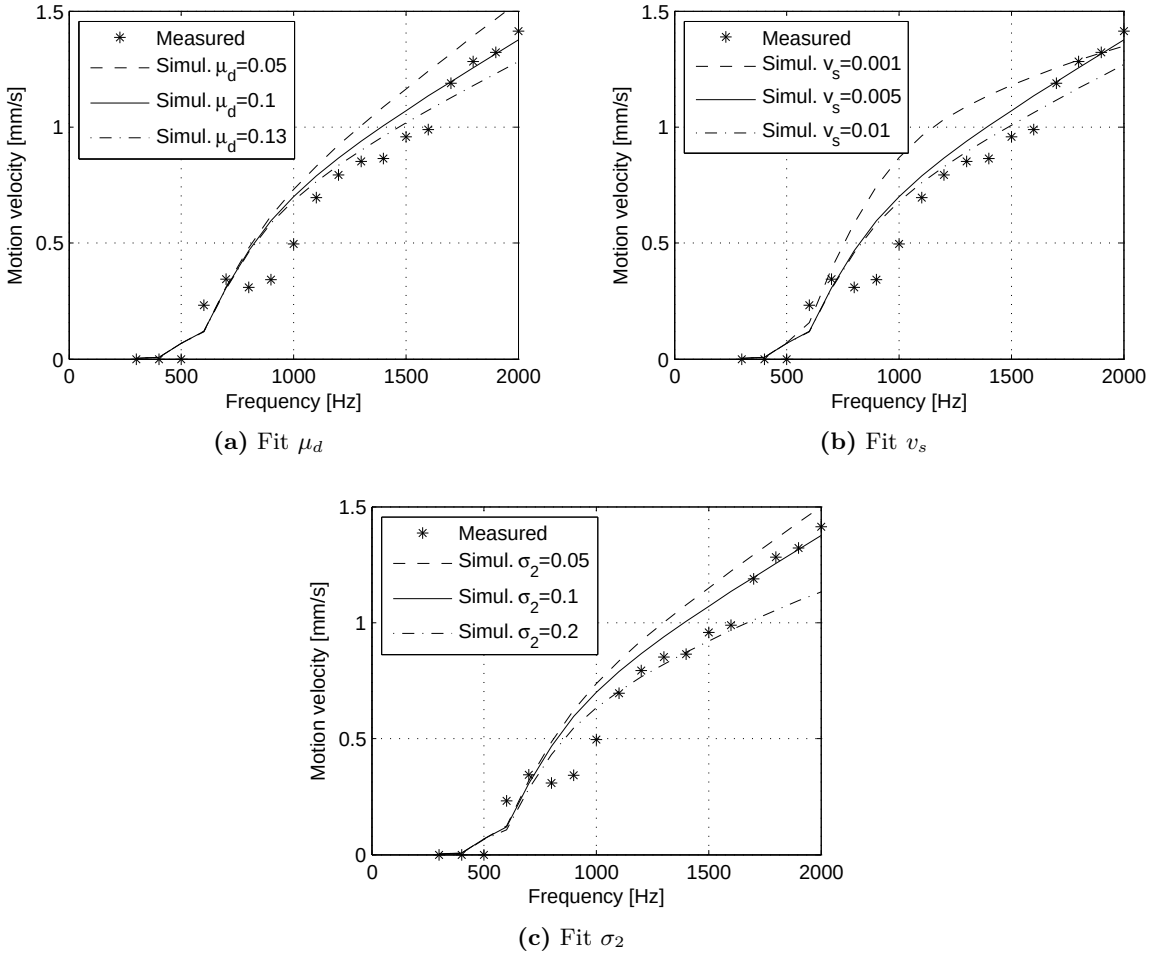


**(a)** Fit $\mu_d$

**(b)** Fit $v_s$

**(c)** Fit $\sigma_2$

**Figure 4.30:** Influence of the friction parameters $\mu_d$, $\sigma_2$, and $v_s$ on the *velocity vs. frequency* profile

complete phase-velocity curve downwards (i.e. in the direction of negative velocity). While for the uphill motion the simulation results seem to fit quite well the measured results, for the downhill motion the simulation results feature a slower velocity increase for increasing inclination than the experimental data. This saturation of the maximum simulated motion velocity was already observed in the *velocity vs. perpendicular acceleration* profile of figure 4.23 on page 105 and is due to the particular shape of the velocity profile of the axial vibration (as discussed in section 4.4.3). However, from the fact that this saturation of the maximum velocity is not present in the measured data could be concluded that the fitted shape of the axial vibration does not correspond to the real vibration shape during locomotion. As discussed in section 4.3.2, it is difficult to know the real vibration shape of the feet as the experimental setup does not allow to measure their displacement during MFID locomotion.

The maximum inclination angle at which uphill locomotion was still possible is $\alpha = 4°$ (see figure 4.31(b)). An inclination of 4° corresponds to an axial load of $M_r g \sin(\alpha) = 0.89$ mN. The dynamic friction force at this angle is equal to $M_r g \cos(\alpha) c_g \mu_d = 1.55$ mN. The generated thrust force is $0.89/1.55 = 57\%$ of this dynamic friction force.

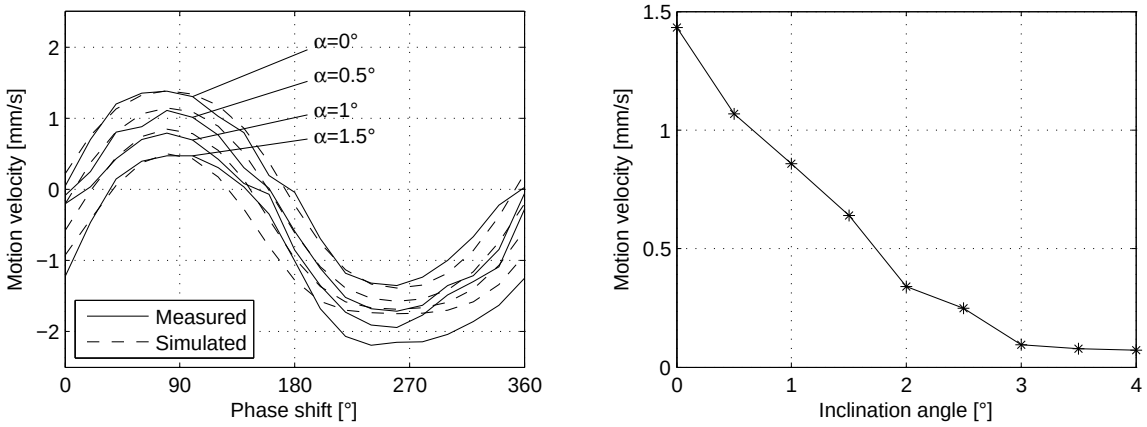


**(a)** Influence on the *velocity vs. phase shift* profile

**(b)** Influence on the uphill velocity at $\phi = 90°$

**Figure 4.31:** Influence of the inclination angle on the motion velocity

### 4.4.7 Influence of the preload

Figure 4.32 shows the influence of the preload on the *velocity vs. perpendicular acceleration* profile at default parameter settings. The perpendicular acceleration and the preload are expressed as a factor of $g$ and these values are to be multiplied with the weight of the shaft $M_r g$ in order to obtain the variation of the contact force and the preload as a real force value. The preload value corresponds to the sum of the weight of the shaft and the additional magnetic preload. Hence, a value of $1g$ corresponds to the case with only a gravitational preload and no additional preload. For every combination of parameter settings five velocity measurements were performed and the error bars on the graph indicate the standard deviation. As already mentioned in section 4.3.2 a remanent magnetization of the shaft has been observed for air gaps of some mm. Therefore, at every change of the magnetic preload the shaft is demagnetized an AC demagnetizer ($E^{ts}$ Braillon & $C^{ie}$, France, Type 180).

The graph shows that for increasing preload there is an increasing threshold value of the perpendicular acceleration below which the shaft does not move at all. For every preload value there is also an increasing second threshold above which the motion becomes unstable and a noise caused by the shaft that is bouncing on the feet can be heard. Above this second threshold value the velocity typically decreases and/or repeatability of the velocity is considerably worse[20]. In order to simplify the graph, the velocity measurements have only been plotted up to the second threshold value. Between these two thresholds the velocity increases more or less linearly with increasing perpendicular acceleration.

Figure 4.33 shows the measured and simulated *velocity vs. phase* profile at a preload of $9.02g$. A comparison of the measured profile with the *velocity vs. phase* profile without any additional preload (see figure 4.19 on page 100) tells that apparently at high preloads the maximum velocity is reached at around 120° and 300° instead of 80° and 260°. In fact this increase in optimal phase shift for increasing preload is similar to the increase in optimal phase shift for decreasing driving frequency observed in figure 4.26(b) on page 109. The explanation for this effect at increasing preload is also similar to the one at decreasing driving frequency. The increasing preload results in an increased friction force and therefore in an increased acceleration and deceleration. Similarly as illustrated by the simulation in figure 4.28, the

[20]This second threshold value is also clearly present in figure 4.23 on page 105.

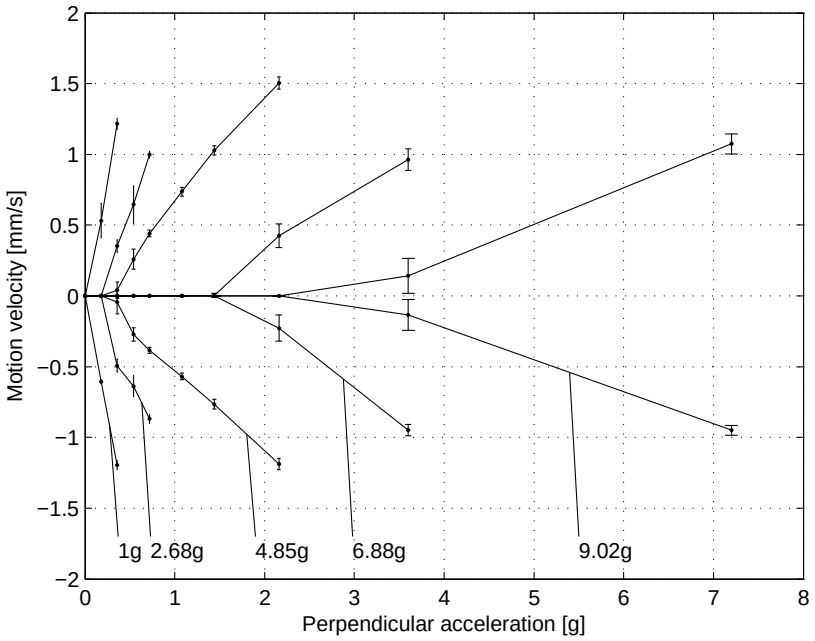


**Figure 4.32:** Influence of the preload on the velocity vs. perpendicular acceleration behavior. Both preload and perpendicular acceleration are expressed in function of the acceleration of gravity $g$.

increased acceleration results in an increased velocity slope during the acceleration phase (and an increased negative velocity slop during the deceleration phase). This increased slope causes the acceleration phase to start earlier and end earlier. As the moment of maximum contact force should be well aligned with the middle of the acceleration phase the optimal phase shift will be shifted.

Figure 4.33 also shows that the simulated *velocity vs. phase* profile with the default setting for the viscous friction coefficient of $\sigma_2 = 0.1$ Ns/m results in a motion velocity that is significantly higher than the measured velocity. Adapting the value for the viscous friction coefficient to $\sigma_2 = 3$ Ns/m, however, results in a fairly good fit. Apparently, a possible explanation for this mismatch could be that the viscous friction coefficient is not independent of the contact force as supposed in the simulation model. An other explanation could be based on a hysteresis introduced by the magnetization of the shaft. As mentioned before, a small remanent magnetization was observed in the shaft after each experiment. As visible in the drawing of the experimental setup shown in figure 4.4 on page 83 the magnetic flux lines in the shaft do not have the same direction at every point in the shaft. Hence, during back and forth motion the magnetization of the shaft is continuously changed. The required energy for this continuous magnetization could cause a hysteresis on the motion velocity, resulting in lower motion velocities than expected by simulation.

Figure 4.34 shows the influence of the inclination on the velocity at a preload of $9.02g$. For every inclination the up-hill velocity has been measured ten times and the average as well as the standard deviation has been plotted on figure 4.34. The experiment was carried out with a phase shift of $\phi = 120°$ at which the maximum experimental velocity is obtained according to figure 4.33. The graph also shows the axial thrust force, which corresponds to the weight of the shaft projected on the axis of the actuator $F_{x,ext} = M_r g \sin(\alpha)$. The graph shows a motion velocity that depends more or less linearly of the inclination. The maximum inclination that still allowed to move uphill is 35°, which corresponds to a maximum thrust

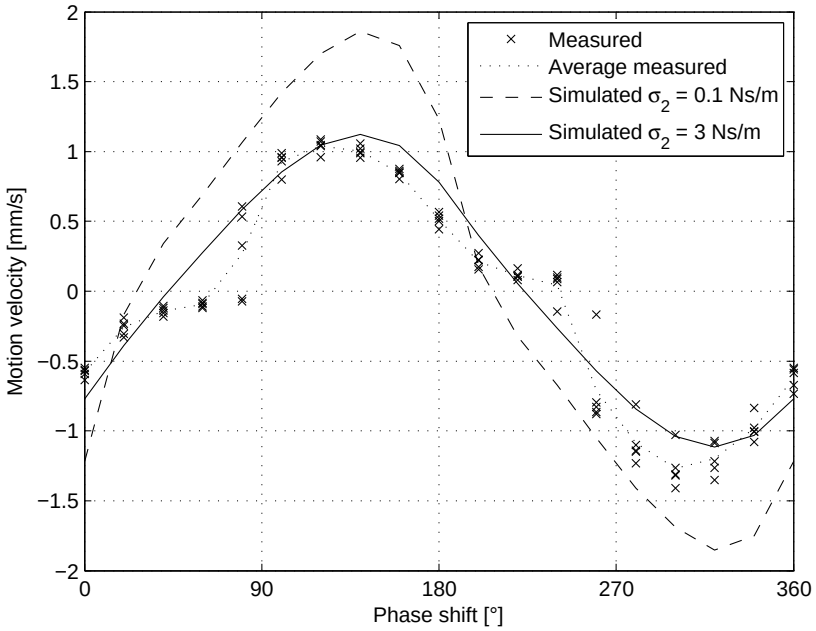


**Figure 4.33:** Influence of the phase shift on the velocity at a preload of $9.02g$ and a perpendicular acceleration of $A_Z = 7.2g$

force of 7.4 mN. However, for inclinations above 20° the dispersion of measured velocity increases considerably.

The experiment shown in figure 4.34 is carried out at a constant air gap between the shaft and the preloading magnets. This means that the preload force is varying in function of the inclination. The contribution of the magnetic force to the preload force does not change with inclination as the gap remains constant. However, the preload due to the weight of the shaft decreases with increasing inclination. Hence the total preload force can be expressed as $F_p = (8.02 + \cos(\alpha))M_r g$. At an inclination angle of $\alpha = 35.3°$ the total preload force corresponds to $F_p = 8.84 M_r g = 113$ mN. The maximum dynamic friction force is thus $\mu_d F_c = \mu_d F_p c_g = 13.8$ mN. The maximum measured thrust force is about $7.4/13.8 = 54\%$ of this value.

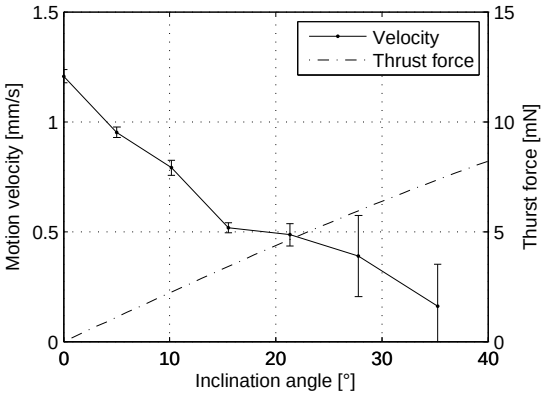


**Figure 4.34:** Influence of the inclination angle on the velocity at a preload of $9.02g$, a perpendicular acceleration of $A_Z = 7.2g$ and a phase shift of $\phi = 120°$

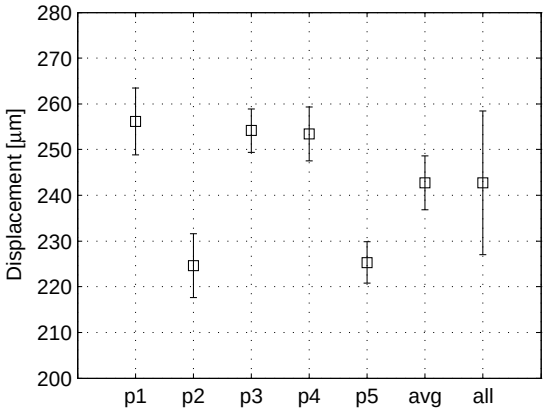


**Figure 4.35:** Average motion distance and standard deviation for 500 locomotion steps at five different positions (p1,p2,p3,p4,p5) of the shaft, based on 50 measurements at every position. The graph also shows the average standard deviation ('avg') and the overall standard deviation over all the measurements ('all')

### 4.4.8 Open loop repeatability and motion resolution

In order to be able to measure the open loop repeatability of the MFID actuator, several experiments consisting of measuring the distance $\Delta x$ traveled after a determined number of locomotion steps (i.e. actuation periods) have been carried out. Figure 4.35 shows the average motion distance $\mu_{\Delta x_i}$ after 500 locomotion steps. The experiment has been repeated 50 times and the standard deviation $\sigma_{\Delta x_i}$ (with $i = 1 \cdots 50$) is calculated. The error bars in the graph delimit the confidence interval $[\mu_{\Delta x_i} - \sigma_{\Delta x_i}, \mu_{\Delta x_i} + \sigma_{\Delta x_i}]$, which covers 68.3% of all measurements. This experiment has been repeated at 5 different positions $p_j$ ($j = 1 \cdots 5$) on the shaft. The graph also shows an average motion distance over all 50 measurements at all 5 positions of $\overline{(\mu_{\Delta x_i})}_{p_j} = 242.7$ $\mu$m. The graph also shows that at each position $p_j$ the standard deviation is relatively small (average $\overline{(\sigma_{\Delta x_i})}_{p_j} = 5.89$ $\mu$m). However, a considerable dispersion is observed between average motion distance $\mu_{\Delta x_i}$ at the different positions $p_j$, resulting in a much larger overall standard deviation (all 50 measurements at all 5 positions) $\sigma_{\Delta x_{i,p_j}} = 15.7$ $\mu$m. Hence, it can be concluded that in general a relative standard deviation of $15.7/242.7 = 6.5\%$ should be taken into account, while for displacements that are repeated at the same position on the shaft the standard deviation is reduced to $5.89/242.7 = 2.42\%$.

In order to judge the capability of the MFID principle to perform high resolution motion, one must study the smallest increment that can be performed in a repeatable way. Figure 4.36 shows the measured displacement after 10, 5, 2 and 1 locomotion steps for four different values of the axial vibration amplitude. Every measurement has been repeated 50 times and the error bars in the graph delimit the $1\sigma$ confidence interval. Each step measurement is performed at a random position on the shaft (within a range of 400 $\mu$m). The graph shows clearly a good linear behavior between the motion distance and the number of locomotion steps as well as a low dispersion. The smallest increment of 38 nm with a standard deviation of 5 nm (13% of increment) is achieved with one locomotion step and an axial vibration amplitude of $X = 22.7$ $\text{nm}_{amp}$ (45.4 $\text{nm}_{p2p}$). These results show that the MFID principle is easily capable of performing sub-micrometer resolution steps. Moreover, the experimental setup also allows for scanning motion, which allows for real nanometric resolution by varying the voltage of the shear mode piezos quasi-statically.

Another point that is important for high precision applications is the smoothness of the motion. Figure 4.37 shows that without any additional preload (only gravity) the motion

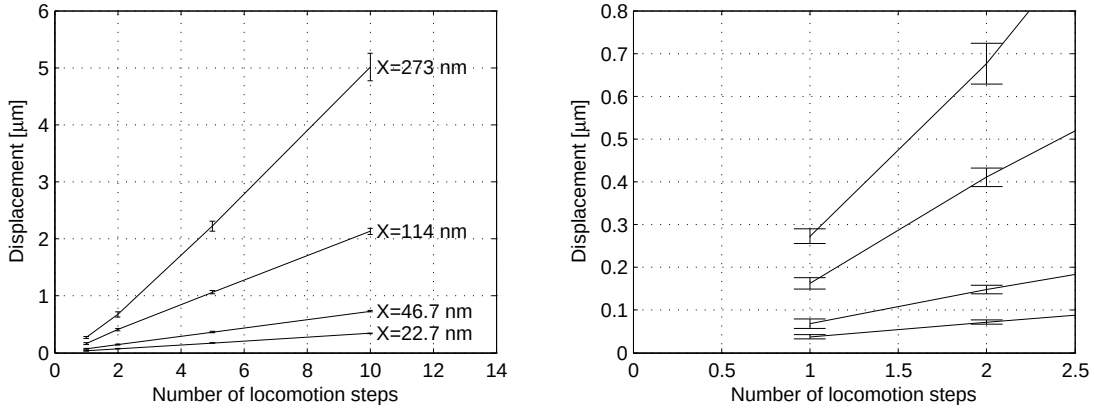


**(a)** Overview **(b)** Close up

**Figure 4.36:** Motion distance in function of the number of locomotion steps for four different values of the axial amplitude $X$

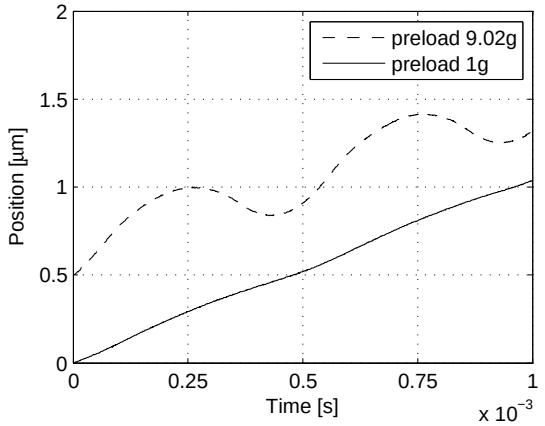


**Figure 4.37:** Measured motion profile at low ($1g$) and high ($9.02g$) preload ($A_{Z,1g} = 0.35g$, $A_{Z,9.02g} = 7.2g$, $\phi_{1g} = 90°$, $\phi_{9.02g} = 140°$)

profile is quite smooth, only a small undulation can be observed. However, at higher preloads (here at a gravity factor of $9.02g$) a considerable undulation including a backward motion in every locomotion step is present. This is because of the fact that the higher preload and the required higher perpendicular vibration amplitude result in higher maximum and minimum friction force. The higher friction forces result in an increase of the slopes of the acceleration and the deceleration phase of the stepping motion (similar as in figure 4.28 on page 110), which causes the velocity to become negative at the end of every deceleration phase. This undulation on the velocity profile could, in certain cases, limit the suitability of the MFID principle for precision applications. Apart from this axial superposed undulation, also the perpendicular vibration could be an issue for certain applications. However, at higher frequencies, the perpendicular vibration amplitude is in the sub-micrometric range (for instance at $f = 2000$ Hz and $A_Z = 0.35g$ the perpendicular vibration amplitude is only $Z = 21.6$ nm. Moreover, if this perpendicular vibration would be an issue it can be avoided by generating the contact force variation through the vibration of an extra inertial mass instead of through the vibration of the contact feet (see section 3.5).

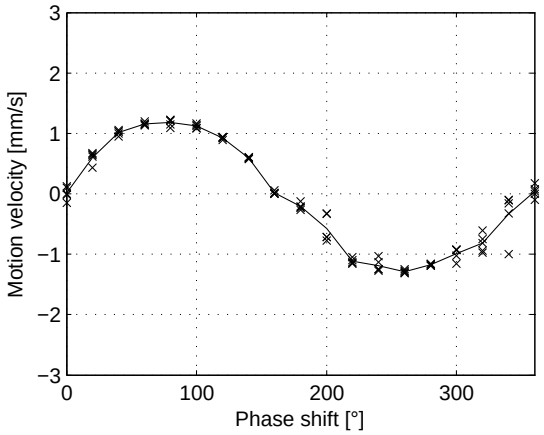


**Figure 4.38:** Influence of the phase shift on the velocity for the inertial inchworm principle

### 4.4.9 Comparison with Inertial Inchworm and Stick-Slip principle

One of the interesting aspects of the developed measurement setup is that it can be used not only for characterization of the MFID principle, but also for the inertial inchworm and the stick-slip drive principle. As explained in section 2.5.4 the inertial inchworm principle is also based on a variation of the contact force by the inertial effect of a vibration that is perpendicular to the actuator axis, as in one of the possible configurations of the MFID principle. However, the difference is that for the inertial inchworm principle the slip generation is not based on a dynamic effect (i.e. the axial vibration of the feet with respect to the body of the slider) as in the MFID principle, but rather on a quasistatic effect (i.e. the differential displacement of the feet with respect to each other). Hence, the inertial inchworm principle does not require a minimum amount of axial acceleration for successful slip generation as the MFID principle. Therefore, the inertial inchworm principle allows for operation at lower frequencies than the MFID principle. However, as the variation of the contact force is based on the inertial effect of a perpendicular vibration, a lower limit to the driving frequency is still present. It should also be noted that at higher frequency operation, the slip generation will in fact be based on a combination of the differential motion of the feet and the inertial effect of the high frequency axial vibration.

For the stick-slip principle the slip generation is also based on the dynamic effect of an axial vibration of the feet with respect to the body of the rotor. However, the net motion after each stepping cycle does not result from the synchronized variation of the friction force, but rather from the asymmetric nature of the axial vibration. A typical signal shape for the axial vibration is the saw tooth signal, which is used in the experiments presented in this chapter.

As shown in figure 4.38 the *velocity vs. phase shift* behavior of the inertial inchworm principle is very similar to that of the MFID principle (see figure 4.19 on page 100). The inertial inchworm principle also reacts in a similar way as the MFID principle to a variation of the perpendicular acceleration amplitude as shown in figure 4.39 (same graph for the MFID principle in figure 4.23 on page 105). The measured *velocity vs. phase shift* profile for each of the values of the vertical acceleration can be found in appendix D. For low accelerations up to $A_Z = 0.35g$ the velocity varies more or less linear with the acceleration amplitude and the dispersion is low. Once passed this first perpendicular acceleration amplitude threshold, the velocity stops increasing and the dispersion becomes important. However, once passed a second perpendicular acceleration amplitude threshold around $A_Z = 1g$ the motion tends to

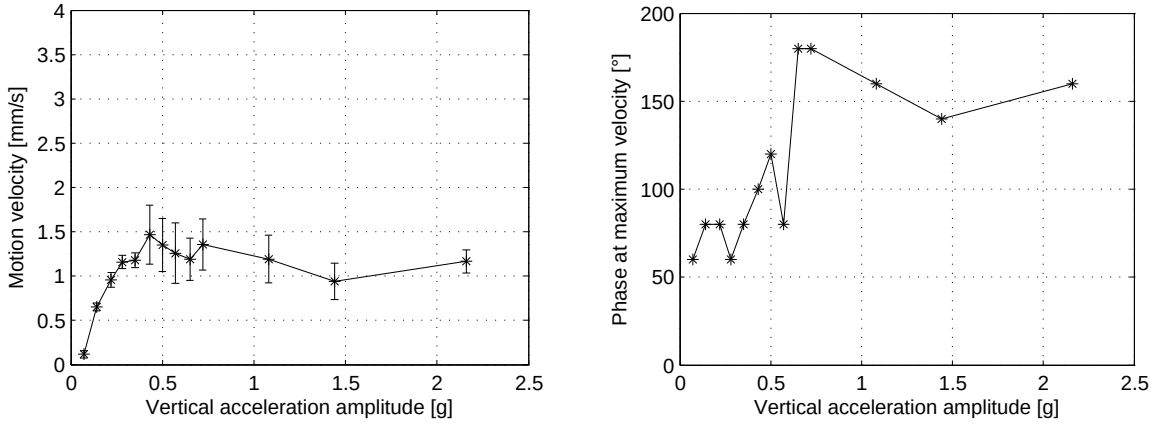


**(a)** Maximum velocity

**(b)** Phase at maximum velocity

**Figure 4.39:** Influence of the perpendicular acceleration on maximum velocity for the inertial inchworm principle

become more stable and the dispersion decreases. As for the MFID principle, for perpendicular acceleration amplitudes below the first threshold the maximum velocity is reached for a phase shift around $\phi = 80°$, while for perpendicular acceleration amplitudes above the second threshold the maximum velocity is reached for a phase shift around $\phi = 160°$. One difference between the inertial inchworm and the MFID principle that is clearly visible when comparing the two graphs in figures 4.39 and 4.23 is that the inertial inchworm principle features lower velocities in the transition zone from $A_Z = 0.35g$ to $A_Z = 1g$, but also a much lower dispersion. In section 4.4.3 it was discussed that this high dispersion is probably due to the parasitic perpendicular acceleration resulting from the hysteresis of the stack piezos, which starts to cause uncontrolled bouncing of the shaft. As in the inertial inchworm principle the moment of minimum contact force on the one end (i.e. the moment when the uncontrolled bouncing occurs) corresponds to the moment of maximum contact force on the other end, it is logical to assume that the bouncing has less negative influence on the motion stability.

Figure 4.40 shows a comparison of the measured *velocity vs. frequency* behavior for the MFID, the inertial inchworm and the stick-slip principle. For all three locomotion principles the linearity of the velocity detoriates for frequencies above 3000 Hz. The best linearity is obtained for the stick-slip drive principle. Although not shown in this graph, it should be noted that the stick-slip principle is the only drive principle of the three discussed here that has not lower limit for the driving frequency. As the acceleration generated by the edge of the saw tooth signal is not dependent on the driving frequency, even at very low frequencies, slip will be generated. Because of this reason, together with the good linearity, the frequency is the best parameter for controlling the velocity of a stick-slip actuator. The inertial inchworm principle shows a good linearity and symmetry (better than the MFID principle) between 1250 Hz and 3000 Hz.

Figure 4.41 shows a comparison of the influence of the inclination on the uphill motion velocity with only gravitational preload for the MFID, inertial inchworm and the stick-slip principle. The behavior seems to be fairly similar between the three different locomotion principles. Especially, the MFID and the inchworm principle show a very close match and they appear to be able to deal with slightly higher inclinations than the stick-slip principle.

Figure 4.42 shows the influence of the inclination angle on the uphill motion velocity at a high preload of $9.02g$ for the MFID, the inertial inchworm and the stick-slip principle.

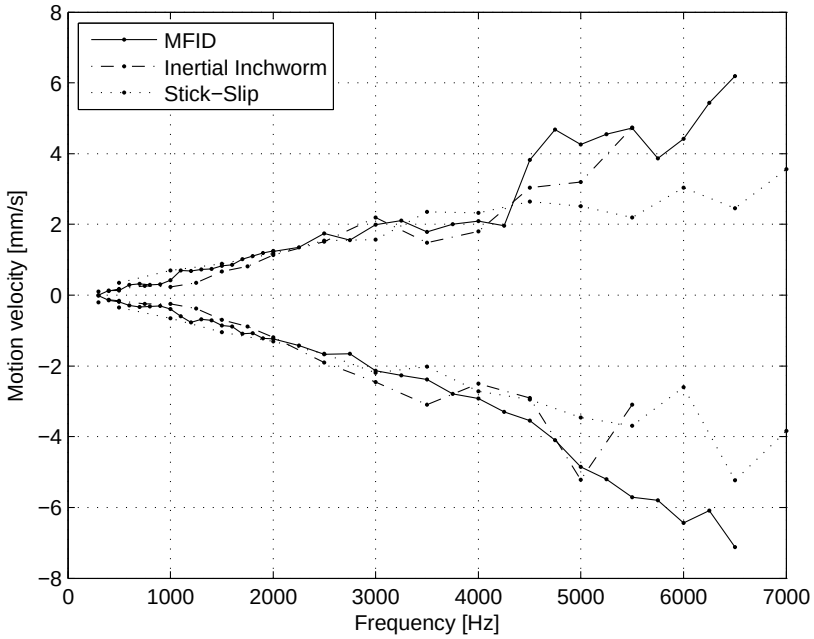


**Figure 4.40:** Comparison of maximum motion velocity in positive and negative direction in function of the frequency for the MFID, inertial inchworm and stick-slip drive principle

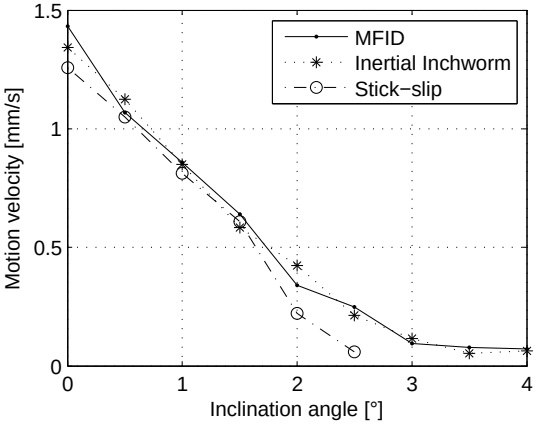


**Figure 4.41:** Comparison of the influence of the inclination angle on the velocity for the MFID, the inertial inchworm and the stick-slip driving principle

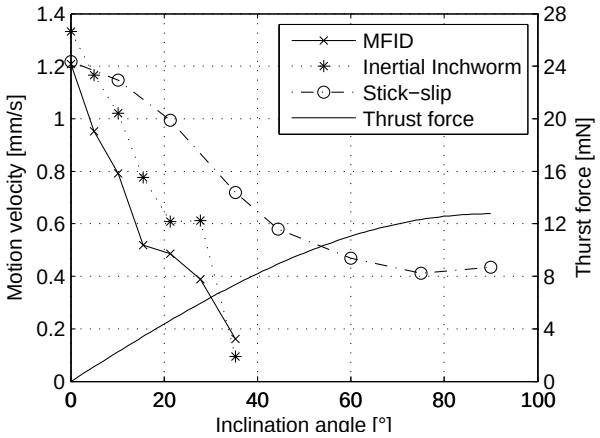


**Figure 4.42:** Influence of the inclination angle on the velocity for the MFID ($\phi = 140°$), the inertial inchworm ($\phi = 120°$) and the stick-slip driving principle at a preload of $9.02g$ and a perpendicular acceleration of $A_Z = 7.2g$

The graph also shows the generated thrust force in function of the inclination angle, which corresponds to the weight of the shaft (12.8 mN) projected on the actuator axis. The graph shows that only the stick-slip principle is capable of vertical upward motion ($\alpha = 90°$), while maintaining a motion velocity that is about 1/3 of the velocity without inclination. The MFID and the inertial inchworm principle are both limited to a inclination angle of $\alpha = 35°$. However, at such a high preload the inertial inchworm principle shows a small advantage in terms of motion velocity compared to the MFID principle. As mentioned before in this section the slip generation in the inertial inchworm principle is based on a combination of the differential axial displacement between the feet and the dynamic effect of the axial vibration, while the MFID principle is only based on the dynamic effect of the axial vibration. At a driving frequency of $f = 2000$ Hz and a axial vibration amplitude of $X = 270$ nm the generated axial acceleration is $A_X = X(2\pi f)^2 = 42.6$ m/s$^2$. At default parameter settings (preload of $1g$) the force ratio is $q_F = 36.6$, which is much larger than 1. Hence, at gravity preload the dynamic effect of the axial vibration is more than sufficient to overcome the friction force, which explains the small difference observed between the MFID and the inertial inchworm principle in figure 4.41. However at a preload of $9.02g$ the force ratio is 9.02 times smaller (i.e. $q_F = 4.1$), which becomes relatively close to 1. Consequently, at higher preloads the contribution of the differential displacement between the contact feet in the inertial inchworm principle becomes more and more important, which explains the higher velocities for the inertial inchworm principle in figure 4.42.

Figure 4.43 shows a comparison of the repeatability at gravity preload between the MFID, the inertial inchworm and the stick-slip driving principle. As in section 4.4.8 the experiments have been conducted by measuring 50 times the displacement after 500 locomotion steps. All measurements were taken at more or less the same position of the shaft. The graph shows the average displacement distance as well as the relative standard deviation. The standard deviation of the MFID principle seems to be the highest, while the inertial inchworm principle seems to feature a repeatability that is slightly better than the stick-slip principle.

Figure 4.44 finally shows a comparison of the motion profile at low and high preload for the MFID, the inertial inchworm and the stick-slip principle. The graph on the left-hand side shows that at gravity preload a small undulation is visible on the MFID motion profile, while the motion profile of the inertial inchworm and the stick-slip principle seem to be completely flat. However, as shown on the graph on the right-hand side, at high preload ($9.02g$) an

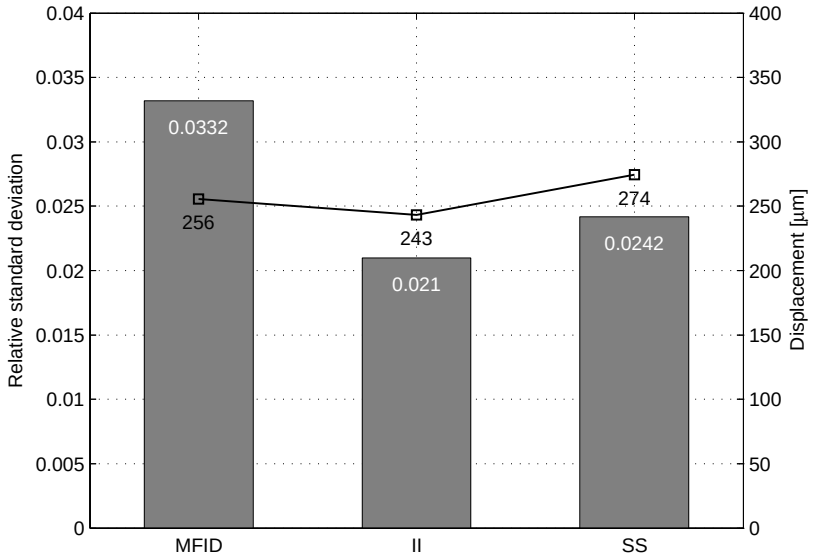


**Figure 4.43:** Comparison of the repeatability of the MFID, the inertial inchworm (II) and the stick-slip (SS) driving principle

important undulation is present in the MFID motion profile, resulting in a considerable backlash at every step. The inertial inchworm principle also shows an undulation, but much lower than MFID principle, while only a very small undulation is visible on the stick-slip motion profile.

## 4.5 Conclusion

The objective of this chapter was to get a thorough understanding of the MFID stepping motion by means of simulation and experimental measurements for the case of a linear MFID actuator.

A dynamic model of the MFID actuator based on the LuGre friction model has been developed. Such a friction model takes into account the tangential compliance of the guiding contacts, which is important in the case of vibration amplitudes in the nanometric region.

In order to be able to validate the dynamic model, an experimental setup of a linear MFID actuator has been developed. Piezoelectric actuators have been selected for the actuation of both the axial and the perpendicular vibration as they meet well the design constraint of a driving frequency of some hundreds of Hz up to several kHz. The frequency range results in a ratio between minimum and maximum vibration amplitude of more than 1 to 400. Moreover, their high resolution allows to test the suitability of the MFID principle for high precision applications. It has proven not to be an easy task to identify the different parameters of the friction model. Also the hysteresis of the piezoelectric actuators has a non-negligible influence as the introduced higher harmonics become important in the velocity and acceleration profile of the generated vibration.

In general there is a good match between measured and simulated results. The simulated stepping motion as well as the influence of phase shift, vibration amplitudes and driving frequencies is close to the experimental one. A saturation occurs in the simulated downhill motion, which is not present in the experimental data. This deviation is believed to be caused by a deviation between measured and real shape of the axial vibration. Deviations between simulated and experimental data also occur in the case of an increased magnetic preload,

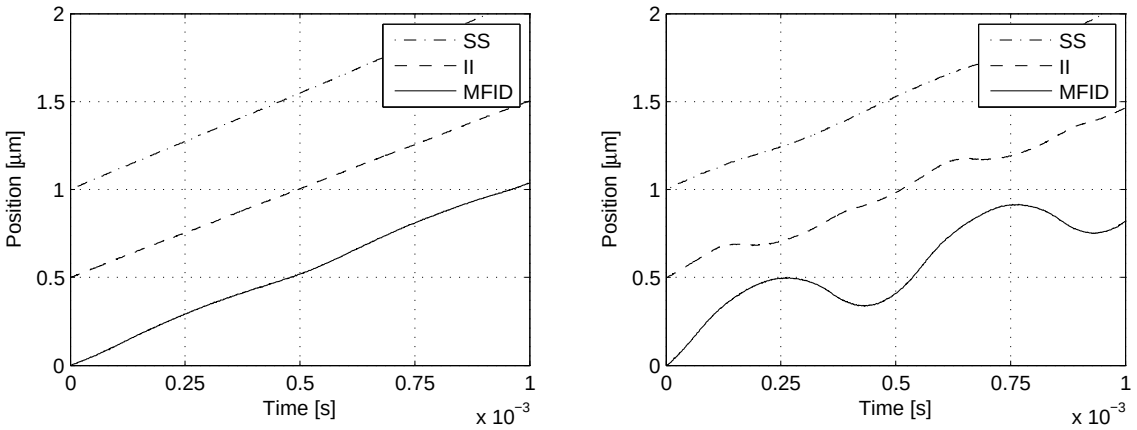


**(a)** Preload $1g$, $A_Z = 0.35g$, $\phi = 90°$

**(b)** Preload $9.02g$, $A_Z = 7.2g$, $\phi_{MFID} = 140°$, $\phi_{II} = 120°$

**Figure 4.44:** Comparison of the measured motion profile at low and high preload for the MFID, the stick-slip (SS) and the inertial inchworm (II) principle

which is believed to be caused either by a dependence of the viscous friction coefficient $\sigma_2$ from the contact force either by hysteresis introduced by the continuous magnetization of the shaft.

The simulated and measured MFID stepping motion consist of an acceleration and a deceleration phase. This causes an undulation of the motion velocity, resulting in a large backlash during each step at low variation amplitude of the contact force, but an almost completely smooth motion at higher contact force variation.

The motion velocity shows a nearly sinusoidal dependence of the phase shift between axial and perpendicular vibration, with a maximum velocity in positive and negative direction around 90° and 270°.

The motion velocity increases with an increasing perpendicular acceleration amplitude. In order to quantify the efficiency with which the axial vibration is transformed into motion velocity the step efficiency $\eta_{step}$ is introduced. The step efficiency increases linearly with increasing perpendicular acceleration and reaches almost $\eta_{step} = 0.4$ at optimal parameter settings ($A_Z = 0.35g$). Above this optimal perpendicular acceleration hopping motion of the shaft already starts to occur, which lowers the stability of the motion. This hopping at accelerations below $1g$ is caused by harmonics in the vibration of the piezoelectric actuators resulting from their hysteresis and partially amplified by the resonance of the shaft.

The axial vibration amplitude appears to be the most interesting parameter to use for velocity control of the MFID actuator as the velocity decreases with good linearity with decreasing axial vibration amplitude. At low axial vibration amplitudes the slip generation becomes critical as the generated axial inertial force is not large enough to overcome the friction force. In order to quantify this effect the force ratio $q_F$ is introduced as the ratio between the maximum instantaneous inertial force generated by the axial vibration and the minimum instantaneous friction force. One of the necessary conditions for MFID locomotion is that $q_F > 1$. Motion stability increases with increasing values of the force ratio. The force ratio can be calculated easily without any simulation or locomotion experiment and is therefore an interesting indicator to be used during the design process of an MFID actuator.

There is a lower limit to the driving frequency below which insufficient inertial force is generated for causing slip, corresponding to a force ratio $q_F$ below 1. For this experimental

setup $q_F$ becomes equal to 1 for a frequency of about 350 Hz, which matches the measured velocity behavior. Above this frequency the velocity increases more or less linearly to about 1.4 mm/s at 2000 Hz. A good symmetry between motion velocity in positive direction and in negative direction is observed up to 2000 Hz. Above this frequency the velocity keeps on increasing up to a velocity of about 6 mm/s at 6500 Hz, but linearity and symmetry get worse. While at 2000 Hz the optimal phase shift is around $\phi = 90°$, for lower frequencies the optimal phase shift tends to increase up to $\phi = 160°$. This shift in optimal phase shift is due to the fact that the acceleration phase starts and ends earlier at lower frequencies, which requires the maximum contact force to occur earlier as well.

The application of an external axial load (inclination of the setup) does not change the optimal phase shift at which maximum velocity is reached. The uphill motion velocity decreases more or less linearly with increasing inclination (thrust force) up to a maximum inclination of $\alpha = 4°$, corresponding to a thrust force that is 57% of the dynamic friction force. An increase of the preload force increases the maximum surmountable inclination, but also increases the minimum amount of perpendicular acceleration that is required to make the actuator move. At a preload of $9.02g$, the maximum inclination that can be surmounted by the actuator is $\alpha = 35°$, corresponding to a thrust force of 7.4 mN, which is 54% of the dynamic friction force. The application of an extra preload causes the optimal phase shift to increase from 80° with only gravitational preload ($1g$) to 120° for a total preload corresponding to $9.02g$. As for the driving frequency, this shift in optimal phase shift is due to a shift of the acceleration phase resulting from the increase of the slope of the acceleration phase in the velocity profile.

Concerning the open loop repeatability, in general a relative standard deviation of 6.5% should be taken into account, while for displacements that are repeated at the same position on the shaft the standard deviation is reduced to 2.42%. A very good linearity is observed between the traveled distance and the number of actuation cycles, allowing for repetitive steps of 50 nm and below with relative standard deviations of less than 10%. Moreover, the studied MFID actuator is also capable of quasistatic scanning motion allowing for a resolution in the range of 1 nm. However, in the case of precision applications the undulation of the velocity at low variation amplitudes of the contact force should be taken into account.

The MFID principle has been experimentally compared to the stick-slip and the inertial inchworm principle. The MFID and the inertial inchworm principle show similar velocity behavior in function of the phase shift and the perpendicular acceleration, with a difference of better stability of the motion velocity for the inertial inchworm principle for hopping motion. The *velocity vs. frequency* behavior is similar for the three principles, but the best linearity is clearly obtained with the stick-slip principle. Without any additional preload the uphill motion velocity of the three principles is influenced comparably by the inclination angle. However, at a preload of $9.02g$ the stick-slip principle is the only principle capable of upward vertical motion, while the inertial inchworm has a small advantage compared to the MFID principle. The open loop repeatabilities of the MFID principle ($\sigma = 3.3\%$), the inertial inchworm principle ($\sigma = 2.1\%$) and the stick-slip principle ($\sigma = 2.4\%$) are in the same order of magnitude. The stick-slip principle features the smoothest motion. Especially at a high preload of $9.02g$ the difference in smoothness is important. The inertial inchworm principle features, as expected, a smoother motion than the MFID principle. In conclusion, the stick-slip principle is clearly best suited for precision applications. The inertial inchworm principle features some advantages compared to the MFID principle at high preload, but this goes with the price of an increased complexity, especially for motion with several DOF.

The next chapter will demonstrate clearly the advantages in terms of simplicity and resonance operation of the MFID principle with respect to the stick-slip principle as well as the combination of on-board and off-board actuation.

# Chapter 5

# Prototypes of MFID mobile microrobots

*"God created a number of possibilities*
*in case some of his prototypes failed*
*— that is the meaning of evolution."*
Graham Greene (1904–1991)

In the previous chapter the stepping behavior of the MFID locomotion principle was investigated into detail by simulation and experimental measurements for a linear MFID actuator. In the current chapter the application of the MFID principle for the locomotion of mobile microrobots is illustrated by the discussion of the design and measured performances of three MFID prototypes of mobile microrobots. The linear actuator in the previous chapter was based on a configuration with only off-board actuation. In this chapter the three other configurations are illustrated. Prototype 1 and 3 are based on two different configurations with a combination of on-board and off-board actuation, while prototype 2 is based on a configuration with only on-board actuation. The three prototypes are presented in an sequence with increasing degree of miniaturization and power efficiency. As all the prototypes in this chapter are only operated for motion in horizontal direction, the terminology "horizontal" and "'vertical" will be used instead of "axial" and "perpendicular" for simplification reasons.

The design and performances of each of the prototypes are presented successively in sections 5.1, 5.2 and 5.3. Moreover, in appendix C two other interesting MFID designs are shortly presented. In section 5.4 the performances of the three prototypes are compared with each other and to the state of the art. The gathered knowledge of the MFID locomotion principle is synthesized in a design methodology for new MFID locomotion platforms.

## 5.1 Prototype with on-board contact force variation

The first prototype presented in this chapter is chronologically also the first prototype that was developed in order to test the feasibility of the MFID principle. The robot design and testing was carried by Blaise Fracheboud in the scope of a student project [341]. The chosen configuration is a combination of on-board friction force variation and off-board slip

generation (configuration 3 in table 3.1 on page 73). This configuration yields a robot design that is very simple, which could — although not pursued for this prototype — allow for miniaturization below 1 $cm^3$ with good power efficiency.

The presentation of the first prototype is structured as follows: (5.1.1) discussion of the design of the actuator, (5.1.2) characterization of the motion of the prototype and finally (5.1.3) a discussion on its power consumption.

### 5.1.1 Design

#### Configuration

The first prototype is based on a configuration with on-board contact force variation and off-board slip generation. The contact force is varied through a vertical ($Z$) vibration of an inertial mass on the robot. The slip between robot and substrate is generated externally by vibrating the substrate horizontally in $X$ and $Y$ direction. A phase shift of 90° is maintained between both horizontal vibrations ($X$ and $Y$), resulting in a circular translation of the substrate. In section 4.4.2 it was observed that the motion velocity of an MFID actuator has a quasi sinusoidal dependance of the phase shift between horizontal and vertical actuation. Consequently, the phase shifts of maximum velocity in positive direction, zero velocity, maximum velocity in negative direction and zero velocity lie within 90° of each other. Hence, a phase shift of 90° between the off-board $X$ and $Y$ vibration causes the point of maximum velocity in $X$ direction to coincide with a point of zero velocity in $Y$ direction and vice versa. For instance, a phase shift of 90° between $X$ and $Z$ vibration, resulting in maximum velocity in $X$ direction, corresponds to a phase shift of 0° or 180° between $Y$ and $Z$ vibration, resulting in zero velocity in $Y$ direction. A gradual transition from optimal phase shift for motion in $X$ direction to optimal phase shift for motion in $Y$ direction will gradually move the motion direction from $X$ to $Y$ direction, allowing for motion in any arbitrary direction within the $XY$ plane. This configuration results in a robot with two independent DOF $(X, Y)$ and only one channel of on-board actuation.

Another way to explain the working principle is to consider the circular translation of the substrate. At a certain moment $t$ the substrate has an instantaneous velocity in the $XY$ plane of which the direction $\theta$ is tangential to the circular motion path. A synchronization of the moment of maximum contact force with this moment $t$ will cause the robot to have an average motion in this direction $\theta$. In fact, cylindrical coordinates would be more appropriate than cartesian coordinates to describe the motion of the robot as the motion direction $\theta$ depends on the phase shift $\phi$ between horizontal and vertical vibration, while the motion velocity depends on driving frequency and driving voltages.

#### Experimental setup design

The horizontal $XY$ vibration is generated by a commercially available piezoelectric $XYZ$ stage[1] (Tritor 101, Piezosystem Jena GmbH, see appendix F.1) on top of which a glass substrate of $68 \times 68$ $mm^2$ has been fixed (see figure 5.1). Figure 5.2 shows the measured frequency response of the $XYZ$ stage when actuated in $X$ and $Y$ direction. An increase in vibration amplitude is observed between 100 Hz and 150 Hz. This is due to an excitement of the resonance frequency of the stage. Without any additional mass the stage features resonance frequencies around 400 Hz. However, the addition of the glass substrate and its clamping mechanism lowers this resonance frequency below 300 Hz. This resonance frequency

[1] The $Z$ degree of freedom of the $XYZ$ stage is not used here as the contact force is varied by a $Z$ vibration on the robot.

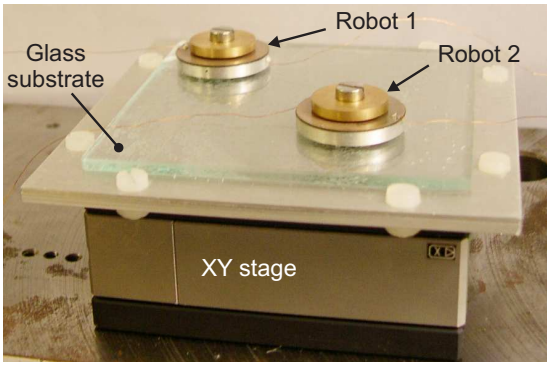


**Figure 5.1:** Experimental setup consisting of a vibrating $XY$ stage with two robots on top

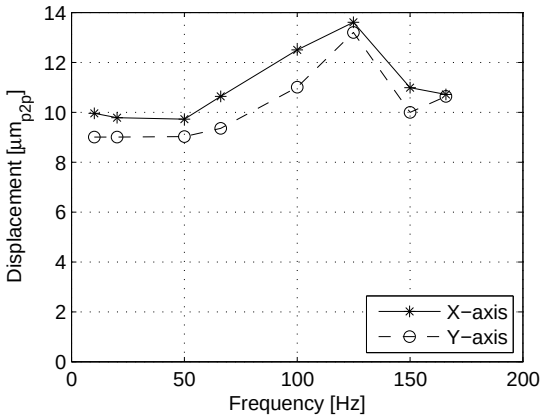


**Figure 5.2:** Displacement of the $XYZ$ stage in $X$ and $Y$ direction in function of the frequency

is excited with signals between 100 Hz and 150 Hz, because the deformation of the sinusoidal input signal resulting from the hysteresis in the piezoelectric actuators adds higher harmonics to the mechanical excitation. It has been experimentally observed that at 147 Hz a relatively clean sinusoidal vibration was obtained.

The robots are sitting on top of the glass substrate that is fixed on the $XYZ$ stage. The robot contains an inertial mass that is vibrated vertically in order to vary the contact force between the robot and the glass substrate. The inertial mass is actuated by a piezoelectric bimorph disk actuator that connects the outer ring of the robot to the vibrating inertial mass (see figure 5.3). The inertial mass consists of two parts that are clamped on the disk actuator by a screw. The piezoelectric disk actuator consists of a sandwich of a 0.1 mm thick steel sheet and a 0.25 mm thick piezoelectric sheet (see appendix F.1). In order to optimize the ratio of inertia (i.e. the ratio between the weight of the inertial mass and the frame) the material selected for the inertial mass is brass ($\rho_{brass} = 8500$ kg/m$^3$), while the frame is made out of aluminum ($\rho_{aluminum} = 2700$ kg/m$^3$). This results in an inertial mass of $M_i = 5.12$ g and a mass of the frame plus the feet that are in contact with the ground of $M_f = 0.98$ g, so a total weight of $M_r = M_f + M_i = 6.10$ g. The ratio of inertia is thus $q_I = M_i/M_f = 5.22$. Three sapphire half spheres serving as robot feet are glued below the outer ring of the robot. The required electrical signal for the on-board piezoelectric actuator is generated by an off-board function generator and high voltage amplifier and supplied to the robot by means of two thin wires (actuation signal and electrical ground).

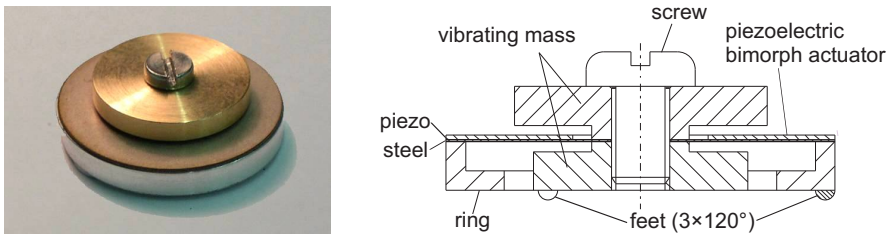


**Figure 5.3:** Robot design (⌀20 mm × 7.5 mm)

Figure 5.4 shows the frequency response of the piezoelectric disk actuator integrated on the robot. At 200 $V_{p2p}$ the actuator shows a static vibration amplitude of about 5 $\mu m_{p2p}$ and a resonance frequency of 800 Hz. The maximum actuation voltage for the piezoelectric actuator is 300 $V_{p2p}$ (i.e. -50 V to +250 V).

### Force ratio

In section 4.4.4 the force ratio $q_F$ has been defined as the ratio between the maximum inertial force $F_{i,X,max}$ generated by the horizontal vibration and the minimum instantaneous static friction force between slider and substrate $F_{t,s,min}$

$$q_F = \frac{F_{i,X,max}}{F_{t,s,min}}. \tag{5.1}$$

One of the conditions for MFID locomotion is that $q_F > 1$.

If the robot (total weight $M_r$) would be sticking on the substrate and follow its vibration $x = X\sin(\omega t)$ an inertial force equal to

$$F_{i,X} = -M_r X\omega^2 \sin(\omega t) \tag{5.2}$$

would have to transmitted by the friction force between robot and substrate.

The contact force $F_c$ between the robot's feet and the substrate, which is expressed by

$$F_c = F_{c,0} + F_{c,amp}\sin(\omega t + \phi). \tag{5.3}$$

For this prototype $F_{c,0} = M_r g$, which corresponds to the total weight of the robot and $F_{c,amp} = M_i Z\omega^2$, which corresponds to the inertial force generated by the vertical vibration of the inertial mass $M_i$ with amplitude $Z$ and pulsation $\omega$. The ratio $M_i/M_r$ can be expressed in function of the ratio of inertia $q_I = M_i/M_f$ with

$$\frac{M_i}{M_r} = \frac{M_i}{M_f + M_i} = \frac{1}{\frac{M_f}{M_i} + 1} = \frac{1}{\frac{1}{q_I} + 1} = \frac{q_I}{1 + q_I}. \tag{5.4}$$

The contact force $F_c$ at the interface between robot and substrate is thus given by

$$F_c = M_r(g + \frac{q_I}{1 + q_I} Z\omega^2 \sin(\omega t + \phi)). \tag{5.5}$$

The amplitude of the sine in the denominator is defined as the equivalent vertical acceleration $A_{Z,eq}$

$$A_{Z,eq} = \frac{q_I}{1 + q_I} Z\omega^2. \tag{5.6}$$

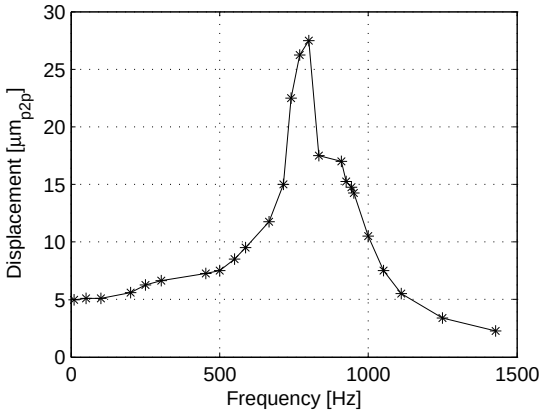


**Figure 5.4:** Displacement of the piezo disk on the locomotion module in function of the frequency at a driving voltage of 200 $V_{p2p}$

The minimum static friction force $F_{t,s,min}$ between robot and substrate at the moment of minimum contact force is now given by

$$F_{t,s,min} = \mu_s F_c = \mu_s M_r (g - A_{Z,eq}). \tag{5.7}$$

The static friction coefficient $\mu_s$ between sapphire and glass has been measured to be $\mu_s = 0.12$ by measuring the inclination of the glass at which the robot starts to slide.

With equations (5.2) and (5.7) the condition $q_F > 1$ becomes

$$q_F = \frac{X\omega^2}{\mu_s(g - A_{Z,eq})} > 1. \tag{5.8}$$

### 5.1.2 Locomotion experiments

Measurements of average locomotion velocity in $X$ direction of the robot have been carried out under a microscope by optical tracking of a target that was fixed to the robot. Figure 5.5 shows the measured motion velocity in function of the phase shift $\phi$ between horizontal and vertical vibration. This experiment was carried out at a driving frequency of $f = 147\ Hz$, a horizontal vibration amplitude of $X = 6\ \mu m_{amp}$ and a vertical vibration amplitude of $Z = 5\ \mu m_{amp}$ corresponding to an equivalent vertical acceleration of $A_{Z,eq} = 0.365g = 3.58\ m/s^2$. Filling in these parameter settings in equation (5.8) yields a force ratio of $q_F = 6.85$, which is well enough above 1 for reliable MFID locomotion.

The maximum motion velocity observed from figure 5.5 is 2.1 mm/s in positive $X$ direction and 2.4 mm/s in negative $X$ direction. These maxima are reached at a phase shift of $\phi = 110°$ and $\phi = 260°$. The graph shows a more or less sinusoidal dependence of the phase shift, which corresponds to the simulation and experimental results obtained with the characterization setup presented in chapter 4. However, the sinusoidal approximation is much rougher than for the motion experiments with the characterization setup. This is probably due to the fact that the vibration of the $XYZ$ stage is less clean (excitation of a resonance frequency around 300 Hz and considerable parasitic motion in $Y$ and $Z$ direction when actuating in $X$ direction) and to the optical measurement setup, which is far less precise than the interferometer used for the characterization setup. This is probably also the reason why the optimal phase shifts do not lie within a distance of 180° from each other as was the case for the characterization setup.

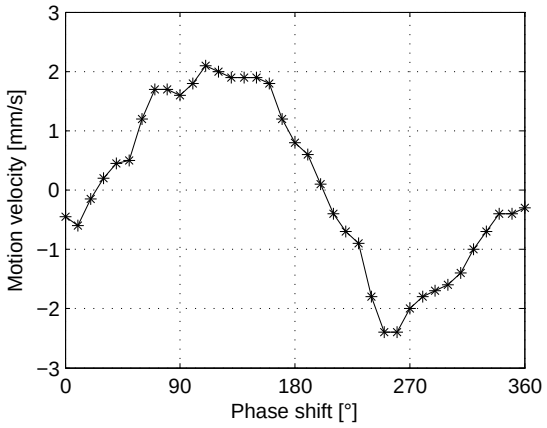


**Figure 5.5:** Influence of the phase shift on the motion velocity in $X$ direction

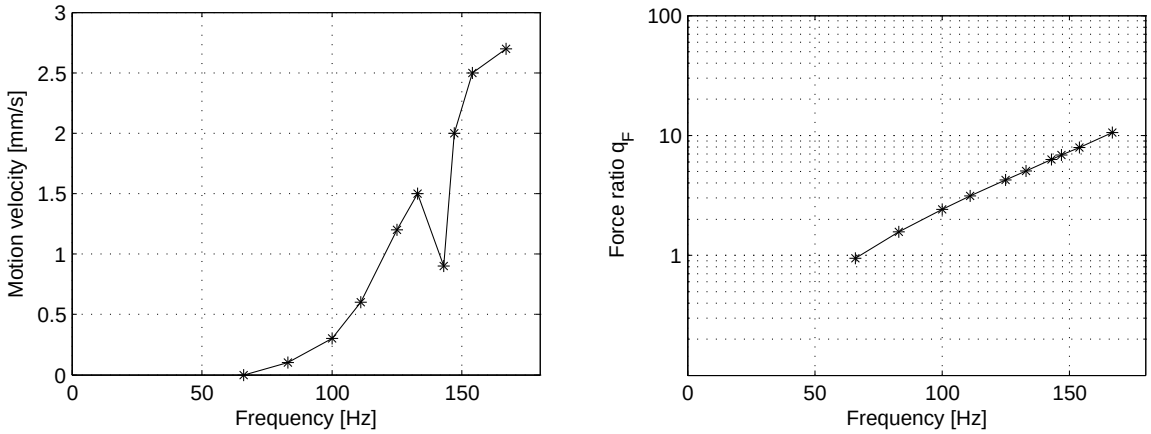


**(a)** Motion velocity

**(b)** Force ratio $q_F$

**Figure 5.6:** Influence of the driving frequency on the motion velocity and the force ratio

In section 4.4.3 the stepping efficiency $\eta_{step}$ was defined as the ratio between the average motion velocity and the maximum instantaneous velocity of the axial vibration. The average between the maximum motion velocity in positive and negative direction is 2.25 mm/s, while the maximum instantaneous velocity of the table is $X\omega = 5.5$ mm/s. This results in a step efficiency of $\eta_{step} = 2.25/5.5 = 0.41$.

Figure 5.6 shows the measured motion velocity and the calculated force ratio $q_F$ in function of the driving frequency for a horizontal vibration amplitude of $X = 6$ $\mu\text{m}_{amp}$, a vertical vibration amplitude of $Z = 5$ $\mu\text{m}_{amp}$ ($A_{Z,eq} = 0.365g = 3.58$ m/s$^2$) and a phase shift of $\phi = 270°$. The experiment shows that a frequency above 66 Hz is required for successful locomotion. This matches with the calculated force ratio, which reaches the value 1 for a driving frequency of 68 Hz. The sudden drop in velocity at 143 Hz is probably due to an excitation of the resonance frequency of the $XYZ$ stage by the harmonics in the piezoelectric vibration as already observed in figure 5.2.

### 5.1.3 Power consumption

The piezoelectric disk actuator has an electrical capacitance of $C = 19.2$ nF. In order to obtain a vertical vibration amplitude of $Z = 5$ $\mu\text{m}_{amp}$ (i.e. 10 $\mu\text{m}_{p2p}$) as in the locomotion

experiments the piezo was driven with a voltage ranging from $U_1 = -50$ V to $U_2 = +250$ V (i.e. 300 $V_{p2p}$). At these driving voltages and a driving frequency of 147 Hz a power of

$$P_{in,piezo} = f\frac{C(U_1^2 + U_2^2)}{2} = 91.7 \text{ mW}. \tag{5.9}$$

is injected in the piezoelectric actuator[2].

In order to evaluate the power efficiency of the locomotion module, one must compare the power consumption to a certain reference power consumption. Typically, this reference power consumption is the theoretical absolute minimum of the power consumption. However, in the case of locomotion in the horizontal plane there is no difference in potential or kinetic energy from non-moving robot at position $p_1$ and the same non-moving robot at position $p_2$. Consequently, the theoretical minimum power consumption for motion from $p_1$ to $p_2$ is zero. Therefore, we will consider as a reference value the power consumption of a particular way to perform the motion from $p_1$ to $p_2$: by pushing with a horizontal constant force without variation of the contact force between robot and substrate. Pushing with a horizontal force implies an energy dissipation due to the friction between robot and substrate. The dynamic friction force between the robot ($M_r$) and the substrate is given by

$$F_{t,d,grav} = \mu_d M_r g = 5.98 \text{ mN}. \tag{5.10}$$

with $\mu_d = 0.1$ the measured dynamic friction coefficient of sapphire on glass. Hence, the reference power consumption of sliding with a constant velocity $v = 2.15$ mm/s is calculated by

$$P_{ref} = vF_{t,d,grav} = 0.013 \text{ mW}. \tag{5.11}$$

The power efficiency $\eta_P$ defined as the ratio between the reference power and the consumed power is thus $\eta_P = 0.013/91.7 = 1.4210^{-4}$, which shows that there is still plenty of room for improvement. The power consumption could be lowered by lowering the driving voltage by driving the piezoelectric actuator in resonance. As can be observed from figure 5.4 the piezoelectric actuator shows a ratio between vibration amplitude at resonance and static vibration amplitude of $27.5/4.96 = 5.5$. Lowering the driving voltage with a factor 5.5 would lower the power consumption with a factor $5.5^2 = 30$. Moreover driving in resonance has the advantage that the actuator can be driven with a square wave signal, while still maintaining a sinusoidal vibration. Driving with a square wave signal simplifies the driving electronics and lowers its power consumption. Higher quality factors of resonance vibration could be obtained by choosing actuators with less internal energy dissipation, such as electromagnetic actuators, which would also drastically reduce the driving voltage. The objective of this first prototype was, however, to proof the feasibility of MFID locomotion with this configuration. Therefore, it has been chosen to design the actuator for operation well below the resonance frequency and to provide the high voltage actuation signals by wires and off-board driving electronics.

Another way for lowering the power consumption of this locomotion module would be by increasing the frequency of operation. This was already derived by Driesen *et al.* [102] for the case of stick-slip actuators with piezoelectric actuators. An increase of the driving frequency with a factor $i$ would lower the required vertical vibration amplitude for the same

[2]It should be noted that the energy injected in the capacitance of the piezoelectric actuator at every stepping period is theoretically not completely lost. Except for the energy dissipated in the hysteresis of the piezo, this energy could be recuperated by an implementation of a charge recovery electronics [342] or by operation at electrical resonance. However, it is a technological challenge to implement a charge recovery electronics and operation at electrical resonance in an on-board electronics of a robot with a size of some $cm^3$.

vertical acceleration amplitude with a factor $1/i^2$. A reduction of the driving voltage of the piezoelectric actuator by a factor $1/i^2$ reduces the energy injected in the piezo at every locomotion step by a factor $1/i^4$. Consequently, as the power consumption depends linearly of $f$, an increase of the frequency of operation with a factor $i$ would reduce the power consumption with a factor $1/i^3$. Or, in other words, for a constant vertical acceleration the power consumption scales with the frequency as $\frac{1}{f^3}$. Because of the resulting reduction of the vibration amplitude, an increase in driving frequency would also allow for further miniaturization of the robot.

### 5.1.4 Conclusion

The first MFID prototype presented in this chapter is based on a configuration with on-board contact force variation and off-board slip generation. The on-board contact force variation is generated by a piezoelectrically actuated vertically vibrating inertial mass on the robot. This configuration results in 2 DOF (motion in any direction within the $XY$ plane) with only one on-board actuation signal. The robot features a size of ∅20 mm × 7.5 mm = 2.36 cm$^3$, which could be easily reduced to less than 1 cm$^3$, if allowing for higher driving frequencies. The first locomotion experiments show a motion velocity of more than 2 mm/s at a driving frequency of 147 Hz and a driving voltage of 300 $V_{p2p}$. The motion stability, however, is not very good, due to the bad quality of the horizontal vibration generated by the external $XYZ$ stage. At 2 mm/s the actuator consumes 91.7 mW, which is about 10'000 times higher than the reference power consumption of simply pushing the robot with a constant horizontal external force. This power consumption could be easily improved, by increasing the operating frequency, by working at resonance or by choosing for another actuation technology, such as electromagnetic actuators. In conclusion, this first prototype has shown the feasibility of the MFID principle and has illustrated that the combination of on-board and off-board actuation can result in a very simple robot design.

## 5.2 Prototype with on-board slip generation and on-board contact force variation

The previous prototype presented in this chapter was based on a configuration with on-board friction force variation and off-board slip generation (configuration 3 in table 3.1 on page 73). With that first prototype the feasibility of the MFID principle was proven experimentally and was illustrated how the MFID principle can lead to a very simple robot. However, the first prototype suffers from a high driving voltage and a relatively high power consumption, which makes it — in its current design — not very well adapted for locomotion of untethered mobile microrobots. Both shortcomings (high driving voltage and high power consumption) can be overcome by an operation in resonance mode.

The second prototype presented here is based on the same actuation technology as the first prototype (i.e. piezoelectric bimorph actuators), but it allows for operation in resonance mode in order to reduce driving voltage and power consumption. Moreover, this second prototype is also intended to test the configuration with only on-board actuation (configuration 4 in table 3.1 on page 73), which results in a robot that is completely independent of its environment without need for synchronization between on-board and off-board actuation. This prototype is also the only prototype presented in this thesis that features all three in-plane degrees of freedom $(X, Y, \theta_Z)$.

The presentation of the second prototype is structured in a similar way as the first prototype: (section 5.2.1) discussion of the design of the actuator, (section 5.2.2) characterization of the vibration of the actuator, (section 5.2.3) characterization of the motion of the prototype and (section 5.2.4) a discussion on its power consumption.

### 5.2.1 Design

The design of the second prototype can be subdivided into two interconnected modules: the actuator module and the robot body. Piezoelectric actuators have been selected for the actuation module because of their high energy density and the suitability for precision applications. The design of the actuator module resembles to the design of a $10 \times 10 \times 1$ mm$^3$ stick-slip locomotion platform for 1 cm$^3$ size mobile microrobots that has been developed by our group [102] within the MiCRoN project. In order to allow for an integration of a vertically vibrating inertial mass the size of the footprint of the actuation module has been increased to $15 \times 15$ mm$^2$. In order to avoid unwanted vertical vibration of the robot's body the stiffness of the actuation module in $Z$ direction has been increased by increasing the height of the actuation module to 3 mm.

The actuation module consists of two parts: a frame that can vibrate in $X, Y, \theta_Z$ direction with connected to it an inertial mass that is vibrating in $Z$ direction (see figure 5.7). Both parts of the actuation module are actuated by piezoelectric monomorph actuators (heterogeneous bimorph actuators) consisting of a sheet of piezoelectric material (see appendix F.1) that is glued to a thin layer of steel. The flexible frame consists of a steel flexible structure with four sheets of piezoelectric material glued to it from the four sides. As illustrated in figure 5.8(a) an actuation of the two $X$ piezos with an opposite voltage results in a bending of the $X$ monomorphs, which causes the inner part of the vibrating frame to move in $X$ direction with respect to its four corners that are attached to the body of the robot. In order to limit the number of actuation channels one of the $X$ piezos is polarized from the inside to the outside (by applying a positive voltage on the flexible frame and a negative voltage on the outer piezo electrodes), while the other $X$ piezo is polarized from the outside to the inside. Hence, an actuation of both $X$ piezos with the same voltage signal causes them to

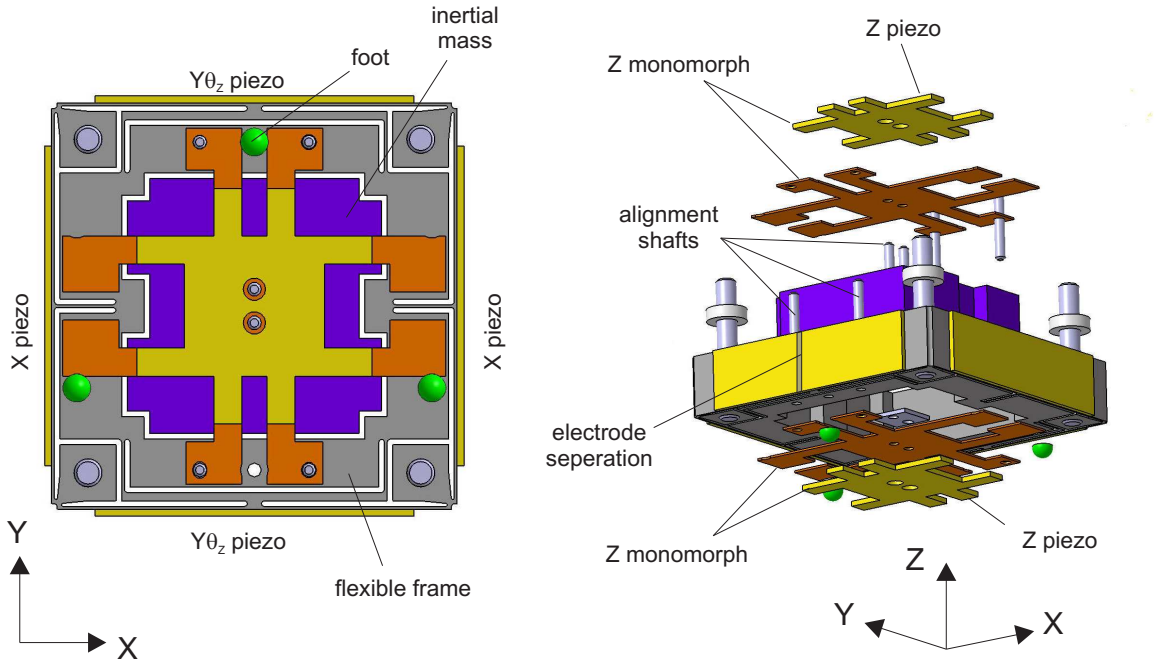


**Figure 5.7:** Design actuator module

deflect both in the same direction.

In the same way as for the $X$ direction the inner part can be moved in $Y$ direction by actuating the $Y\theta_Z$ piezos (see figure 5.8(b)). In order to allow for $\theta_Z$ actuation the electrodes of the $Y\theta_Z$ piezos is split in two. An actuation of both electrode halves with an opposite voltage causes the $Y\theta_Z$ monomorphs to deform into an S-shape (see figure 5.8(c)). The resulting rotation of the center of each S-shaped monomorph is transmitted to the inner part of the flexible frame by a rigid bar with two flexures at each end.

Two fabrication technologies have been considered for the $15 \times 15 \times 3$ mm$^3$ steel flexible frame: wire electro discharge machining (EDM) of the complete 3 mm thick module and laser cut and stacking of 3 plates of a thickness of 1 mm each. The best precision of the total module would be probably achieved by wire EDM, but for the first version of this prototype laser cut has been preferred due to the lower lead time and the higher flexibility. Four shafts are inserted in the corners of the flexible frame in order to align the individual plates and to connect the actuation module to the body of the robot.

The vertically vibrating inertial mass is connected to the inner part of the flexible frame by means of one $Z$ monomorph actuator on the top and one on the bottom of the module (see figure 5.7). Alignment between flexible frame, $Z$ monomorphs and the inertial mass is done by six alignment shafts. As for the $X$ and the $Y\theta_Z$ piezos one of the Z monomorphs is polarized in positive $Z$ direction and the other in negative $Z$ direction, which causes both $Z$ monomorphs to deflect in the same direction when actuated with the same voltage signal (see figure 5.8(d)). Consequently, the overall actuation module features vibrations in 4 DOF $(X, Y, Z, \theta_Z)$ with four actuation signals (1 for the $X$ piezos, 2 for the $Y\theta_Z$ piezos and 1 for the $Z$ piezos). Moreover, all these 4 DOF can be actuated simultaneously allowing for real holonomic locomotion inside the $XY$ plane.

The body of the robot consists of a stack of four $Al_2O_3$ plates as shown in figure 5.9. Holes and slits are cut out in the plates in order to pass the electrical wires from the connector to the electrodes of the piezoelectric actuators. The $Al_2O_3$ plates are aligned and assembled to

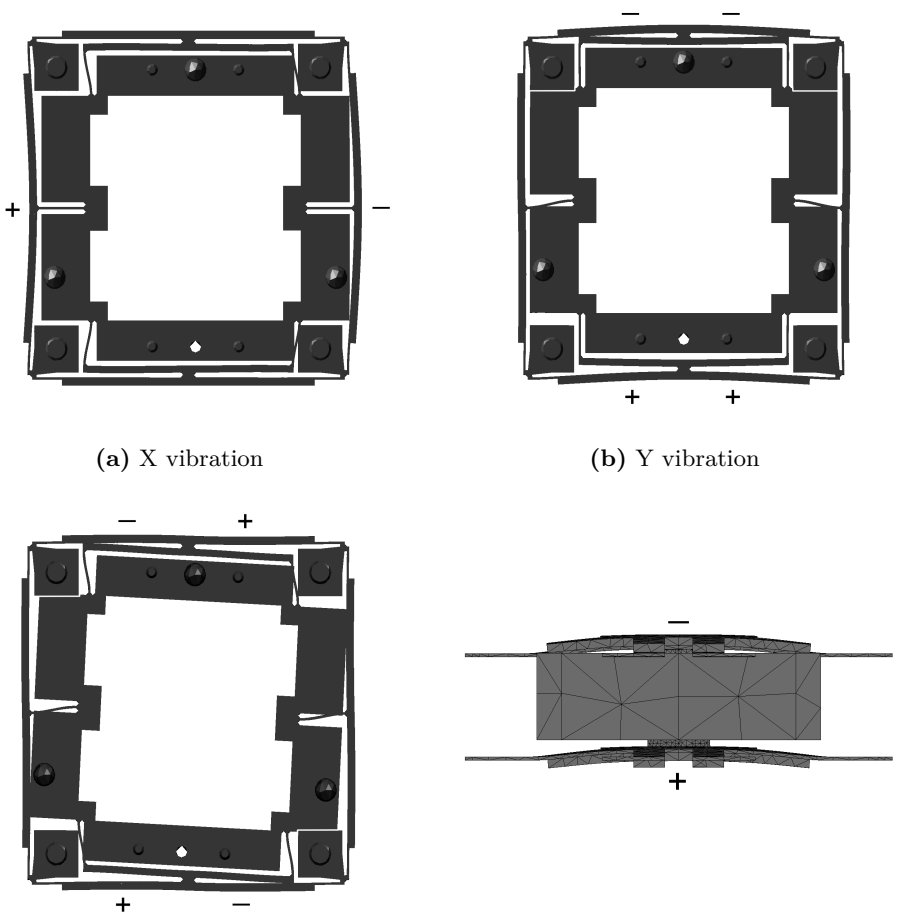


**(a)** X vibration

**(b)** Y vibration

**(c)** $\theta_Z$ vibration

**(d)** Z vibration

**Figure 5.8:** Monomorph actuation principle for the 4 DOF of the actuation module. The + (-) sign stands for an actuation resulting in an electric field in the same (opposite) direction as the polarization field.

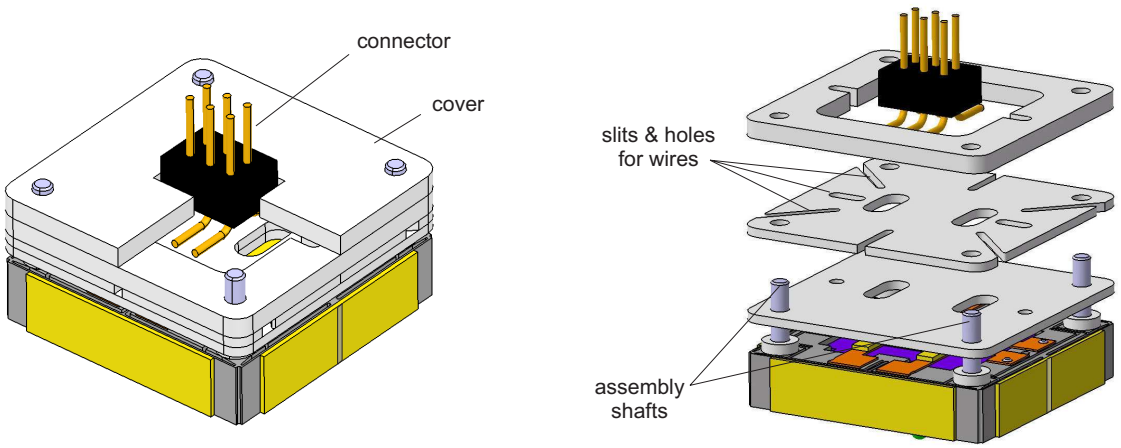


**Figure 5.9:** Design robot body

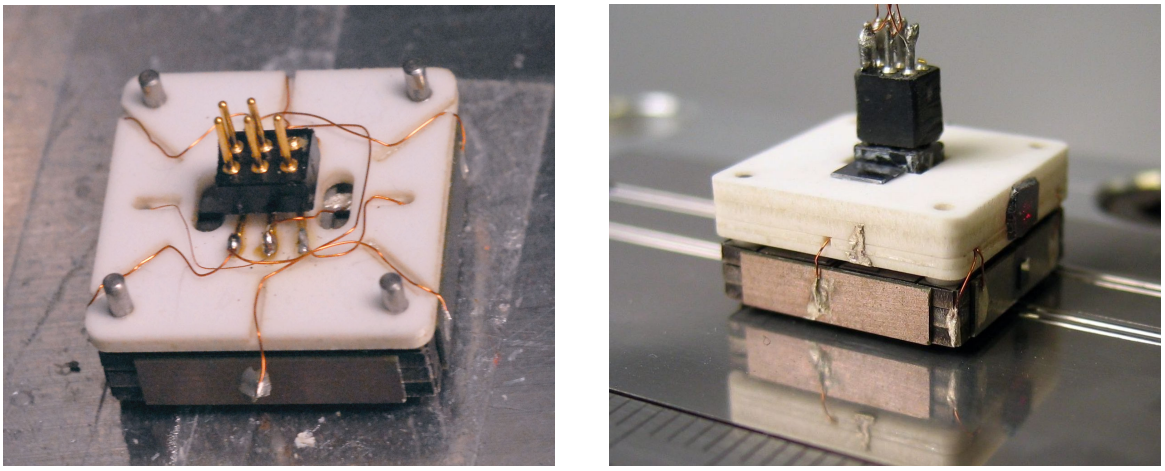

**Figure 5.10:** Pictures of the fabricated prototype without cover (left) and with cover on the measurement setup (right)

the actuation module by four assembly shafts. The electrical connector has 5 connections: 1 ground and 4 channels. Figure 5.10 shows a fabricated prototype without the cover on the left hand side and a prototype on the measurement setup on the right hand side. In order to allow for measurement of $X$ and $Y$ motion velocity by interferometer (specifications in appendix F.4), the measurement setup is provided with two pairs of steel shafts that serve as linear guideways: for motion in the robot's $X$ direction the two lower feet in figure 5.7 are guided in one guideway, while the third foot is guided on a flat surface. For locomotion in $Y$ direction one of the two lower feet is guided in one guideway, while the upper foot is guided in the other guideway.

### 5.2.2 Characterization of the vibration amplitudes

In order to know the resonance frequency and the vibration amplitudes of the prototype the frequency response of the actuation module has been measured by interferometer for the different degrees of freedom. Figure 5.11 shows the vibration amplitude and phase lag in function of the driving frequency for $X$, $Y$ and $Z$ vibration[3]. The frequency response for the $X$ and $Y$ vibration were measured without any clamping of the robot's body. The robot was positioned upside down on top of a flexible mousse and the position of the inner part of the flexible frame was measured by interferometer. The frequency response of the $Z$ vibration was measured by clamping the robot's body upside down and measuring the position of the inertial mass. The measured resonance frequencies are $f_{r,X} = 1984$ Hz, $f_{r,Y} = 1233$ Hz and $f_{r,Z} = 1710$ Hz. The resonance frequency for the vibration in $X$ direction is higher than the one in $Y$ direction because 4 flexures have to be deformed for motion in $X$ direction, while only 2 for motion in $Y$ direction. Moreover, the "rigid" bar connecting $Y$ monomorphs to the flexures also has a certain compliancy and a certain mass, which also lowers the stiffness of the flexible structure and increases the inertia of the vibrating mass in $Y$ direction.

The transfer function of a second order mass-damper-spring system with mass $m$, damping coefficient $c$ and spring constant $k$ is given by

$$\frac{A}{F} = \frac{1}{ms^2 + cs + k}. \tag{5.12}$$

[3]The frequency response for the $Y$ vibration is limited to 1300 Hz because above that frequency a higher vibration mode is excited, which causes the measurement results to be unreliable.

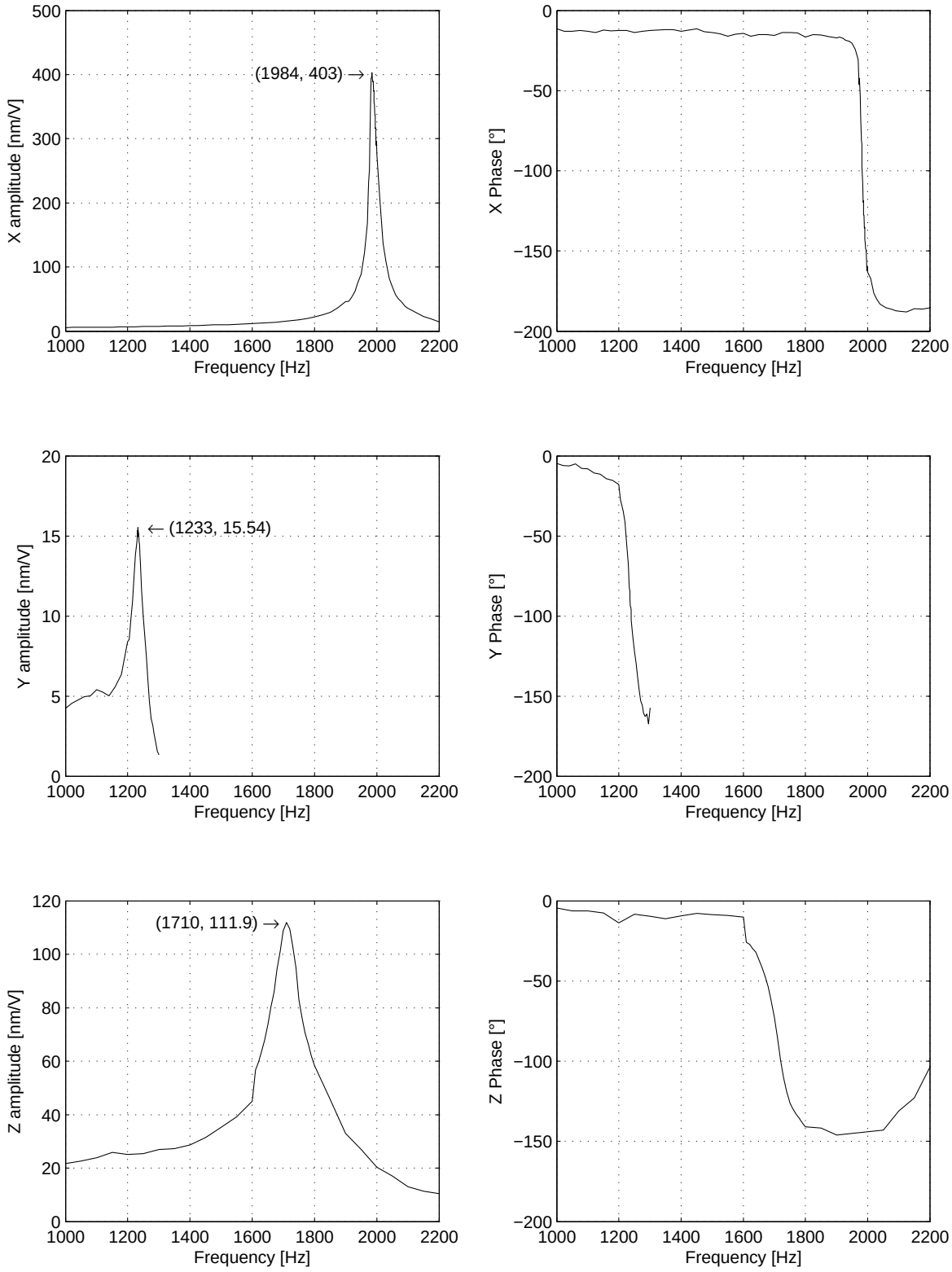


**Figure 5.11:** Frequency response of the $X$, $Y$ and $Z$ vibration

The quality factor for such a system is given by

$$Q = \frac{\sqrt{km}}{c}. \tag{5.13}$$

This quality factor can be easily obtained from the frequency response by measuring the ratio between the resonant frequency $f_r$ and the bandwidth $\Delta f$, i.e. the width of the range of frequencies for which the amplitude is at least $1/\sqrt{2}$ times its peak value.

It can be easily deduced that the quality factor of a mass-damper-spring system also corresponds to the ratio between the vibration amplitude at the natural frequency $\omega_n = \sqrt{k/m}$ and the static vibration amplitude. The amplitude at 0 Hz is equal to $A_0 = \frac{1}{k}F$. The amplitude at the natural frequency $\omega_n$ is $A_{\omega_n} = \frac{1}{c\omega_n}F = \frac{1}{c}\sqrt{\frac{m}{k}}F$. Hence, the quality factor $Q'$, defined as the ratio between the amplitude at $\omega_n$ and the DC amplitude equals to

$$Q' = \frac{A_{\omega_n}}{A_0} = \frac{\frac{1}{c}\sqrt{\frac{m}{k}}F}{\frac{1}{k}F} = \frac{\sqrt{km}}{c}. \tag{5.14}$$

In the case of low damping the natural frequency is close to the resonance frequency, so the quality factor $Q'$ can be approximated by the ratio between the measured amplitude at resonance and the measured quasistatic displacement.

The quasistatic displacements of the $X$, $Y$ and $Z$ vibration of the actuation module are $X_0 = 14.0$ nm/V, $Y_0 = 7.07$ nm/V and $Z_0 = 17.4$ nm/V. The displacement in $Y$ direction is higher than the one in $X$ direction due to the higher stiffness of the flexible frame in $X$ direction.

The quality factors $Q$ of the three resonances calculated as the ratio between the resonance frequency $f_r$ and the bandwidth $\Delta f$ are $Q_X = 90.0$, $Q_Y = 39.2$ and $Q_Z = 17.6$. The measured quality factors $Q'$ calculated as the ratio between the vibration amplitude at resonance and the quasistatic vibration amplitude are $Q'_X = 151$, $Q'_Y = 5.0$ and $Q'_Z = 6.4$. It is not clear why the values of the quality factors $Q$ calculated by the bandwidth and $Q'$ by the ratio of vibration amplitudes are that different. The quality factor $Q'_Y$ for $Y$ vibration appears to be much lower than the one for $X$ vibration. This is partly due to the lower stiffness of the flexible frame in $Y$ direction (see equation 5.13). However, this can not be the only reason. An observation under an optical microscope has shown that one of the $Y$ piezos is not well glued to the flexible frame. This is due to the fact that the flexible structures that are cut out by laser appear to be slightly undulated due to the thermal stress induced by the laser. Moreover, the undulation is not the same in all three parts of which the flexible frame is constituted. The resulting gap between piezo and steel flexure is filled by epoxy glue and might induce additional damping, which explains the lower quality factor. Better results could be probably obtained by fabricating the flexible frame by wire EDM.

The robot has a total mass (body + actuation module) of $M_r = 6.73$ g. For every actuation direction ($X$, $Y$ and $Z$) the vibration occurs between two masses: the one that is in contact with the guideways by the feet ($M_f$) and the rest of the robot that serves as an inertial mass ($M_i$) in order to generate the required inertial force. The distribution of the weight of the robot between these two masses $M_f$ and $M_i$ is different for every vibration direction. The mass $M_f$ is slightly larger for vibration in $Y$ direction than in $X$ direction because the two rigid bars connecting the $Y$ piezos to the flexures do also vibrate in $Y$ direction, but not in $X$ direction. In $X$ direction the distribution of the masses is $M_{feet,X} = 3.15$ g and $M_{inert,X} = 3.78$ g, while in $Y$ direction it is $M_{feet,Y} = 3.28$ g and $M_{inert,Y} = 3.65$ g. For $Z$ vibration the $M_i$ corresponds to the vertically vibrating part in the inside of the flexible frame plus half of the mass of the two $Z$ monomorph actuators. The part to which the feet are attached also includes the mass of the body of the robot. The mass distribution for $Z$ vibration is thus $M_{feet,Z} = 5.28$ g and $M_{inert,Z} = 1.65$ g.

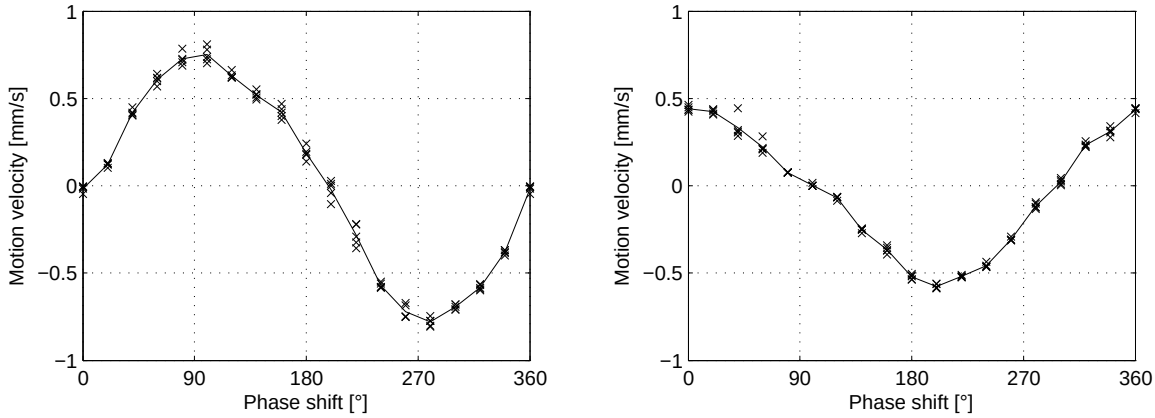


**(a)** Motion in $X$ direction

**(b)** Motion in $Y$ direction

**Figure 5.12:** Influence of the phase shift on the motion velocity

### 5.2.3 Characterization of the motion velocity

The $X$ and $Y$ motion velocity of the second MFID prototype has been studied in function of the phase shift, the driving frequency, the horizontal vibration amplitude and the vertical acceleration amplitude. No detailed measurements of the rotational ($\theta_Z$) motion velocity have been carried out, but first experiments have shown a rotational velocity of about 10 °/s for a driving frequency of 2236 Hz. The suitability of this design for precision applications is investigated by characterizing the repeatability of the traveled distance with 500 locomotion steps and the minimal increment. Finally, the suitability for autonomous operation is investigated by an analysis of the power consumption.

#### Influence of the phase shift on motion velocity

Figure 5.12 shows the influence of the phase shift between horizontal and vertical actuation on the measured $X$ and $Y$ motion velocity. The measurements were taken at a driving frequency of 1150 Hz, which corresponds to resonance operation for $Y$ motion. For motion in $X$ direction the frequency of resonance operation is much higher, however a driving frequency of 1150 Hz was used also for $X$ motion in order to be able to easily compare the velocity in $X$ and $Y$ directions. The horizontal actuation voltage amplitude and the vertical acceleration amplitude were set to the maximum values at which stable operation is still possible. Hence, for $X$ motion the horizontal actuation voltage is $U_X = 30$ $V_{amp}$ (i.e. 60 $V_{p2p}$) and the vertical acceleration amplitude is $A_Z = 0.54g$, corresponding to an actuation voltage of $U_Z = 14.9$ $V_{amp}$, i.e. 29.8 $V_{p2p}$. For $Y$ motion the horizontal actuation voltage is $U_Y = 10$ $V_{amp}$ (i.e. 20 $V_{p2p}$) and the vertical acceleration amplitude is $A_Z = 0.63g$, corresponding to an actuation voltage of $U_Z = 17.4$ $V_{amp}$, i.e. 34.8 $V_{p2p}$.

Figure 5.12 shows that at 1150 Hz the maximum motion velocity in positive (negative) $X$ direction is reached for a phase shift of $\phi = 100°$ ($\phi = 280°$). This corresponds to the results obtained with the characterization setup (see figure 4.19 on page 100) and the first prototype discussed in this chapter (see figure 5.5 on page 130). For motion in $Y$ direction, however, maximum velocities are reached at $\phi = 0°$ and $\phi = 200°$. This extra phase shift of about 90° is resulting from the resonance mode operation for motion in $Y$ direction.

The optimal parameter settings used in this experiment with the optimal phase shift of $\phi = 100°$ for $X$ motion and $\phi = 0°$ for $Y$ motion will be considered as the default parameter

| | Symbol | Unit | $X$ motion | $Y$ motion |
|---|---|---|---|---|
| Frequency | $f$ | Hz | 1150 | 1150 |
| Phase shift | $\phi$ | ° | 100 | 0 |
| Hor. actuation voltage | $U_X$, $U_Y$ | $V_{amp}$ | 30 | 10 |
| | | $V_{p2p}$ | 60 | 20 |
| Vert. acceleration amp. | $A_Z$ | $g$ | 0.54 | 0.63 |
| Max. motion velocity | $v_{r,avg,X}$, $v_{r,avg,Y}$ | mm/s | 0.72 | 0.51 |

**Table 5.1:** Default input parameter settings for the locomotion experiments with the second prototype

settings for the all the locomotion experiments for this prototype. Table 5.1 summarizes these default parameter settings

### Influence of the driving frequency on motion velocity

Figure 5.13 shows the influence of the driving frequency on the motion velocity in $X$ and $Y$ direction at default parameter settings (see table 5.1). The measured velocity in $Y$ direction reaches a maximum value of 0.51 mm/s at 1150 Hz, which is a bit lower than the measured resonance frequency of 1233 Hz for free vibration in $Y$ direction (see figure 5.11). This frequency reduction is due to the friction between the feet of the robot and the guideways. The frequency response of the $X$ and $Y$ vibration of the actuation module shown in figure 5.11 was measured without clamping nor the robot's feet, nor the robot's body. It was experimentally measured that while clamping the feet the $X$ resonance frequency is reduced from 1984 Hz to around 1200 Hz and the $Y$ resonance frequency from 1233 Hz to around 745 Hz. The friction between the robot's feet and its guideways that is present during locomotion could intuitively be considered as a condition that lies between free motion and rigidly clamping, which explains why the resonance frequency decreases at the presence of friction. Consequently, as the resonance frequency during locomotion is different from the resonant frequency during free vibration, the vibration amplitude will also be different during locomotion and during free vibration. Therefore, it is difficult to predict the vibration amplitude during locomotion at resonance, without measuring it in a locomotion experiment. The measured velocity profile reaches a motion velocity that is $\sqrt{2}$ times lower than the maximum velocity at driving frequencies $f_1 = 1117$ Hz and $f_2 = 1187$. The resulting quality factor of the $Y$ motion at resonance is $Q = 1150/(1187 - 1117) = 16.4$. This quality factor is 2.4 times lower than the quality factor $Q_Y = 39.2$ of the free vibration. This drop in quality factor is caused by the introduction of additional damping due to the friction between robot's feet and the guideways.

The measured velocity in $X$ direction reaches a maximum value of 0.72 mm/s at 1150 Hz, which is surprisingly much lower than the measured resonance frequency of 1984 Hz for free vibration in $X$ direction. During the locomotion experiment it was also observed that for driving frequencies above 1150 Hz a low noise resulting from hopping motion of the robot could be heard. The experiment was, however, carried out at a constant vertical acceleration because the vertical vibration amplitude was reduced quadratically with the increasing frequency. Even when exciting the horizontal vibration without any vertical vibration, the robot started to jump when increasing the frequency above a certain threshold value. Apparently a parasitic $Z$ motion is superposed on the $X$ vibration, which causes the robot to jump when the resulting vertical acceleration surpasses the acceleration of gravity. This parasitic motion is probably due to the fact that the flexible frame of the actuation module is a stack of three

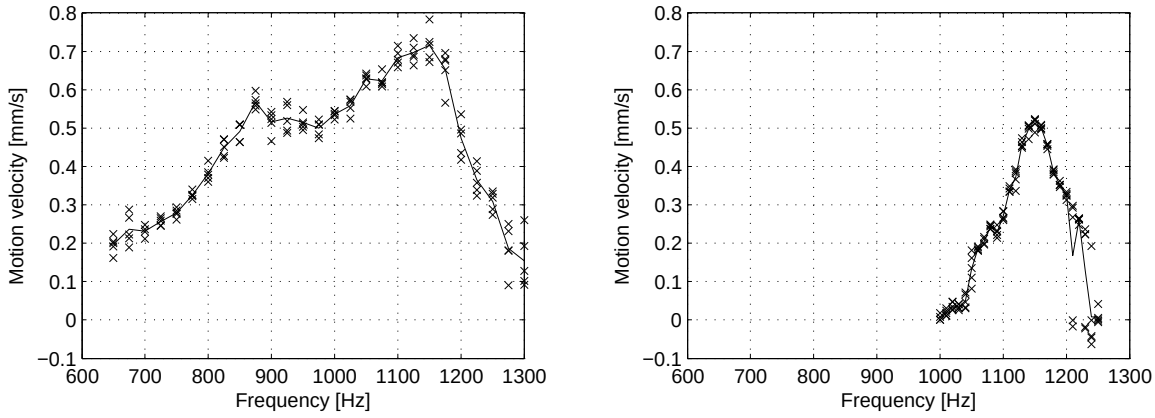


**(a)** $X$ **(b)** $Y$

**Figure 5.13:** Influence of the driving frequency on the motion velocity

laser cut flexible frames of 1 mm thickness. As already discussed in section 5.2.2 the laser cut flexures were slightly undulated due to a residual internal thermal stress induced by the laser beam. This undulation causes an unwanted gap between the flexures and the piezos that are glued to it, which reduces the efficiency of the monomorph actuators. The observed difference in undulation between the three layers of the flexible frame is probably the cause to the apparent parasitic $Z$ motion. As already suggested earlier the quality of the flexible frame and the monomorph actuators can be probably improved by opting for a fabrication of the flexible frame by wire EDM.

### Influence of the horizontal vibration amplitude on motion velocity

Figures 5.14(a) and 5.14(b) show the influence of the actuation voltage of the horizontal vibration on the motion velocity for $X$ and $Y$ motion at default parameter settings. The velocity increases with increasing horizontal actuation voltage up to a maximum value of 60 $V_{p2p}$ for $X$ motion and 20 $V_{p2p}$, above which the dispersion increases and the velocity starts to decrease again. This threshold to the horizontal vibration amplitude was not present for the characterization setup (and is also not present for the third prototype presented later in this chapter). The threshold in the current prototype is caused by the parasitic vertical motion superposed on the horizontal vibration, which causes the robot to jump as was already observed in the *velocity vs frequency* profile for $X$ motion shown in figure 5.13.

Normally, the phase shift between the horizontal vibration and its parasitic vertical vibration is 0°, so no superposed MFID motion is generated by this parasitic vibration. However, in the case of resonance operation the parasitic vertical vibration is not synchronized anymore with the horizontal vibration because the parasitic vibration is not subjected to an extra phase shift due to resonance operation as the resonance frequency for the vertical vibration mode is much higher. This is the reason why an offset of -0.07 mm/s can be observed on the *phase vs. velocity profile* for $Y$ motion shown in figure 5.12.

Figures 5.14(c) and 5.14(d) show the influence of the horizontal vibration amplitude on the force ratio. The force ratio for $Y$ motion starts to be larger than 1 for driving voltages above 8 V, which is also the voltage at which the motion velocity starts to increase. The motion velocity reaches a maximum at around 20 V ($q_F = 2.24$), above which hopping motion occurs due to the parasitic vertical vibration, which causes the motion to be instable. The force ratio for the $X$ direction also reaches $q_F = 1$ for a driving voltage around 10 V, while

locomotion could still be measured even at a driving voltage of 4 V. This is because the force ratio is calculated with vibration amplitude measured during free vibration. If the robot's feet would be sticking to the base, the resonance frequency for $X$ vibration would drop to 1200 Hz. This means that this resonance would be excited by the driving frequency of 1150 Hz, resulting in a larger $X$ vibration amplitude and therefore a larger inertial force that is sufficient to overcome the friction force. Hence, the real force ratio during locomotion is larger than the one calculated based on vibration amplitudes measured with a clamped frame, which explains why MFID motion in $X$ direction is possible for a calculated force ratio smaller than 1.

A comparison of the measured motion velocity at equal horizontal actuation voltage (20 $V_{p2p}$) for $X$ motion (0.18 mm/s) and $Y$ motion (0.51 mm/s), shows the advantage of increased velocity for operation at resonance[4].

As already concluded for the characterization setup, the horizontal vibration amplitude is the best input parameter to vary in order to perform velocity control of a MFID actuator. Firstly, because of its good linear behavior (here at least in the case of $X$ motion) and secondly because of the fact that when the velocity is reduced, the step size is also reduced, which allows for higher resolution positioning.

#### Influence of the vertical acceleration amplitude on motion velocity

Figure 5.15 shows the influence of the vertical acceleration amplitude on the motion velocity for $X$ and $Y$ motion at default parameter settings. The vertical acceleration amplitude is expressed as a fraction of the acceleration of gravity. As for the first prototype (see section 5.1.1) the acceleration amplitude in the graphs in figure 5.15 is compensated for the mass ratio between the vertically vibrating inertial mass and the rest of the robot by multiplying with a factor $M_{inert,Z}/M_r = 0.238$, so that a value of $1g$ corresponds to the value above which the robot would theoretically start to jump.

For $X$ motion the velocity increases linearly with increasing vertical acceleration amplitude and reaches a maximum at $0.54g$. Above this value the velocity rapidly decreases while the dispersion on the measured velocity increases. During the experiment a sound due to hopping motion of robot could also be heard above $0.54g$. The reason that the robot starts hopping already at $0.54g$ and not at $1g$ is probably because of the additional vertical acceleration resulting from the parasitic vertical motion that is superposed on the horizontal vibration of the actuation module.

For motion in $Y$ direction the maximum motion velocity is reached at $0.63g$ above which the motion becomes unstable. Below $0.63g$ the velocity decreases with decreasing acceleration, but the velocity already reaches zero velocity at $0.36g$. This is effect is similar to the one observed in figure 5.14(b) and is also caused by a motion instability at a low force ratio combined with resonance operation with a large frequency shift between resonance of free vibration and resonance with clamped feet.

#### Open loop repeatability and motion resolution

In order to able to evaluate the suitability of this prototype for high resolution motion the repeatability of the locomotion step size and the smallest increment is investigated.

In a first experiment the relative standard deviation (i.e. the ratio between the standard deviation and the average) on 50 measurements of the traveled distance by 500 locomotion

[4]It should be noted that, if the quality factor in $Y$ direction ($Q'_Y = 5.0$) would be as high as the one in $X$ direction ($Q'_X = 151$), the gain in motion velocity due tot he resonance operation would be much larger.

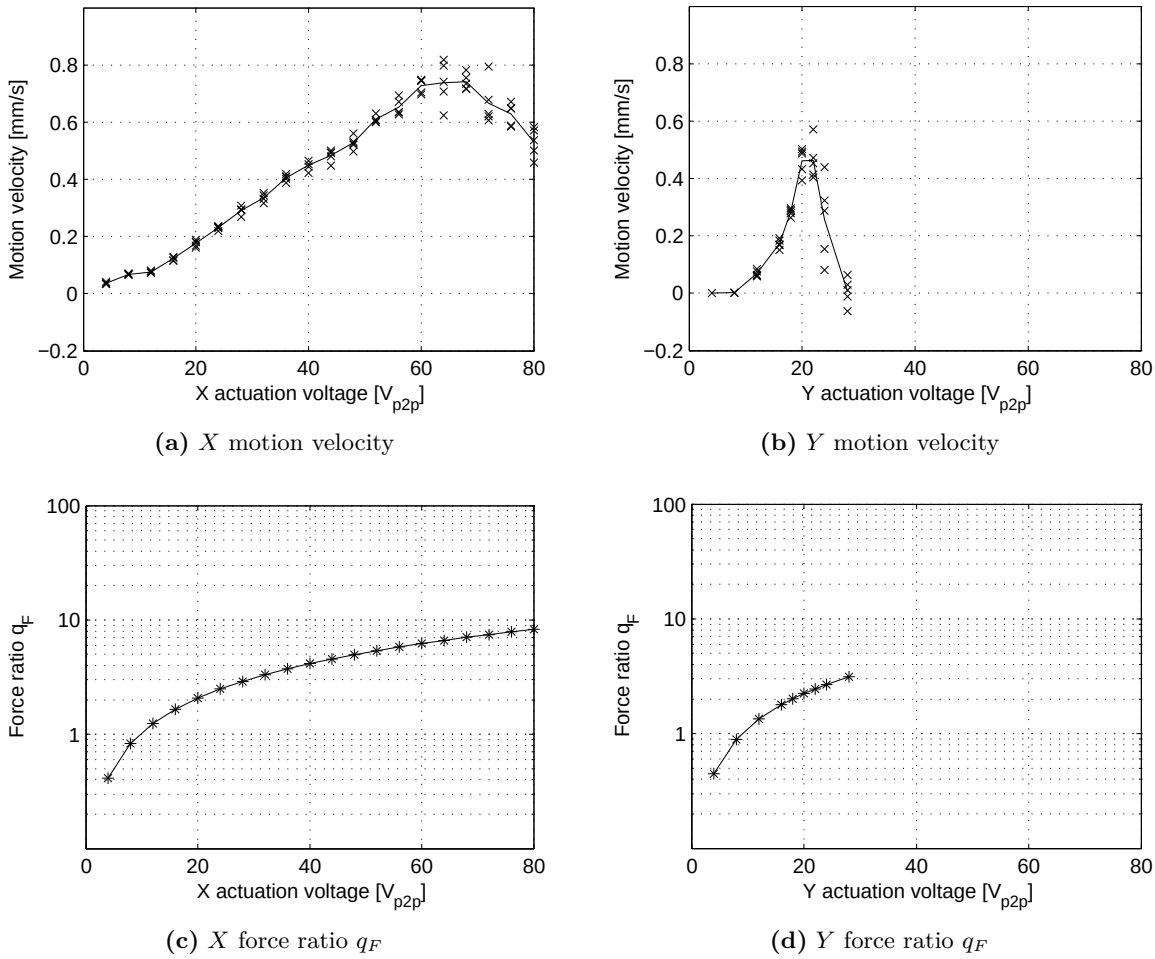


**(a)** $X$ motion velocity

**(b)** $Y$ motion velocity

**(c)** $X$ force ratio $q_F$

**(d)** $Y$ force ratio $q_F$

**Figure 5.14:** Influence of the actuation voltage of the horizontal vibration on the motion velocity and on the force ratio

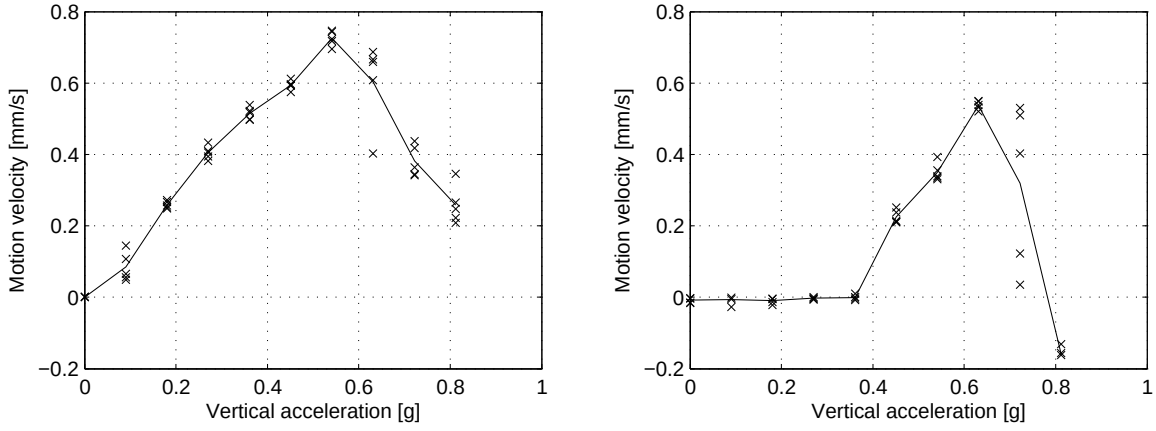


**(a)** $X$

**(b)** $Y$

**Figure 5.15:** Influence of the vertical acceleration amplitude (expressed as a fraction of g) on the motion velocity

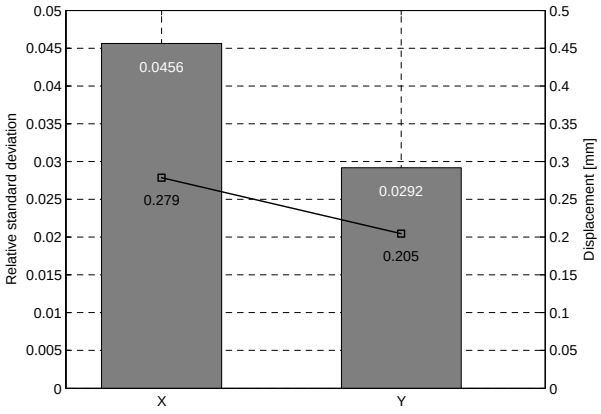


**Figure 5.16:** Repeatability of traveled distance by 500 locomotion steps

steps has been measured (see figure 5.16). The experiment resulted in a higher relative standard deviation for $X$ motion (4.6%) than for $Y$ motion (2.9%).

A second experiments studies the smallest increment that can be carried out with an acceptable dispersion. Figure 5.17 shows the measured $X$ and $Y$ displacements after 1, 2 , 5, 10 and 15 steps at three different driving voltages. Every measurement has been repeated 50 times and the error bars in the graph delimit the $1\sigma$ confidence interval. The graph shows that a high dispersion for $X$ motion at a driving voltage of 60 $V_{p2p}$, which could indicate that the robot is hopping now and then[5]. The criterium of "acceptable dispersion" is set to a maximum relative dispersion of 20%. With this criterium the minimum repeatable increment in $X$ direction is 0.65 $\mu$m for a relative dispersion of 6.1%, which is reached for 2 steps at a horizontal actuation voltage of 20 $V_{p2p}$. The minimum repeatable increment in $Y$ direction is 0.187 $\mu$m for a relative dispersion of 17%, which is reached for 2 steps at a horizontal actuation voltage of 18 $V_{p2p}$.

Better resolutions can be achieved by operating the locomotion module in quasistatic scanning mode. For a driving voltage of 60 $V_{p2p}$ (i.e. the voltage at which maximum $X$ velocity is reached), the range of the scanning mode motion in $X$ direction is 60 V $\times$ 14.0 nm/V = 840 $nm_{p2p}$. For $Y$ direction a scanning range of 20 V $\times$ 7.07 nm/V = 141 $nm_{p2p}$ is obtained for a driving voltage of 20 $V_{p2p}$ (i.e. the voltage at which maximum $Y$ velocity is reached). The resolution of the scanning mode is equal to the scanning range divided by the number of increments of the DAC of the driving electronics. Hence, for an 8 bit DAC a resolution of about 3 nm is obtained in $X$ direction and about 0.6 nm in $Y$ direction. In $X$ direction the scanning range is larger than the minimum repeatable MFID increment (0.65 $\mu$m), which is required for being able to perform scanning motion around any arbitrary position. However, for $Y$ direction the scanning range is slightly smaller than the minimum repeatable MFID increment (0.187 $\mu$m). Smaller MFID increments in $Y$ direction can be performed, however, at the expense of a higher dispersion (for instance increments of 0.111 $\mu$m with a relative dispersion of 38% are achieved for 2 steps of 14 $V_{p2p}$).

A comparison of the measured increments for a driving voltage of 20 V in $X$ direction to those obtained at 22 V in $Y$ direction shows that for 15 locomotion steps the increment is larger in $Y$ than in $X$ direction, while for 1 and 2 locomotion steps the increment is clearly larger in $X$ direction. This is due to fact that for $Y$ motion the robot is actuated in resonance mode and not for $X$ motion. In resonance operation a certain number of actuation cycles is

[5]This would also explain the higher dispersion for $X$ motion measured in the repeatability experiment discussed before.

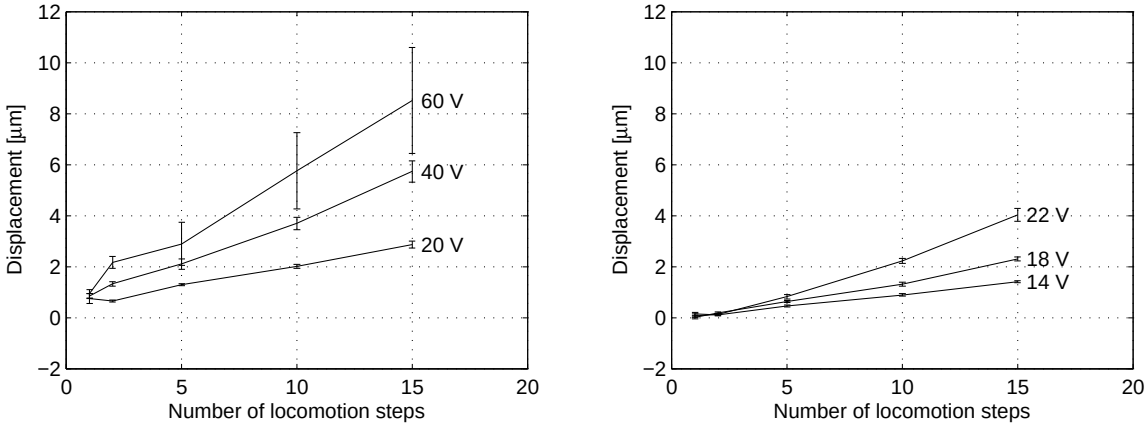


**(a)** $X$ motion **(b)** $Y$ motion

**Figure 5.17:** Traveled displacement in function of the number of locomotion steps and the driving voltage of the horizontal vibration

required before the maximum vibration amplitude is reached. This is also clearly visible in figure 5.18, which shows the transient response of the stepping motion for $X$ and $Y$ motion. The upper two graphs show the position of the body of the robot ($M_i$) and the position of the feet of the robot ($M_f$). The MFID actuation is started at $t = 0$ s. For better clarity of the graph the position of the body of the robot is shifted 2 $\mu$m upwards. The lower two graphs show the instantaneous velocity of the feet of the robot ($M_f$) that has been obtained by derivation of the position after filtering with a $6^{th}$-order Butterworth filter at 2000 Hz. These graphs clearly show that in the $X$ direction stable stepping motion is already reached after a few locomotion periods, while for the $Y$ direction the stepping motion only stabilizes after about 0.01 s, which corresponds to 12 locomotion periods.

From the velocity profile shown in the two lower graphs of figure 5.18 the step efficiency $\eta_{step}$ can be calculated as the ratio between the average motion velocity and the peak slip velocity. The peak slip velocity of the feet in the guideways has an average value of 2.2 mm/s for $X$ motion and 0.9 mm/s for $Y$ motion. Hence, for a measured $X$ and $Y$ motion velocity of 0.72 mm/s and 0.51 mm/s the step efficiency can be calculated as $\eta_{step,X} = 0.72/2.2 = 0.33$ and $\eta_{step,Y} = 0.51/0.9 = 0.57$ respectively. It is surprising to notice that the step efficiency for $Y$ motion is considerably higher than for $X$ motion. A detailed observation of the $Y$ stepping motion shown in figure 5.18(d) tells that some kind of ripple is superposed on the vibration of the feet. This might be caused by the instability of the $Y$ motion due to the low force ratio, which could allow for the feet to stick to the guideways during certain parts of the locomotion cycle.

### 5.2.4 Power consumption

The power consumption of a piezoelectric actuator with electrical capacitance $C$ that is driven with a sinusoidal waveform with frequency $f$ and a voltage amplitude $U$ (so $2U$ peak-to-peak

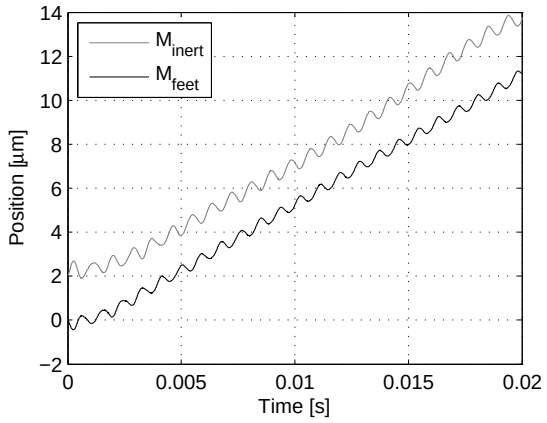


**(a)** $X$ position

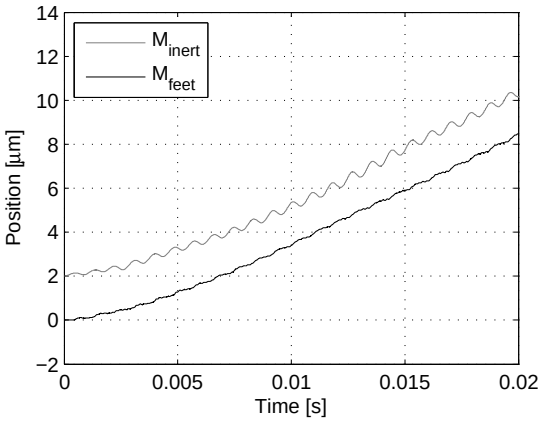


**(b)** $Y$ position

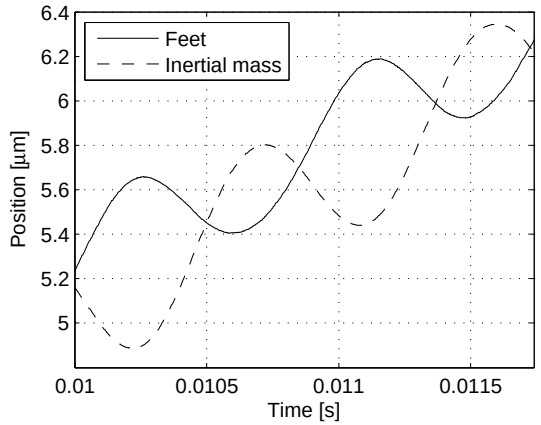


**(c)** $X$ position - zoom in

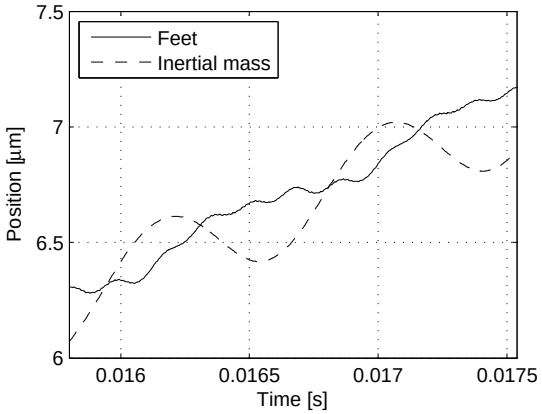


**(d)** $Y$ position - zoom in

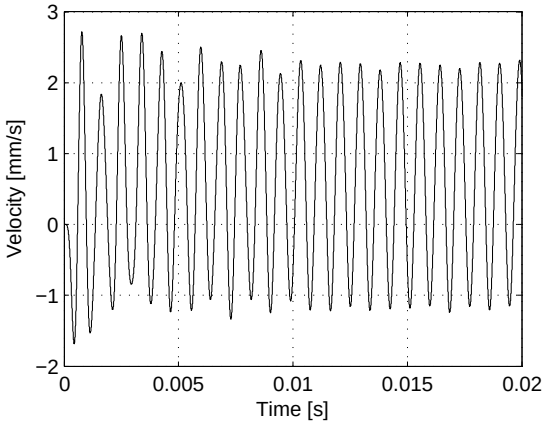


**(e)** $X$ Velocity of $M_f$

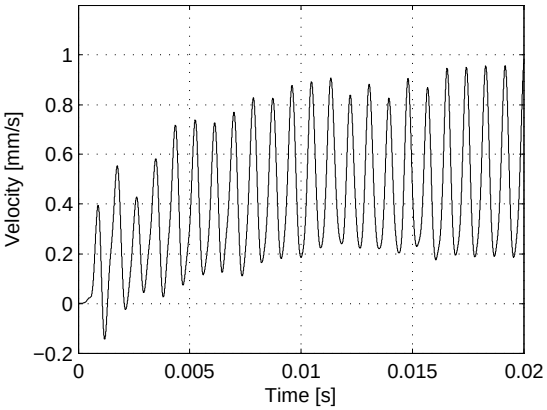


**(f)** $Y$ Velocity of $M_f$

**Figure 5.18:** Closeup of the transient response at the start of a actuation signal

voltage value) is given by[6]

$$P_{in} = 2f\frac{CU^2}{2}. \tag{5.15}$$

The factor 2 in the beginning of the formula comes from the fact that during every actuation period the capacitance is charged twice: once up to a positive voltage $+U$ and once down to a negative voltage $-U$. The electrical capacitance of the two $X$ piezos, the two $Y\theta_Z$ piezo halves and the two $Z$ piezos have been measured to be $C_X = 5.4$ nF, $C_{Y\theta_Z 1/2} = 2.7$ nF and $C_Z = 4.0$ nF respectively. At the default parameter settings for motion in $X$ direction (see table 5.1 on page 140) the following power consumption is obtained

$$P_{in,X} = 2f\frac{C_X U_X^2 + C_Z U_Z^2}{2} = 13.2 \text{ mW}. \tag{5.16}$$

For motion in $Y$ direction at the default conditions the power consumption is

$$P_{in,Y} = 2f\frac{C_{Y\theta_Z 1/2} U_Y^2 + C_Z U_Z^2}{2} = 4.02 \text{ mW}. \tag{5.17}$$

A comparison of the power consumption of $X$ and $Y$ motion illustrates the interest of working in resonance mode. A reduction in the driving voltage decreases the power consumption a lot as the power consumption varies quadratically with the driving voltage.

In order to evaluate the power efficiency of the locomotion module, one must compare the power consumption to a certain reference power consumption. As for the first prototype we will consider as a reference value the power consumption of a particular way to perform the motion from $p_1$ to $p_2$: by pushing with a horizontal constant force without variation of the contact force between robot and substrate. Pushing with a horizontal force implies an energy dissipation due to the friction between robot and substrate. The dynamic friction force between the robot (mass $M_r = 6.93$ g) and a flat substrate is given by

$$F_{t,d,grav} = \mu_d M_r g = 6.80 \text{ mN}. \tag{5.18}$$

with $\mu_d = 0.1$ the measured dynamic friction coefficient of sapphire on glass[7]. Hence, the reference power consumption of sliding with a constant velocity $v_X = 0.72$ mm/s and $v_Y = 0.51$ mm/s is calculated as

$$P_{ref,X} = v_X F_{t,d,grav} = 4.90 \ \mu\text{W}, \tag{5.19}$$

$$P_{ref,Y} = v_Y F_{t,d,grav} = 3.47 \ \mu\text{W}. \tag{5.20}$$

The power efficiency $\eta_P$ defined as the ratio between the reference power and the consumed power is thus $\eta_{P,X} = 3.7 \times 10^{-4}$ and $\eta_{P,Y} = 8.6 \times 10^{-4}$ for $X$ and $Y$ motion respectively. The higher power efficiency for $Y$ motion is due to the resonance operation in $Y$ direction[8]. Although, the power efficiency of this prototype is still very low, it is better than the one from the first prototype presented in this chapter ($\eta_P = 1.42 \times 10^{-4}$), although the slip generation was generated off-board for the first prototype. The reason for this is the low

[6] As already mentioned for the first prototype the energy accumulated in the capacitance of the piezoelectric actuator is not completely lost and the major part of it could theoretically be reused by implementing a charge recovery electronics [342]. However, it is not easy to integrate such a charge recovery electronics in a cm$^3$ size mobile robot.

[7] As the robot features 3 DOF locomotion ($X$, $Y$, $\theta_Z$) in normal use the robot would be walking on a flat substrate (typically glass) and not on the steel guideways of the measurement setup as shown in figure 5.10(b)

[8] As for the motion velocity, the gain in power efficiency could be much higher if the quality factor of the resonance in $Y$ direction ($Q'_Y = 5.0$) would be as high as the one in $X$ direction ($Q'_X = 151$).

driving frequency for the first prototype (147 Hz) as discussed in section 5.1.3. Increasing the driving frequency linearly allows for — at constant motion velocity — a linear decrease of the horizontal driving voltage and for — at constant vertical acceleration — a quadratic decrease of the vertical driving voltage. As the power consumption of a piezoelectric actuator depends quadratically on the driving voltage, the power consumption can be reduced considerably by increasing the driving frequency.

### 5.2.5 Conclusion

The objective of this second prototype was threefold: (1) test the MFID locomotion in resonant operation (2) test the configuration with only on-board actuation (configuration 4 in table 3.1 on page 73) and (3) realize a robot with all 3 in-plane DOF ($X$, $Y$, $\theta_Z$). The developed prototype is based on piezoelectric actuation and features an overall size of $15 \times 15 \times 7 = 1.575$ cm$^3$.

The actuation module of this second prototype features good resonant behavior for actuation in $X$ direction with a high quality factor, which would allow for a significant reduction in driving voltage and power consumption. The vibration in $Y$ direction appears to suffer from some fabrication and assembly problems, resulting in a much lower quality factor. Because of the same reason a parasitic vertical vibration seems to be superposed on the horizontal vibration both in $X$ and $Y$ direction. This parasitic vertical vibration causes an additional vertical acceleration, which makes the robot jump when exceeding a certain driving frequency or a certain horizontal actuation voltage. Unfortunately, the vibration direction with the best quality factor (i.e. the $X$ direction) occurs at the highest resonant frequency, which can not be reached due to the parasitic vertical acceleration.

Resonant mode MFID locomotion was tested for locomotion in $Y$ direction. An optimal driving frequency is clearly visible in the *velocity vs. frequency* profile. This optimal driving frequency occurs at a frequency a bit lower than the frequency of free resonant vibration in that direction due to the friction between the robot's feet and its guideways. The phase lag resulting from the resonant vibration causes also a phase shift in the *velocity vs. phase* profile of about 90° with respect to non-resonant mode operation ($X$). In optimal parameter settings a motion velocity in $X$ direction of 0.72 mm/s and in $Y$ direction of 0.51 mm/s was measured for a driving voltage of $U_X = 60$ V$_{p2p}$ and $U_Y = 20$ V$_{p2p}$ respectively. These results illustrate the reduction in driving voltage due to resonant operation: for a driving voltage that is 3 times lower, $Y$ motion features a velocity that is only $0.72/0.51 = 1.41$ times lower. The gain in motion velocity due to resonance operation would be much higher if the vibration in $Y$ direction would feature a higher quality factor.

The motion velocity in $X$ direction features a good linearity with the horizontal vibration amplitude and the vertical acceleration amplitude. The parasitic vertical vibration, however, limits the maximum velocity that can be reached. Motion in $Y$ direction shows the same trends, but the velocity drops faster to zero due to a lower force ratio.

The second MFID prototype is suitable for applications requiring 3 DOF motion with nanometric resolution. The traveled distance after 500 locomotion steps features a relative standard deviation below 5% in $X$ and $Y$ direction. A smallest increment of about 187 nm with a relative dispersion of less than 20% has been demonstrated. Moreover, the design of the actuation module also allows for scanning mode operation with which resolution in the order of 1 nm can be reached. The resonance operation in $Y$ direction is also visible in the transient response of the locomotion as it results in a response time of the motion velocity of more than 10 locomotion cycles, while the motion in $X$ direction already stabilizes after a few locomotion cycles.

A total power consumption of piezoelectric actuators (horizontal and vertical vibration) of 13.2 mW for $X$ motion and 4.02 mW for $Y$ motion have been calculated at maximum motion velocities. These values clearly illustrate the reduction in power consumption resulting from the resonant mode operation in $Y$ direction. However, even for $Y$ motion the power consumption is still about 1000 times higher than the reference power consumption of simply moving the robot with the same motion velocity by pushing with a constant external horizontal force. Nevertheless, this power efficiency is an improvement of about a factor 10 with respect to the first prototype. The reduction in power consumption is mainly due to resonance operation and a higher driving frequency.

In conclusion in can be said that, despite of some issues due to fabrication and assembly imperfections, this prototype has illustrated the advantages (i.e. reduced driving voltage and power consumption) of resonant operation. The third prototype presented in the next section features an on-board vibration with higher quality factor, which allows to illustrate even more clearly the advantages of resonant operation.

## 5.3 Prototype with on-board slip generation

The first prototype presented in this chapter was based on a configuration featuring only on-board contact force variation, while the second prototype integrated both contact force variation and slip generation on the robot. The third prototype presented in this chapter is based on a third MFID configuration: the one with on-board slip generation and off-board contact force variation (configuration 2 in table 3.1 on page 73).

From the first to the second prototype there was a trend of increased degree of miniaturization and of reduced driving voltage and power consumption. For this third prototype, these trend are continued. Miniaturization is pushed one step further by choosing for MEMS fabrication technology. The quality factor of the on-board resonant vibration is improved in the third prototype by choosing for electrostatic actuators and a silicon flexible frame. The obtained higher quality factor results in a higher locomotion velocity for a driving voltage similar to the one of the second prototype. The high quality factor also results finally in a much lower power consumption and a power efficiency close to 1.

Figure 5.19 shows the concept of the locomotion module presented in this section. The module is sitting on top of a substrate that is vibrating vertically in order to vary the contact force between the robot and the substrate. On the robot the slip is generated by a vibration of two on-board inertial masses. Inphase actuation of these two masses results into translational motion ($X$), while counterphase actuation results into rotational motion ($\theta_Z$). Hence the robot features 2 DOF nonholonomic motion. The variant with vibrating inertial masses has the advantage that the weight of the robot does not have to be carried by the actuator exciting the horizontal vibration. Moreover, this variant allows for an encapsulation of the vibrating masses (and its actuator), which would increase considerably the robustness of the locomotion module.

This prototype also illustrates the realization of a MFID actuator with MEMS fabrication technologies. MEMS fabrication technologies allow to scale down the size of the locomotion module to the mm-range. The two most commonly used actuation technologies for in-plane actuation of MEMS are electrostatic comb drive actuators and thermal actuators. Compared to thermal actuators the electrostatic comb drive actuators clearly show an advantage of low power consumption and high bandwidth. As powering is currently still the major bottleneck in microrobotics, the technology of comb drive actuators has been selected. This technology also features a well established fabrication technology and good resonance behavior with high quality factors. One of the drawbacks of electrostatic comb drive actuators is the low power density. However, as shown by the results of the locomotion experiments with the locomotion module presented in this section, the power density is still large enough for locomotion of microrobots on a flat surface.

The discussion of the third prototype starts with a description of the actuator design

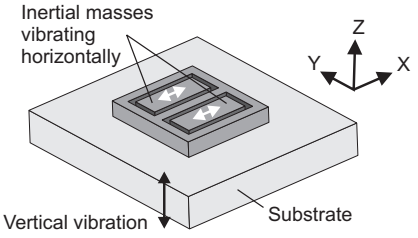


**Figure 5.19:** Concept of a 2 DOF $(X, \theta_Z)$ locomotion module with two on-board horizontally vibrating masses and a vertically vibrating substrate

(section 5.3.1) and its fabrication (section 5.3.2). Then, the displacement (section 5.3.3) and the resonance frequency (section 5.3.4) of the comb drive actuator are calculated analytically and numerically and compared to the experimentally measured performances (section 5.3.5). A description and characterization of the experimental setup (section 5.3.6) precedes the main part of the presentation of this third prototype: i.e. the study of its MFID locomotion velocity and the influence of the different input parameters (section 5.3.7). The power consumption of this locomotion platform is studied in detail section 5.3.8. Finally, before concluding this discussion of the third prototype, the rotational motion (section 5.3.9) and some perspectives for further miniaturization (section 5.3.10) are discussed.

### 5.3.1 Actuator design

The comb drive actuator that generates the vibration of the two inertial masses of the locomotion module should meet the following design constraints:

- *The weight of the vibrating mass should be as large as possible.* The vibration of the inertial mass is supposed to cause a vibration of the whole robot resulting into a slip between the robot and the substrate. Therefore the weight of the inertial mass should be as large as possible compared to the weight of the whole robot
- *The size of the locomotion module is limited.* The constraint of the total size of the robot and the first constraint of maximum vibrating inertia impose that the guiding flexures should take as little space as possible and should be well integrated within the locomotion module.

#### Arrangement of comb fingers and guiding flexures

Figure 5.20 shows the comb drive design with folded flexures that is most commonly used in literature for comb drive actuators: a double folded flexure assures the guiding from the inside, while the "push-pull"[9] comb actuators with rotor and stator comb fingers are integrated on each of the outer ends of the actuator. However this design does not meet the design constraints mentioned above. First of all the weight of the vibrating mass should be increased. The desired shape of the inertial mass (rectangular and vibrating in the direction of its longest axis, see figure 5.19) also implies that it is better in terms of guiding stability to fix the guiding flexures on the outer ends of the mass and to integrate the push-pull comb actuators in the inside (see figure 5.21(a)). However, in this design the flexures take quite a lot of space as they are not well integrated around the vibrating mass. An integration of both the upper and the lower flexure would be a little bit too complicated in terms of mechanical and electrical connections. Therefore, figure 5.21(b) shows a design with only the upper flexure that is integrated around the vibrating mass. However, one of the problems of the latter design is the electrical connection of the upper stator comb fingers. Figure 5.21(c) shows a design that solves this problem as the interconnection between the two flexure halves is removed. The removal of this interconnection lowers the transversal in-plane ($Y$) stiffness of the guiding, but this is not a big issue for this prototype as the second resonance mode is an out-of-plane mode ($Z$). However, the removal of the interconnecting bar also deteriorates the straightness of the linear guiding: each of the two separated flexures induces a parasitic torque on the inertial mass (indicated by the arrows in figure 5.21(c)). If the two flexures have the same orientation the torques of the two flexures are added. Because of the lower transversal stiffness of the separated flexures, this total parasitic torque would result in an

[9] "Push-pull" refers here to the fact that the actuator can exert a force to the left and to the right. It should be noted however that in fact the electrostatic actuation force is always an attractive force.

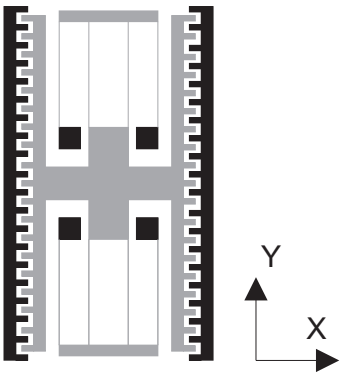


**Figure 5.20:** Comb drive design with folded flexures most commonly used in literature

in-plane rotation of the inertial mass. Therefore, figure 5.21(d) shows a design in which one of the two flexures is flipped. In this configuration, the parasitic moments of the two flexures are in opposite direction, which causes them to cancel out each other.

Figure 5.22 gives a complete overview of the chosen design for the locomotion module: two horizontally vibrating inertial masses guided by a folded flexure at each end of the mass and actuated by push-pull comb drive actuators integrated in the inside of the inertial mass.

#### Comb finger and flexure dimensions

On the mask the comb fingers (see figure 5.23(a)) have a length of $l_f = 100$ $\mu$m, an overlap of $x_f = 20$ $\mu$m and a clearance of $c_f = l_f - x_f = 80$ $\mu$m. The fingers have a width of $w_f = 15$ $\mu$m, a finger gap $d_f = 8$ $\mu$m and a pitch of $p_f = d_f + w_f = 23$ $\mu$m. The finger height is $h_f = 200$ $\mu$m (i.e. the thickness of the device layer) and each vibrating mass features $n_f = 126$ fingers for "push" and $n_f = 126$ fingers for "pull" actuation. The guiding flexures (see figure 5.23(b)) are aligned with the <110> direction and feature a length on the mask of $l_s = 3355$ $\mu$m, a width $w_s = 50$ $\mu$m and a height of $h_s = 200$ $\mu$m (i.e. the thickness of the device layer). These parameters have been chosen in function of the limits of the fabrication process.

### 5.3.2 Actuator fabrication

#### Fabrication process

The locomotion units are fabricated with the process flow depicted in figure 5.24. A detailed description of the different fabrication steps can be found in appendix E. The wafers used in the process are 4" Silicon On Insulator wafers (SOI) consisting of a silicon support layer of 380 $\mu$m and a <100> crystal orientation, 2 $\mu$m of buried silicon oxide and 200 $\mu$m of <100> silicon device layer. The fabrication process consists of three photolithographic steps: (I) aluminium structuring to make the electrical bonding pads, (II) structuring of the comb fingers and the flexures in the device layer and (III) back side structuring of the support layer to liberate the vibrating comb-drive structures.

In a first step an aluminium layer of 1 $\mu$m thick is deposited on the front side by sputtering (1). A 2 $\mu$m photo resist is spun on top of this aluminium layer, exposed and developed (2). The aluminium layer is structured in a chlorine based ($Cl_2/BCl_3$) reactive ion etching (RIE) process (3) and the photo resist is stripped (4).

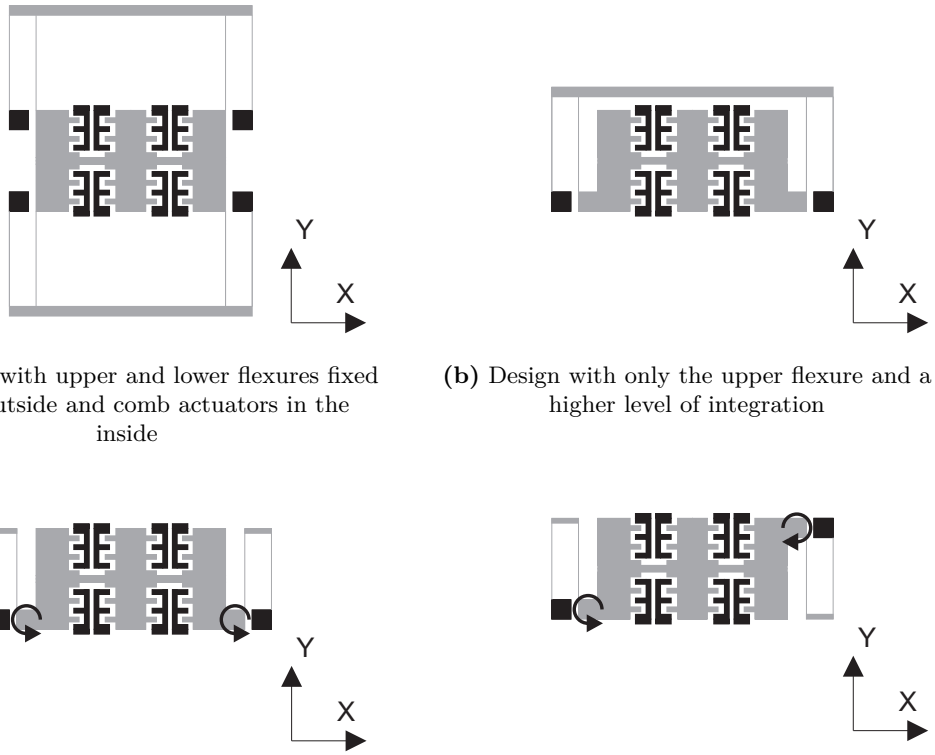


**(a)** Design with upper and lower flexures fixed on the outside and comb actuators in the inside

**(b)** Design with only the upper flexure and a higher level of integration

**(c)** Design with better access to upper comb actuators for electrical connection (arrows indicate the torque induced by the flexures when deformed along positive X axis)

**(d)** Design without parasitic rotation (arrows indicate the torque induced by the flexures when deformed along positive X axis)

**Figure 5.21:** Different designs of the comb drive actuator and the guiding flexures

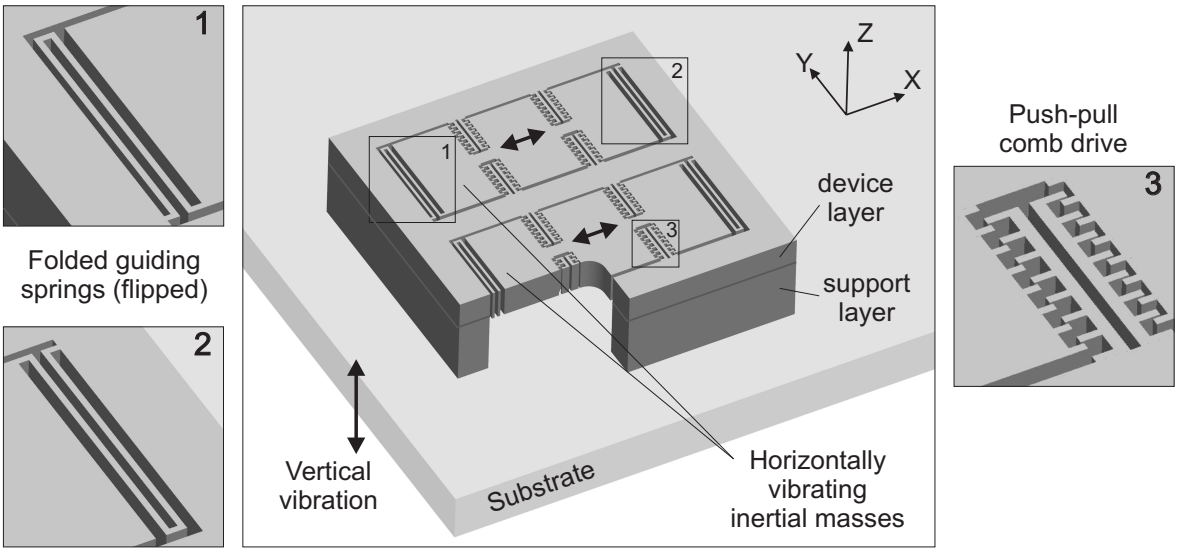


**Figure 5.22:** MFID locomotion module (overall size $10 \times 10 \times 0.582$ mm$^3$) with two on-board horizontally vibrating masses, resulting in two degrees of freedom $(X, \theta_Z)$. In order to improve the readability of this figure, the thickness of the mass has been increased and only a limited number of comb fingers has been drawn in this figure.

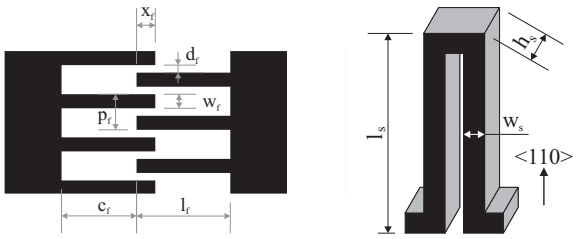


**(a)** Comb fingers **(b)** Guiding flexures

**Figure 5.23:** Definitions of symbols used for physical dimensions

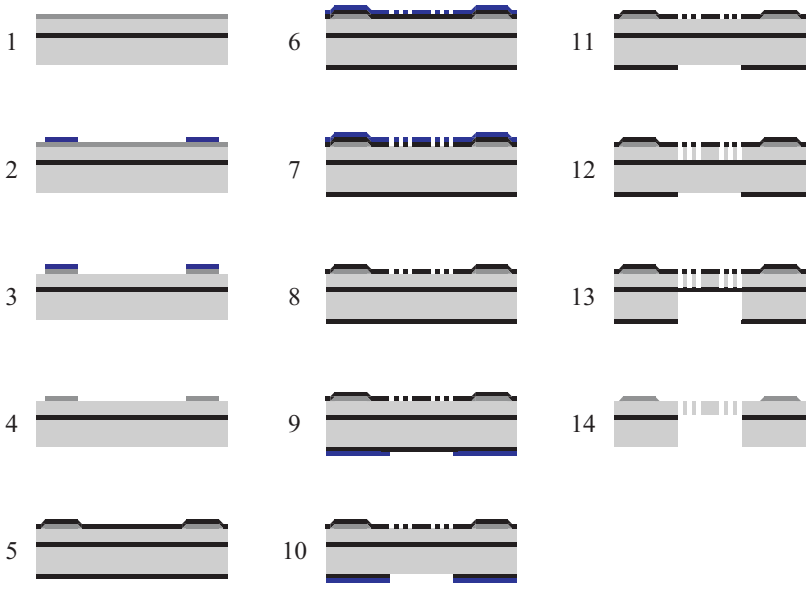


**Figure 5.24:** Process flow of the friction drive locomotion module

A low temperature silicon oxide (LTO) layer of 3 $\mu$m that will serve later as the mask for the deep reactive ion etching (DRIE) process is deposited on front side (on top of the aluminium bonding pads) and on the back side by Low Pressure Chemical Vapor Deposition (LPCVD) (5). A 3 $\mu$m photo resist is spun on the front side, exposed with alignment to the structured aluminium layer and developed (6). The front oxide layer is structured by a DRIE process based on a $C_4F_8$ chemistry (7). The front side photo resist is stripped (8). The backside oxide layer is structured in the same way: photolithography with back side alignment (9), DRIE (10) and photo resist stripping (11).

Now, the SOI wafer has a hard mask (silicon oxide) on both front and backside and is ready for DRIE of the silicon. In the most critical step the device layer of the wafer (200 $\mu$m) is structured by a high resolution Bosch DRIE process (12). Consequently the wafer is flipped and also the handle layer is etched by DRIE (13). Finally, the oxide (buried and deposited) is removed by a wet etching process (SILOX) that does not attack the aluminium bonding pads (14).

Wafer dicing is not a very good solution for separation of individual comb drive actuator due to the fragility of the comb drive teeth and the sensitivity to dust. Therefore dedicated suspending structures that can easily be broken off by applying a small pressure with a pair of tweezers were integrated into the layout of the device layer (see figure 5.25). The width of

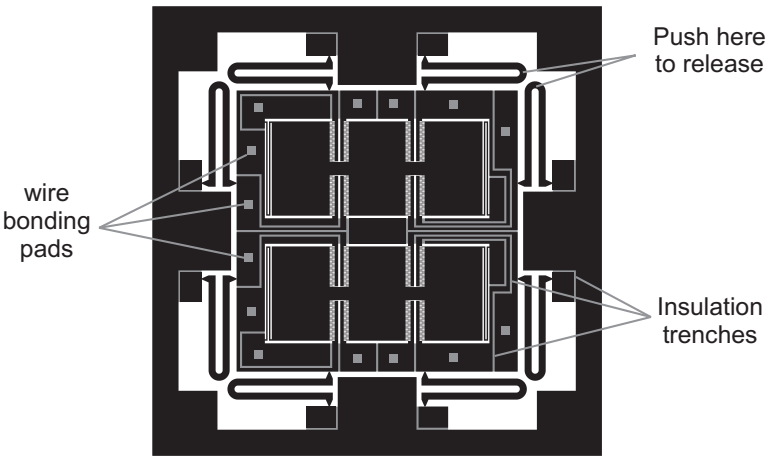


**Figure 5.25:** Release structures that can be easily broken off in order to release the individual comb drive actuators

the section that will be broken off is 32 $\mu$m.

As silicon is a semiconductor, an electrical insulation can only be obtained by physically separating the different parts in the silicon device layer. The module does, however, not fall apart as the different parts in the device layer are connected trough the buried oxide layer to the frame in the support layer. In figure 5.25 this frame in the support layer is visible in grey trough isolating trenches in the device layer. The figure also shows the square aluminium bonding pads that are used for performing the electrical connection of the locomotion module by wire bonding, as well as the isolating air trenches between the different parts of electrically insulated silicon.

### Fabrication results

Figure 5.26 shows several images of the fabricated prototypes. As can be seen in the Scanning Electron Microscope (SEM) images shown in Figure 5.26(c) and 5.26(d) the etched side walls are very smooth. An observation of the profile of the fingers by SEM has shown that when going from top to bottom the finger width first decreases down to a minimum value that is about 1 $\mu$m smaller than the finger width at the top and then increases up to a maximum value that is about 1 $\mu$m larger than the finger width at the top. Therefore, it was concluded that the finger width measured at the top is a good approximation for the average value of the finger width over the full thickness of the device layer (i.e. 200 $\mu$m). It should also be noted that even after calibration there is an uncertainty of maximum 5% on the magnification factor of the SEM microscope. Hence, an error up to 5% of the absolute measured distance should be taken into account. These SEM measurements resulted in a finger width of $w_f = 11.9$ $\mu$m, a finger gap of $d_f = 11.1$ $\mu$m and a flexure width of $w_s = 44.9$ $\mu$m. The weight of the inertial mass ($m = 10.0$ mg) has been calculated by measuring the dimensions on the fabricated prototypes and considering a density for silicon of 2.33 mg/mm$^3$. Finally, an average capacitance of 28.5 pF has been measured for each of the four channels of the actuators.

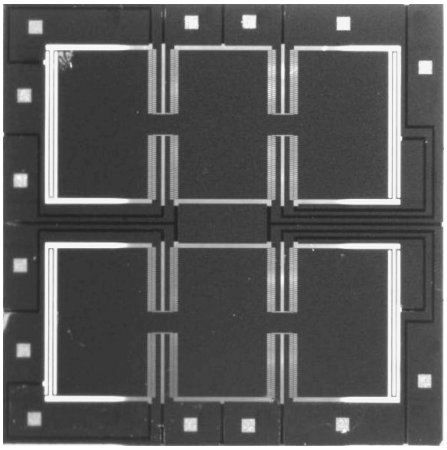

**(a)** The complete locomotion module ($10 \times 10$ mm$^2$)

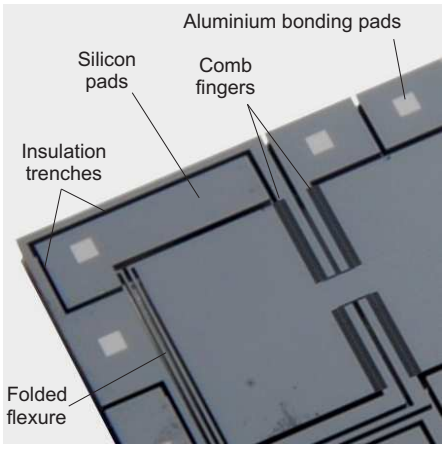


**(b)** Closeup picture of the locomotion module

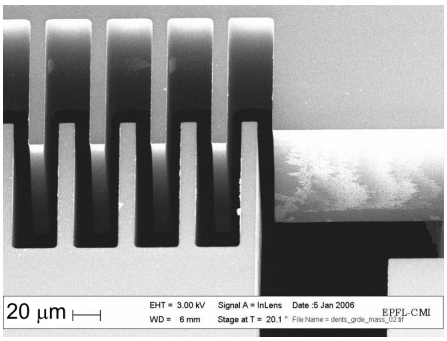


**(c)** SEM image of comb fingers

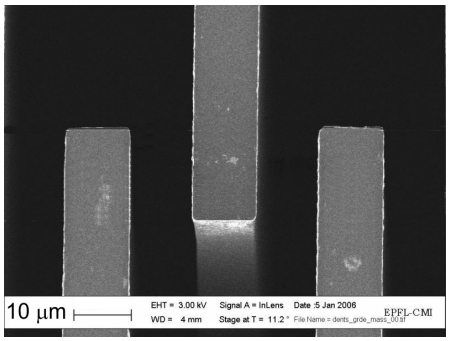


**(d)** SEM close-up of comb fingers

**Figure 5.26:** Images of the fabricated prototype

### 5.3.3 Calculation of actuator displacement

#### Analytic calculation

The electrostatic axial (here in $X$ direction) force $F_{el}$ generated by a comb drive actuator driven by a voltage $V$ can be approximated by the partial derivation of the energy in the electric field $W_{el}$ between the overlapping parts of the comb fingers

$$F_{el} = \frac{\partial W_{el}}{\partial x} = \frac{1}{2}\frac{\partial C_f}{\partial x}V^2 \approx \frac{n_f \epsilon_0 h_f}{d_f}V^2. \tag{5.21}$$

The rigidity of the two flexures in parallel for small deflections up to 10% of the flexure length can be approximated by [135]

$$k_s = \frac{E_Y h_s w_s^3}{l_s^3}. \tag{5.22}$$

With the measured dimensions the total flexure rigidity gives $k_{s,ana} = 80.8$ N/m (Young's modulus for silicon in the <110> direction $E_Y = 168$ GPa)[10]. Hence, the static displacement $\Delta x_0$ can be calculated as a result of the electrostatic force $F_{el}$ on the guiding flexures with spring constant $k_s$:

$$\Delta x_0 = \frac{F_{el}}{k_s}. \tag{5.23}$$

[10]The subscript $_{ana}$ stands for results obtained through analytical calculation.

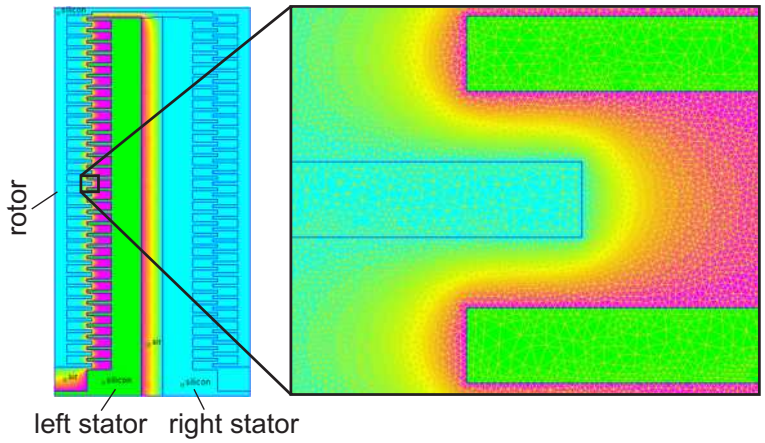


**Figure 5.27:** Simulated voltage density when applying 16 V to the left stator and 0 V to the rotor and the right stator

For a driving voltage of $V = 16$ V, an electrostatic force of $F_{el,ana} = 5.14$ $\mu$N and a static displacement of $X_{0,ana} = 63.7$ nm is obtained.

#### Numerical simulation

A planar Finite Element Analysis has been carried out for calculation of the generated electrostatic force using FEMM 4.0 [343] with an element mesh consisting of 1'043'849 first-order triangular elements. The finite element model has been generated based on the measured dimensions of the fabricated prototypes. For simplicity reasons only one of the four sets of comb fingers has been included in the simulation model. Figure 5.27 shows the simulated voltage density plot with a voltage of 16 V applied to the left stator and a voltage of 0 V applied to the right stator and the rotor (the inertial mass). The simulation shows a total force of $F_{el,num} = 5.09$ $\mu$N, which matches well the value that was calculated analytically[11]. The finite element analysis also gives a simulated capacitance of 1.71 pF per channel, which is much smaller than the measured value of 28.5 pF. This mismatch is caused by the large parasitic capacitance formed between the device layer and the substrate layer of the SOI wafer, which are separated by a 2 $\mu$m thick layer of $SiO_2$. This parasitic capacitance could be reduced significantly by reducing the area of the silicon pads below the bonding pads (see figure 5.26(b)).

### 5.3.4 Calculation of actuator resonance modes

#### Analytic calculation

As the damping in comb drive actuators is very low, the first resonance frequency of the vibrating mass can be approximated by the natural frequency of a second order spring-mass system

$$f_{r1,ana} \approx \frac{1}{2\pi}\omega_n = \frac{1}{2\pi}\sqrt{\frac{k_s}{M_i}}. \tag{5.24}$$

In order to take into account the weight of the flexures, 12/35 (i.e. Rayleigh quotient [135]) of their mass (0.10 mg) has been added to the weight of the vibrating mass. Hence, for a total mass of $M_i = 10.1$ mg and a spring constant of $k_{s,ana} = 80.8$ N/m, a resonance frequency of $f_{r1,ana} = 450$ Hz is calculated.

[11] The subscript $_{num}$ stands for results obtained through numerical simulation.

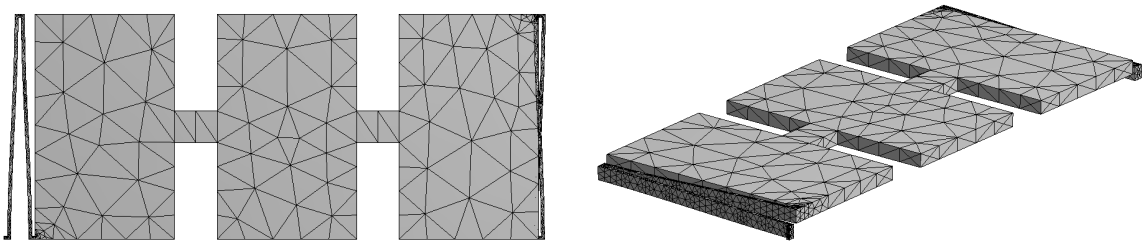

**(a)** $1^{st}$ mode: 449 Hz **(b)** $2^{nd}$ mode: 1541 Hz

**Figure 5.28:** Finite element analysis results of the first and the second vibration mode

### Numerical simulation

A Finite Element Analysis of the mechanical resonance modes has been carried out with ANSYS Workbench 11.0. The finite element model has been generated based on the measured dimensions of the fabricated prototypes and is constituted of 5063 quadratic tetrahedron elements. For simplicity reasons the comb fingers on the vibrating mass have not been modeled individually, but for every set of comb fingers a corresponding virtual volume with the same mass as the comb fingers has been added to the inertial mass.

Figure 5.28 shows the simulation result of the first resonance mode, which is a pure translation in the actuation direction of the comb drive. The second resonance mode corresponds to a vertical out-of-plane translational vibration of the inertial mass. The first mode has been simulated at $f_{r1,num} = 449$ Hz, which corresponds very well to the value calculated analytically. The resonance frequency of the second mode is simulated at $f_{r2,num} = 1541$ Hz, which is high enough compared to the first mode in order to ensure sufficient decoupling.

The stiffness in $X$ direction has been simulated to be $k_{s,exp} = 81.2$ N/m. With this stiffness the simulated electrostatic force $F_{el,num} = 5.09$ $\mu$N causes a static displacement of $X_{0,num} = 62.6$ nm, which corresponds very well to the value calculated analytically ($X_{0,ana} = 63.7$ nm). The stiffness in $Y$ direction of the guiding flexures is simulated as $k_{s,y} = 2.35 \cdot 10^4$ N/m, which results in a stiffness ratio of $k_{s,y}/k_s = 289$.

## 5.3.5 Actuator experimental characterization

In order to be able to measure the displacement of the comb drive actuators experimentally one small piece of silicon ($M_{mirror} = 2.24$ mg) serving as a mirror for position measurement by interferometer (specifications in appendix F.4) was glued vertically on top of the vibrating masses. As the mirror is interconnecting both inertial masses, an additional mass of $M_{mirror}/2 = 1.12$ mg should be considered for each inertial mass, resulting in a corrected inertial mass of $M_i' = M_i + M_{mirror}/2 = 11.2$. This additional mass will decrease the resonance frequency calculated above by a factor $\sqrt{M_i/M_i'} = 0.95$, but it is the only way to measure the displacement amplitude of this actuator by interferometer, which allows for static and dynamic characterization with nanometric precision. The corrected analytically and numerically calculated resonance frequency are $f'_{r1,ana} = 0.95 f_{r1,ana} = 427$ Hz and $f'_{r1,num} = 0.94 f_{r1,num} = 426$ Hz respectively.

Figure 5.29 shows the measured frequency response and voltage response of the vibration of the inertial masses with a clamped frame. This response shows a quasistatic (at 50 Hz) displacement of $X_{0,exp} = 59.5$ $\text{nm}_{p2p}$ and a resonance vibration amplitude of $X_{f_{r1},exp} = 33.5$ $\mu\text{m}_{p2p}$ at the resonance frequency ($f_{r1,exp} = 424.1$ Hz) for a peak-to-peak (p2p) driving

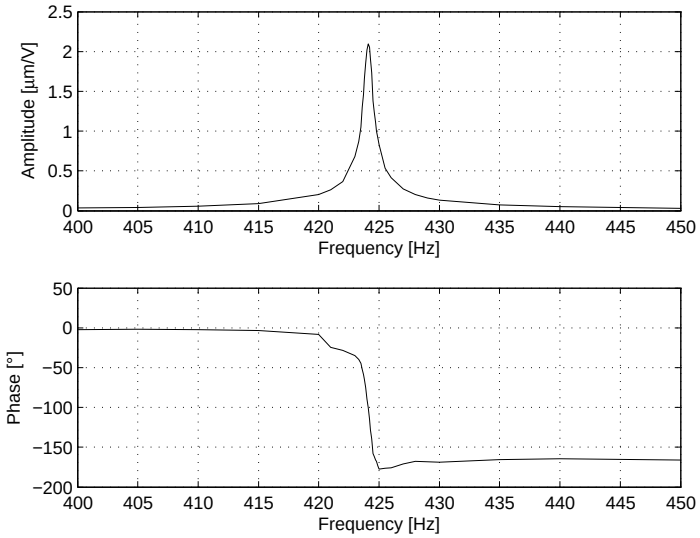


**Figure 5.29:** Bode plot around the resonance frequency of the comb drive actuator when actuated in "pull" mode with 16 $V_{p2p}$

voltage of 16 $V_{p2p}$. These amplitude measurements were carried out at atmospheric pressure[12] and in simple pull mode (so with only one channel per vibrating mass). Hence, the amplitude can still be doubled if the actuator would be excited in push-pull mode (two channels per vibrating mass). The measured static displacement of $X_{0,exp} = 59.5$ $nm_{p2p}$ matches well the calculated $X_{0,ana} = 63.7$ $nm_{p2p}$ and simulated $X_{0,num} = 62.6$ $nm_{p2p}$. A good agreement is also found between the measured resonance frequency of $f_{r1,exp} = 424.1$ Hz the corrected analytically calculated resonance frequency $f'_{r1,ana} = 427$ Hz and the corrected numerically calculated resonance frequency $f'_{r1,num} = 426$ Hz.

The frequency response shown in figure 5.29 reaches $1/\sqrt{2}$ of the resonance vibration amplitude at 423.71 Hz and 424.47 Hz. Hence, a quality factor of $Q = 424.1/(424.47 - 423.71) = 558$ is obtained (see equation 5.13 on page 138). This value is rather high for operation at atmospheric pressure at a frequency of some hundreds of Hz [135]. Furthermore, the actuator reaches a static amplitude of 59.5 nm and an resonance amplitude of 33.5 $\mu$m. As expressed in equation 5.14 the quality factor of a second order system can also be approximated by the ratio between the vibration amplitude at resonance and the quasistatic vibration amplitude. This results in $Q' = 33500/59.5 = 563$, which corresponds well to the quality factor calculated just above. The high value of the quality factor can be explained on the one hand by the low viscous damping ($c$) resulting from the absence of the support layer below the comb drive actuator and on the other hand by the large weight of the vibrating mass $m$ (see equation 5.13 on page 138).

Figure 5.30 shows the measured vibration amplitude at resonance frequency in function of the comb drive actuation voltage for different signal shapes (sine wave and square wave) and different actuation modes ("pull" and "push-pull"). All three curves show a quadratic behavior up to vibration amplitudes of around 50 $\mu m_{p2p}$, above which the vibration amplitude starts to saturate against an upper limit of about 97 $\mu m_{p2p}$. This saturation is due to the gap between two flexure halves, which is only 52.9 $\mu$m, limiting the motion of the inertial

[12]The pressure has no influence on the static displacement of a comb drive actuator but it does have an important influence on the resonance displacement as the damping of a silicon comb drive actuator is dominated by air damping.

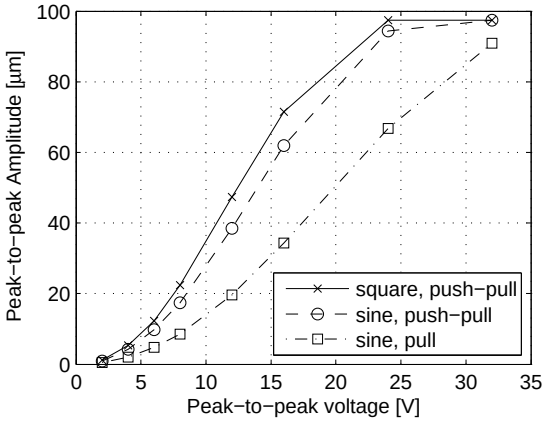


**Figure 5.30:** Vibration amplitude versus driving voltage of the comb drive actuator used for the locomotion experiments when actuated at resonance frequency (424.1 Hz) with a sine wave in "pull" mode and in "push-pull" mode and with a square wave in "push-pull" mode

mass to a peak-to-peak amplitude of 105.8 $\mu m_{p2p}$. The measured vibration amplitude already saturates at lower values than this mechanical stop, due to the squeeze film damping, which becomes very important when the gap between the two flexure halves becomes in the range of some $\mu$m (note that the flexures have a height of 200 $\mu$m).

Figure 5.30 also shows that as long as no saturation occurs the actuation in "push-pull" mode gives a vibration amplitude that is the double of the one obtained in the "pull" mode. Moreover, the graph also shows that at resonance a square wave signal yields to a higher vibration amplitude than a sine wave signal. However, due to the high quality factor, an excitation with a square wave signal still results in a sinusoidal vibration of the inertial masses. When considering the Fourier series of a square wave signal with unity amplitude

$$\begin{aligned} U_{square}(t) &= \frac{4}{\pi}\sum_{k=1}^{\infty}\frac{\sin((2k-1)2\pi ft)}{(2k-1)} \\ &= \frac{4}{\pi}\left(\sin(2\pi ft)+\frac{1}{3}\sin(6\pi ft)+\frac{1}{5}\sin(10\pi ft)+\ldots\right) \end{aligned} \tag{5.25}$$

it is clear that the term at the fundamental frequency $f$ has an amplitude of $4/\pi = 1.27$. This corresponds to the measured values: for a driving voltage of 2, 4, 6 and 8 V (i.e. the voltages at which no saturation occurs yet) the ratios between the measured vibration amplitude for a square wave and a sine wave input signal are 1.26, 1.28, 1.26 and 1.28 respectively.

### 5.3.6 Experimental setup for locomotion experiments

A measurement setup for characterization of the linear velocity of the comb drive locomotion module has been developed. The experimental setup consists of two parts: the vertical vibration stage and the comb drive locomotion module. The function of the vertical vibration stage is to generate an off-board variation of the contact force between the locomotion module and its guiding substrate, while the slip is generated on-board by the comb drive actuator. Two cylindrical shafts and a flat surfaces for linear guiding of the locomotion module are glued on top of the vibrating stage (see figure 5.31).

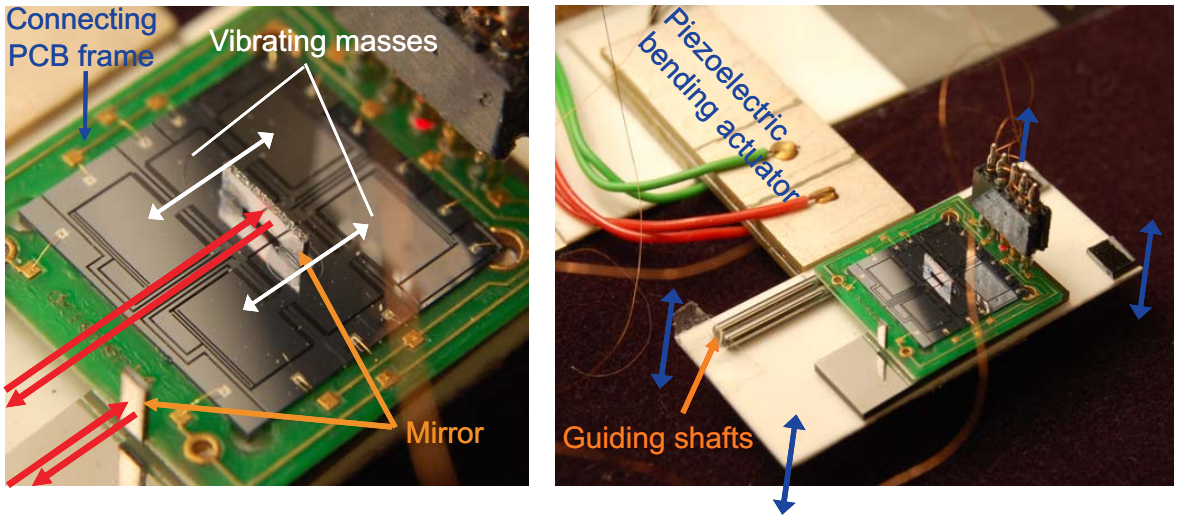


**Figure 5.31:** Setup for characterization of the linear velocity of the comb drive locomotion module

### Vertical vibration stage

The vertical vibration is generated by a piezoelectric bending actuator. The bender consists of a trimorph structure: two piezoelectric layers with a passive support layer in between (see figure 5.32). In order to have a pure vertical translation of the vibrating stage, the electrodes on the bender actuator have been cut in two segments. Each electrode halve of the bender is actuated with an opposite voltage resulting in an opposite curvature, which compensates the parasitic rotation of a single bender actuator. The static response (ratio between vertical displacement $Z$ and actuation voltage $V$) of such a double trimorph actuator can be deduced from the piezoelectric bending theory presented in [344]:

$$\frac{Z}{V} = 2\frac{12d_{31}E_{Y,p}(h_p + h_s)}{E_{Y,s}h_s^3 + 2E_{Y,p}h_p(4h_p^2 + 6h_ph_s + 3h_s^2)}\frac{(l/2)^2}{2} \tag{5.26}$$

The bender actuator in the experimental setup features an active length $l_p = 16$ mm, a width $w_p = 10$ mm, a thickness of the piezoelectric layers of $h_p = 1$ mm and a support layer thickness of $h_s = 0.5$ mm. The used piezoelectric material is PIC 151 ($E_{Y,p} = 66.7$ GPa, $d_{31} = -210$ pm/V, see also appendix F.1), while the support layer is in Alumina-Oxide ($E_{Y,s} = 360$ GPa). Filling in all these parameters in equation 5.26 gives a total displacement of 15.0 nm/V.

Figure 5.33 shows the measured frequency response of the vertical vibration stage. This frequency response has been measured by interferometer at two different points: one at the position of the guiding shafts and one at the position of the guiding surface[13] (see figure 5.32). The graph in figure 5.33 shows the average between these two measurements. A static displacement of 17.6 nm/V and a resonance frequency of 890 Hz is observed. The measured static displacement is a bit higher than the calculated one, which is probably due to variations in the piezoelectric constant $d_{31}$. In the frequency region of interest (420-440 Hz) no significant phase shift is observed, but a small increase in vibration amplitude is present: 21.0 nm/V @ 420 Hz and 21.6 nm/V @ 440 Hz.

[13] A comparison of the measured amplitudes at these two points allowed to measure the parasitic rotation of the vibration platform about the motion axis. This parasitic rotation has been compensated for by applying

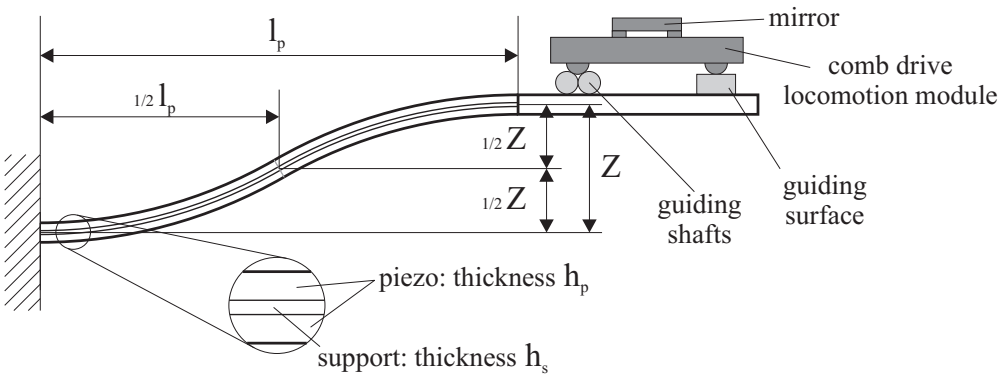


**Figure 5.32:** Trimorph structure for vertical vibration of comb drive locomotion module experimental setup

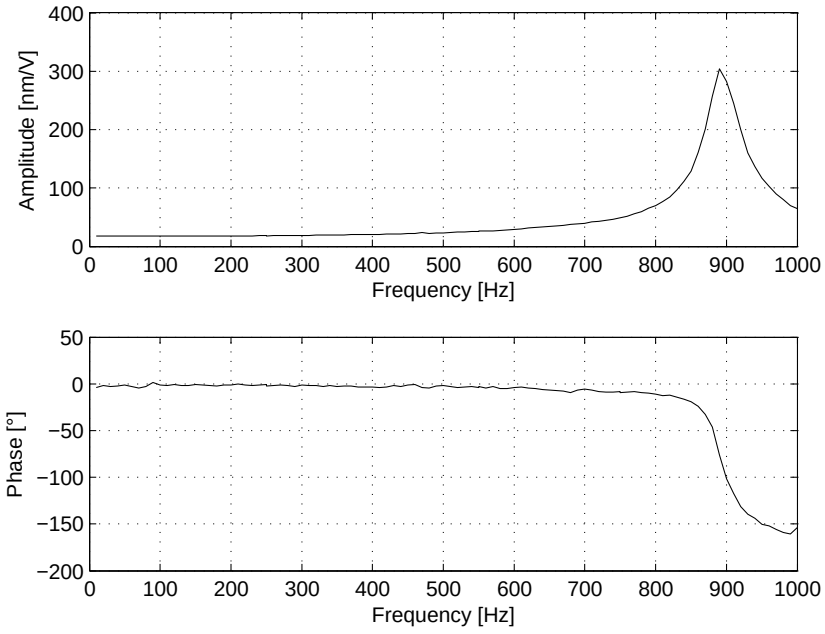


**Figure 5.33:** Frequency response of the vertical vibration of the measurement setup for the comb drive locomotion module

**Comb drive locomotion module**

For the locomotion experiments the comb drive actuator is glued inside a small PCB $14 \times 13 \times 0.5$ mm$^3$ on which a connector is soldered (see figure 5.31). On the bottom of this PCB three feet (sapphire half spheres of ∅1 mm × 0.6 mm) are glued, two of which are guided linearly by the two shafts (∅1 mm) fixed on the vertically vibrating stage (see figure 5.32). The position of the vibrating inertial masses and of the frame are measured by interferometer (specifications in appendix F.4), of which the beam is reflected on the mirrors glued between the inertial masses and on the side of the PCB (see figure 5.31).

The total weight of the locomotion module is $M_r = 504$ mg (including PCB and connector) and the total vibrating inertial mass (two vibrating masses of 10.1 mg + mirror of 2.24 mg) weights $2M_i = 22.4$ mg. Hence, the weight of the frame to which the feet are glued is $M_f = 482$ mg and the ratio of inertia $q_I$ defined as the ratio between the weight of the inertial mass and the inertia of the frame is $q_I = 2M_i/M_f = 0.046$. The linear guiding of two of the spherical feet by the two shafts on the vibrating stage causes a slight increase in contact force, as was also the case for the characterization setup (see figure 4.5). As the shafts and the spheres both have a diameter of ∅1 mm, the contact angle is $\beta = 30°$. The two feet that are guided by the two shafts support half of the weight of the robot. Therefore, the contact geometry coefficient $c_g$ defined in section 4.3.2 as the ratio between the contact force and the vertical load is given by

$$c_g = \frac{F_c}{F_p} = \frac{1}{2}(1 + \frac{1}{\cos(30°)}) = 1.08. \tag{5.27}$$

The static friction coefficient of sapphire feet on stainless steel shafts has been identified in section 4.3.2 to be $\mu_s = 0.15$. The static friction force between the locomotion module and the slider at a vertical load only due to gravity (so without vertical vibration) is

$$F_{t,s,grav} = \mu_s c_g M_r g = 801 \ \mu\text{N}. \tag{5.28}$$

$F_{t,s,grav}$ is the minimum inertial force that must be generated by the vibration of the inertial masses in order to allow the creation of slip at the absence of any vertical vibration. In the case of a vertical vibration with acceleration amplitude $A_Z$ the static friction force at the moment of minimum contact force is

$$F_{t,s,min} = F_{t,s,grav}(1 - \frac{A_Z}{g}). \tag{5.29}$$

$F_{t,s,min}$ is the absolute minimum inertial force that must be generated by the inertial masses in order to allow for locomotion with a vertical vibration with acceleration amplitude of $A_Z$. In the case of a vertical acceleration of $A_Z = 0.8g$ as is used in most of the motion experiments presented later in this section this results in a minimum friction force of $F_{t,s,min} = 160$ $\mu$N.

It has been calculated analytically in section 5.3.3 that for a driving voltage of 16 V the comb drive actuator generates an electrostatic force of about $F_{el,16\text{V}} = 5.14$ $\mu$N on each inertial mass. Consequently, in the case of a driving voltage of 32 V as used in most of the motion experiments presented later in this section a total electrostatic force (sum of the force exerted on both masses) of $F_{el,tot,32\text{V}} = 2 \cdot 4 \cdot F_{el,16\text{V}} = 41.1$ $\mu$N is generated.

In section 4.4.4 the force ratio $q_F$ has been defined as the ratio between the maximum inertial force $F_{i,X,max}$ generated by the axial ($X$) vibration and the minimum instantaneous

a small correction factor to the ratio between the two voltages applied to the two electrode halves of the trimorph bender.

| | Symbol | Unit | Default value |
|---|---|---|---|
| Frequency | $f$ | Hz | 433 |
| Phase shift | $\phi$ | $^\circ$ | 20 |
| Hor. actuation voltage | $U_X$ | $V_{p2p}$ | 32 |
| | | $V_{amp}$ | 16 |
| Vert. acceleration amp. | $A_Z$ | $g$ | 0.8 |
| Max. motion velocity | $v_{r,avg}$ | mm/s | 3.0 |

**Table 5.2:** Default input parameter settings for the locomotion experiments with the third prototype

static friction force between slider and substrate $F_{t,s,min}$

$$q_F = \frac{F_{i,X,max}}{F_{t,s,min}}. \tag{5.30}$$

One of the conditions for MFID locomotion is that $q_F > 1$. If we would consider an inertial force $F_{i,X,max}$ equal to electrostatic force generated by the comb drive actuator $F_{el,tot,32V} = 41.1\ \mu$N and a minimum friction force of $F_{t,s,min} = 160\ \mu$N as calculated above for the case of a vertical acceleration of $A_Z = 0.8g$, the force ratio $q_F = 41.1/160 = 0.26$ would be smaller than 1 and no locomotion would be possible. However, actuation in resonance mode allows for an accumulation of kinetic and potential energy, which results in an increased vibration amplitude and therefore an increased inertial force. Hence, for actuation at 32 V a gain in vibration amplitude of at least $1/0.26 = 3.8$ is required in order to allow for locomotion.

### 5.3.7 Locomotion experiments

The experimental setup consisting of the vertical vibration stage and the comb drive locomotion module has been used for several locomotion experiments. A first experiment takes a closer look to the stepping behavior of the MFID actuator. In the following set of experiments the average motion velocity is considered and the influence of phase shift, driving frequency, horizontal vibration amplitude and vertical acceleration amplitude is investigated. In a last set of experiments the open loop repeatability and the motion resolution of the comb drive locomotion module is investigated.

Except if explicitly specified otherwise, the motion experiments with this prototype have been carried out at the default parameter settings as listed in table 5.2.

#### Measured stepping behavior

Figure 5.34 shows an interferometer measurement of the stepping behavior of the comb drive locomotion module when actuated in "push-pull" mode when actuated at default parameter settings (see table 5.2). The average vibration amplitude of the inertial mass is 69.8 $\mu m_{p2p}$, while the frame advances with steps of 7.7 $\mu$m. From the vibration amplitude obtained in figure 5.30 for a square wave "push-pull" actuation at a driving voltage of 12 $V_{p2p}$ (47.3 $\mu m_{p2p}$) it can be extrapolated that at 32 $V_{p2p}$ a vibration amplitude of $(32/12)^2 47.3 = 336\ \mu m_{p2p}$ would have been obtained if no mechanical stops and no squeeze film damping would occur within the guiding flexures. Hence, the vibration amplitude of the inertial mass during locomotion is $69.8/336 = 21\%$ of the one obtained when the frame would be rigidly clamped. Figure 5.34 also shows that it is during the backward motion of the inertial mass that the frame makes its forward step. This is logically explained by the fact that the frame and the

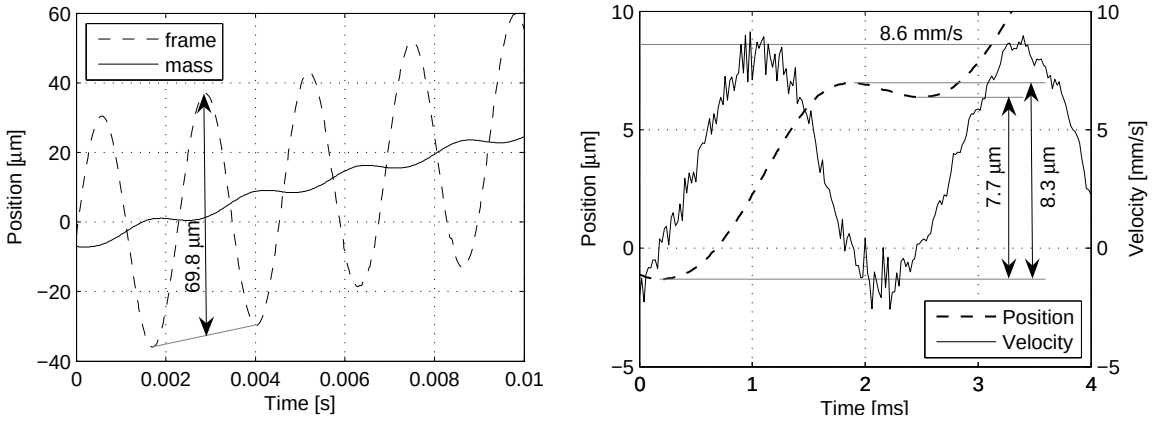


**(a)** Position of frame and inertial mass

**(b)** Closeup of position and velocity of frame

**Figure 5.34:** Measured stepping motion of the comb drive locomotion module

mass are interconnected by a spring, which makes it a mass-spring-mass system, in which the masses always move in opposite direction.

In section 4.4.3 the stepping efficiency $\eta_{step}$ was defined as the ratio between the average motion velocity and the maximum instantaneous velocity of the axial vibration. Figure 5.34 shows that the motion of the frame features a peak instantaneous velocity of 8.6 mm/s. A step size of 7.7 $\mu$m at a driving frequency of 433 Hz results in an average motion velocity of 3.3 mm/s. Hence, a step efficiency of $\eta_{step} = 0.35$ is obtained.

In the next paragraphs the influence of the different parameters of the input signals on this average motion velocity will be studied. The measurements have been carried out automatically with a LabVIEW program (the same as the one used in section 4.3.1) that contains several nested loops, which allow to change the input parameters and measure the average motion velocity automatically.

### Influence of the phase shift on motion velocity

Figure 5.35 shows the influence of the phase shift between the actuation of horizontal and vertical vibration on the motion velocity in the case of a sine wave and a square wave actuation. For every value of the phase shift the velocity was measured five times and the solid line traces the averages of these measurements. The graph shows that the maximum velocity in positive direction is obtained for a phase shift of 20°, while the maximum velocity in negative direction is obtained at a phase shift of 200°. Zero velocity is reached at 110° and 300°. These values are quite different form those obtained from the characterization setup (80° and 260° respectively) as discussed in section 4.4.2. This difference is due to the extra phase lag that is introduced because of the fact the actuator is actuated at resonance. Figure 5.35 also shows that higher motion velocities are obtained with a square wave signal than with a sine wave signal, which is due to the higher vibration amplitude as shown in figure 5.30).

### Influence of the driving frequency on motion velocity

Figure 5.36 shows the influence of the driving frequency on the motion velocity at default parameter settings. At each frequency value five velocity measurement have been carried out and the solid line traces the average of these measurements. A maximum velocity of 3.0 mm/s is reached at a frequency of 433 Hz. This optimal frequency is higher that the

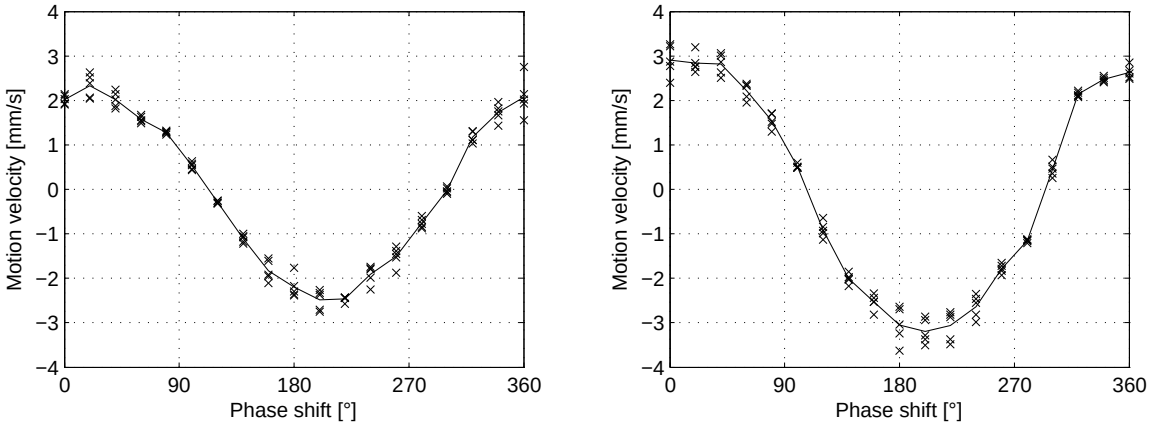


**(a)** Sine wave **(b)** Square wave

**Figure 5.35:** Influence of the phase shift on the motion velocity for a sine wave and a square wave actuation signal at a driving frequency of 433 Hz

resonance frequency observed from the frequency response of the comb drive module when the frame is clamped (see figure 5.29). During locomotion, however, the frame of the comb drive module is free to slide — with a certain amount of friction — within its linear guiding. When both masses (frame $M_f = 482$ mg and inertial masses $M_i = 22.4$ mg) are unconstrained, both masses will be vibrating around a virtual immobile point that is located inside the guiding flexure. Hence the spring with stiffness $k_s$ can be considered as two springs with stiffnesses $k_{s,f}$ and $k_{s,i}$ in series (with $1/k_s = 1/k_{s,f} + 1/k_{s,i}$) connecting this internal, immobile point to $M_f$ and $M_i$ respectively. Resonance of the complete system occurs when both subsystems $(M_f, k_{s,f})$ and $(M_i, k_{s,i})$ enter the resonance mode. The resonance frequency of both subsystems must coincide, which is expressed by the condition

$$\frac{k_{s,f}}{M_f} = \frac{k_{s,i}}{M_i}, \tag{5.31}$$

or by using the ratio of inertia $q_I = M_i/M_f$ the conditions becomes $k_{s,i} = q_I k_{s,f}$. Replacing $k_{s,f} = (1/k_s - 1/k_{s,i})^{-1}$ yields

$$k_{s,i} = k_s(q_I + 1). \tag{5.32}$$

So, the resonance frequency of the unconstrained mass-spring-mass system will be a factor $\sqrt{q_I + 1} = 1.023$ higher than the case were the frame was clamped. This calculation results in a unconstrained resonance frequency of $1.023 \cdot 424.1 = 433.8$, which corresponds very well to the frequency of 433 Hz at which the maximum motion velocity has been measured.

The measured motion velocity reaches a value of $3.0/\sqrt{2}$ mm/s at a frequency of 431.52 Hz and 434.10 Hz, giving a frequency interval of 2.58 Hz and thus a quality factor of $Q_{loc} = 433/2.58 = 168$. This quality factor during locomotion is 3.3 times lower than the one extracted from the frequency response of the comb drive module with a clamped frame ($Q = 558$). This loss in quality factor is caused by the increased energy losses due to the friction between locomotion module and its linear guiding. The measured frequency-velocity behavior also indicates that a mismatch of 1 Hz between the frequency generated by the driving electronics and the unconstrained resonance frequency of the comb drive module would only have a limited impact on the motion velocity.

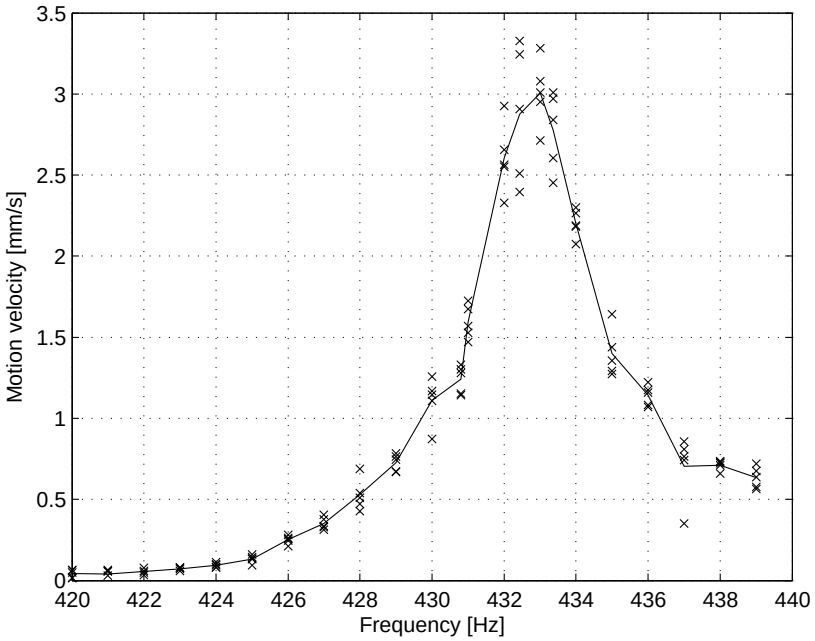


**Figure 5.36:** Influence of the driving frequency on the motion velocity for a phase shift of 20° and a square wave signal

### Influence of the horizontal vibration amplitude on motion velocity

Figure 5.37(a) shows the measured influence of the comb drive actuation voltage to the motion velocity at default parameter settings. As the vibration amplitude of the comb drive actuator depends quadratically of the driving voltage, the voltage axis is represented with a quadratic scale. For every value of the horizontal vibration amplitude the velocity was measured ten times and the solid line traces the averages of these measurements. As expected, the motion velocity decreases with decreasing horizontal vibration amplitude (comb drive actuation voltage), however, the velocity decreases faster than linearly with respect to the vibration amplitude[14].

As discussed in section 5.3.6 on page 160 one of the conditions for MFID locomotion is that the force ratio $q_F = F_{i,X,max}/F_{t,s,min}$ is larger than 1. It was already calculated in equation 5.29 on page 163 that at a vertical acceleration amplitude of $A_Z = 0.8g$ the minimum force that must be generated by the vibration of the inertial masses in order to allow for the generation of slip is $F_{t,s,min} = 160$ $\mu$N. The inertial force generated by the horizontal vibration is given by

$$F_{i,X,max} = M_i A_X = M_i X (2\pi f)^2. \tag{5.33}$$

Hence, from the condition $q_F = F_{i,X,max}/F_{t,s,min} = 1$, the minimum horizontal vibration amplitude $X_{min}$ at which locomotion is still possible can be deduced as

$$X_{min} = \frac{F_{t,s,min}}{M_i (2\pi f)^2}. \tag{5.34}$$

At resonance frequency ($f = 433$ Hz) and for $M_i = 22.4$ mg the resulting minimum vibration amplitude is $X_{min} = 0.97$ $\mu m_{amp} = 1.93$ $\mu m_{p2p}$. The vibration amplitudes of the inertial mass

[14] A quadratic decrease of the velocity with the comb drive voltage would result in a straight line in figure 5.37(a), as the voltage scale is quadratic and the vibration amplitude depends quadratically of the driving voltage (as illustrated in figure 5.30).

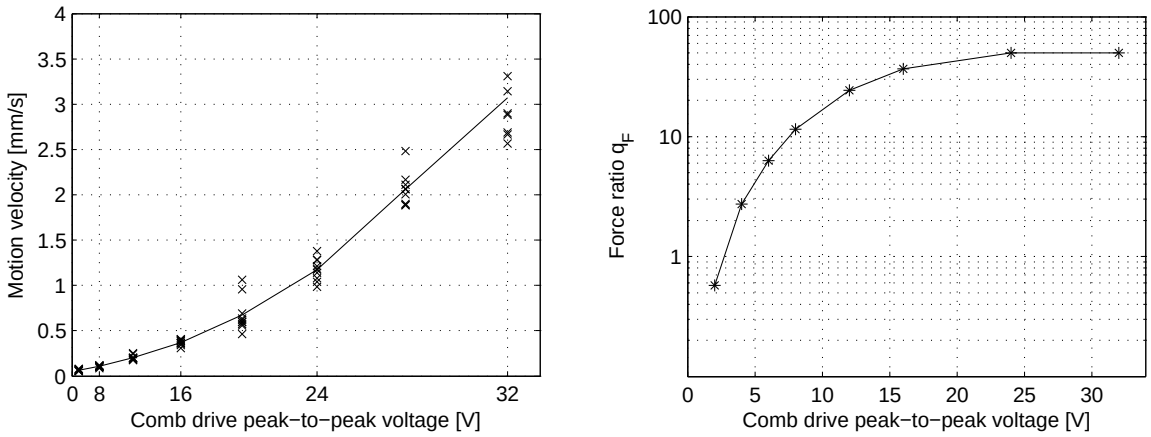


**(a)** Motion velocity

**(b)** Force ratio $q_F$

**Figure 5.37:** Influence of the comb drive voltage on the motion velocity and on the force ratio

in function of the comb drive voltage have been measured before in the experiment shown in figure 5.30. Figure 5.37(b) shows the calculated force ratio in function of the comb drive voltage based on these experimental data. The graph shows that only for a driving voltage of 2 V ($q_F = 0.57$) the force ratio is smaller than 1. This is confirmed by the experimental observation, which has shown that no stable motion for voltage below 4 V could be obtained. The graph also shows that already for driving voltages above 8 V a force ratio of more than 10 is obtained, which is more than enough for stable motion[15].

### Influence of the vertical acceleration amplitude on motion velocity

Figure 5.38 shows in the influence of the vertical acceleration amplitude (expressed as a fraction of $g$) on the motion velocity at default parameter settings. For every value of the acceleration amplitude the velocity was measured ten times and the solid lines traces the averages of these measurements. The graph shows a linear increase of the motion velocity with the acceleration amplitude up to a maximum reached at $0.9g$. At an acceleration amplitude of $1g$ the measured velocity drops to a lower value and the dispersion increases. This velocity drop is caused by the fact that at a vertical acceleration of $1g$ the locomotion module starts to jump, which causes uncontrolled bouncing of the feet, resulting in unstable motion. Similar behavior was observed for the characterization setup (see section 4.4.3). No measurements for vertical accelerations above $1g$ have been carried out with this comb drive prototype, because the resulting bouncing of the feet combined with the parasitic force exerted by the wires caused the locomotion module to go out of its linear guiding. The same problem occurs now and then at a vertical acceleration of $0.9g$. That's why the locomotion experiments with the comb drive locomotion module were carried out at a default vertical acceleration of $0.8g$.

[15] As was observed from figure 5.30 a saturation of the vibration amplitude occurs for driving voltages above 15 V due to the air damping within the guiding flexures. In reality, this saturation will result in acceleration peaks that are higher than the ones calculated by equation (5.33). However, as for higher actuation voltages the force ratio is much higher than 1, this effect has not been considered here.

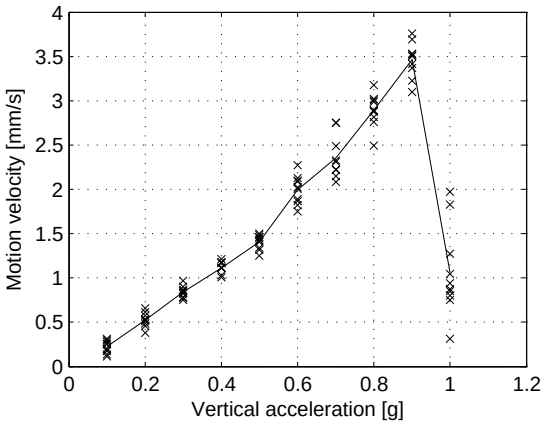


**Figure 5.38:** Influence of the vertical acceleration amplitude (expressed as a fraction of g) on the motion velocity

### Open loop repeatability and motion resolution

In order to be able to measure the open loop repeatability of the comb drive locomotion module, experiments consisting of measuring the distance $\Delta x$ traveled after 500 locomotion steps (i.e. actuation periods) have been carried out. The experiment has been carried out at default parameter settings and has been repeated 50 times and the standard deviation is calculated for a comb drive actuation signal with a sine shape and a square shape. The experiment resulted in an average traveled displacement of 2.82 mm and 3.55 mm for the sine wave and the square wave actuation signal respectively and a relative standard deviation of 1.9% and 2.5%. The higher velocity and dispersion was already visible from figure 5.35. Moreover, the ratio between both average displacements $3.55/2.82 = 1.26$ is close to the theoretical ratio $4/\pi = 1.27$ of the resonance vibration amplitude with a square and a sine wave signal (see section 5.3.6). The measured relative standard deviations are close to the one measured for the piezoelectric characterization setup (2.4%, see figure 4.35 on page 116).

In order to judge the capability of this comb drive locomotion module to perform high resolution motion, one must study the smallest step that can be performed with an "acceptable" repeatability. The condition for "acceptable" repeatability is defined here by a relative standard deviation below 20%. Figure 4.36 shows the measured displacement after 10, 5, 2 and 1 locomotion steps for three different values of the comb drive actuation voltage. Every measurement has been repeated 10 times and the error bars in the graph delimit the $1\sigma$ confidence interval. Each step measurement is performed at a random (within a range of 400 $\mu$m) position on the shaft. The experimental results show a large dispersion on the traveled distances. The smallest increment with a relative standard deviation below 20% is reached for a driving voltage of 24 V and 5 locomotion steps, which results in an average increment of 1.12 $\mu$m with a standard deviation of 0.21 $\mu$m (i.e. 19% of the average increment).

A comparison of the experimental data shown in figure 4.36 with the ones obtained with the piezoelectric characterization setup (see figure 4.36 on page 117) learns that — apart from the higher dispersion — the increments of the comb drive locomotion module show a dependence of the number of locomotion steps that is much less linear than for the characterization setup. This is caused by the fact that the comb drive locomotion module is operated in resonance mode. Due to the high quality factor, the comb drive module needs a large amount of actuation periods before the maximum vibration amplitude is reached[16].

[16] An alternative to reduction of the step size by reduction of the comb drive voltage would be by a deviation

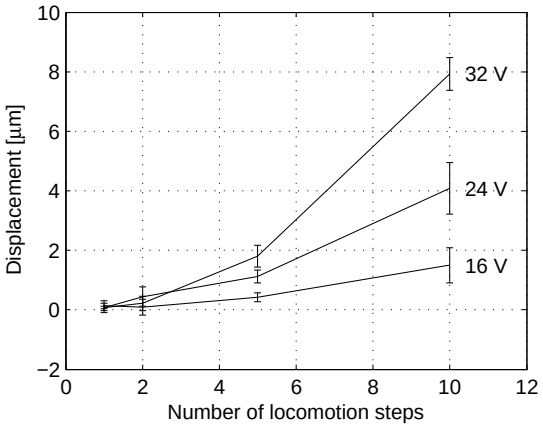


**Figure 5.39:** Traveled displacement in function of the number of locomotion steps and the comb drive voltage

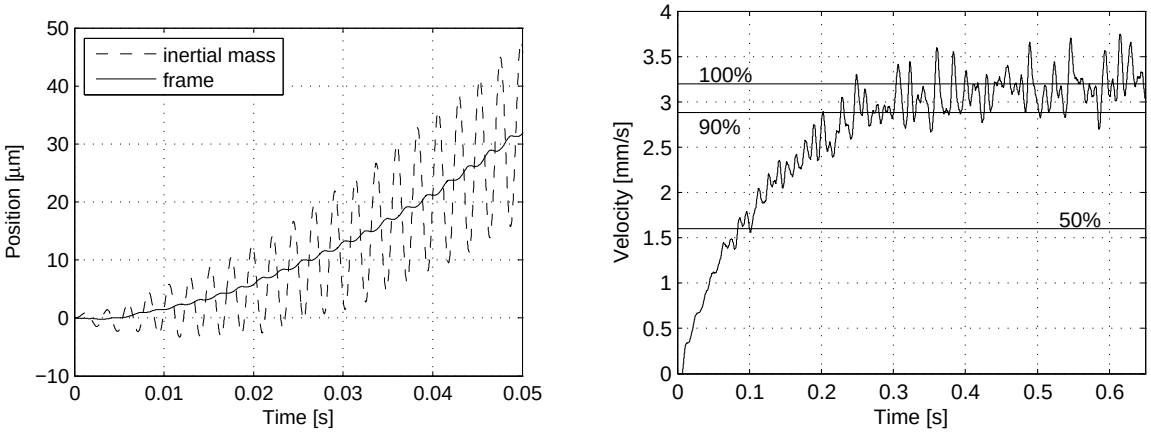


**(a)** Frame and mass position

**(b)** Frame Velocity

**Figure 5.40:** Closeup of the transient response at the start of a actuation signal

Figure 5.40(a) shows the transient response of the comb drive locomotion module at the start of the actuation signal. Figure 5.40(a) shows the transient velocity response of the frame obtained by derivation of the position and filtering with a $4^{th}$-order Butterworth filter at 100 Hz. These graphs clearly show that many actuation periods are required before stabilization of the motion velocity. Figure 5.40(a) shows that 50% of the steady state average motion velocity is reached after 85 ms or about 37 actuation periods and 90% after 280 ms or about 120 actuation periods. This transient response explains the non-linear characteristic of the results in figure 5.39.

### 5.3.8 Power consumption

This section calculates the power consumption and the power efficiency for the comb drive locomotion module in the case of an actuation with parameter settings and performances as the experiment shown in figure 5.34: i.e. push-pull mode with a square wave signal at optimal driving frequency ($f = 433$ Hz), with a comb drive voltage of $U = 32$ V, an externally gen-

from the resonance frequency. This could result in a reduction of this observed transient effect due to the resonance mode operation.

erated vertical vibration with acceleration amplitude of $0.8g$ resulting in a measured motion velocity of $v = 3.0$ mm/s.

The power consumption of a MFID actuator can be calculated in different ways, depending on what is included. First of all, the comb drive locomotion module is based on a combination of on-board and off-board actuation. For this calculation we will only consider the on-board power consumption. But for calculation of the on-board power consumption there are still different possibilities. A first possibility is to consider only the power that is injected into the vibration of the inertial mass ($P_{in,mass}$) in order to evaluate purely the power consumption of the locomotion principle. A second possibility is to consider the power input to the electrostatic comb drive actuators by calculating the power necessary to charge the capacitances ($P_{in,act}$). Finally, a third possibility is to consider the power input to the driving electronics ($P_{in,elec}$).

In order to evaluate the power efficiency of the locomotion module, one must compare the different power consumptions mentioned above to a certain reference power consumption. As for the previous prototypes we will consider as a reference value the power consumption of simply pushing with a horizontal constant force without variation of the contact force between slider and base. Pushing with a horizontal force implies an energy dissipation due to the friction between slider and base. Analogously to equation (5.28) on page 163 the dynamic friction force between the comb drive locomotion module (mass $M_r = 504$ mg) and its linear guiding that is given by

$$F_{t,d,grav} = \mu_d c_g M_r g = 534 \ \mu\text{N}. \tag{5.35}$$

with $c_g = 1.08$ and $\mu_d = 0.1$ the dynamic friction coefficient of sapphire on stainless steel as identified for the characterization setup from figure 4.18 on page 99. Hence, the reference power consumption of sliding with a constant velocity $v = 3.0$ mm/s is calculated by

$$P_{ref} = v F_{t,d,grav} = 1.76 \ \mu\text{W}. \tag{5.36}$$

The power injected into the vibration of the inertial mass ($P_{in,mass}$) can be obtained by integration of the electrostatic force $F_{el}$ over the comb drive actuator displacement $\Delta x$. As calculated in section 5.3.6 at 32 V the comb drive fingers generate a total (sum of both masses) electrostatic force of $F_{el,32\text{V}} = 41.1$ $\mu$N. Figure 5.34 shows that at default parameter settings the inertial mass is vibrating with a vibration amplitude of $X = 69.8$ $\mu\text{m}_{p2p}$. Hence, for one actuation period (back and forth motion of the mass) the power input in the inertial mass is given by

$$W_{in,mass} = 2 F_{el,32\text{V}} X = 5.74 \text{ nJ}. \tag{5.37}$$

The power consumption for an actuation frequency $f = 433$ Hz is then given by

$$P_{in,mass} = f W_{in,mass} = 2.48 \ \mu\text{W}. \tag{5.38}$$

This power consumption $P_{in,mass}$ is only a bit higher than the reference power consumption $P_{ref} = 1.76$ $\mu$W calculated above.

In order to calculated the power $P_{in,act}$ required for actuation of the two comb drive actuators, one must know the value of the electrical capacitance of the different channels of the actuator. As mentioned in section 5.3.3 a capacitance of 1.71 pF per channel at rest position was calculated by finite element analysis. However, experimentally a capacitance of 28.5 pF was measured for each of the channels. This mismatch between calculated and measured capacitance is caused by the large parasitic capacitance formed between the device layer and the substrate layer of the SOI wafer as already discussed in section 5.3.3 on page 157.

| | | $P_{ref}$ | $P_{in,mass}$ | $P_{in,act}$ | $P_{in,elec}$ |
|---|---|---|---|---|---|
| Power consumption | [$\mu$W] | 1.76 | 2.48 | 25.3 | >50.6 |
| Ratio $P_{ref}/P_{in}$ | | 1 | 0.71 | 0.070 | <0.035 |

**Table 5.3:** Summary of the different power consumption calculations of the comb drive locomotion module and comparison with the reference power consumption of pushing with a horizontal external force

Driving four such capacitances of 28.5 pF with a $f = 433$ Hz square wave voltage between $U = 0$ V and $U = 32$ V requires a power consumption of

$$P_{in,act} = 4f\frac{CU^2}{2} = 25.3\ \mu\text{W}. \tag{5.39}$$

As the actuator can be driven with a square wave voltage signal, the driving electronics becomes very simple. A digital output from the controlling device (microcontroller or other) driving a digital switch supplied at 32 V is sufficient. So, there is no need for Digital-to-Analogue (DAC) converters or any amplifier, which reduces considerably the complexity of the driving electronics as well as its power consumption. When charging a capacitance with a switch and a fixed supply voltage, the efficiency is maximum 50% as half of the supplied energy is lost in the internal resistances of the switch and the voltage supply. Therefore, the power consumption of the actuator together with its driving circuit will be at least $P_{in,elec} \geq 50.6\ \mu$W. The efficiency of the driving electronics can still be improved and the supply voltage can be lowered by driving with a RLC-circuit. However, this increases the complexity of the driving electronics, which is especially an issue for an overall robot size of 1 cm$^3$ and below.

As seen earlier in this section, the motion velocity of the comb drive locomotion module can be reduced by on-board control by reducing the horizontal vibration amplitude. This is illustrated in figure 5.37(a) by adjusting the horizontal vibration amplitude through variation of the comb drive actuation voltage. As the comb drive actuator is operated at resonance frequency, the horizontal vibration amplitude can also be adjusted through Pulse Width Modulation (PWM), which is very easy to implement with a digital driving circuit.

Table 5.3 summarizes the values of the different power consumptions $P_{ref}$, $P_{in,mass}$, $P_{in,act}$ and $P_{in,elec}$ and compares them to the reference power consumption $P_{ref}$ of simply pushing the robot with an external force. It should be reminded that these values do not include the power consumption of the externally generated vertical vibration. A first conclusion to be drawn from the table 5.3 is that motion with this MFID prototype at default parameter settings is almost as efficient as simply pushing. Secondly, although the power consumption of the actuator $P_{in,act}$ is low (some tens of $\mu$Ws), a comparison with $P_{in,mass}$ shows that there is still room for improving the efficiency of the actuator. As already mentioned in section 5.3.3 the parasitic capacitance of the comb drive actuator can be easily reduced significantly by reducing the area of the silicon pads in the frame of the device layer (see figure 5.26(b) on page 156). Finally, it should be stressed that the fact that this actuator can be actuated with a square wave voltage signal can potentially result in a driving electronics that is very simple and efficient in terms of power consumption.

### 5.3.9 Rotational motion

All the locomotion experiments presented above study the linear ($X$) motion of the 2 DOF ($X, \theta_Z$) locomotion module. The rotational motion ($\theta_Z$) has not been tested in this work. The main reason for this is that the wires for supply of the actuation signals, although only

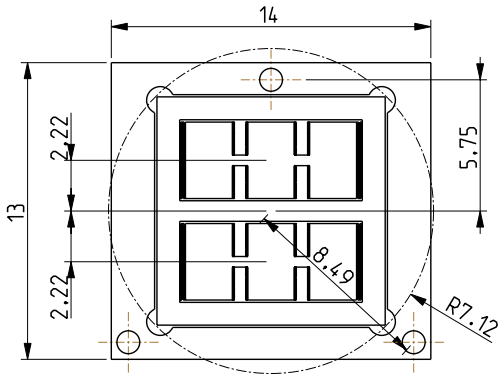


**Figure 5.41:** Radii of feet and masses with respect to the center of the locomotion module

$\varnothing$50 $\mu$m thick, exert a non-negligible force (and torque) on the locomotion module. Hence, when putting the locomotion module on a flat substrate without linear guiding, large parasitic motion will occur. The best solution for 2 DOF motion experiments with a robot of only 504 mg would be through untethered operation. A solution with on-board powering and on-board electronics would be the most flexible solution, but such a development requires a very large investment. A simpler solution could be to connect the power source directly to the comb drive actuators. The power could then be transmitted wirelessly through an inductive link or by solar cells. Within the I-Swarm project high voltage solar cell modules based on a technology in which several amorphous silicon cell elements are structure and connected in series have been developed by the IMT at the University of Neuchatel in cooperation with EPFL [345].

The feasibility of rotational motion can be studied by comparing the force ratio $q_F$ (i.e. the ratio between the inertial effect of the horizontal vibration and the friction between slider and substrate) for linear and rotational motion. In the case of rotational motion the force ratio $q_F$ is not a ratio between forces, but rather between torques. This means that the distance from the center of rotation at which the inertial force or the friction force is generated has an important influence. As can be seen in figure 5.41 the center of gravity of the inertial masses are at a radius 2.22 mm from the center of rotation. The feet, however, are positioned at a larger distance. Half of the weight of the locomotion module is supported by the foot in the middle, which is at 5.75 mm from the center of rotation. The other half of the robot is supported by the two feet in the corners, which are at a radius of 8.49 mm from the center of rotation. The average of these two feet radii is 7.12 mm, which is 3.2 times larger than the radius at which the inertial force is generated. Hence, if assuming the same vibration amplitude of the inertial masses, the force ratio for rotational motion will be 3.2 times smaller than in the case of linear motion. This means that the curve in graph 5.37(b) on page 168 is shifted downwards with a factor 3.2. This increases the minimum voltage at which rotational motion can be achieved to around 5 V. At 32 V the force ratio is reduced to $q_F = 50/3.2 = 15.6$, which is still far above the limit of $q_F = 1$.

In the case of rotational motion the ratio of inertia $q_I$ also becomes a ratio between moments of inertia $q_I = I_2/I_1$ instead of a ratio of masses. For rotational motion the ratio of inertia is equal to $q_I = 0.23/19.6 = 0.012$, which is 3.8 times lower than the ratio of inertia for linear motion ($q_I = 0.046$). Consequently, the resonance frequency without clamping the frame will be only $\sqrt{q_I + 1} = 1.006$ times higher than the resonance frequency with a clamped frame (i.e. 424.1 Hz). As a good match between the unclamped resonance frequency and the frequency of maximum motion velocity is observed for the case of linear motion (see

figure 5.36 on page 167), the maximum rotational velocity can be expected at a frequency of $1.006 \cdot 424.1 = 426.6$ Hz.

Finally, still remains the question of what will happen with the quality factor during rotational motion. As for linear motion the quality factor during rotational motion will be lower than the quality factor of clamped vibration. But how much this reduction will be is difficult to predict at this stage. An estimation of the rotational velocity could, however, be made by an energy analysis. If we consider that the energy dissipation is dominated by the friction between the robot's feet and the substrate and if we apply the same input energy to the actuator (i.e. same voltage, (more or less) the same frequency and the same capacitance), then we can expect to obtain the same vibration amplitude of the feet during rotational motion as during linear motion. Based on this theory, a tangential velocity of the feet of 3 mm/s would for an average radius of the feet position of 7.12 mm result in a rotational velocity of $\arctan(3/7.12) = 23$ °/s.

### 5.3.10 Miniaturization

The simplicity of the MFID locomotion module resulting from the combination of on-board and off-board actuation as well as the choice of silicon comb drive actuators fabricated by MEMS technologies allow for miniaturization of the locomotion module to a size of only a few mm$^2$. Figure 5.42 shows two locomotion modules of a size of $2 \times 2$ mm$^2$ fabricated on the same wafer as the $10 \times 10$ mm$^2$ locomotion modules used for the locomotion experiments presented previously in this section[17]. The module with two vibrating masses (figure 5.42(a)) features 2 DOF $(X, \theta_Z)$, while the one with only one vibrating mass only features linear motion $(X)$. The major issue with these mm-size locomotion modules is not to fabricated them but rather to find a way to test them. Powering by wires was problematic, but still possible for linear motion of the $10 \times 10$ mm$^2$ module, but is not feasible anymore for modules of a size of only a few mm. Hence, testing of mm-size locomotion modules must be done wirelessly by on-board integration of a powering module. Actuation for linear motion in "pull-mode" (i.e. by using only one of the pair of stationary "push-pull" comb fingers) requires only two electrical contacts: one channel and one ground. So, linear motion could maybe also be tested by means of two sliding electrical contacts. However, due to the very low contact forces, contact resistances due to a very thin oxide layer on the conductive tracks could be a problem. The use of sliding electrical contacts for powering of mm-size locomotion modules has already been reported in literature by [241]. They also had some problems with electrical contacting, but this could be solved by applying a thin layer of an electrically conductive grease.

Table 5.4 shows the performances of the $10 \times 10$ mm$^2$ locomotion module together with the estimated performances of the two mm-size locomotion modules shown in figure 5.42. The estimated performances are obtained by extrapolation from the results obtained with the $10 \times 10$ mm$^2$ module. The values for the stiffness of the guiding flexures are obtained analytically by filling in the measured flexure dimensions in equation 5.22 on page 156. The values for the inertial masses are also based on measured dimensions and include the weight of the mirror for the $10 \times 10$ mm$^2$ design. The resonance frequency is obtained analytically from stiffness and mass. The quality factor for the $10 \times 10$ mm$^2$ design has been measured with a clamped frame. The quality factors for the $2 \times 2$ mm$^2$ designs were obtained by extrapolation from the value for the $10 \times 10$ mm$^2$ design and by assuming that

[17] The size of the connecting PCB around the $10 \times 10$ mm$^2$ locomotion module is not taken into account when considering the overall size of the locomotion module, because the PCB is only there for being able to connect the module electrically to an external amplifier. In the case of an integration of an on-board electronics on top of the robot, the overall footprint size of the robot could be very close to $10 \times 10$ mm$^2$.

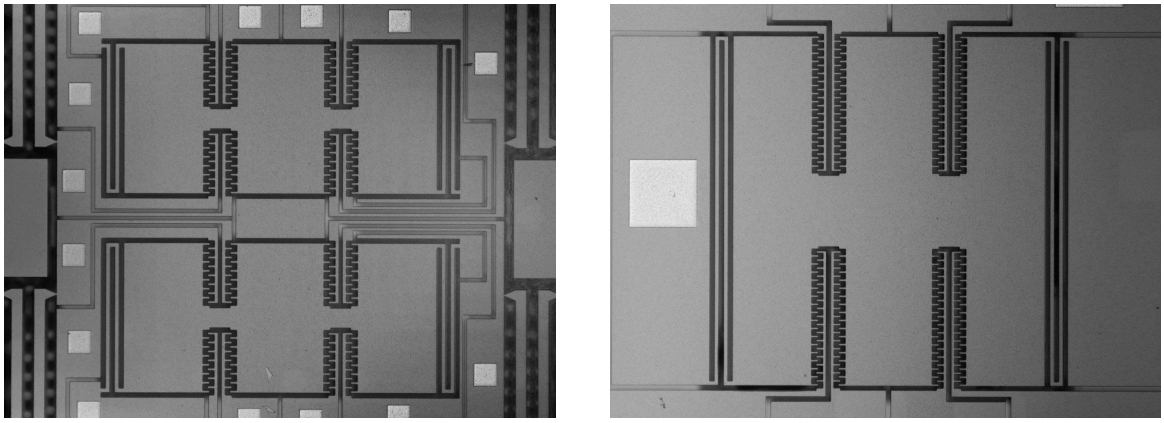

**(a)** Module with two DOF $(X, \theta_Z)$ **(b)** Module with one DOF $(X)$

**Figure 5.42:** Pictures of comb drive locomotion modules of a size of $2 \times 2$ mm$^2$

the quality factor is proportional to $\sqrt{km}/c$ (see equation 5.13 on page 138) with the damping coefficient $c$ that is considered proportional to the number of fingers. The electrostatic force is calculated analytically with equation 5.21 on page 156 based on measured dimensions. The static displacement is obtained by division of the electrostatic force by the flexure stiffness. The resonance displacement is obtained by multiplication of the static displacement by the quality factor[18]. The step size for the $2 \times 2$ mm$^2$ designs was obtained by extrapolation from the measured results of the $10 \times 10$ mm$^2$ design by assuming the same ratio between step size and the vibration amplitude of the inertial mass at resonance. This assumption is probably not completely correct, so the obtained step size for the $2 \times 2$ mm$^2$ designs is only a rough estimation. The maximum locomotion velocity is obtained by multiplication of step size and resonance frequency. The obtained motion velocity for the two $2 \times 2$ mm$^2$ designs is in the same order of magnitude than the velocity of the $10 \times 10$ mm$^2$ design, which illustrates that the scaling laws for electrostatic actuators are advantageous. The value for the power consumption of the $10 \times 10$ mm$^2$ design is the one of the power injected in the comb drive actuator, which can still be reduced considerably by reduction of the parasitic capacitance between device and support layer. The values for the power consumption of the $2 \times 2$ mm$^2$ designs have been obtained by assuming that this parasitic capacitance will scale proportionally with the surface in the silicon frame, so a factor of $5^2 = 25$.

In conclusion it can be said that, although the extrapolated values in table 5.4 should be interpreted with care, locomotion with velocities of some mm/s, a power consumption in the order of 1 $\mu$W for a driving voltage of 32 V should be possible with the fabricated $2 \times 2$ mm$^2$ MFID locomotion modules.

### 5.3.11 Conclusion

In this section a MFID locomotion module based on a configuration with *off-board* contact force variation and *on-board* slip generation has been presented. The contact force variation

[18]It should be noted that these resonance displacements are only virtual displacements because for the $10 \times 10$ mm$^2$ design and for the $2 \times 2$ mm$^2$ design with one inertial mass they can never be obtained due to a mechanical stop in the guiding flexures limiting the maximum displacement in each direction to 52.9 $\mu$m and 24.3 $\mu$m respectively. However, this is not a problem during locomotion as the additional energy dissipation resulting from the friction force between the locomotion module and the substrate will lower the quality factor, resulting a lower vibration amplitude of the inertial mass (for the $10 \times 10$ mm$^2$ design the vibration amplitude of the inertial mass was reduced to 69.8 $\mu m_{p2p}$ during locomotion).

| Size | [mm$^2$] | $10 \times 10$ | $2 \times 2$ | $2 \times 2$ |
|---|---|---|---|---|
| # Inertial masses | | 2 | 2 | 1 |
| Flexures stiffness | [N/m] | 80.8 | 462.6 | 34.7 |
| Inertial mass | [mg] | 11.22 | 0.36 | 0.86 |
| Resonance frequency | [Hz] | 433.8 | 5705 | 1011 |
| Number of comb fingers | | 126 | 30 | 70 |
| Quality factor | | 558 | 1004 | 182.2 |
| Electrostatic force @ 32 V | [$\mu$N] | 20.6 | 4.46 | 10.49 |
| Static displacement | [nm$_{amp}$] | 255 | 9.63 | 303 |
| Resonance displacement | [$\mu$m$_{amp}$] | 142 | 9.67 | 55.2 |
| Step size | [$\mu$m] | 6.9 | 0.469 | 2.68 |
| Max. motion velocity | [mm/s] | 3.0 | 2.68 | 2.71 |
| Power consumption | [$\mu$W] | 25.3 | <1.01 | <1.01 |

**Table 5.4:** Estimated performances of the two mm-size comb drive locomotion modules

results from the inertial effect of a vertical vibration of the guiding substrate of the locomotion module. The slip is generated by the inertial effect of the in-plane vibration of two on-board inertial masses. An inphase vibration of both masses results in a linear motion ($X$), while a counterphase vibration results in a rotation ($\theta_Z$). Both masses are actuated in resonance mode, which allowed to test the resonance actuation as one of the advantages of the proposed MFID principle.

MEMS technology has been chosen for the fabrication of the locomotion module in order to allow for further miniaturization to the mm-scale. The developed actuator module features a size of $10 \times 10 \times 0.6$ mm$^3$. The masses are actuated by electrostatic comb drive actuators fabricated on a SOI (Silicon On Insulator) wafer by Deep Reactive Ion Etching (DRIE). The chosen variant of vibrating inertial masses allows for a complete encapsulation of the inertial masses and its actuators, which would improve considerably the robustness of these microfabricated actuators. A good match between analytically calculated, numerically calculated and experimentally measured static displacement and resonance frequency was observed. Moreover, high quality factors above 500 have been measured due to the low damping of silicon comb drive actuators.

A linear motion velocity of 3.0 mm/s has been measured for a driving voltage of 32 V, a vertical acceleration of $0.8g$ and optimal phase shift and driving frequency. At these parameter settings the locomotion step size is 7.7 $\mu$m and the vibration amplitude of the inertial mass is 69.8 $\mu$m. This vibration amplitude is only 19% of the vibration amplitude obtained with clamped feet. This reduction of vibration amplitude at resonance is caused by the energy dissipation in the slip between the locomotion module and the guiding substrate. Besides, at these optimal parameter settings the locomotion module features a stepping efficiency (i.e. the ratio between average motion velocity and maximum instantaneous velocity) of $\eta_{step} = 0.35$.

The optimal phase shift between axial (horizontal) and perpendicular (vertical) actuation for maximum velocity in positive and negative direction are 20° and 200° respectively, from which can be concluded that an extra phase shift of $-60°$ is introduced by the actuation in resonance mode. The measured optimal driving frequency is 433 Hz, which matches very well the resonance frequency of the actuator without clamping of the frame. The measured velocity peak around the resonance frequency has a quality factor of 168, which is — due to the additional damping caused by the slip — 3.4 times lower than the quality factor of the

comb drive actuator with a clamped frame. If no amplification of the vibration amplitude due to the resonance would be present an actuation at 433 Hz and 32 V would result in a force ratio (i.e. the ratio between generated axial inertial force and minimum static friction force) of $q_F = 0.26$, which is too low for MFID motion. However, due to the high quality factor at resonance a force ratio of $q_F = 50$ is obtained. Another advantage of the resonance mode operation is that the comb drive actuator can be driven by a square wave signal, which is much easier to generate than a sinusoidal signal. Moreover, the square wave signal results in a motion velocity that is 1.26 times higher than with a sinusoidal signal, which matches well to theoretical calculation.

The motion velocity decreases with decreasing comb drive actuation voltage and the lower voltage limit (between 2 V and 4 V) at which no more stable motion can be obtained, corresponds to a force ratio of $q_F = 1$. The resonance operation allows for a variation of the vibration amplitude by Pulse Width Modulation (PWM), which is very efficient in terms of power consumption of the driving electronics. The velocity can also be varied by varying the amplitude of the externally generated vertical acceleration. A good linearity from 0 to $0.9g$ has been observed.

A relative dispersion of about 2% is measured on the distance traveled with 500 locomotion steps. The smallest increment with acceptable repeatability consists of 5 locomotion cycles with a total increment size of 1.12 $\mu$m. This smallest increment is limited by the slow transient response resulting from the large quality factor at resonance. This shows that a MFID actuator driven in resonance is less suited for precision applications.

When actuated at the optimal parameter settings mentioned above, resulting in a motion velocity of 3.0 mm/s, a power if 2.65 $\mu$W is injected into the vibration of the inertial mass. This value is just a bit higher than the reference power dissipated when simply pushing the locomotion module with a constant axial force (1.76 $\mu$W). The power injected into the capacitance of the comb drive actuators is about 10 times higher than the power injected into the vibration of the inertial mass, which shows that there is still room for optimization. However, the fact that this MFID locomotion module can be driven with a square wave signal of 32 V and below allows for very efficient digital electronics with a total power consumption close to the power consumption of the locomotion module of 25.3 $\mu$W.

Future works include the testing of the rotational motion, untethered operation and testing of the smaller mm-size prototypes that have already been fabricated. Based on an energy analysis a rotational velocity of 23 °/s is expected. Extrapolation of the results obtained with the $10 \times 10$ mm$^2$ locomotion module show that locomotion with these mm-size prototypes with velocities of some mm/s and power consumption in the range of 1 $\mu$W should be feasible.

In conclusion it can be said that the presented comb drive locomotion module illustrates very well the advantages of the MFID principle: (1) simplicity, allowing for further miniaturization, (2) relatively low voltages, (3) low power consumption and (4) square wave operation, allowing for efficient driving electronics.

## 5.4 Discussion

### 5.4.1 Comparison of the three MFID prototypes

In chapter 4 the basic behavior of a MFID actuator has been studied by comparing simulation and experimental results on a linear characterization setup. In the current chapter the suitability of the MFID principle for locomotion of mobile microrobots has been illustrated by the presentation of the design and the characterization of three different prototypes. Table 5.5 gives an overview of the properties, driving conditions and performances of these three MFID prototypes[19]. The three prototypes are based on three different configurations: two of them are based on a combination of on-board and off-board actuation (prototype 1 and 3) and one with only on-board actuation (prototype 2). The three prototypes also have three different sets of degrees of freedom (DOF). Prototype 2 has all three in-plane DOF and therefore allows for full holonomic locomotion within the plane, which is an important advantage when using the robots for some kind of manipulation task. The third prototype has only two DOF ($X$, $\theta_Z$), but can still reach all positions within the plane by means of non-holonomic motion. The first prototype is not capable of rotation by itself. However, by bringing two such robots into contact with each other and having them move along a circular path around each other rotational motion could be obtained as a result of cooperative behavior.

According to the definition given in section 2.3 the body length ($L$) corresponds to the geometric mean of the footprint dimensions. For the third prototype the connection PCB around the silicon locomotion module is not included in the physical dimensions as its function is only electrical connection allowing for tethered operation. The electrical interconnection could, if desired, be integrated in the silicon frame around the vibrating masses. There is a trend of increasing degree of miniaturization from the first to the third prototype. Moreover, the third prototype offers very promising perspectives for further miniaturization, due to the choice of MEMS fabrication technologies. Millimeter size prototypes have already been fabricated, but not yet tested because at that size tethered operation is really not an option anymore, which complicates considerably the locomotion experiments. The first two prototypes are based on piezoelectric actuators. For the second prototype this has the advantages of motion with nanometric resolution because it is the only prototype which allows for quasistatic scanning motion of the robot's body with respect to its feet.

Of all three prototypes the first prototype operates at the lowest driving frequency, which has the disadvantage to result in a high driving voltage and a high power consumption. The second prototype is operated at the highest driving frequency, which allows for lower driving voltages, but has the major drawback of an increased sensitivity to parasitic vertical vibration and therefore requires a better guiding quality of the flexible frame.

The first prototype is not operated at resonance, which — in combination with the low driving frequency — results in a very high driving voltage. The voltages for horizontal and vertical vibration of the second prototype are much lower due to a combination of resonant operation and high driving frequency. Despite of the average operation frequency of the third prototype, its driving voltage is still relatively low, which is due to the resonance operation and the good quality factor of the resonance of the comb drive actuators.

The first prototype features only 1 on-board actuation channel for 2 DOF[20]. For a given

[19]The values for the second prototype apply for motion in $Y$ direction as this is the only direction that is operated in resonance. Only for the step efficiency the value for $X$ motion is given as the one for $Y$ motion is not very representative due to the ripple on the $Y$ vibration of the feet observed in figure 5.18(d) on page 146.

[20]It is the possibility for actuation with only 1 on-board channel that allowed for the prototype with on-board electrostatic clamping presented in appendix section C.1 to have 2 DOF motion that are driven and controlled wirelessly by a projector.

| | | 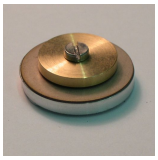 Prototype 1 | 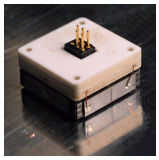 Prototype 2 | 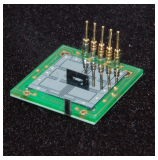 Prototype 3 |
|---|---|---|---|---|
| Slip generation | | off-board | on-board | on-board |
| Force variation | | on-board | on-board | off-board |
| DOF | | $X$, $Y$ | $X$, $Y$, $\theta_Z$ | $X$, $\theta_Z$ |
| Size | $mm^3$ | $\varnothing 20 \times 7.5$ | $15 \times 15 \times 7$ | $10 \times 10 \times 0.6$ |
| Body length ($L$) | mm | 20 | 15 | 10 |
| On-board actuation principle | | Piezoelectric | Piezoelectric | Electrostatic |
| Frequency | Hz | 147 | 1150 | 433 |
| Voltage hor. vibration | $V_{p2p}$ | – | 20 | 32 |
| Voltage vert. vibration | $V_{p2p}$ | 300 | 34.8 | – |
| Number of channels | | 1 | 4 | 2 |
| Number of channels per DOF | | 0.5 | 1.3 | 1 |
| Step size | $\mu$m | 13.6 | 0.443 | 6.93 |
| Step efficiency $\eta_{step}$ | | 0.41 | 0.33 | 0.35 |
| Vertical acceleration | $g$ | 0.37 | 0.63 | 0.8 |
| Force ratio $q_F$ | | 10.6 | 2.24 | 50 |
| Motion velocity | mm/s | 2 | 0.51 | 3 |
| Specific velocity | L/s | 0.1 | 0.034 | 0.3 |
| Relative Dispersion | % | – | 2.9 | 2.5 |
| Smallest increment | $\mu$m | – | 0.187 | 1.12 |
| Power consumption | mW | 92 | 4.02 | 0.025 |
| Specific power consumption | $\frac{\text{mW}}{\text{mm/s}}$ | 46 | 7.9 | 0.0083 |
| Power efficiency | | 0.00014 | 0.00086 | 0.091 |

**Table 5.5:** Comparison of the three MFID prototypes

frequency of the off-board actuation, the robot velocity can be varied by the on-board actuation voltage, while the motion direction can be varied with the phase shift. The second prototype has only on-board actuation, which explains why it features 1.3 on-board actuation channels per DOF, which is the highest of all three MFID prototypes, but still low compared to other robots reported in the state of the art.

The highest motion velocity is obtained with the third prototype (0.3 L/s (body lengths per second)), again due to the resonant operation with high quality factor. The motion velocity of the second prototype is limited on the one hand by the low quality factor of the $Y$ vibration (much lower than $X$ vibration) and on the other hand by the parasitic vertical motion of the flexible frame (both limitations can probably be overcome by a change in fabrication technology).

The relative dispersion of the traveled distance after 500 locomotion steps is about the same for the second and the third prototype[21]. The smallest increment with acceptable repeatability is about six times smaller for the second than for the third prototype. This is partly due to fact that the locomotion steps of the third prototype are much larger due to the lower driving frequency. The high quality factor of the resonance of the third prototype also results in a slower transient response. It should also be noted that the second prototype is the only prototype that allows for scanning motion, which results in nanometric resolution. Because of this reason and because of its 3 DOF, the second prototype is the best suited for precision applications.

Despite of the on-board integration of both slip generation and contact force variation the power consumption of the second prototype is lower than that of the first prototype due to the smaller size, higher driving frequency and the resonant operation. The power consumption of the third prototype is much lower even than the second prototype, due to the on-board integration of only slip generation, the smaller size, the better quality factor of the resonance and because of the choice of electrostatic actuators instead of piezoelectric actuators. The same trend is observed in the power efficiency. The best power efficiency of almost 10% obtained with the third prototype could even be improved relatively easily, by a reduction of the parasitic capacitance between the support layer and the device layer of the SOI wafer out of which the comb drive actuator is fabricated. Moreover, because of the resonance operation with a high quality factor, the third prototype can be actuated with a square wave signal, which allows for a digital driving electronics with a much lower power consumption than for an analogue electronics with Digital to Analogue Convertor and amplifier. The third prototype features a specific power consumption of only 0.0083 $\frac{\text{mW}}{\text{mm/s}}$, which is the lowest specific power consumption reported in the literature[22].

### 5.4.2 Comparison with other locomotion principles

In chapter 2 a classification of locomotion principles was defined and the suitability of each locomotion class for driving mobile microrobots was evaluated quantitatively (see table 2.9 on page 68) based on the following criteria:

- specific motion velocity ($v_s$) expressed in body lengths per second
- specific power consumption ($P_s$) expressed in $\frac{\text{mW}}{\text{mm/s}}$
- the number of DOF
- the simplicity and power consumption of an on-board driving electronics (elec)
- ease of fabrication and assembly for a size of 1 $\text{cm}^3$

[21] The repeatability and the smallest increment have not been measured for the first prototype

[22] at least for those mobile microrobots for which power data was provided or could be calculated

| | $v_s$ [L/s] | $P_s$ [$\frac{\text{mW}}{\text{mm/s}}$] | DOF | Elec | 1 cm$^3$ | Res |
|---|---|---|---|---|---|---|
| Wheels | $1 \cdots 10$ | $10^{-1} \cdots 10$ | 2 | | | |
| Walking | $10^{-2} \cdots 1$ | $10 \cdots 10^4$ | 2-3 | | | |
| Inchworm | $10^{-3} \cdots 10^{-2}$ | $10^3 \cdots 10^4$ | 2-3 | | | |
| $IF_c$ | $1 \cdots 10$ | $10^{-1} \cdots 10^2$ | 2-3 | | | |
| $D\mu$ | $10^{-1} \cdots 10$ | | 0.5-1 | | | |
| $I\mu$ | $10^{-1} \cdots 10$ | | 1-1.5 | | | |
| Inertial drive | $10^{-2} \cdots 1$ | $1 \cdots 10^3$ | 3 | | | |
| **MFID** | $10^{-1} \cdots 1$ | $10^{-3} \cdots 10$ | 2-3 | | | |

**Table 5.6:** Comparison of MFID principle with other locomotion classes

- motion resolution (res)

Table 5.6 shows an evaluation of the suitability of the MFID principle for locomotion of mobile microrobots together with the evaluation of the other locomotion classes already shown in table 2.9. The evaluation of the MFID principle is based on representative results obtained with the three MFID prototypes presented in this chapter. As already discussed in section 3.1 the MFID principle with contact force variation corresponds by definition to the $IF_c$ locomotion class. This explains why the differences in evaluation between MFID and $IF_c$ are small[23].

The low velocity of the second prototype is not considered for the evaluation of the specific velocity of the MFID principle as for that prototype the velocity was limited by the parasitic vertical motion, which can be improved considerably by a second iteration with fabrication by wire EDM. The upper limit to the specific velocity is set to 1 L/s, as the velocity of the third prototype can certainly be increased by a second prototype pushing to the limits the number of comb fingers and the electrostatic gap.

The larger specific power consumption of the first prototype is not considered for this evaluation, as this value is not representative for MFID locomotion in general. The objective of the first prototype was a first test of the feasibility of the MFID principle and the combi-

[23]Evaluation of the MFID principle and the $IF_c$ class are not exactly the same as the MFID prototypes developed in this thesis are not yet included in the evaluation of the $IF_c$ class.

nation of on-board and off-board actuation. The power consumption of this first prototype can be easily lowered by operation at higher frequencies and in resonance mode. This optimization was not yet implemented in this first iteration for simplification reasons. The third prototype achieves a specific power consumption that is an order of magnitude lower than the lowest value that could be calculated from data available in literature. This illustrates very well the advantage of resonance operation, certainly in the case of electrostatic actuators. The power consumption of the third prototype can even be decreased further by a reduction of the parasitic capacitance in the silicon frame around the vibrating masses.

Although a MFID prototype with 3 DOF has been demonstrated, the orientation of the MFID principle towards simplification and low power consumption will often result in designs with only 2 DOF. The number of channels per DOF can be kept lower than 2 and can, for certain configurations, even be less than 1 (as for the first prototype). This limited number of actuation channels, the relatively low voltages and the possibility for square wave driving allows for simple and power efficient driving electronics. The voltages are still higher than typically for wheeled locomotion, which justifies the rating of 4/5.

Its simplicity and the possibility for resonance operation and a combination of on-board and off-board actuation make the MFID principle very well suited for driving robots of a size well below 1 $cm^3$ (as very well illustrated by the sub-millimeter size robot developed at ETHZ shown in figure 2.13(a) on page 47).

Resonance operation with high quality factors and MFID motion with nanometric resolution has shown not to be compatible. However, operation below resonance can reduce the transient effect due to resonance operation. Moreover, MFID locomotion can be compatible to quasistatic scanning mode motion with nanometric resolution as illustrated by the second prototype[24].

It can be concluded from this evaluation that the MFID locomotion principle allows for a unique combination of fast motion, low power consumption, 2 or 3 bidirectional DOFs, simple electronics, simplicity allowing for miniaturization and good motion resolution.

### 5.4.3 Design methodology for MFID locomotion modules

When conceiving the locomotion module for a mobile microrobot, the design specifications are typically composed of the following points:

- *DOF*
- size
- environmental limitations (external actuation possible or required autonomy)
- motion velocity
- motion resolution
- thrust force (can be defined indirectly by the inclination angle)
- power consumption

With this set of specifications a logical design methodology of the MFID locomotion module is listed below and discussed more in detail in the following:

1. Choose the *configuration* and *variants*
2. Decide for *resonance operation* or not
3. Choose the *actuator technology*
4. Choose *target driving frequency and vibration amplitudes*

[24]Scanning mode operation does require a DAC and linear amplifier, which makes the on-board electronics more complicated.

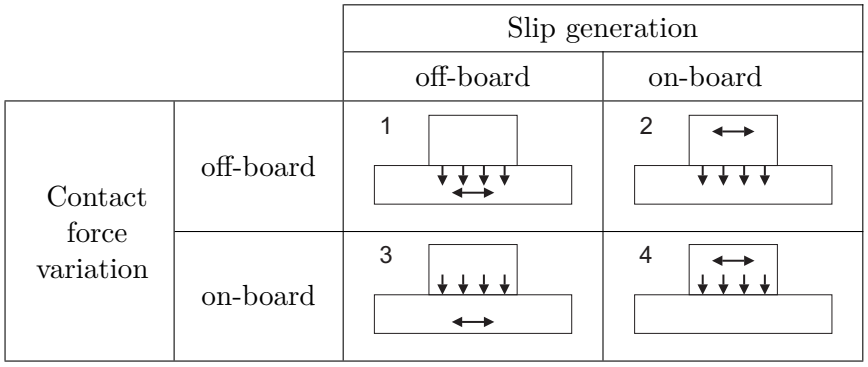


**Table 5.7:** MFID configurations (repeated from table 3.1)

5. *Design the actuators*
6. Control the *force ratio and motion resolution*
7. Estimate the maximum *thrust force* (or inclination angle)
8. Calculate the *power consumption*

Loops in the design process (i.e. returning to a previous step in order to adjust a certain choice) are probably necessary and for certain designs the order of some of the steps can be reversed.

### Step 1: Choice of the configuration

Four different MFID configurations were identified in chapter 3 (see also table 5.7) depending on the choice for on-board or off-board realization of the slip generation and the contact force variation. Table 5.8 summarizes the advantages and disadvantages of the different MFID configurations.

The configuration with only off-board actuation features the advantage of a passive robot, which means that there is no disturbance of electrical wires to the robot or no issue of on-board power consumption and no synchronization between on-board and off-board actuation. For these reasons this configuration was chosen for the characterization setup. However, the major disadvantages is that it is difficult to obtain with this configuration an independent control of several robots (with several DOF each). An external actuation typically results in lower actuation frequencies because the mass of the substrate on which the robot is walking is normally much higher than the mass of the robot, typically resulting in a lower bandwidth for the external actuators[25].

The configuration of only on-board actuation features the major advantage that the robot is independent of the environment and that no synchronization is required between on-board and off-board actuation. Moreover, only on-board actuation typically allows for higher driving frequencies (the second prototype presented in this chapter is based on only on-board actuation and has the highest driving frequency of the three robot prototypes). On the other hand, integration of both slip generation and contact force variation results in an increased on-board complexity and power consumption.

The two configurations based on a combination of on-board and off-board actuation allow for simpler robots with lower on-board power consumption. Particularly the configuration with on-board contact force variation and off-board slip generation can result in a very simple

[25]The characterization setup is based on a configuration with only off-board actuation, but still allows for a driving frequency of several kHz. This is because the characterization setup is a 1 DOF actuator. A 1 DOF actuator does not require for large (two dimensional) substrate to be vibrated horizontally and vertically.

robot as illustrated by prototype 1, which features 2 DOF $(X, Y)$ motion with only 1 on-board actuator. Holonomic 3 DOF motion could be obtained with two on-board vertically vibrating masses (so two on-board actuation channels). Inphase vibration results in translation $(X, Y)$, while counterphase vibration would result in rotation $(\theta_Z)$. As illustrated by the prototype with electrostatic clamping presented in appendix section C.1 this configuration can result in a robot without any moving parts, which is interesting for miniaturization and robustness. On the other hand, the configuration with on-board slip generation and off-board contact force variation allows for individual scanning motion of several robots, resulting in a higher motion resolution. Moreover, the latter configuration allows for better independent velocity control of several robots simultaneously, as the horizontal vibration is the best parameter for velocity control. In order to be able to judge which of these two configurations result in the lowest power consumption, one should study the required vibration amplitude for horizontal and vertical actuation for a given motion velocity and vertical acceleration. In the case of a sinusoidal vibration with amplitude $X$ and frequency $f$ the MFID motion velocity is given by $v = \eta_{step} 2\pi f X$. Hence, for a given motion velocity $v$ and when assuming a step efficiency of $\eta_{step} = 1/\pi = 0.32$ (corresponding to the motion velocity of a ideal stick-slip actuator with the same driving amplitude and frequency) the required horizontal vibration amplitude is given by

$$X = \frac{v}{\eta_{step} 2\pi} \frac{1}{f}. \tag{5.40}$$

In the case of a sinusoidal vertical vibration with amplitude $Z$ and frequency $f$ the generated vertical acceleration is given by $A_Z = Z(2\pi f)^2$. Hence, for a given acceleration amplitude of $A_Z$ the required vertical vibration amplitude is given by

$$Z = \frac{A_Z}{(2\pi)^2} \frac{1}{f^2}. \tag{5.41}$$

Figure 5.43 plots the required horizontal and vertical vibration amplitude for a motion velocity of 0.5, 1 and 2 mm/s and a vertical acceleration of $0.3g$, $0.5g$ and $0.9g$ in function of the driving frequency. The graph shows for instance for the case of a motion velocity of 1 mm/s and a vertical acceleration of $0.5g$ that for a driving frequency below 248 Hz the required vertical vibration amplitude is larger than the horizontal, while for a frequency above 248 Hz the required horizontal vibration amplitude is the largest. Hence, as the power consumption increases with increasing vibration amplitude, for a driving frequency *below* 248 Hz the configuration with on-board slip generation would theoretically result in the lower power consumption, while for a driving frequency *above* 248 Hz the configuration with on-board contact force variation would feature the lowest power consumption.

As discussed in chapter 3 for a given configuration different variants are still possible (see also table 5.9). For instance an on-board slip generation can be generated either by a horizontal vibration of the feet of the robot with respect to the body of the robot, either by a horizontal vibration of an inertial mass fixed to the body of the robot. The advantages of the variant with vibrating feet is that almost the complete vibration amplitude is transformed into slip of the robot's feet on the substrate. Moreover, the vibrating feet variant allows for quasistatic scanning motion, resulting in a very high motion resolution. On the other hand the variant with the horizontally vibrating inertial mass (as in prototype 3) results in a lower shift of the resonance frequency between vibration with and without clamping of the robot's feet, which can contribute to the stability of the robot's motion. Moreover, the variant with inertial mass allows for the use of fragile actuator technologies (such as comb drive actuators in prototype 3) as the total weight of the robot does not have to be carried by the actuator. The protection of the vibrating inertial mass could even be improved by a complete encapsulation.

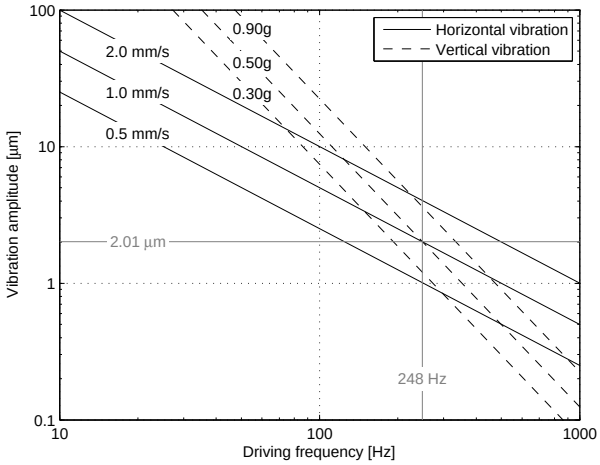


**Figure 5.43:** Required horizontal and vertical vibration amplitude for a motion velocity of 0.5, 1 and 2 mm/s ($\eta_{step} = 1/\pi$) and a vertical acceleration of $0.3g$, $0.5g$ and $0.9g$

| | | Slip generation | |
|---|---|---|---|
| | | off-board | on-board |
| Contact force variation | off-board | + on-board simplicity<br>+ no on-board power<br>+ no on-board electronics<br>+ no synchronization<br>– limited multi-DOF<br>– limited multi-robot control | + on-board simplicity<br>+ low on-board power consumption<br>+ good on-board velocity control<br>+ on-board scanning motion<br>– synchronization |
| | on-board | + on-board simplicity<br>+ low on-board power consumption<br>– synchronization | + independent of environment<br>+ no synchronization<br>+ good on-board velocity control<br>+ on-board scanning motion<br>– on-board complexity<br>– on-board power consumption |

**Table 5.8:** Pros and cons for the 4 MFID configurations

| Slip generation | Slip variation | |
|---|---|---|
| Inertial | Inertial | Direct force |
| 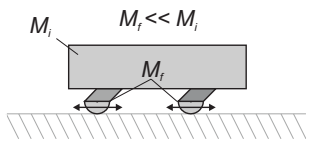  Vibrating feet | 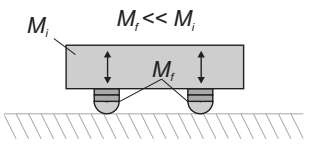  Vibrating feet | 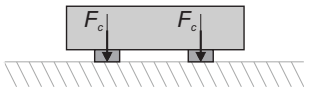  |
| 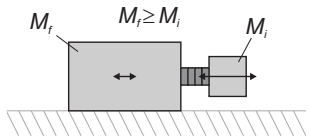  Vibrating Mass | 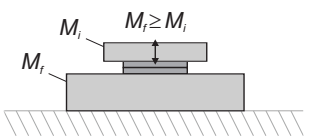  Vibrating Mass | |

**Table 5.9:** MFID variants for slip generation and slip variation (repeated from table 3.2)

Such encapsulation also allows to protect the actuator for environmental conditions such as dust or to provide a special atmosphere to the actuator such as a lower air pressure in order to decrease the air damping.

Also for the on-board generation of the variation of the contact force there are different variants possible. A first possibility is to generate this contact force variation by the inertial effect of a vertical vibration. This variant has the advantage that it can result in a low power consumption, especially when operating in resonance mode or at higher frequencies as shown in figure 5.43. The disadvantage is that such a vertical vibration is a dynamic effect and does not allow for a quasistatic control of the contact force. Moreover, contact force variation by vertical vibration typically only allows to increase the contact force up to the double of the contact force generated by the weight of the robot. As for the horizontal vibration, the vertical vibration can be generated by vibrating the feet of the robot or by the vertical vibration of an inertial mass. As for the horizontal vibration the variant of vibrating feet features a better efficiency. The variant of a vertically vibrating inertial mass has — apart from the better protection of the actuator — the advantage that the body of the robot is not vibrating vertically, which can be required in the case of high precision applications. The second possibility to generate the variation of the contact force is by means of a direct force such as a magnetic, electrostatic or mechanical clamping force. The advantage of such a direct force is that it allows for a quasistatic variation of the contact force and that the absence of a vertical mechanical vibration can be an advantage in the case of precision applications. Moreover, as the generated force is independent of the driving frequency, a contact variation by a direct force allows for efficient low frequency operation. The disadvantages of magnetic clamping is that it can disturb the environment, for instance by stray magnetic fields (which is an important issue for the operation inside of electron microscope). Moreover, magnetic clamping consumes power even at a constant clamping force. An important issue with electrostatic clamping is that it requires a very flat, smooth surface and no large dust particles. Besides, electrostatic clamping suffers from sensitivity to charge accumulation and unwanted clamping due to a vacuum effect between robot and substrate. Mechanical clamping is not that easy to implement in the case of 3 DOF motion and, as it is typically driven by piezoelectric actuators, the low clamp displacement can cause a sensitivity to wear and mechanical tolerances of the clamping interfaces.

**Step 2: Resonance operation or not**

As already mentioned several times resonance operation allows for a reduction of the driving voltages (currents) and power consumption. Moreover, an actuator driven in resonance mode can be driven with a square wave generated by a simple digital electronics. A digital driving electronics is much simpler and has a much lower power consumption than an electronics with a Digital to Analogue Convertor (DAC) and amplifier as typically required for the generation of sinusoidal signals (and saw tooth signals in the case of inertial drives).

An initially less obvious advantage of resonance operation is that the resulting vibration automatically has a very good sinusoidal shape. This is particularly an important advantage in the case of a variation of the contact force by a vertical vibration as even small deviation on the vibration shape can have a large influence on the acceleration profile. Such deviations can be due to noise (for instance quantization noise from the DAC) or higher harmonics superposed on the sinusoidal vibration typically resulting from the hysteresis of piezoelectric actuators. Even operation at a frequency a bit lower than the resonance frequency can be interesting because it still filters out higher harmonics due to hysteresis. This can also be an advantage in the case of off-board actuation. This advantage is very well illustrated by comparing the *velocity vs. vertical acceleration* profile of the characterization setup (see figure 4.23 on page 105) and that of the third prototype (see figure 5.38 on page 169). The stack piezos generating the vertical vibration on the characterization setup are driven with a smooth sinusoidal voltage signal[26]. Nevertheless, several harmonics are superposed on the measured vibration of the stack piezos. These harmonics become very important in the acceleration profile and cause the slider to jump when the fundamental sinus only generates a vertical acceleration of $0.4g$. As the resonance frequency of the stack piezos is far above the driving frequency (unloaded resonance frequency >300 kHz), these harmonics are not filtered by the bandwidth of the stack piezos. The vertical vibration platform for the third prototype is also actuated by piezoelectric actuators that also suffer from hysteresis. However, as the third prototype is operated at 433 Hz and the resonance frequency of the vertical vibration platform is 890 Hz, most of the harmonics[27] introduced by this hysteresis are filtered out. The result is that the *velocity vs. vertical acceleration* profile increases linearly up to a vertical acceleration of $0.9g$.

One of the disadvantages of resonance operation is that a certain number (depending on the quality factor) of actuation cycles is necessary before reaching the steady state operation, which results in lower response times of the actuator (both when starting motion and when stopping motion). This lower response time also results in a larger smallest increment as typically more than one actuation cycle is necessary for the generation of a stable displacement. The second disadvantage of resonance operation is that it requires the driving electronics to output a particular frequency with a certain precision. Specially in the case of an high quality factor the required precision can be an issue for a miniaturized on-board electronics that can typically suffer from a relatively large uncertainty of the integrated clock frequency. The frequency of the motion velocity of the third prototype (see figure 5.36 on page 167) shows that driving frequency should be set at $433 \pm 1.3$ Hz if a drop in motion velocity by a factor $1/\sqrt{2}$ is allowed. This requires a relative precision of the driving frequency of 1.3/433=0.3%. Moreover, this resonance frequency might differ from robot to robot, which would require

[26]The voltage signal at the input of the stack piezos is a smooth sinus because any quantization noise introduced by the DAC of the analogue output board is filtered by the limited bandwidth of the electrical amplifier.

[27]As the driving frequency is a bit lower than half of the resonance frequency of the vertical vibration platform, there is a risk to amplify the second harmonics. However as shown by the harmonic fit in equation (4.21) on page 89 the third and the fifth harmonics ar much more important than the second harmonics.

| Pros | Cons |
|---|---|
| + lower power consumption<br>+ lower driving voltage<br>+ square wave input signal<br>+ smoother sine wave (less harmonics, no noise from electronics) | – slower response times<br>– narrow driving frequency band (multi robot synchronization)<br>– more difficult to predict (quality factor)<br>– instability if large shift in resonance frequency between clamped and free vibration |

**Table 5.10:** Pros and cons for resonance operation

every robot to be calibrated individually and even on the same robot the resonance frequency can drift over time for instance due to fatigue or changes in temperature and humidity. A possible solution would be to implement a driving electronics with a phase lock loop. But even in that case a too large deviation in resonance frequency between the different robots can be an issue if the chosen configuration is based on a combination of on-board and off-board actuation. The off-board actuation is common to all robots, which requires all robots to operate at the same frequency. Also the matching — if required — of resonance frequency of horizontal vibration and vertical vibration is not an easy task. Finally, if there is large shift in resonance frequency between free vibration and vibration with clamped feet, resonance operation can lead to some instability issues.

As illustrated in appendix section C.2 an interesting alternative to resonance operation that is also very efficient in terms of power consumption, but does not suffer from the limitation of a narrow frequency band is the generation of the vibration by a rotation. As for resonance operation the kinetic energy in a rotating actuator does not have to be absorbed and regenerated at every actuation cycle (rotation). An important advantage of the rotation, however, is that this efficient operation is not only reached within a narrow frequency band, but at every driving frequency. It should be noted however that it is very difficult to miniaturize a solution with on-board rotation in order to fit in a robot with an overall size of less than 1 $cm^3$.
Table 5.10 summarizes the pros and cons of resonance operation.

### Step 3: Choose the actuating technology

Most of the actuators presented in this thesis are piezoelectric actuators. The pros and cons of *piezoelectric actuators* are:

+ high energy density
+ high resolution
+ high bandwidth
+ no power consumption for maintaining a certain position[28]
– high driving voltages (important issue for the on-board driving electronics)
– low displacements, requiring for high driving frequencies
– non linearities such as hysteresis, which does not only detoriates the open loop precision of the actuator and increases the energy dissipation, but also introduces higher

[28]It should be noted, however, that in order to maintain a certain position with a piezoelectric actuator, the driving electronics typically does consume power. This is particularly important in the case of small actuators and small electronics because the power consumption of the driving electronics is often more important than the power consumption of the actuator itself.

harmonics on a sinusoidal vibration
- in-plane displacements are difficult to miniaturize, because not compatible to MEMS fabrication technologies

The on-board horizontal vibration of the third prototype is based on electrostatic actuators. The pros and cons of *electrostatic* actuators are
+ low power consumption
+ low internal damping, resulting in a good quality factor at resonance
+ allows for miniaturization down to the mm scale and below as scale laws are favorable for miniaturization and because of the compatibility with MEMS fabrication technologies
– low energy density
– high driving voltage
– sensitive to dust

Another interesting actuation technology for MFID locomotion, that has not been tested yet, is electromagnetic actuators. The pros and cons of *electromagnetic actuators* are
+ low driving voltage
+ allows for large displacements
+ low internal damping, resulting in a high quality factor
– generation of stray magnetic fields
– miniaturization to the mm scale complicated because of the required 3D integration and a scaling law that is unfavorable for miniaturization
– consumes power to maintain a certain position

A fourth actuation technology that could be considered is that of *thermal actuators*, which have the following pros and cons
+ allows for miniaturization down to the mm scale and below as scale laws are favorable for miniaturization and because they can be realized by MEMS fabrication technologies
+ allows for monolithic integration of in-plane and out-of-plane actuation
+ relatively large displacement for out-of-plane motion
+ low driving voltage
– low power efficiency
– low response times (although it improves with decreasing dimensions, the response time still remains slow)

It is obvious that the constraints imposed by the actuation technology chosen for the horizontal and the vertical vibration should match. In the case of a configuration with only off-board or only on-board actuation it is more likely to opt for the same actuation technology for both actuations as the masses to be vibrated in each direction are of comparable size (which is usually not the case of a configuration based on a combination of off-board and on-board actuation).

**Step 4: Choose target driving frequency and vibration amplitudes**

As illustrated by figure 5.43 the choice of the driving frequency can have an important influence on the power consumption. The power consumption of an MFID actuator scales linearly with the driving frequency and typically scales quadratically with the driving voltage[29]: $P \propto fU^2$.

[29]Piezoelectric and electrostatic actuators represent a capacitive load, of which the power consumption scales with $U^2$. Also in the case of electromagnetic and thermal actuators the power scales quadratically with the driving current $I^2$ (The symbol $U$ should be interpreted as a generalized actuation amplitude, which can also stand for the driving current $I$).

| | $X, Z \propto U$ | $X, Z \propto U^2$ |
|---|---|---|
| $P_X$ | $\propto \frac{1}{f}$ | $\propto 1$ |
| $P_Z$ | $\propto \frac{1}{f^3}$ | $\propto \frac{1}{f}$ |

**Table 5.11:** Scaling laws of the power consumption for horizontal $X$ and vertical $Z$ vibration in function of the type of actuation for the case of contact force variation by vertical vibration

For some actuators (piezoelectric and some electromagnetic actuators such as voice coil or moving magnet motors) the generated displacement ($X$ or $Z$) scales *linearly* with the actuation amplitude $X, Z \propto U$. For a given motion velocity, the required horizontal vibration amplitude scales as $X \propto 1/f$ with the driving frequency. Consequently, for a given motion velocity the power consumption $P_X$ of the horizontal actuation decreases inversely proportionally with the driving frequency:

$$P_X \propto fU^2 \propto fX^2 \propto \frac{1}{f}. \tag{5.42}$$

For a given vertical acceleration and in the case of a variation of the contact force by the inertial effect of a vertical vibration, the required vertical vibration amplitude scales as $Z \propto 1/f^2$ with the driving frequency. Consequently, for a given vertical acceleration the power $P_Z$ consumed by the vertical actuation decreases inversely cubically with the driving frequency:

$$P_Z \propto fU^2 \propto fZ^2 \propto \frac{1}{f^3}. \tag{5.43}$$

On the other hand for some other actuators (electrostatic, thermal and some electromagnetic actuators such as reluctance motors) the generated displacement ($X$ or $Z$) scales *quadratically* with the actuation amplitude $X, Z \propto U^2$. In that case, for a given motion velocity the power consumption of the horizontal actuation does not depend on the driving frequency:

$$P_X \propto fU^2 \propto fX \propto 1 \tag{5.44}$$

and for a given vertical acceleration the power consumed by the vertical actuation decreases inversely proportionally with the driving frequency

$$P_Z \propto fU^2 \propto fZ \propto \frac{1}{f}. \tag{5.45}$$

The scaling of the power consumption of the horizontal and vertical actuation with the frequency for the two different types of actuators is summarized in table 5.11. It can be concluded that the choice of the actuation technology has an important influence on the scaling of the power consumption (and therefore on the optimal choice of the driving frequency), but that in general it is not very efficient in terms of power consumption to operate at low driving frequency. It should be noted that in order to optimize the overall power consumption of a mobile robot, the power consumption of the driving electronics — if any — should also be taken into account. Typically, the power consumption of the driving electronics increases considerably with increasing supply voltages, which also motivates the increase of the driving frequency in order to decrease the actuation voltages.

Apart from the interesting scaling of the power consumption for increasing driving frequency, the smaller step size that results from higher driving frequencies for a given motion

velocity can lead to a better motion resolution of the locomotion platform. The driving frequency can also be increased in order to obtain vibration amplitudes that fit the limits of certain actuator technologies such as piezoelectric actuators.

The increase in resonance frequency is typically limited by the bandwidth of the actuators and the risk of excitation of resonance modes of other actuators and tools on the robot. Another limitation, which is less obvious, is the guiding quality of the horizontal vibration. The parasitic vertical motion superposed on the horizontal vibration of the locomotion module of the second prototype presented in this chapter causes the robot to start to jump when actuated above a certain driving frequency. The guiding quality $Q_g$ of an actuator could be defined as the ratio between the axial (horizontal) and the parasitic (vertical) displacements it generates: $Q_g = X/Z_{para}$. In order to avoid too much disturbance of the MFID motion by this parasitic vertical displacement, the generated parasitic displacement $Z_{para}$ should be considerably smaller than the vertical vibration amplitude $Z$ required for locomotion

$$Z_{para} = \frac{X}{Q_g} \ll Z. \tag{5.46}$$

Hence, a design constraint for the guiding quality is given by

$$Q_g \gg \frac{X}{Z}. \tag{5.47}$$

As for a given frequency $f$ the required horizontal and vertical vibration amplitude scale with the frequency as $X \propto 1/f$ and $Z \propto 1/f^2$, the lower limit for the guiding quality $Q_g$ increases linearly with increasing driving frequency. So, the higher the driving frequency, the higher the quality of the guiding of the horizontal actuation should be. This tendency is well illustrated by the fact that the prototype that is driven at the highest frequency (prototype 2) suffers from the biggest problems in terms of guiding quality. The guiding quality can be optimize by an optimized design and a proper choice of fabrication and assembly technologies.

Once the target frequency is chosen the required vibration amplitudes can be calculated from the specified motion velocity and a supposed step efficiency and vertical acceleration amplitude. As listed in table 5.5 the step efficiencies at optimal parameter settings of the three prototypes are 0.41, 0.33 and 0.35 respectively, while the step efficiency measured for the characterization setup was 0.38. Based on these values, we could consider a estimated step efficiency of $\eta_{step} = 0.4$ in order to be able to advance in the design process.

**Design rule 1**

Step efficiency: $\eta_{step} = 0.4$

The vertical acceleration amplitudes at optimal parameter settings of the three prototypes and the characterization setup are $0.37g$, $0.63g$, $0.8g$ and $0.35g$ respectively. The two lowest values of $0.37g$ and $0.35g$ were obtained with prototype 1 and the characterization setup respectively in which the vertical acceleration is generated by a piezoelectric actuator that is driven far below its resonance frequency. The vertical vibration of the second prototype ($0.63g$) is driven a bit below its resonance frequency, but the vertical acceleration is limited by the parasitic vertical acceleration introduced by the horizontal vibration. The third prototype features the highest optimal vertical acceleration ($0.8g$) because of its lower driving frequency, a better guiding quality resulting from the monolithic fabrication process by DRIE and because of a vertical vibration with less harmonics. Hence, it can be concluded that depending on how many harmonics and parasitic vertical vibration is expected the optimal vertical vibration amplitude should be estimated between $0.4g$ and $0.8g$

**Design rule 2**

Vertical acceleration amplitude: $A_Z = 0.4 \ldots 0.8g$

With these two design rules and with equations (5.40) and (5.41) the horizontal and vertical vibration amplitude required for the chosen driving frequency can be estimated.

**Step 5: Design of the actuators**

Once decided upon the configuration (step 1), operation at resonance frequency or not (step 2), the actuator technology (step 3) and the target driving frequency and horizontal and vertical vibration amplitudes have been fixed (step 4) a first iteration of the design of the actuators of the locomotion module can be started. It is possible that during the actuator design appears that all these constraints can not be met. Then, one or several iterations of adjusting the previous choices and redesigning the actuator will be necessary.

If chosen for resonance operation, there will be a large uncertainty on the real vibration amplitude of the actuator, as it is quite difficult to estimate accurately the quality factor of the resonance without doing any measurements. Moreover, it is also difficult to estimate how much of that quality factor will remain during locomotion. For the third prototype a quality factor of $Q = 558$ was measured for the vibration with clamped feet, while during locomotion the quality factor was only 168 (i.e. a reduction by a factor 3.3). For the second prototype the quality factor was reduced by a factor 2.4 from 39.2 at free vibration to 16.4 in the *velocity vs. frequency* profile. The reduction factor of the quality factor will depend very much from actuator to actuator and is difficult to predict without performing any locomotion experiments or detailed simulation.

**Step 6: Control the force ratio and motion resolution**

The force ratio $q_F$ quantifies the ratio between the maximum horizontal inertial force and the minimum friction force. A force ratio smaller than 1 means that no MFID locomotion is possible. The calculation of the force ratio requires the driving frequency, vibration amplitudes, the vertical preload on the robot (typically its weight) and the parameters of the friction between the feet and the substrate to be known.

However, friction parameters are not always that stable and important local variations can occur due to dirt, oxidation and local surface roughness variations. Therefore, the force ratio should be sufficiently above 1 in order to allow for stable motion. Moreover, a force ratio just above one does not allow for good velocity control, because the motion will become rapidly instable when reducing the velocity. At optimal driving parameters the force ratio for the characterization setup and the three prototypes were 37, 10.6, 2.24 and 50 respectively. It has been observed that the second prototype ($q_F = 2.24$) shows indeed instability problems when reducing the motion velocity as shown in figure 5.14(d) on page 143. The lower design limit for force ratio at specified velocity will be set to 10. If this condition is not met the best solution is to try to increase the driving frequency.

**Design rule 3**

Force ratio at specified velocity $q_F = 10$

The smallest increment of the MFID actuator is very difficult to estimate. A rough estimation can be obtained by calculating the minimum horizontal vibration amplitude for which a force ratio of $q_F = 1$ is obtained and then calculate the step size with the help of the

step efficiency. In the case of resonance operation things get even more complicated because of the transient increase in vibration amplitude. The resolution of scanning motion can be easily estimated by dividing the quasistatic peak-to-peak displacement of the actuator by the number of increments of the driving electronics.

**Step 7: Estimate the maximum thrust force**

The maximum thrust force has only been measured on the characterization setup by measuring the maximum inclination angle for which uphill motion is still possible. At only gravitational preload a maximum thrust force of 0.89 mN could be generated, which is 57% of the dynamic friction force. At a total preload of $9.02g$, the maximum thrust force was 7.4 mN, which is 54% of the dynamic friction force. The dynamic friction force depends on the weight of the robot, any additional preload, some geometrical parameters such as the angle of inclination if any and the friction parameters of the interface between robot and substrate. At this stage of the design process all these parameters are known (at least approximately). Depending on the chosen materials for substrate and robot feet, the friction parameters (essentially the dynamic friction coefficient $\mu_d$) might be difficult to find in literature. However, this parameter can be estimated by measuring the maximum inclination angle at which the robot (or any dummy robot with the same material) stops sliding once slip was initiated by shortly pushing it. The maximum thrust force generated by the robot should be in the order of 50–60% of that dynamic friction force.

**Step 8: Calculate the power consumption**

The calculation of the power consumption requires the design of the actuators (typically their capacitance or electrical resistance), their driving frequency and driving voltages (currents) to be known. Piezoelectric actuators are a capacitive load for the driving electronics. In theory the energy that is stored in these capacitances at every locomotion cycle is not completely lost. The energy could be recovered in some kind of electrical resonant circuit or by a charge recovery electronics [342]. However, in practice it is difficult to miniaturize such a resonant circuit or a or charge recovery electronics in order to fit in a robot of a size of 1 $cm^3$. Therefore, the energy stored in the charged capacitances should be considered as really lost.

An important issue when calculating the power consumption of the mobile microrobot is to included also the power consumption of the driving electronics. In the case of an operation at resonance, which allows for driving with a digital electronics this power consumption can be relatively low. Theoretically, for a capacitance $C$, driving frequency $f$ and driving voltage $V$ the minimum power consumption of the actuator plus the driving electronics is $P = 2\frac{CV^2}{2}$. Half of this energy is stored in the capacitance and the other half is dissipated in the internal resistance of the digital driving electronics (if charging with a constant voltage as usually is the case).

## 5.5 Conclusion

After a detailed study of the stepping behavior on a characterization setup based on a linear MFID actuator in the previous chapter, the current chapter illustrated the application of the MFID principle for the locomotion of mobile microrobots. Two of the prototypes are based on piezoelectric actuators, while the third prototype is based on electrostatic actuators fabricated by MEMS technology. MEMS technology allows for further miniaturization of the

robot size to the mm range, as illustrated by the fabrication of two locomotion modules of a size of $2 \times 2 \times 0.6$ mm$^3$.

The four MFID actuators presented in this thesis illustrated the four possible MFID configurations of on-board and off-board actuation. The prototypes show clearly the increased on-board simplicity obtained with a configuration that combines on-board and off-board actuation. The four MFID actuators also illustrated clearly the advantages of resonance operation (i.e. lower power consumption, lower driving voltage, simpler electronics and smoother vibration profile) as well as the drawbacks (i.e. slower response time, narrow driving frequency band, difficulty to predict the motion velocity and some instability issues).

The first MFID prototype is interesting because of its simplicity with only one on-board actuator for 2 DOF. Increasing the operation frequency and resonance operation could result in a very low on-board power consumption. The simplicity of this configuration also allowed for a demonstration of wireless MFID actuation with 2 DOF of mobile microrobots with only on-board clamping electrodes (see appendix section C.1). The second prototype is optimized for high resolution motion in 3 DOF. If further optimized this configuration could combine fast motion in resonance with average driving voltages, with nanometric resolution scanning mode operation in 3 DOF. The third prototype has demonstrated very well how MFID resonance operation with a high quality factor can result in fast velocities and very low power consumption. Moreover, this design features very interesting perspectives in terms of miniaturization because of the choice of MEMS technologies for the fabrication of the electrostatic actuator.

A comparison of the results obtained with these three MFID prototypes with other locomotion solutions for mobile microrobots presented in literature demonstrate that the MFID principle allows for fast locomotion in several DOF with nanometric resolution, very low power consumption, simple driving electronics and robot sizes from the centimeter scale down to the millimeter scale.

The choice of the driving frequency has proven to be an important design parameter. It has an influence on the optimal choice of the configuration: at low (high) driving frequencies the on-board integration of only the slip generation (contact force variation) will lead to the highest power efficiency. Moreover, an increase of the driving frequency generally reduces the power consumption. The resulting smaller step size (for a given motion velocity) also results in higher motion resolution and allows to meet the low displacement constraint of some types of actuators (e.g. piezoelectric). The driving frequency is limited by the bandwidth of the actuators, the guiding quality of the horizontal (axial) vibration and the excitation of any resonance modes of the robot's body.

All the knowledge gained in this chapter with the study of the stepping behavior and the design and characterization of the MFID prototypes is synthesized in a design methodology for new MFID locomotion platforms. Eight design steps have been proposed and discussed, as well as three empirical design rules, which allow to estimate the performances of MFID motion of the designed locomotion platform without performing any simulation or experimental measurements.

# Chapter 6

# Conclusion and outlook

*"In science one tries to tell people,*
*in such a way as to be understood by everyone,*
*something that no one ever knew before.*
*But in poetry, it's the exact opposite."*
Paul Dirac (1902–1984)

## 6.1 Contribution of this thesis

A first contribution of this thesis is the systematic study of locomotion principles for mobile microrobots. Two essential functions of a locomotion principle based on stepping motion have been identified: slip generation and slip variation. Based upon the possible solutions for these two functions a classification of locomotion principles by stepping motion has been derived. For each locomotion class solutions proposed in literature are systematically reviewed and the suitability of each class for locomotion of mobile microrobots has been evaluated. Such a review of locomotion principles as well as the proposed functional classification is new to the field of mobile microrobotics.

The major contribution of this thesis is the definition and the elaboration of the *Modulated Friction Inertial Drive (MFID)* principle. Apart from the MFID principle a more general concept of a combination of on-board and off-board actuation is proposed. This concept aims at a trade-off between on-board simplicity and power consumption on the one hand and on-board motion controllability on the other hand, enabling further miniaturization of mobile microrobots. Four different configurations of the MFID principle have been derived based on the combination of on-board and off-board actuation.

The fundamental aspects of the stepping motion of a MFID actuator have been exposed and a dynamic model allowing for simulation for design and optimization of MFID actuators has been proposed and experimentally validated. A small deviation from the MFID principle is made by the definition of the *inertial inchworm* concept and its characterization. A quantitative comparison of performances of the MFID, inertial inchworm and stick-slip principle is made based on experimental results carried out on the same experimental setup, allowing for an optimal comparison with the same operating conditions.

The MFID principle has been illustrated by the development, characterization and comparison of three MFID locomotion modules for mobile microrobots. Together with the experimental setup these three prototypes have illustrated the implementation of the four MFID configurations of on-board and off-board actuation. A comparison of the performances of these prototypes with the state of the art in locomotion for mobile microrobots has proven

the added value of the MFID principle in general and the three robot designs in particular.

A concept of parallel, wireless actuation of a large number of mobile microrobots by means of a projector and on-board solar cells has been proposed and demonstrated.

Based upon the experience gained with the experimental characterization setup and the three MFID prototypes a design methodology for MFID actuators has been derived.

## 6.2 Originality of this thesis

A review of the whole field of locomotion for mobile microrobots moving on a solid substrate has never been reported before. Previous reviews are either focussing on actuation principles either they are limited to a certain locomotion class (such as wheel driven or walking robots), a particular fabrication technology (such as MEMS fabrication for walking robots) or a particular applications (such as in-pipe operation). Moreover, a functional classification and a systematic evaluation of locomotion principles was also nonexistent up to now. Such a classification and evaluation is indispensable for getting a clear overview of locomotion solutions and to pick the optimal principle for a certain set of requirements.

Experience from previous microrobotic projects allowed the author to achieve a good understanding of the constraints and the requirements of a locomotion module for mobile microrobots. This experience concerns in particular the influence of the choice of the actuation technology, driving voltages, currents, frequencies, signal shape and number of actuation channels on the complexity and power consumption of the driving electronics. This insight was applied in this thesis for finding an optimal trade-off between locomotion performances and driving complexity. Hence, the proposed MFID concept as well as the developed prototypes have resulted from a well-defined set of requirements for a specific application ("application pull approach") and not from a "technology push" approach as is for instance the case for certain MEMS robots based on walking motion.

Most locomotion solutions for mobile microrobots follow the approach of only on-board actuation, in order to achieve real autonomy. However, for robot sizes in the $cm^3$ range this often results in tethered operation, which causes the major advantages of "mobile" robotics (i.e. mobility and flexibility) to be partially lost. As robot sizes get smaller, there is a tendency towards off-board actuation in order to simplify the robot. Although off-board actuation has allowed for the creation of sub-millimeter size mobile microrobots, this approach is often not scalable to independent, multi-DOF control of several microrobots. The proposed concept of a combination of on-board and off-board actuation allows to find an optimal trade-off between robot simplicity and power consumption on the one hand and on-board motion control on the other hand. The definition of this concept as well as its demonstration in two prototypes is an original contribution of this thesis and offers very interesting perspectives to the field of mobile microrobotics — and related fields.

Last but not least, the originality of this thesis also lies in the proposed MFID principle itself. The idea of creating motion by a combination of a horizontal vibration and variation of the contact force is not new by itself, but a systematic study decoupling both actuations has not yet been done before for the field of microrobotics.

## 6.3 Major results related to the MFID principle

A dynamic model allowing for numeric simulation of a MFID actuator has been presented. An experimental setup of a linear MFID actuator with contact variation by the inertial effect of a vibration perpendicular to the actuation axis has been developed and characterized. A

good agreement between simulated and experimental data has been observed. It should be noted, however, that it has proven to be difficult to find the right values for the frictional parameters without performing any experimental characterization.

Two parameters characterizing the MFID stepping behavior have been introduced. The step efficiency $\eta_{step}$ has been defined as the ratio between the average motion velocity and the maximum instantaneous velocity of the axial vibration. The step efficiency expresses the efficiency with which the actuator is capable of transforming the axial vibration in net motion. A typical value for the step efficiency of a MFID actuation is $\eta_{step} = 0.4$. The force ratio $q_F$ has been defined as the ratio between the maximum instantaneous inertial force generated by the axial (horizontal) vibration and the minimum instantaneous friction force. The force ratio expresses the ease with which slip is generated. A requirement for MFID locomotion is that $q_F > 1$, while stable motion is only achieved if $q_F \gg 1$.

Simulation and experimental results have allowed to characterize the influence of the phase shift, vibration amplitudes and driving frequency on the MFID motion velocity. The velocity varies sinusoidal with the phase shift reaching generally a maximum velocity in positive and negative direction around 90° and 270°. However, if the force ratio $q_F$ approaches to 1 (at low frequencies or high perpendicular preloads), the optimal phase shift moves towards 180° and 360°. The motion velocity increases with increasing perpendicular acceleration (variation of the contact force) due to an increasing step efficiency. Instable operation has been observed in the region of 0.5-1 $g$ due to higher harmonics in the perpendicular vibration introduced by the hysteresis of the perpendicularly vibrating piezoelectric actuators. For perpendicular accelerations above 1 $g$ hopping motion occurs with an optimal phase shift at 180° and 360°. The axial vibration amplitude is the best parameter for velocity control of a MFID as good linearity is observed. The motion velocity also varies with the driving frequency, but the linearity is worse. The minimum driving frequency for MFID motion is determined by the frequency at which the force ratio becomes equal to 1.

The trust force of the MFID actuator has been measured to be about 50-60% of the dynamic friction force. The standard deviation of the repeatability of the traveled distance with a fixed number of steps has found to be in the order of some %. Minimum MFID steps of some tens of nanometer have been measured in the case of non-resonant operation, while the MFID principle can, depending on the design, allow for quasistatic scanning motion with resolutions down to 1 nm.

An experimental comparison of the performances of the MFID principle with the stick-slip and the inertial inchworm principle have shown similar velocity behavior with best linearity and thrust force for the stick-slip principle. Experimental results have also shown that the MFID principle is quite sensitive to an uncontrolled variation of the contact force, as for instance caused by deviations in the vibration shape of the perpendicular vibration or by parasitic perpendicular vibration superposed on the axial vibration.

The suitability of the MFID principle for mobile microrobotic locomotion has been demonstrated by the development and characterization of three locomotion modules. The three prototypes have illustrated the advantages of the MFID principle in terms of on-board simplicity as well as the advantages of resonance operation (i.e. lower power consumption, lower driving voltage, simpler electronics and smoother vibration profile) as well as the drawbacks (i.e. slower response time, narrow driving frequency band, difficulty to predict the motion velocity and some instability issues). The best quantitative demonstration of the advantage of the MFID principle is given by the specific power consumption of only 0.0083 $\frac{\text{mW}}{\text{mm/s}}$ for the third prototype, which is the lowest value that could be calculated from the data provided for mobile microrobots reported in literature.

## 6.4 Future work

An interesting direction for future work on the MFID principle would be the development of a dynamic model including resonance operation. Such a model would allow for studying the shift in resonance frequency, reduction in quality factor and transient response typical to resonant MFID motion. Another limitation of the dynamic model used in this thesis is that it is limited to permanent contact between robot's feet and substrate. Modeling of hopping motion (take-off, free flight and landing) would allow for studying the difference between permanent and intermittent contacts in terms of phase shift, power efficiency, thrust force and motion velocity. It would also be interesting to model other types of contact force variation than a perpendicular vibration with a sinusoidal shape. Electrostatic clamping driven by a digital electronics, for instance, would result in a square wave shape of the variation of the contact force and would only allow for increasing the contact force, not for decreasing it.

The three developed MFID prototypes are all just a first iteration allowing for a qualitative demonstration of the MFID principle and its configurations and a first quantitative characterization of the proposed designs. The performance of each of the prototypes could be improved considerably by a second design iteration. For instance, increasing the operation frequency and resonant operation of the first design would reduce considerably its power consumption. It would also be interesting to develop a prototype for this first design based on electromagnetic actuators. The variant of the first design with on-board slip generation by an eccentric motor proposed in appendix section C.2 is also very promising in terms of efficiency and cost. The second prototype could be improved by choosing for fabrication by wire EDM, possibly resulting in lower parasitic vertical vibration. The third prototype can be improved by an increase of the number of comb fingers and a reduction of the electrostatic gap. It would also be interesting to push the miniaturization of this design and test the $2 \times 2$ mm$^2$ that have already been fabricated. The characterization of such mm size prototypes requires, however, untethered operation. Moreover, the rotational motion of both the third and the second prototype also remains to be characterized.

Integration of on-board powering, for instance by solar cells, with or without on-board driving electronics would be the next logical step for the third MFID prototype. This would be a real demonstration of the application of the MFID principle for driving untethered mobile microrobots.

Finally, the author hopes on a future contribution of the mobile microrobotics community to a further elaboration of the proposed classification of locomotion principles, of the MFID principle and of the concept of a combination of on-board and off-board actuation. It would very satisfactory to see the development of other MFID designs that find their application in real autonomous mobile microrobots of a size of 1 cm$^3$ and below performing tasks that could not be performed otherwise[1].

[1]The nice thing about scientific research is that it grants the right for daydreaming... But as Einstein said *"If at first, the idea is not absurd, then there is no hope for it."*

# Appendix A

# List of symbols

| | |
|---|---|
| $a$ | Acceleration |
| $A$ | Acceleration amplitude of vibration |
| $A_{Z,g}$ | Acceleration amplitude of vibration expressed as a fraction of $g$ |
| $\alpha$ | Inclination angle of the motion direction of the robot (slider) with respect to the horizontal plane |
| $\beta$ | Contact angle |
| $C$ | Electrical capacitance |
| $C_f$ | Electrical capacitance between comb fingers |
| $c$ | Viscous damping coefficient |
| $c_f$ | Comb finger clearance |
| $c_g$ | Contact geometry coefficient expressing the ratio between contact force and preload force |
| $d_{el}$ | Electrostatic gap |
| $d_f$ | Comb finger gap |
| $d_{ij}$ | Piezoelectric coupling coefficients (i: direction of electric field, j: strain direction with polarization along the 3 (Z) axis) |
| $d_{sphere}$ | Diameter of the half spheres guiding the moving shaft on the experimental setup |
| $D_{shaft}$ | Diameter of the moving shaft on the experimental setup |
| $\delta$ | Absolute strain |
| $\Delta t$ | Time interval |
| $\Delta X_{slip}$ | Slip distance |
| $E_Y$ | Young's modulus |
| $\epsilon_0$ | Permittivity of vacuum |
| $\epsilon_r$ | Relative permittivity of an isotropic material |
| $\epsilon_{ij}$ | Relative permittivity of a piezoelectric material (i: direction of polarization, j: direction of electric field) |
| $\eta_{step}$ | Step efficiency (defined as the ratio between $v_{r,avg}$ and $v_{X,max}$) |
| $\eta_P$ | Power efficiency (defined as the ratio between the reference power and the consumed power) |
| $f$ | Frequency |
| $f_r$ | Resonance frequency |
| $f_{r1,ana}$ | Analytically calculated first resonance frequency |
| $f_{r1,num}$ | Numerically calculated first resonance frequency |
| $f'_{r1,ana}$ | Analytically calculated first resonance frequency with correction for the weight of the mirror glued on the vibrating mass (comb drive prototype) |

| | |
|---|---|
| $f'_{r1,num}$ | Numerically calculated first resonance frequency with correction for the weight of the mirror glued on the vibrating mass (comb drive prototype) |
| $f_{r1,exp}$ | Experimentally measured first resonance frequency |
| $F_1(e)$ | Correction factor for elliptical contact area in the Hertz theory |
| $F_b$ | Blocking force |
| $F_c$ | Contact force (total of all contacts) |
| $F_{ci}$ | Contact force at an individual contact |
| $F_{c,0}$ | Static contact force |
| $F_{c,0,g}$ | Static contact force due to gravity |
| $F_{c,0,add}$ | Static contact force due to an additional contact force |
| $F_{c,amp}$ | Amplitude of variation of the contact force |
| $F_t$ | Friction force |
| $F_{t,d,grav}$ | Dynamic friction force at gravity preload |
| $F_{t,s,min}$ | Minimum static friction force |
| $F_{i,X,max}$ | Maximum inertial force in axial direction |
| $F_{el}$ | Electrostatic comb drive force |
| $F_{X,ext}$ | External thrust force applied on the robot (slider) in $X$ direction |
| $h_f$ | Comb finger height |
| $h_p$ | Thickness piezoelectric actuator |
| $h_s$ | Flexure height |
| $I$ | Electrical current |
| $k_s$ | Flexure stiffness |
| $l_f$ | Comb finger length |
| $l_p$ | Length piezoelectric actuator |
| $l_s$ | Flexure length |
| $L$ | Robot's body length (defined as the geometric mean of the footprint dimensions for robots moving on a plane or as the geometric mean of the robot diameter and the robot length for in-pipe robots ) |
| $M$ | Mass |
| $M_r$ | Robot (slider) mass |
| $M_f$ | Mass of the part of the robot that is in contact with the substrate (feet) |
| $M_i$ | Mass of the part of the robot that is *not* in contact with the substrate (inertial mass) |
| $M'_i$ | Mass of the part of the robot that is *not* in contact with the substrate (inertial mass) corrected for the weight of the mirror (comb drive prototype) |
| $M_{mirror}$ | Mass of the mirror used for position measurement by interferometer |
| $\mu$ | Average |
| $\mu_d$ | Dynamic friction coefficient |
| $\mu_s$ | Static friction coefficient |
| $\nu_s$ | Stribeck velocity of friction model |
| $\nu$ | Poisson coefficient |
| $n_f$ | Number of comb fingers |
| $P$ | Power consumption |
| $P_s$ | Specific power consumption (ratio between power and motion velocity) |
| $P_{ref}$ | Reference power consumption (when sliding with a constant velocity under gravity preload) |
| $p_f$ | Comb finger pitch |
| $p_m$ | Maximum contact pressure |

| | |
|---|---|
| $Q$ | Quality factor measured as the ratio between resonance frequency and bandwidth |
| $Q'$ | Quality factor measured as the ratio between resonance amplitude and quasistatic amplitude |
| $Q_g$ | Guiding quality (defined as the ratio between axial vibration amplitude and parasitic vertical vibration amplitude) |
| $q_F$ | Force ratio (defined as the ratio between $F_{i,X,max}$ and $F_{t,s,min}$) |
| $q_I$ | Ratio of inertia |
| $R_m$ | Tensile strength of a material |
| $R_e$ | Equivalent contact radius |
| $R_{c,e}$ | Equivalent radius of an elliptical contact area |
| $s_{ij}$ | Elastic constant (i: stress direction, j: strain direction) |
| $\sigma$ | Standard deviation |
| $\sigma_0$ | Contact stiffness of the friction model |
| $\sigma_1$ | Viscous damping coefficient of the contact deformation of the friction model |
| $\sigma_2$ | Viscous friction coefficient of the friction model |
| $t$ | Time |
| $U$ | Voltage |
| $v$ | Velocity |
| $v_{r,avg}$ | Average motion velocity of the robot (slider) |
| $v_s$ | Specific average motion velocity (body lengths per second) |
| $v_{X,max}$ | Maximum velocity of the axial vibration |
| $V$ | vibration velocity amplitude |
| $\phi$ | Phase shift |
| $W$ | Energy |
| $w_f$ | Comb finger width |
| $w_p$ | Width piezoelectric actuator |
| $w_s$ | Flexure width |
| $x_f$ | Comb finger overlap |
| $x_s$ | Presliding deformation of the contact in the friction model |
| $x$ | Position of the vibration in $X$ direction |
| $x$ | Position of the robot (slider) in $X$ direction |
| $X$ | Vibration amplitude in $X$ direction |
| $X_{min}$ | Minimum axial vibration amplitude at which locomotion is still possible (force ratio $q_F$ equal to 1) |
| $X_{0,ana}$ | Analytically calculated quasistatic vibration amplitude |
| $X_{0,num}$ | Numerically calculated quasistatic vibration amplitude |
| $X_{0,exp}$ | Experimentally measured quasistatic vibration amplitude |
| $X_{f_{r1,exp}}$ | Experimentally measured vibration amplitude at first resonance frequency |
| $\dot{x}$ | Relative velocity of the friction model |
| $Y$ | Vibration amplitude in $Y$ direction |
| $z$ | Position vibration in $Z$ direction |
| $z_c$ | Contact deformation of the friction model |
| $\dot{z_c}$ | Velocity of contact deformation of the friction model |
| $Z$ | Vibration amplitude in $Z$ direction |
| $\omega$ | Pulsation $\omega = 2\pi f$ |

# Appendix B

# List of abbreviations

| | |
|---|---|
| AC | Alternating Current |
| ASIC | Application Specific Integrated Circuit |
| CMOS | Complementary MetalŰOxideŰSemiconductor |
| CPU | Central Processing Unit |
| DAC | Digital to Analogue Convertor |
| DC | Direct Current (i.e. opposite of AC) |
| DDL | Degré(s) De Liberté |
| $D\Delta t$ | Locomotion class based on Differential slip generation and asymmetric actuation ($\Delta t$) |
| DEA | Dielectric Elastomer Actuator |
| $DF_c$ | Locomotion class based on Differential slip generation and contact force ($F_c$) variation |
| DLP | Digital Light Processing |
| DOF | Degree(s) Of Freedom |
| $D\mu$ | Locomotion class based on Differential slip generation and directional friction ($\mu$) |
| DRIE | Deep Reactive Ion Etching |
| EAP | ElectroActive Polymer |
| EDM | Electro Discharge Machining |
| GCA | Gap-Closing Actuators |
| GMA | Giant Magnetostrictive Alloy |
| IC | Integrated Circuit |
| ICPF | Ionic Conducting Polymer gel Film |
| $I\Delta t$ | Locomotion class based on Inertial slip generation and asymmetric actuation ($\Delta t$) |
| $IF_c$ | Locomotion class based on Inertial slip generation and contact force ($F_c$) variation |
| II | Inertial Inchworm |
| $I\mu$ | Locomotion class based on Inertial slip generation and directional friction ($\mu$) |
| IPMC | Ionic Polymer Metal Composite |
| IR | InfraRed |
| LED | Light-Emitting Diode |
| LuGre | Lund Grenoble friction model |
| MARV | Mini Autonomous Robot Vehicle |
| MEMS | MicroElectroMechanical Systems |

| | |
|---|---|
| MFID | Modulated Friction Inertial Drive |
| MPA | Monolithic Piezo Actuator |
| MRI | Magnetic Resonance Imaging |
| op-amp | operational amplifier |
| p2p | peak to peak |
| PCB | Printed Circuit Board |
| PIPT | Photo-Induced Phase Transition |
| PLD | Programmable Logic Device |
| PSD | PhotoSensitive Device |
| PWM | Pulse Width Modulation |
| PZT | Lead Zirconate Titanate ($Pb[Zr_xTi_{1-x}]O_3$, $0 < x < 1$), a piezoelectric material |
| RIE | Reactive Ion Etching |
| RMS | Root Mean Square |
| SAW | Surface Acoustic Wave |
| SEM | Scanning Electron Microscope |
| SMA | Shape Memory Alloy |
| SMD | Surface Mounted Device |
| SoC | System on Chip |
| SOI | Silicon On Insulator |
| SPM | Scanning Probe Microscope |
| SS | Stick-Slip |
| SWUM | Standing Wave Ultrasonic Motor |
| TEM | Transmission Electron Microscope |
| TWUM | Traveling Wave Ultrasonic Motor |

# Appendix C

# Other interesting MFID mobile microrobot designs

## C.1 On-board electrostatic clamping

### C.1.1 Concept

The first prototype presented in this chapter was based on an external slip generation by a vibration of the substrate in $X$ and $Y$ direction and an on-board contact force variation by a vertical vibration of an inertial mass on the robot. This section presents a similar configuration with the difference that the contact force variation is generated by a variable electrostatic clamping force. The advantage of using on-board electrostatic clamping are the extreme on-board simplicity (the robot only consists of electrodes and a dielectric layer, so no moving pars) and the low on-board power consumption. The drawbacks are that electrostatic clamping only allows for increasing the contact force and not for decreasing it and that it suffers from sensitivity to surface roughness, dust, electrical charges, humidity and a vacuum clamping effect.

The chosen configuration is illustrated in figure C.1(a). A conductive substrate is vibrated in $X$ and $Y$ direction. On top of this substrate there are several robots that contain on their underside two electrodes, between which a voltage difference $U$ is applied. If we consider the substrate to be at zero potential, the two electrodes will be at a potential of $-U/2$ and $+U/2$. As the vibration in $X$ and $Y$ direction are phase shifted over 90°, the substrate follows, in the case of sinusoidal vibration, a translation along a circular path. Such a circular translation can be generated easily and efficiently with a DC motor that drives an eccentric that is connected to the vibrating substrate. Generation of vibration by rotation of an eccentric is very efficient as the kinetic energy is not absorbed and regenerated during each actuation period. The driving voltage for the on-board clamping electrodes is generated by on-board high voltage solar cells. Several robots can be moving at the same time on the vibrating substrate, while their solar cells are all simultaneously illuminated by an external projector (beamer) (see figure C.1(b)). The eccentric motor is driven at 15 Hz, while the projector is operated at 60 Hz (60 frames per second) and is synchronized to the rotation of the motor. The projector generates cycles of 1 white frame and three black frames with a cycle period of $60/4 = 15$ Hz, causing the robot to adhere to the vibrating substrate by electrostatic clamping during 1 quadrant of the circular motion path. As illustrated in figure C.2 successive clamping to the vibrating substrate during 1 quadrant causes the robot move in the direction of the motion of the substrate during that quadrant. Hence, selective illumination during 1 of the 4 quadrants of the substrate vibration allows for motion in $+X$, $-Y$, $-X$ and $+Y$ direction.

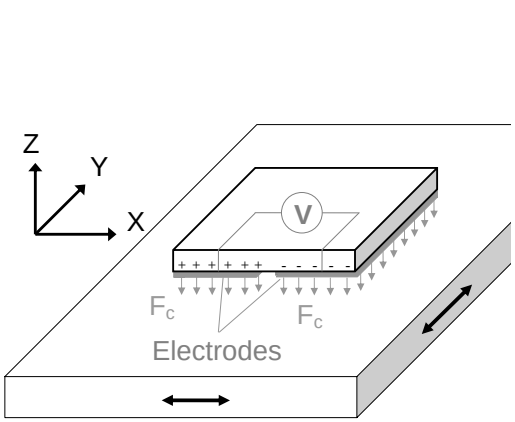


**(a)** MFID configuration based on external slip generation in $X$ and $Y$ direction and on-board contact force variation by electrostatic clamping

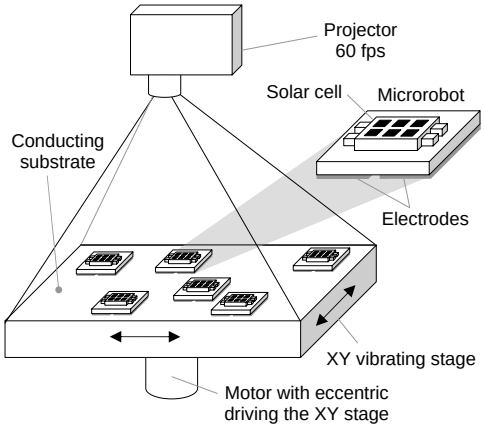


**(b)** Parallel powering and control of several mobile microrobots with on-board solar cells illuminated by a projector

**Figure C.1:** Configuration and operating principle of the prototype setup for MFID motion with electrostatic clamping

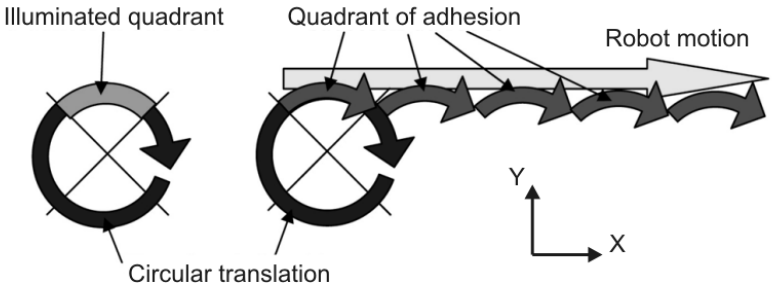


**Figure C.2:** Operation principle of MFID motion obtained from electrostatic clamping during one quadrant of the circular translation of the substrate

Moreover, each robot can be illuminated independently by the projector by projecting frames with local black and local white areas. This allows for independent, simultaneous driving and control in $X$ and $Y$ direction of a large number of robots.

### C.1.2 Experimental setup

Figure C.3 depicts the experimental setup developed by Christophe Groux in the framework of a master thesis [346]. It consists of an $XY$ stage that is guided in $X$ and $Y$ direction by a set of flexures that are cut out of a sheet of steel by laser. The vibrating stage has a measured out-of-plane resonance frequency of about 150 Hz, which is much higher than the maximum horizontal actuation frequency of 15 Hz. The vibrating $XY$ stage is driven by a brushed DC motor (S 2332, 15 W from Maxon Motor AG, Switzerland). An exchangeable eccentric connects the output axis of the motor to a rotary bearing fixed at the bottom of the vibrating stage. A silicon wafer of ∅150 mm is fixed on top of the vibrating substrate. The silicon wafer is covered with a PMMA cover leaving a gap for the microrobots. This cover allows the silicon wafer and the robots to be cleaned in a cleanroom environment (class 100), to put the robots on the wafer and close with the cover in order to allow for operation

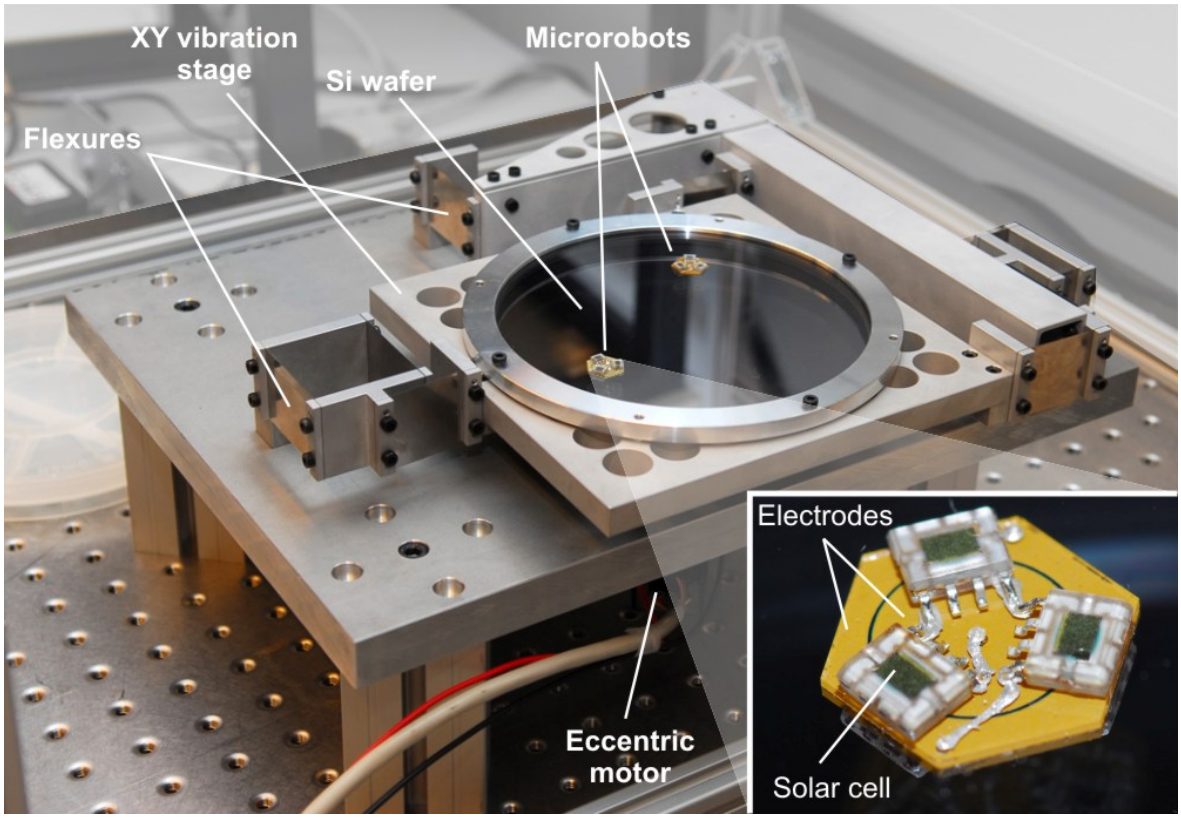


**Figure C.3:** Developed setup consisting of a flexure guided $XY$ stage driven by an eccentric motor and robots with screen printed electrodes on the bottom side powered by solar cells [346]

outside of a cleanroom without risk for dust deposition on the silicon wafer[1]. The complete setup is illuminated with a BenQ 3000 ANSI lumen projector based on the DLP (Digital Light Processing) technology[2] from Texas Instruments Inc. For optimization of the amount of projected light, the color wheel in the projector, which filters out the projected colors during each frame, is removed.

The microrobots (see the inset in figure C.3) consist of a float glass substrate (thickness 0.5 mm) that is diced into a hexagonal shape (outer diameter about 15 mm). Two concentric electrodes of equal area and thickness of about 8 $\mu$m are printed on the underside of the robot by screen printing with a silver filled glass paste (ESL 590G). The electrodes are covered by an 8 $\mu$m layer of dielectric (lead-borosilicate glass with a relative permittivity of about $\epsilon_r = 8$). The electrical connection of the electrodes on the underside of the robot are passed to the upper side by means of vias in the glass substrate that were fabricated by sand blasting before the screen printing step.

The voltage for the electrostatic clamping is generated by three high voltage solar cells (CPC1840, Clare Inc., USA) that are connected in series. The solar cells have a rated open circuit voltage of 16 V and short circuit current of 15 $\mu$A at an illumination of 6000 lux (direct sunlight). Lower voltages were measured, however, when illuminated by the projector. This

[1]Dust between the robot and the silicon wafer would cause an air gap, which decreases considerably the electrostatic clamping force

[2]The DLP technology is based on a matrix of microfabricated mirrors that can be tilted in order to project the light or not in the lens of the projector. In fact, this technology allows for much faster switching rates than 60 Hz if accessing directly to the DLP chip.

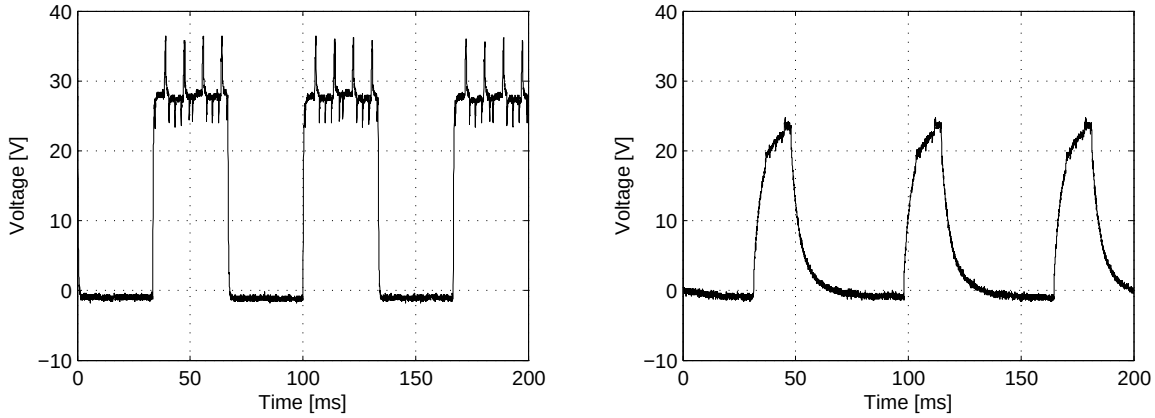


**(a)** Open circuit voltage response for a 50% duty cycle (2 white frames, 2 black frames at 60 fps)

**(b)** Voltage response for a 25% duty cycle (1 white frame, 3 black frames at 60 fps) with robot in contact with the silicon wafer

**Figure C.4:** Voltage response of the microrobot's electrodes

is due to the fact that the light of a projector contains much less infrared than natural sunlight[3], while the maximum sensitivity of the used solar cells is typically around $\lambda = 870$ nm. Figure C.4(a) shows the open circuit voltage response[4] of three solar cells connected in series while illuminated with the projector with a 50% duty cycle (2 white frames, 2 black frames at 60 fps). The maximum average voltage is about 28 V (which is quite a bit lower than the expected 48 V). When the solar cells are connected to the electrodes on the robot and the robot is put on top of the silicon wafer the maximum voltage decreases even more because of the limited rise time of the solar cells that have to charge the capacitive load formed between the electrodes and the substrate. Figure C.4(b) shows a maximum voltage of about 23 V with the robot in contact with the silicon wafer for an illumination with a duty cycle of 25% (i.e. 1 white frame and 3 black frames at 60 fps). With this voltage an electrostatic clamping force of 2.3 mN is generated, which corresponds to about 64% of the weight of the robot ($M_r = 368$ mg).

### C.1.3 Proof of concept

The experiments have proven the feasibility of the proposed concept. The robot remains sticking to the vibrating substrate when illuminated and sliding when not illuminated. The robot motion could be controlled roughly in $X$ and $Y$ direction. However, the motion has shown to be very sensitive to dust and charge accumulation. Moreover, undesired sticking of the robot to the substrate due to a creation of a small vacuum between robot and substrate was sometimes observed. Operation on a silicon wafer with ⌀100 $\mu$m holes fabricated by Deep Reactive Ion Etching (DRIE) has proven to decrease the sticking due to the vacuum effect. Motion velocities in the order of $v_{r,avg} = 5$ mm/s were observed in $X$ and $Y$ direction for an actuation at $f = 15$ Hz with an eccentricity of $X = 0.5$ mm. This actuation frequency and eccentricity correspond to a horizontal tangential velocity amplitude of $v_{x,max} = V_X = 2\pi f X = 47$ mm/s and thus a step efficiency (see equation 4.24 on page 104) of

$$\eta_{step} = \frac{v_{r,avg}}{v_{x,max}} = 0.11, \tag{C.1}$$

[3]The spectrum of projectors is usually optimized for visible light (i.e. $\lambda = 380 \cdots 750$ nm).

[4]The observed voltage peaks during the illumination phase are due to the fast switching of the DLP mirrors.

which is quite low compared to other MFID prototypes.

For the same parameter settings a horizontal centripetal acceleration of $A = (2\pi f)^2 X = 4.4$ m/s$^2$ is generated, which corresponds to an inertial force of $F_i = M_r A = 1.6$ mN ($M_r = 368$ mg). For a static friction coefficient of glass on silicon of $\mu_s = 0.14$ [347], a minimum static friction force between robot and substrate of $F_{t,s,min} = \mu_s M_r g = 0.51$ mN is obtained. Hence, the force ratio (see equation 4.25 on page 106) is equal to

$$q_F = \frac{F_i}{F_{t,s,min}} = 3.1. \tag{C.2}$$

This force ratio is larger than 1, which is a necessary condition for MFID motion, but not much. The sensitivity to dust, electric charges and vacuum clamping could be improved by increasing this force ratio.

### C.1.4 Discussion

An interesting, innovative concept of wireless powering and control of several MFID microrobots is proposed and an experimental setup is developed. The first results have proven the feasibility of the concept, but have also shown the sensitivity of the electrostatic clamping to dust, accumulation of charges and vacuum clamping. Nevertheless, the concept offers interesting perspectives, for instance in terms of control. Velocity control can be obtained by illuminating with gray scale colors in stead of black and white. Rotation of the robots could be achieved cooperatively by bringing two robots into contact and have them move in a circular path around each other. Moreover, illumination with a projector allows to define individually the motion direction and velocity at any arbitrary point on the wafer independently of the fact if there is a robot present at that point or not. In this way vector fields with potential wells could be generated in which robots can be trapped without the need for tracking the robot's position. Miniaturization of the robot size is also certainly possible. Very small robot sizes and batch fabrication could be obtained by fabricating the high voltage solar cells and the electrodes and dielectric in the same fabrication process on the same wafer. Of course it is also possible to integrate an on-board electronics on the robot and use the solar cells only for powering under constant illumination. In that case synchronization between on-board and off-board actuation would be required (for instance by IR communication or an on-board accelerometer).

## C.2 On-board eccentric vibration

In the previous prototype with on-board electrostatic clamping the horizontal vibration in $X$ and $Y$ direction is generated by the rotation of an eccentric mass about a vertical axis. As already mentioned before, such a rotation is very efficient as kinetic energy of the rotation is not lost or dissipated in each vibration period, just as for resonance operation. Rotation of an eccentric mass has the advantage with respect to the resonance vibration in the horizontal plane that with only one actuation signal vibration in 2 DOF can be generated. A second advantage is that rotation is efficient at nearly any rotation frequency, while resonance operation is only efficient around the resonance frequency. Moreover, the resonance frequency band becomes smaller with increasing quality factor. This small frequency band requires first of all that the actuation signal is generated by the electronics with an accurate frequency. Secondly, the small frequency band complicates considerably the task of integrating both efficient slip generation and efficient contact force variation on the robot. Both actuation must be synchronized, so their resonance frequency should match. Matching of resonance

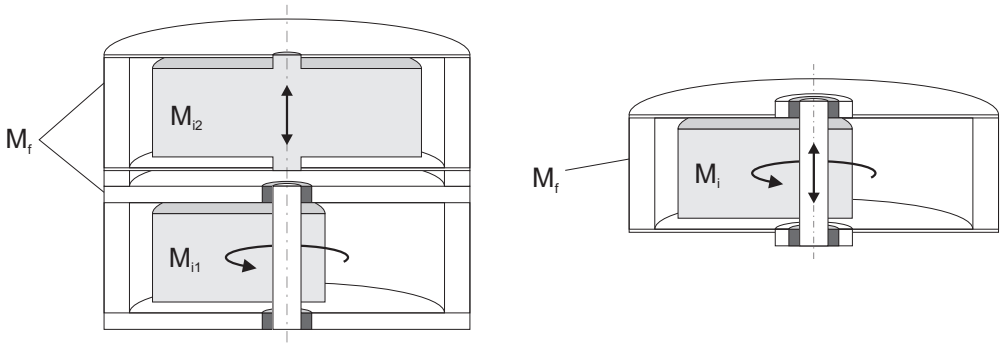


**(a)** Design with separated eccentric mass and vertically vibrating inertial mass

**(b)** Design with only one inertial mass

**Figure C.5:** MFID configuration with on-board slip generation by the rotation of an eccentric about a vertical axis and on-board contact variation by a vibration of an inertial mass

frequencies with high quality factors requires either very tight fabrication tolerances or the possibility of adapting one of the resonance frequencies by a variation of the mass or of the stiffness. Rotation of an eccentric mass requires, as for resonance vibration, a considerable rise time (and fall time). In the case of rotation this rise time goes with a variation of the actuation frequency. Moreover, the coupling of $X$ and $Y$ vibration causes during motion in a given direction a parasitic vibration in the perpendicular direction. Therefore, eccentric rotation is not well suited for precision operation with small step sizes or for operation that requires to change motion velocity and direction very often.

Figure C.5 illustrates a possible on-board integration of both $XY$ slip generation by eccentric vibration and contact force variation by vertical vibration. The eccentric mass and the inertial mass for vertical vibration can either be two different masses $M_{i1}$ and $M_{i2}$ (as in figure C.5(a)) or can be the same mass $M_i$ (as in figure C.5(b)). The advantage of two different masses is that two separated modules for rotation and vertical vibration can be used. Such modules could be very low cost off-the-shelf modules such as eccentric motors (such as for cell phones) for the rotation and for instance loudspeakers (voice coil or piezoelectric) for the vertical vibration. The advantage of using only one inertial mass is that it can allow for smaller robot sizes (though smaller than 1 $cm^3$ will be difficult).

The configuration shown in figure C.5 features 2 DOF motion in $X$ and $Y$ direction (with 2 actuation channels). Holonomic motion with 3 DOF would require rotational motion ($\theta_Z$). Rotation could be obtained by repeatedly accelerating and decelerating the inertial mass. Another possibility is to separate the vertically vibrating mass in two and vibrate them in counterphase for rotational motion. A third possibility would be to excite the inertial mass in a rotational ($\theta_X$ or $\theta_Y$) vibration mode.

Another advantage the proposed microrobot design is that all moving parts can be encapsulated. Such encapsulation allows for a very high robustness of the robot in terms of mechanical manipulation, but also in terms of environmental conditions (such as operation on water or on sand). Moreover, the design allows for a simple driving electronics with few actuation channels, low voltage operation in DC mode or with square waves. The low cost, high efficiency and robustness of this locomotion solution make it an ideal design for toy or gadget robots.

# Appendix D

# Additional experimental results for the inertial inchworm principle

This appendix shows some additional measurements concerning the characterization of the inertial inchworm principle discussed in section 4.4.9. Figure D.1 and D.2 show the influence of the perpendicular acceleration amplitude on the *velocity vs. phase shift* profile. The maximum motion velocity and the phase shift at which this maximum motion velocity is reached are also summarized in figure 4.39 on page 119. The same behavior as for the MFID principle is observed (see figures 4.20 and 4.21 on pages 101 and 102), except that a better motion stability is achieved, with the inertial inchworm for accelerations ranging from $0.43g$ to $0.72g$.

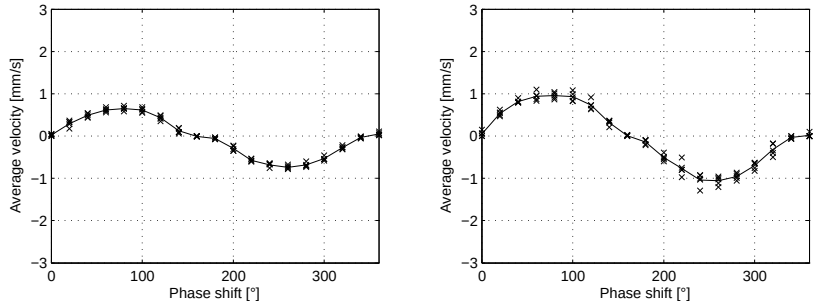


**(a)** $A_Z = 0.14g$ **(b)** $A_Z = 0.22g$

**(c)** $A_Z = 0.28g$ **(d)** $A_Z = 0.35g$

**Figure D.1:** Measured motion velocity of the inertial drive principle in function of the phase shift for a perpendicular acceleration amplitude ranging from $0.14g$ to $0.35g$ ($f = 2000$ Hz, $X = 270$ nm)

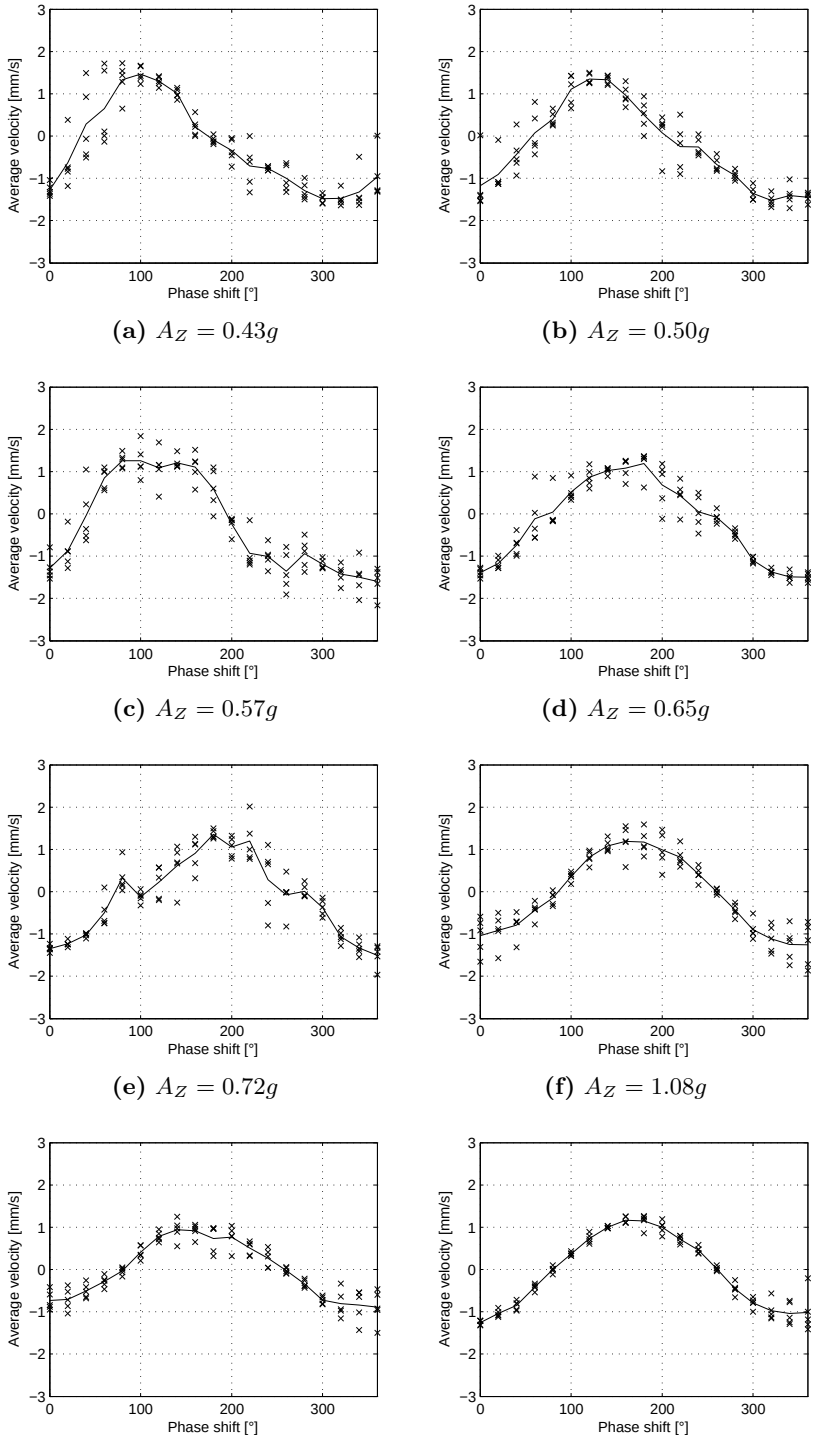


**(a)** $A_Z = 0.43g$ **(b)** $A_Z = 0.50g$

**(c)** $A_Z = 0.57g$ **(d)** $A_Z = 0.65g$

**(e)** $A_Z = 0.72g$ **(f)** $A_Z = 1.08g$

**(g)** $A_Z = 1.44g$ **(h)** $A_Z = 2.16g$

**Figure D.2:** Measured motion velocity of the inertial drive principle in function of the phase shift for a perpendicular acceleration amplitude $A_Z$ ranging from $0.43g$ to $2.16g$ ($f = 2000$ Hz, $X = 270$ nm)

# Appendix E

# Fabrication process of the comb drive actuators

**Project** : **Comb drive vibrating masses** **Created** : 15.11.2005 **Last revision** : 10.01.2006
**Operator** : **W. Driesen / A. Rida** **Substrates** : SOI, 4", 200-2-380 Si-SiO2-Si

| Step | Description | Equipment | Program / Parameters | Target | Actual | Remarks |
|---|---|---|---|---|---|---|
| **1** | **WAFER PREPARATION** | | | | | |
| 1.1 | Stock out | | | | | 3 wafers |
| 1.2 | Check | | | | | |
| **2** | **AL SPUTTERING - front** | | | | | |
| 2.1 | DC sputter Al/Si 1% | Z4/Spider | | 2min30 | | 1 um @405 nm/min |
| **3** | **PHOTOLITHOGRAPHY 1 - front** | | | | | |
| 3.1 | S1818 coating | Z1/RiteTrack | C_S1818_2um | 2 um | | 5600 rpm, EBR |
| 3.2 | PR bake | Z1/RiteTrack | C_S1818_2um | | | Prox. 115°C 90s, EBR |
| 3.3 | PR expose | Z1/MA150 | First mask, HC, 50 mJ/cm2 | | 7s | test mode 6, 7, 8, 10 s |
| 3.4 | PR develop | Z1/RiteTrack | dev_S1818_up2_6 | | | |
| 3.5 | PR postbake | Z1/RiteTrack | dev_S1818_up2_6 | | | Prox. 115°C 90s |
| 3.6 | Inspection | Z6/uScope | Resolution and alignment | | | |
| **4** | **AL DRY ETCHING - front** | | | | | |
| 4.1 | AL dry etch | Z2/STS Multiplex ICP | Al_etch | 5min | | 0.2 à 0.5 um/min, 20°C |
| **5** | **RESIST STRIP WET** | | | | | |
| 5.1 | Remover 1165 | Z2/WB_PR_Strip | Old bath, 5 min, 70°C | | | |
| 5.2 | Remover 1165 | Z2/WB_PR_Strip | New bath, 5 min, 70°C | | | |
| 5.3 | Quick dump rinse | Z2/WB_PR_Strip | 5min | | | |
| 5.4 | Cascade Tank | Z2/WB_PR_Strip | 5min | | | |
| 5.5 | Plasma O2 Clean | Z2/Oxford | O2 20min. | | | total time 30 min |
| 5.6 | Inspection | Z2/uScope | | | | |
| **6** | **LPCVD LTO OXIDE DEPOSITION** | | | | | |
| 6.1 | LTO Oxidation | Z3/EPFL3_1 | 6-9 nm/min, temps?? | 3 um | | 2 plaques 100/P/DS/01-05 ajoutés |
| **7** | **PHOTOLITHOGRAPHY 2 - front** | | | | | |
| 7.1 | HMDS | Z6/YES3 | Prog 0 | | | 25 min |
| 7.2 | AZ92XX coating | Z1/RiteTrack | C_ AZ92XX_3um_BSR_only | 3 um | | 3450 rpm, 45s, no EBR |
| 7.3 | PR bake | Z1/RiteTrack | C_ AZ92XX_3um_BSR_only | | | Prox. 115°C, 120s, no EBR |
| 7.4 | PR expose | Z1/MA150 | First mask, HC, 50 mJ/cm2 | | 15s | test mode 13, 14, 15, 16 s |
| 7.5 | PR develop | Z1/RiteTrack | Dev_AZ_92XX_3um | | | |
| 7.6 | PR postbake | Z1/RiteTrack | Dev_AZ_92XX_3um | | | Prox. 115°C, 5s |
| 7.7 | Inspection | Z6/uScope | Resolution and alignment | | | |
| **8** | **OXYDE DRY ETCHING – front** | | | | | |
| 8.1 | Oxyde dry etch | Z2/Alcatel AMS 200 | SiO2_PR_1 :1 | | ??s | 0°C, RF, 0.3 um/min |
| 8.2 | Inspection | Z2/uScope | | | | |

**Figure E.1:** Runcard for the fabrication of the electrostatic comb drive actuators used for the third prototype discussed in section 5.3 (continued in figure E.2)

**Project : Comb drive vibrating masses** **Created : 15.11.2005 Last revision : 10.01.2006**
**Operator : W. Driesen / A. Rida** **Substrates : SOI, 4", 200-2-380 Si-SiO2-Si**

| Step N° | Description | Equipment | Program / Parameters | Target | Actual | Remarks |
|---|---|---|---|---|---|---|
| **9** | **RESIST STRIP WET** | | | | | |
| 9.1 | Plasma O2 Clean | Z2/Oxford | O2 20min. | | | still PR on backside after clean |
| 9.2 | Remover 1165 | Z2/WB_PR_Strip | Old bath, 5 min, 70°C | | | |
| 9.3 | Remover 1165 | Z2/WB_PR_Strip | New bath, 5 min, 70°C | | | |
| 9.4 | Quick dump rinse | Z2/WB_PR_Strip | 5min | | | |
| 9.5 | Cascade Tank | Z2/WB_PR_Strip | 5min | | | |
| 9.6 | Plasma O2 Clean | Z2/Oxford | O2 20min. | | | no more PR on backside |
| 9.7 | Inspection | Z2/uScope | | | | |
| **10** | **PHOTOLITHOGRAPHY 3 - back** | | | | | |
| 10.1 | HMDS | Z6/YES3 | Prog 0 | | | 25 min |
| 10.2 | AZ92XX coating | Z1/RiteTrack | C_ AZ92XX_3um_BSR_only | 3 um | | 3450 rpm, 45s, no EBR |
| 10.3 | PR bake | Z1/RiteTrack | C_ AZ92XX_3um_BSR_only | | | Prox. 115°C, 120s, no EBR |
| 10.4 | PR expose | Z1/MA150 | First mask, HC, 50 mJ/cm2 | 15s | 15s | |
| 10.5 | PR develop | Z1/RiteTrack | Dev_AZ_92XX_3um | | | |
| 10.6 | PR postbake | Z1/RiteTrack | Dev_AZ_92XX_3um | | | Prox. 115°C, 5s |
| 10.7 | Inspection | Z6/uScope | Resolution and alignment | | | |
| **11** | **OXYDE DRY ETCHING – back** | | | | | |
| 11.1 | Oxyde dry etch | Z2/Alcatel AMS 200 | SiO2_PR_1 :1 | 7min | ??s | 0°C, RF, 0.3 um/min, DFA |
| 11.2 | Inspection | Z2/uScope | | | | |
| **12** | **RESIST STRIP WET** | | | | | |
| 12.1 | Remover 1165 | Z2/WB_PR_Strip | Old bath, 5 min, 70°C | | | |
| 12.2 | Remover 1165 | Z2/WB_PR_Strip | New bath, 5 min, 70°C | | | |
| 12.3 | Quick dump rinse | Z2/WB_PR_Strip | 5min | | | |
| 12.4 | Cascade Tank | Z2/WB_PR_Strip | 5min | | | |
| 12.5 | Plasma O2 Clean | Z2/Oxford | O2 20min. | | | finally not executed |
| 12.6 | Inspection | Z2/uScope | | | | |
| **13** | **DEEP REACTIVE ION ETCH – front** | | | | | |
| 13.1 | DRIE etch | Z2/Alcatel AMS 200 | SOI_Accurate | 44-67 min | 72.5 min | 20°C, RF, Bosch Process, 3 à 4.5 um/min |
| 13.2 | Inspection | Z2/uScope | | | | |
| **14** | **DEEP REACTIVE ION ETCH – back** | | | | | |
| 14.1 | DRIE etch | Z2/Alcatel AMS 200 | SOI_standard | 76 min | 100 min | 20°C, RF, Bosch Process, 5 um/min |
| 14.2 | Inspection | Z2/uScope | | | | |
| **15** | **OXYDE ETCH** | | | | | |
| 15.1 | SILOX | Z2/PLADE | SILOX, 20°C | 50 min | 50 min | 40 nm/min WetOx, 240 nm/min LTO |
| 15.2 | Inspection | Z2/uScope | | | | |
| **16** | **SEM inspection** | | | | | |
| 16.1 | Inspection | Z1/LEO | | | | |

**Figure E.2:** Runcard for the fabrication of the electrostatic comb drive actuators used for the third prototype discussed in section 5.3 (continued from figure E.1)

# Appendix F

# Specifications of components and instruments

This appendix gives an overview of the specifications of the piezoelectric actuators, mechanical components, electrical devices and measurement equipment used within this thesis.

## F.1 Piezoelectric actuators

### Stack piezoelectric actuators

The table below lists the specifications of the piezoelectric stack actuators that have been used for the perpendicular vibration of the characterization setup shown in figure 4.4 on page 83. The measured free stroke and the electrical capacitance of the two actuators assembled on the experimental setup differ a bit, so both values are listed below.

Manufacturer Noliac A/S
Model CMA-P4

| | Units | Value |
|---|---|---|
| length | mm | 5 |
| width | mm | 5 |
| height | mm | 3 |
| Voltage range | V | [0, 150] |
| Free stroke | $\mu m_{p2p}$ | 3.458 / 4.080 |
| Blocking force | N | 1000 |
| Capacitance | nF | 219 / 231 |
| Stiffness | N/$\mu$m | 208 |
| Unloaded resonance freq. | kHz | >300 |

### Shear mode piezoelectric actuators

The table below lists the specifications of the shear mode actuators that have been used for the axial vibration of the characterization setup shown in figure 4.4 on page 83.

Manufacturer Fuji Ceramics Corporation
Material C82

| | Units | Value |
|---|---|---|
| length | mm | 4 |
| width | mm | 3 |
| height | mm | 1 |
| Voltage range | V | [-200 200] |
| Piezoelectric constant ($d_{15}$) | pm/V | 781 |
| Free stroke (amp) | nm | $\pm$268 |
| Dielectric constant ($\epsilon_{11}$) | | 3090 |
| Capacitance | pF | 360 |
| Transversal elasticity ($Y_{11}^E$) | GPa | 62 |
| Transversal stiffness ($k_{11}^E$) | N/$\mu$m | 744 |
| Shearing elasticity ($Y_{55}^E$) | GPa | 22 |
| Shearing stiffness ($k_{55}^E$) | N/$\mu$m | 264 |

### PZT sheets for transversal and thickness mode actuation

The table below lists the specifications of the soft piezoelectric material used for the bimorph actuators generating the on-board vertical vibration on prototype 1 (see figure 5.3 on page 128) and for the on-board horizontal and vertical vibration on prototype 2 (see figure 5.7 on page 134).

Manufacturer Physik Instrumente GmbH
Material PIC 151

| | Units | Value |
|---|---|---|
| thickness | mm | 0.25 / 0.5 / 1 |
| Piezoelectric constant ($d_{33}$) | pm/V | 450 |
| Piezoelectric constant ($d_{31}$) | pm/V | -210 |
| Dielectric constant ($\epsilon_{33}$) | | 2400 |
| Axial elasticity ($Y_{33}^E$) | GPa | 52.6 |
| Transversal elasticity ($Y_{11}^E$) | GPa | 66.7 |

### Piezoelectric $XYZ$ stage

The table below lists the specifications of the piezoelectric $XYZ$ stage used for the horizontal vibration in $X$ and $Y$ direction of the walking substrate for the first prototype (see figure 5.1 on page 127).

Manufacturer Piezosystem Jena GmbH
Product Tritor 101

| | Units | Value |
|---|---|---|
| length | mm | 68 |
| width | mm | 68 |
| height | mm | 30 |
| displacement ($X, Y, Z$) | $\mu$m | 100 |
| unloaded resonance freq. ($X, Y, Z$) | Hz | 420 / 410 / 360 |
| stiffness ($X, Y, Z$) | N/$\mu$m | 1 |
| driving voltage | V | [-10, 150] |
| capacitance | $\mu$F | 1.7 |

## F.2 Mechanical components

### Mobile shaft experimental setup

The table below lists the physical and mechanical properties of the mobile shaft on the characterization setup shown in figure 4.4 on page 83. Material properties were provided by the manufacturer except for the tensile strength obtained from [348].

Manufacturer ADAX SA
Material DIN 1.4034 + S (X 46 CrS 13)

| | Units | Value |
|---|---|---|
| diameter | mm | 2.5 |
| length | mm | 35 |
| Density | $kg/m^3$ | 7600 |
| Young's Modulus | GPa | 210 |
| Poisson's ratio | | 0.3 |
| Hardness (Rockwell) | HRc | 55 |
| Hardness (Vickers) | HV | 600 |
| Tensile strength ($R_m$) | MPa | 1995 |
| Roughness on ⌀ ($R_a$) | $\mu$m | $< 0.1$ |
| Roughness on ends ($R_a$) | $\mu$m | $\ll 0.1$ |

### Sapphire half spheres

The table below lists the physical and mechanical properties of the sapphire half spheres used to guide the mobile shaft on the characterization setup shown in figure 4.4 on page 83.

Manufacturer Saphirwerk Industrieprodukte AG
Material Sapphire (99.99% $Al_2O_3$)

| | Units | Value |
|---|---|---|
| diameter | mm | 1 |
| height | mm | 0.6 |
| Density | $kg/m^3$ | 3990 |
| Young's Modulus | GPa | 430 |
| Poisson's Ratio | | 0.29 |
| Hardness (Vickers) | HV | 2300 |
| Compression strength | MPa | 2100 |

## F.3 Equipment for electrical signal generation

### Analogue output board

The table below lists the specifications of the analogue output board used to generate the sinusoidal signals that, after amplification, are driving the piezoelectric actuators on the characterization setup as well as on all three prototypes developed in this thesis.

Manufacturer National Instruments Corporation
Product NI 6713

| | Units | Value |
|---|---|---|
| number of channels | | 8 |
| update rate | kHz | 740 to 1000 |
| voltage range | $V_{amp}$ | ±10 |
| resolution | bits | 12 |

### High voltage amplifier

The table below lists the specifications of the high voltage amplifier that has been used to amplify the signals generated by the analogue output board mentioned above and drive the piezoelectric actuators for the characterization setup and all three prototypes. This amplifier was developed at the Laboratoire de Systèmes Robotiques (EPFL) for stick-slip actuation of piezoelectric actuators with capacitances of some nF. Experience has shown, however, that the amplifier is not well adapted for driving capacitive loads of some hundreds of nF as is the case for the stack piezos on the experimental setup. The frequency response shown in figure F.1 shows an important decrease in amplification factor and a significant phase lag when driving the stack piezos (capacitance 220 nF) with a sinusoidal signal of some kHz. The reduction in amplification factor and the phase lag have been characterized and compensate for as described in section 4.3.2.

| | Units | Value |
|---|---|---|
| Number of channels | | 8 |
| Output voltage range | $V_{amp}$ | ±200 |
| Input voltage range | $V_{amp}$ | ±10 |
| Amplification factor | | 20 |
| Slew rate (@ 1 nF load) | V/$\mu$s | 400 |
| Peak current (@ 1 nF load) | mA | 200 |

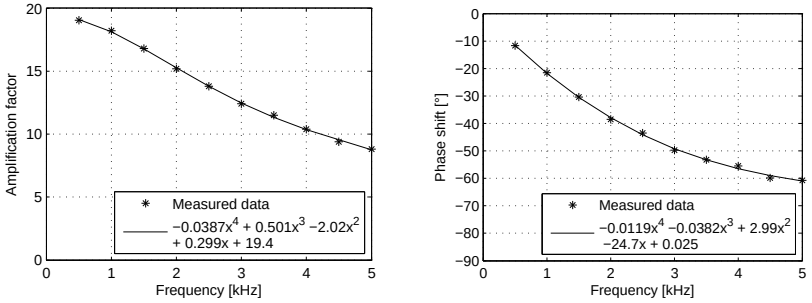


**Figure F.1:** Measurement of the amplification factor and the phase lag of the electrical amplifier in function of the driving frequency with an input voltage swing of 0.2 $v_{p2p}$ (offset 3.75 V) and a capacitive load of about 220 nF.

## F.4 Measurement equipment

### Interferometer

The table below lists the most important specs of the interferometer used for the position measurements for the characterization setup as well as for the second and third prototype.

Manufacturer SIOS Meßtechnik GmbH
Product Miniature Plane-Mirror Interferometer, SP-2000

| | Units | Value |
|---|---|---|
| Measurement range | mm | 200 |
| Resolution | nm | 1 |
| Nominal laser wave length | nm | 632.8 |
| Laser warm-up period | min | 10 – 20 |
| Maximum velocity | mm/s | 600 |
| Alignment tolerance | ’ | ±2 |
| Max. measurement rate | MHz | 1 |

### Vibrometer

The table below lists the most important specs of the vibrometer used for the measurement of the vertical vibration of the piezo stacks on the characterization setup (see figure 4.12 on page 92). The vibrometer controller features three sensitivity settings (125, 25 and 5 mm/sV). The data in the table below apply for the setting of 5 mm/sV, which was used during the measurements. The noise-limited resolution is defined as the signal amplitude (RMS) at which the signal-to-noise ratio is 0 dB with 1 Hz spectral resolution.

Manufacturer Polytec GmbH
Product OFV 512 Fiber-Optic Sensor with OFV 2601 Laser RVA controller

| | Units | Value |
|---|---|---|
| sensitivity | $\frac{\text{mm}}{\text{sV}}$ | 5 |
| Max. velocity | mm/s | 50 |
| Max. acceleration | $g$ | 8000 |
| Frequency range | Hz | $[0.5, 250 \cdot 10^3]$ |
| Linearity error | % | ±1 |
| Resolution | $\frac{\mu\text{m}}{s}\sqrt{Hz}$ | 0.1 |
| Typical spot size @ 76 mm | $\mu$m | 16 |
| Laser wavelength | nm | 633 |

### Lock-in amplifier

The table below lists the most important specs of the lock-in amplifier used to filter and measure the output from the vibrometer mentioned above.

Manufacturer EG&G Instruments
Product 7260 DSP Lock-in amplifier

| | Units | Value |
|---|---|---|
| Max. sensitivity | nV | 10 |
| Frequency response | Hz | $[0.5, 2 \cdot 10^6]$ |
| Phase measurement accuracy | ° | 0.01 |
| Max. input voltage | $V_{p2p}$ | 20 |
| Gain Accuracy | % | ±0.3 |

# Appendix G

# Curriculum Vitae

**Walter DRIESEN**
Sentier de la Fleur-de-Lys 7
CH-1008 Prilly, VD
+41 76 546 93 10
walter.driesen@gmail.com

**MECHANICAL ENGINEER**
29 years old (October 31st, 1978), married, 1 child
Belgian, B permit

## KEY SKILLS

- 7 years experience in R&D
  - miniature actuators
  - microsystems
  - microfabrication
- Analytical mind, systematic approach
- Teamwork, communication skills
- Experience in project management

## EDUCATION

**EPFL** (Ecole Polytechnique Fédérale de Lausanne) 2004 – June 2008
Robotic Systems Laboratory (LSRO)
**PhD in Microengineering**

- Design, modeling and prototyping of a new locomotion principle for mobile microrobots
- Major challenges: miniaturization, integration, microfabrication, energy efficiency

**KUL** (Katholieke Universiteit Leuven), Belgium 1996 – 2001
**Master in Mechanical-Electrical Engineering**

- Master project: "Study of micro Electro Discharge Machining (EDM) for the production of 3D micromoulds for hot embossing"

## PROFESSIONAL EXPERIENCE

**ALLERGAN Medical SA** 2008
**Independent consultant**

- Development of a new actuator for medical implants
- Concept study, market analysis and actuator design

**EPFL** (Ecole Polytechnique Fédérale de Lausanne) 2002 – 2008
Robotic Systems Laboratory (LSRO)
**Research engineer**

- Development of mobile microrobots of a size from 1 $cm^3$ down to some $mm^3$ for applications in micromanipulation and high precision robotics
- Design (Pro/Engineer) of piezoelectric and electrostatic actuators
- Actuator characterization by high precision measurements (interferometer, vibrometer, vision, …)
- MEMS microfabrication (comb drive) in a clean room environment
- Implementation in C++ of a robot control system based on optical tracking
- Active in two European projects with +10 partners
    - Work package leader
    - Robot integration: definition of interfaces between the modules produced by each partner
    - Participation to submission of a new project
- Coordination and implementation of a new web site for the lab
- Management of +20 student projects
- +20 publications: 1 journal, 1 invited speaker, 2 best paper awards
- Several reviews of scientific articles for the Journal of Micromechanics and Microengineering

**KUL** (Katholieke Universiteit Leuven), Belgium 2001 – 2002
Micro and Precision Engineering Research Group
**Research engineer**

- Study of micro Electro Discharge Machining (EDM) for the fabrication of 3D micromoulds
- Development of a process for EDM electrode shaping for the fabrication of noncircular shapes, small features and deep holes
- State of the art of batch microfabrication techniques by replication
- 2 publications

## COMPUTER SKILLS

- Windows, MS Office, Latex, HTML
- Pro/Engineer, Pro/Mechanica, Matlab, Simulink, C/C++, LabVIEW, ANSYS Workbench

## LANGUAGE SKILLS

- Dutch: native speaker
- English: fluent, orally and written
- French: fluent, orally and written
- Spanish: intermediate
- German: basic understanding

## HOBBIES & INTEREST

- Sports: karate (during +15 years, brown belt, assistant trainer)
- Music: piano, guitar

# Appendix H

# List of publications


W. Driesen, A. Bergander, T. Varidel, and J. M. Breguet, "Energy Consumption of Piezoelectric Actuators for Inertial Drives," in *Proc. IEEE Int. Symp. on Micromechatronics and Human Science, MHS '03*, pp. 51–58, 2003.

A. Bergander, W. Driesen, T. Varidel, and J.-M. Breguet, "Development of Miniature Manipulators for Applications in Biology and Nanotechnologies," in *Proc. Microrobotics for Biomanipulation Workshop, IEEE/RSJ Int. Conf. on Intelligent Robots and Systems, IROS '03*, pp. 11–35, 2003.

W. Driesen, T. Varidel, S. Régnier, and J.-M. Breguet, "Micro manipulation by adhesion with two collaborating mobile micro robots," in *Proc. Int. Workshop on Microfactories, IWMF '04*, 2004.

A. Bergander, W. Driesen, T. Varidel, and J.-M. Breguet, "Monolithic piezoelectric actuators for miniature robotic systems," in *Proc. Int. Conf. on New Actuators, ACTUATOR '04*, pp. 114–117, 2004.

A. Bergander, W. Driesen, A. Lal, T. Varidel, M. Meizoso, H. Bleuler, and J. M. Breguet, "Position Feedback for Microrobots based on Scanning Probe Microscopy," in *Proc. IEEE/RSJ Int. Conf. on Intelligent Robots and Systems, IROS '04*, vol. 2, pp. 1734 – 1739, 2004.

A. Bergander, W. Driesen, T. Varidel, M. Meizoso, and J.-M. Breguet, "Mobile cm3-microrobots with tools for nanoscale imaging and micromanipulation," in *Proc. IEEE Int. Conf. on Mechatronics & Robotics, MechRob '04*, pp. 1041–1047, 2004.

T. Varidel, W. Driesen, A. Bergander, and J.-M. Breguet, "High resolution miniature rotary microactuator," in *Proc. Int. Conf. on New Actuators, ACTUATOR '04*, pp. 517–520, 2004.

W. Driesen, T. Varidel, S. Mazerolle, A. Bergander, and J. M. Breguet, "Flexible micro manipulation platform based on tethered cm3-sized mobile micro robots," in *Proc. IEEE Int. Conf. on Robotics and Biomimetics, ROBIO '05*, vol. 2005, pp. 145–150, 2005.

W. Driesen, T. Varidel, S. Régnier, and J. M. Breguet, "Micro manipulation by adhesion with two collaborating mobile micro robots," *Journal of Micromechanics and Microengineering*, vol. 15, no. 10, pp. S259–S267, 2005.

J. Brufau, M. Puig-Vidal, J. López-Sánchez, J. Samitier, N. Snis, U. Simu, S. Johansson, W. Driesen, J. M. Breguet, J. Gao, T. Velten, J. Seyfried, R. Estaña, and H. Wörn, "MICRON: Small autonomous robot for cell manipulation applications," in *Proc. IEEE Int. Conf. on Robotics and Automation, ICRA '05*, vol. 2005, pp. 844–849, 2005.

W. Driesen, A. Rida, J. M. Breguet, and R. Clavel, "Comb drive actuator for mm3 robots and other LSRO projects at CMI," in *MicroNanoFabrication Annual Review Meeting, EPFL*, 2006.

W. Driesen, J. M. Breguet, and R. Clavel, "Classification of locomotion principles for micro robotics," in *Workshop "Arc et Senans 2006", atelier LEA*, 2006.

W. Driesen, J. M. Breguet, and R. Clavel, "Novel locomotion principle for mobile micro robots," in *Proc. Int. Conf. on New Actuators, ACTUATOR '06*, pp. 386–389, 2006.

T. Cimprich, F. Kaegi, W. Driesen, A. Ferreira, and J. M. Breguet, "Ultrasonic monolithic piezoelectric multi DOF actuators for mobile microrobots," in *Proc. Int. Conf. on New Actuators, ACTUATOR '06*, pp. 114–117, 2006.

J. M. Breguet, S. Johansson, W. Driesen, and U. Simu, "A review on actuation principles for few cubic millimeter sized mobile micro-robots," in *Proc. Int. Conf. on New Actuators, ACTUATOR '06*, pp. 374–381, 2006.

M. Dafflon, B. Lorent, W. Driesen, and R. Clavel, "Characterization of an inertial micro gripper based on adhesion forces," in *Proc. Int. Workshop on Microfactories, IWMF '06*, 2006.

A. Boletis, A. Brunette, W. Driesen, and J. M. Breguet, "Solar Cell Powering with Integrated Global Positioning System for mm3 Size Robots," in *Proc. IEEE/RSJ Int. Conf. on Intelligent Robots and Systems, IROS '06*, pp. 5528–5533, 2006.

W. Driesen, A. Rida, J.-M. Breguet, and R. Clavel, "Friction based locomotion module for mobile MEMS robots," in *Proc. IEEE/RSJ Int. Conf. on Intelligent Robots and Systems, IROS '07*, pp. 3815–3820, 2007.

J. M. Breguet, W. Driesen, F. Kaegi, and T. Cimprich, "Applications of piezo-actuated micro-robots in micro-biology and material science," in *Proc. IEEE Int. Conf. on Mechatronics and Automation, ICMA '07*, pp. 57–62, 2007.

# Bibliography


[1] "Microscopes - Time Line." `http://nobelprize.org/educational_games/physics/microscopes/timeline/index.html`.

[2] R. P. Feynman, "There's plenty of room at the bottom (Talk delivered at California Institute of Technology, Pasadena, CA, USA, December 29, 1959)," *Engineering and Science, Caltech*, vol. 23, pp. 22–36, 1960.

[3] D. M. Eigler and E. K. Schweizer, "Positioning single atoms with a scanning tunnelling microscope," *Nature*, vol. 344, no. 6266, pp. 524–526, 1990.

[4] J.-M. Breguet, C. Schmitt, and R. Clavel, "Micro/nanofactory: Concept and state of the art," in *Proc. of SPIE - Microrobotics and Microassembly II*, vol. 4194, pp. 1–12, 2000.

[5] N. Ooyama, "Desktop machining microfactory," in *Proc. Int. Workshop on Microfactories, IWMF '00*, pp. 14–17, 2000.

[6] J. M. Breguet and A. Bergander, "Toward the personal factory?," in *Proc. of SPIE - Microrobotics and Microassembly III*, vol. 4568, pp. 293–303, 2001.

[7] Y. Okazaki, N. Mishima, and K. Ashida, "Microfactory - Concept, history, and developments," *Journal of Manufacturing Science and Engineering, Transactions of the ASME*, vol. 126, no. 4, pp. 837–844, 2004.

[8] A. M. Flynn, R. A. Brooks, W. M. Wells Iii, and D. S. Barrett, "Intelligence for miniature robots," *Sensors and actuators*, vol. 20, no. 1-2, pp. 187–196, 1989.

[9] T. Ebefors and G. Stemme, "Microrobotics," in *The MEMS Handbook* (M. Gad-el Hak, ed.), pp. 28.1–28.42, Boca Raton, FL: CRC Press, 2005.

[10] D. Lixin and B. J. Nelson, "Robotics in the Small, Part II: Nanorobotics," *Robotics & Automation Magazine, IEEE*, vol. 14, no. 3, pp. 111–121, 2007.

[11] I. Shimoyama, "Scaling in microrobots," in *Proc. IEEE/RSJ Int. Conf. on Intelligent Robots and Systems, IROS '95*, vol. 2, pp. 208–211, 1995.

[12] J. Peirs, *Design of micromechatronic systems: scale laws, technologies, and medical applications*. Phd thesis, Katholieke Universitiet Leuven, Belgium, 2001.

[13] G. Caprari, T. Estier, and R. Siegwart, "Fascination of Down Scaling - Alice the Sugar Cube Robot," *Journal of Micromechatronics*, vol. 1, no. 3, pp. 177–189, 2002.

[14] T. Hayashi, "Micromechanism and their characteristics," in *Proc. IEEE Micro Electro Mechanical Systems, MEMS '94*, pp. 39–44, 1994.

[15] J. J. Abbott, Z. Nagy, F. Beyeler, and B. J. Nelson, "Robotics in the Small, Part I: Microrobotics," *Robotics & Automation Magazine, IEEE*, vol. 14, no. 2, pp. 92–103, 2007.

[16] P. Dario, R. Valleggi, M. C. Carrozza, M. C. Montesi, and M. Cocco, "Microactuators for microrobots: a critical survey," *Journal of Micromechanics and Microengineering*, vol. 2, no. 3, pp. 141–157, 1992.

[17] G. Caprari, *Autonomous Micro-Robots: Applications and limitations*. Phd thesis, Swiss Federal Institue of Technology Lausanne, 2003.

[18] H. Suzuki, N. Ohya, N. Kawahara, M. Yokoi, S. Ohyanagi, T. Kurahashi, and T. Hattori, "Shell-body fabrication for micromachines," *Journal of Micromechanics and Microengineering*, vol. 5, no. 1, pp. 36–40, 1995.

[19] T. Yasuda, I. Shimoyama, and H. Miura, "Microrobot locomotion in a mechanical vibration field," *Advanced Robotics*, vol. 9, no. 2, pp. 165–176, 1995.

[20] K. B. Yesin, K. Vollmers, and B. J. Nelson, "Modeling and control of untethered biomicrorobots in a fluidic environment using electromagnetic fields," *International Journal of Robotics Research*, vol. 25, no. 5-6, pp. 527–536, 2006.

[21] K. Vollmers, D. Frutiger, B. Kratochvil, and B. J. Nelson, "Wireless Resonant Magnetic Actuators for Untethered Mobile Microrobots." `http://www.iris.ethz.ch/msrl/research/micro/resonant_magnetic_actuators/`, 2007.

[22] T. Akiyama and K. Shono, "Controlled stepwise motion in polysilicon microstructures," *Journal of Microelectromechanical Systems*, vol. 2, no. 3, pp. 106–110, 1993.

[23] B. R. Donald, C. G. Levey, C. D. McGray, I. Paprotny, and D. Rus, "An untethered, electrostatic, globally controllable MEMS micro-robot," *Journal of Microelectromechanical Systems*, vol. 15, no. 1, pp. 1–15, 2006.

[24] G. M. Patel, G. C. Patel, R. B. Patel, J. K. Patel, and M. Patel, "Nanorobot: A versatile tool in nanomedicine," *Journal of Drug Targeting*, vol. 14, no. 2, pp. 63–67, 2006.

[25] "Miniaturised Co-operative Robots advancing towards the Nanorange - MiCRoN." `http://microrobotics.ira.uka.de/`.

[26] T. Idogaki, H. Kanayama, N. Ohya, H. Suzuki, and T. Hattori, "Characteristics of piezoelectric locomotive mechanism for an in-pipe micro inspection machine," in *Proc. IEEE Int. Symp. on Micro Machine and Human Science, MHS '95*, pp. 193–198, 1995.

[27] N. Mitumoto, K. Tsuruta, T. Shibata, and N. Kawahara, "Wireless link system for communication and energy transmission of microrobot," in *Proc. IEEE Int. Symp. on Micromechatronics and Human Science, MHS '01*, pp. 57–62, 2001.

[28] S.-I. Aoshima, T. Tsujimura, and T. Yabuta, "Miniature mobile robot using piezo vibration for mobility in a thin tube," *Journal of Dynamic Systems, Measurement and Control, Transactions of the ASME*, vol. 115, no. 2 A, pp. 270–278, 1993.

[29] P. Dario, M. C. Carrozza, B. Allotta, and E. Guglielmelli, "Micromechatronics in medicine," *IEEE/ASME Transactions on Mechatronics*, vol. 1, no. 2, pp. 137–148, 1996.

[30] M. Quirini, R. J. Webster Iii, A. Menciassi, and P. Dario, "Design of a pill-sized 12-legged endoscopic capsule robot," in *Proc. IEEE Int. Conf. on Robotics and Automation, ICRA '07*, pp. 1856–1862, 2007.

[31] J. B. Mathieu, G. Beaudoin, and S. Martel, "Method of propulsion of a ferromagnetic core in the cardiovascular system through magnetic gradients generated by an MRI system," *IEEE Transactions on Biomedical Engineering*, vol. 53, no. 2, pp. 292–299, 2006.

[32] D. Reynaerts, J. Peirs, and H. Van Brussel, "Shape memory micro-actuation for a gastro-intestinal intervention system," *Sensors and Actuators, A: Physical*, vol. 77, no. 2, pp. 157–166, 1999.

[33] H. Wörn, J. Seyfried, F. St, A. Buerkle, and F. Schmoeckel, "Flexible microrobots for micro assembly tasks," in *Proc. IEEE Int. Symp. on Micromechatronics and Human Science, MHS '00*, pp. 135–43, 2000.

[34] W. Driesen, T. Varidel, S. Mazerolle, A. Bergander, and J. M. Breguet, "Flexible micro manipulation platform based on tethered cm3-sized mobile micro robots," in *Proc. IEEE Int. Conf. on Robotics and Biomimetics, ROBIO '05*, vol. 2005, pp. 145–150, 2005.

[35] W. Driesen, T. Varidel, S. Régnier, and J. M. Breguet, "Micro manipulation by adhesion with two collaborating mobile micro robots," *Journal of Micromechanics and Microengineering*, vol. 15, no. 10, pp. S259–S267, 2005.

[36] "Golem - Bio-Inspired Assembly of Meso-Scale Components." `http://www.golem-project.eu/`.

[37] F. Schmoeckel, S. Fahlbusch, J. Seyfried, A. Buerkle, and S. Fatikow, "Development of a microrobot-based micromanipulation cell in an SEM," in *Proc. of SPIE - Microrobotics and Microassembly II*, vol. 4194, pp. 129–140, 2000.

[38] H. Aoyama and O. Fuchiwaki, "Flexible micro-processing by multiple micro robots in SEM," in *Proc. IEEE Int. Conf. on Robotics and Automation, ICRA '01*, vol. 4, pp. 3429–3434, 2001.

[39] A. Kortschack, A. Shirinov, T. Trüper, and S. Fatikow, "Development of mobile versatile nanohandling microrobots: Design, driving principles, haptic control," *Robotica*, vol. 23, no. 4, pp. 419–434, 2005.

[40] S. Fatikow, T. Wich, H. Hülsen, T. Sievers, and M. Jähnisch, "Microrobot system for automatic nanohandling inside a scanning electron microscope," *IEEE/ASME Transactions on Mechatronics*, vol. 12, no. 3, pp. 244–252, 2007.

[41] C. Canales, F. Kaegi, C. Groux, J. M. Breguet, C. Meyer, U. Zbinden, and A. Steinecker, "A nanomanipulation platform for semi automated manipulation of nano-sized objects using mobile microrobots inside a Scanning Electron Microscope," in *Proc. IFAC World Congress*, vol. 17, 2008.

[42] H. Aoyama, " Precise Miniature Robots and Desktop Flexible Production," in *Proc. Int. Workshop on Microfactories, IWMF '98*, pp. 145–156, 1998.

[43] A. Sulzmann, P. Boillat, and J. Jacot, "New developments in 3D computer vision for microassembly," in *Proc. of SPIE - Microrobotics and Micromanipulation*, vol. 3519, pp. 36–47, 1998.

[44] H. Aoyama, S. Hiraiwa, F. Iwata, J. Fukaya, and A. Sasaki, "Miniature robot with micro capillary capturing probe," in *Proc. IEEE Int. Symp. on Micro Machine and Human Science, MHS '95*, pp. 173–178, 1995.

[45] "Swarm-bots project." `http://www.swarm-bots.org/`.

[46] "I-SWARM: Intelligent Small World Autonomous Robots for Micro-manipulation." `http://www.i-swarm.org/`.

[47] "The Official Stiquito Homepage." `http://www.stiquito.com/`.

[48] "e-puck educational robot." `http://www.e-puck.org/`.

[49] Epson, "Monsieur - The ultraminiature robot that propelled itself into the Guinness Book." `http://www.epson.co.jp/e/company/milestones_23_monsieur.htm`, 2003.

[50] "LEURRE - Artificial life control in mixed societies." `http://leurre.ulb.ac.be/`.

[51] W. Andre and S. Martel, "Initial design of a bacterial actuated microrobot for operations in an aqueous medium," in *Proc. Ann. Int. Conf. of the IEEE Engineering in Medicine and Biology*, pp. 2824–2827, 2006.

[52] "SMART DUST - Autonomous sensing and communication in a cubic millimeter." `http://www-bsac.eecs.berkeley.edu/archive/users/warneke-brett/SmartDust/index.html`.

[53] Epson, "News Release: Epson to Unveil a Prototype Microrobot with Ultra-thin, Ultrasonic Motor and Power-Saving Bluetooth Module." `http://www.epson.co.jp/e/newsroom/news_2003_03_10.htm`, 2003.

[54] I. Hayashi and N. Iwatuki, "Micro moving robotics," in *Proc. IEEE Int. Symp. on Micromechatronics and Human Science, MHS '98*, pp. 41–50, 1998.

[55] M. Sitti, "Microscale and nanoscale robotics systems [Grand Challenges of Robotics]," *Robotics & Automation Magazine, IEEE*, vol. 14, no. 1, pp. 53–60, 2007.

[56] P. Koeneman, I. Busch-Vishniac, and K. Wood, "Feasibility of micro power supplies for MEMS," *Journal of Microelectromechanical Systems*, vol. 6, no. 4, pp. 355–362, 1997.

[57] J. Peirs, D. Reynaerts, and F. Verplaetsen, "A microturbine for electric power generation," *Sensors and Actuators, A: Physical*, vol. 113, no. 1, pp. 86–93, 2004.

[58] J. Peirs, T. Waumans, P. Vleugels, F. Al-Bender, T. Stevens, T. Verstraete, S. Stevens, R. D'Hulst, D. Verstraete, P. Fiorini, R. Van den Braembussche, J. Driesen, R. Puers, P. Hendrick, M. Baelmans, and D. Reynaerts, "Micropower generation with microgasturbines: A challenge," *Proceedings of the Institution of Mechanical Engineers, Part C: Journal of Mechanical Engineering Science*, vol. 221, no. 4, pp. 489–500, 2007.

[59] P. H. Humble, J. N. Harb, and R. LaFollette, "Microscopic nickel-zinc batteries for use in autonomous microsystems," *Journal of the Electrochemical Society*, vol. 148, no. 12, pp. A1357–A1361, 2001.

[60] "Cymbet Corporation." `http://www.cymbet.com`.

[61] S. M. Martel, W. Garcia de Quevedo, and I. W. Hunter, "Techniques for continuous power delivery to a group of 15-watt +3.3 to ±150 VDC miniature wireless instrumented and fast-stepping robots through several thousand intermittent contacts between the robot's legs and the walking surface," in *Proc. of SPIE - Microrobotics and Microassembly II*, vol. 4194, pp. 168–77, 2000.

[62] C. F. Andren, M. A. Fadali, V. L. Gott, and S. R. Topaz, "The skin tunnel transformer. A new system that permits both high efficiency transfer of power and telemetry of data through the intact skin," *IEEE Transactions on Biomedical Engineering*, vol. 15, no. 4, pp. 278–280, 1968.

[63] C. Sauer, M. Stanacevic, G. Cauwenberghs, and N. Thakor, "Power harvesting and telemetry in CMOS for implanted devices," *IEEE Transactions on Circuits and Systems I: Regular Papers*, vol. 52, no. 12, pp. 2605–2613, 2005.

[64] G. Wang, W. Liu, M. Sivaprakasam, and G. A. Kendir, "Design and analysis of an adaptive transcutaneous power telemetry for biomedical implants," *IEEE Transactions on Circuits and Systems I: Regular Papers*, vol. 52, no. 10, pp. 2109–2117, 2005.

[65] G. Vandevoorde and R. Puers, "Wireless energy transfer for stand-alone systems: a comparison between low and high power applicability," *Sensors and Actuators, A: Physical*, vol. 92, no. 1-3, pp. 305–311, 2001.

[66] J. Gao, "Traveling magnetic field for homogeneous wireless power transmission," *IEEE Transactions on Power Delivery*, vol. 22, no. 1, pp. 507–514, 2007.

[67] R. Estaña and H. Wörn, "The MiCRoN Robot Project," in *Autonome Mobile Systeme 2007*, pp. 334–340, Springer Berlin Heidelberg, 2008.

[68] G. Yan, D. Ye, P. Zan, K. Wang, and G. Ma, "Micro-robot for endoscope based on wireless power transfer," in *Proc. IEEE Int. Conf. on Mechatronics and Automation, ICMA '07*, pp. 3577–3581, 2007.

[69] B. R. Donald, C. G. Levey, C. D. McGray, D. Rus, and M. Sinclair, "Power delivery and locomotion of untethered microactuators," *Journal of Microelectromechanical Systems*, vol. 12, no. 6, pp. 947–959, 2003.

[70] T. Yasuda, I. Shimoyama, and H. Miura, "Microrobot actuated by a vibration energy field," in *Proc. Int. Conf. on Solid-State Sensors and Actuators, Transducers '93*, pp. 42–45, 1993.

[71] T. Shibata, Y. Aoki, M. Otsuka, T. Idogaki, and T. Hattori, "Microwave energy transmission system for microrobot," *IEICE Transactions on Electronics*, vol. E80-C, no. 2, pp. 303–307, 1997.

[72] T. Sakakibara, H. Izua, T. Shibata, H. Tarui, K. Shibata, S. Kiyama, and N. Kawahara, "Multi-source power supply system using micro-photovoltaic devices combined with microwave antenna," *Sensors and Actuators, A: Physical*, vol. 95, no. 2-3, pp. 208–211, 2002.

[73] J. Lee, Z. Chen, M. Allen, A. Rohatgi, and R. Arya, "A miniaturized high-voltage solar cell array as an electrostatic MEMS power supply," *Journal of Microelectromechanical Systems*, vol. 4, no. 3, pp. 102–108, 1995.

[74] J. Ohsawa, K. Shono, and Y. Hiei, "High-voltage micro solar cell arrays of GaAs with output voltage up to 100 V," in *Conf. Digest IEEE/LEOS Int. Conf. on Optical MEMS*, pp. 103–104, 2002.

[75] T. Sakakibara, H. Izu, H. Tarui, and S. Kiyama, "Development of high voltage photovoltaic micro-devices for driving micro actuators," *IEICE Transactions on Electronics*, vol. E80C, no. 2, pp. 309–313, 1997.

[76] "Clare, Inc. - A global leader in high voltage integrated circuits." `http://www.clare.com`.

[77] C. L. Bellew, S. Hollar, and K. S. J. Pister, "An SOI process for fabrication of solar cells, transistors and electrostatic actuators," in *Proc. Int. Conf. on Solid-State Sensors, Actuators and Microsystems, Transducers '03*, vol. 2, pp. 1075–1078 vol.2, 2003.

[78] F. X. D'Amato, J. M. Berak, and A. J. Shuskus, "Fabrication and test of an efficient photovoltaic cell for laser optical power transmission," *IEEE Photonics Technology Letters*, vol. 4, no. 3, pp. 258–260, 1992.

[79] S. Hollar, A. Flynn, C. Bellew, and K. S. J. Pister, "Solar powered 10 mg silicon robot," in *Proc. IEEE Micro Electro Mechanical Systems, MEMS '03*, pp. 706–711, 2003.

[80] J. Meier, J. Spitznagel, U. Kroll, C. Bucher, S. Fay, T. Moriarty, and A. Shah, "Potential of amorphous and microcrystalline silicon solar cells," *Thin Solid Films*, vol. 451-452, pp. 518–524, 2004.

[81] A. Boletis, A. Brunette, W. Driesen, and J. M. Breguet, "Solar Cell Powering with Integrated Global Positioning System for mm3 Size Robots," in *Proc. IEEE/RSJ Int. Conf. on Intelligent Robots and Systems, IROS '06*, pp. 5528–5533, 2006.

[82] O. Ohmichi, Y. Yamagata, and T. Higuchi, "Micro impact drive mechanisms using optically excited thermal expansion," *Journal of Microelectromechanical Systems*, vol. 6, no. 3, pp. 200–207, 1997.

[83] O. J. Sul, M. R. Falvo, R. M. Taylor, S. Washburn, and R. Superfine, "Thermally actuated untethered impact-driven locomotive microdevices," *Applied Physics Letters*, vol. 89, no. 20, 2006.

[84] D. J. Denninghoff, L. A. Starman, P. E. Kladitis, and C. E. Perry, "Autonomous power-scavenging MEMS robots," in *Proc. Midwest Symp. on Circuits and Systems*, vol. 2005, pp. 367–370, 2005.

[85] "Open-source micro-robotic project." `http://www.swarmrobot.org/`.

[86] M. Szymanski and H. Wörn, "JaMOS - A MDL2e based operating system for swarm micro robotics," in *Proc. IEEE Swarm Intelligence Symposium, SIS '07*, pp. 324–331, 2007.

[87] "CITIZEN's miniature robot in development - The name is Eco-Be!." `http://www.eco-be.com/about.html`.

[88] S. Martel, P. Madden, L. Sosnowski, I. Hunter, and S. Lafontaine, "NanoWalker: a fully autonomous highly integrated miniature robot for nanoscale measurements," in *Proc. of SPIE - Microsystems Metrology and Inspection*, vol. 3825, pp. 111–22, 1999.

[89] S. M. Martel, J. Kaufman, C. Helm, T. Fofonoff, J. Bevilacka, R. Dyer, J. Levine, J. Au, and I. W. Hunter, "NanoRunner: a very small wireless robot with three piezo-actuated legs suited for design experimentations and validations through preprogrammed behaviors," in *Proc. of SPIE - Microrobotics and Microassembly II*, vol. 4194, pp. 149–56, 2000.

[90] P. Valdastri, P. Corradi, A. Menciassi, T. Schmickl, K. Crailsheim, J. Seyfried, and P. Dario, "Micromanipulation, communication and swarm intelligence issues in a swarm microrobotic platform," *Robotics and Autonomous Systems*, vol. 54, no. 10, pp. 789–804, 2006.

[91] A. Ferreira and P. Minotti, "Control of a multidegree of freedom standing wave ultrasonic motor driven precise positioning system," *Review of Scientific Instruments*, vol. 68, no. 4, pp. 1779–1786, 1997.

[92] F. Tagliareni, M. Nierlich, O. Steinmetz, T. Velten, J. Brufau, J. Lopez-Sanchez, M. Puig-Vidal, and J. Samitier, "Manipulating biological cells with a micro-robot cluster," in *Proc. IEEE/RSJ Int. Conf. on Intelligent Robots and Systems, IROS '05*, pp. 1414–1419, 2005.

[93] B. Warneke, M. Last, B. Liebowitz, and K. S. J. Pister, "Smart dust: communicating with a cubic-millimeter computer," *Computer*, vol. 34, no. 1, pp. 44–51, 2001.

[94] S. Martel, M. Sherwood, C. Helm, W. Garcia de Quevedo, T. Fofonoff, R. Dyer, J. Bevilacqua, J. Kaufman, O. Roushdy, and I. Hunter, "Three-Legged Wireless Miniature Robots for Mass-Scale Operations at the Sub-Atomic Scale," in *Proc. IEEE Int. Conf. on Robotics and Automation, ICRA '01*, vol. 4, pp. 3423–3428, 2001.

[95] P. Hannoyer, K. Kim, and S. Martel, "Cooling an array of high-powered miniature robots using forced air convection," *IEEE Transactions on Automation Science and Engineering*, vol. 4, no. 3, pp. 373–381, 2007.

[96] "Miniaturised Robot for Micro Manipulation : MINIMAN." `http://microrobotics.ira.uka.de/`.

[97] P. Miribel-Catala, E. Montane, J. LÃşpez-Sánchez, M. Puig-Vidal, S. A. Bota, J. Samitier, U. Simu, and S. Johansson, "Smart power integrated circuit for a piezoelectric miniature robot," *Analog Integrated Circuits and Signal Processing*, vol. 33, no. 2, pp. 191–200, 2002.

[98] J. Lopez-Sanchez, P. Miribel-Catala, E. Montane, M. Puig-Vidal, S. A. Bota, J. Samitier, U. Simu, and S. Johansson, "High accuracy piezoelectric-based microrobot for biomedical applications," in *Proc. IEEE Int. Conf. on Emerging Technologies and Factory Automation, ETFA '01*, vol. 2, pp. 603–609 vol.2, 2001.

[99] R. Casanova, A. Saiz-Vela, A. Arbat, J. Colomer, P. Miribel, A. Dieguez, M. Puig-Vidal, and J. Samitier, "Integrated Electronics for a 1cm3 Robot for Micro and Nanomanipulation Applications: MiCRoN," in *Proc. IEEE/RAS-EMBS Int. Conf. on Biomedical Robotics and Biomechatronics, BioRob '06*, pp. 13–18, 2006.

[100] "Miniaturised Co-operative Robots advancing towards the Nanorange - MiCRoN," Public Report, European FP5 project, IST-2001-33567, `http://lsro.epfl.ch/page66048.html`, 2006.

[101] R. Casanova, A. Dieguez, A. Sanuy, A. Arbat, O. Alonso, J. Canals, and J. Samitier, "An ultra low power IC for an autonomous mm3-sized microrobot," in *Proc. IEEE Asian Solid-State Circuits Conference, ASSCC '07*, pp. 55–58, 2007.

[102] W. Driesen, A. Bergander, T. Varidel, and J. M. Breguet, "Energy Consumption of Piezoelectric Actuators for Inertial Drives," in *Proc. IEEE Int. Symp. on Micromechatronics and Human Science, MHS '03*, pp. 51–58, 2003.

[103] S. Fatikow, J. Seyfried, S. Fahlbusch, A. Buerkle, and F. Schmoeckel, "A Flexible Microrobot-Based Microassembly Station," *Journal of Intelligent and Robotic Systems*, vol. 27, pp. 135–169, 2000.

[104] A. Bergander, W. Driesen, T. Varidel, M. Meizoso, and J.-M. Breguet, "Mobile cm3-microrobots with tools for nanoscale imaging and micromanipulation," in *Proc. IEEE Int. Conf. on Mechatronics & Robotics, MechRob '04*, pp. 1041–1047, 2004.

[105] A. Eisinberg, K. Houston, I. Izzo, A. Menciassi, P. Dario, R. Gustafsson, U. Simu, and S. Johansson, "Design and fabrication of PZT-actuated tools for micromanipulation," *Journal of Micromechatronics*, vol. 3, no. 3, pp. 329–357, 2006.

[106] A. Eisinberg, A. Menciassi, P. Dario, J. Seyfried, R. Estaña, and H. Wörn, "Teleoperated assembly of a micro-lens system by means of a micro-manipulation workstation," *Assembly Automation*, vol. 27, no. 2, pp. 123–33, 2007.

[107] Y. Song, M. Li, L. Sun, and L. Qin, "Design and control structure of a miniature robot for micro operation task," in *Proc. IEEE Int. Conf. on Robotics, Automation and Mechatronics, RAM '06*, 2006.

[108] A. Bergander, W. Driesen, A. Lal, T. Varidel, M. Meizoso, H. Bleuler, and J. M. Breguet, "Position Feedback for Microrobots based on Scanning Probe Microscopy," in *Proc. IEEE/RSJ Int. Conf. on Intelligent Robots and Systems, IROS '04*, vol. 2, pp. 1734 – 1739, 2004.

[109] J. Otero, A. Saiz, J. Brufau, J. Colomer, R. Ruíz, J. LÃşpez, P. Miribel, M. Puig, and J. Samitier, "Reduced dimensions autonomous AFM system for working in microbiorobotics," in *Proc. IEEE/RAS-EMBS Int. Conf. on Biomedical Robotics and Biomechatronics, BioRob '06*, vol. 2006, pp. 1200–1205, 2006.

[110] H. Aoyama, F. Iwata, and A. Sasaki, "Miniature robots for a desktop flexible micro manufacturing system," *IEEE Control Systems Magazine*, vol. 16, no. 1, pp. 6–12, 1996.

[111] O. Fuchiwaki, N. Tobe, H. Aoyama, D. Misaki, and T. Usuda, "Automatic micro-indentation and inspection system by piezo driven micro robot with multiple inner sensors," in *Proc. IEEE Int. Conf. on Robotics and Automation, ICRA '05*, pp. 83–88, 2005.

[112] F. De Ambroggi, L. Fortuna, and G. Muscato, "PLIF: Piezo Light Intelligent Flea - new micro-robots controlled by self-learning techniques," in *Proc. IEEE Int. Conf. on Robotics and Automation, ICRA '97*, vol. 2, pp. 1767–1772, 1997.

[113] R. H. Byrne, D. R. Adkins, S. E. Eskridge, J. J. Harrington, E. J. Heller, and J. E. Hurtado, "Miniature mobile robots for plume tracking and source localization research," *Journal of Micromechatronics*, vol. 1, no. 3, pp. 253–261, 2001.

[114] R. Estaña and H. Wörn, "Moire-based positioning system for microrobots," in *Proc. of SPIE - Optical Measurement Systems for Industrial Inspection III*, vol. 5144, pp. 431–442, 2003.

[115] H. Aoyama, O. Fuchiwaki, and D. Misaki, "Piezo based micro robots system for precise micro bio and chemical applications," in *Proc. Int. Conf. on New Actuators, ACTUATOR '04*, pp. 164–167, 2004.

[116] H. Ishihara, T. Fukuda, K. Kosuge, F. Arai, and K. Hamagishi, "Approach to distributed micro robotic system - development of micro line trace robot and autonomous micro robotic system," in *Proc. IEEE Int. Conf. on Robotics and Automation, ICRA '95*, vol. 1, pp. 375–380, 1995.

[117] "NANOHAND - Micro-Nano System for Automatic Handling of Nano-Objects." `http://www.nanohand.eu`.

[118] J. M. Breguet, S. Johansson, W. Driesen, and U. Simu, "A review on actuation principles for few cubic millimeter sized mobile micro-robots," in *Proc. Int. Conf. on New Actuators, ACTUATOR '06*, pp. 374–381, 2006.

[119] J. M. Hollerbach, I. W. Hunter, and J. Ballantyne, "A comparative analysis of actuator technologies for robotics," *The Robotics Review 2*, vol. 2, pp. 299–342, 1991.

[120] I. W. Hunter and S. Lafontaine, "Comparison of muscle with artificial actuators," in *Technical Digest - IEEE Solid-State Sensor and Actuator Workshop*, pp. 178–185, 1992.

[121] I. J. Busch-Vishniac, *Electromechanical Sensors and Actuators*. New York: Springer, 1998.

[122] H. Janocha, *Actuators: Basics and Applications*. Springer, 2004.

[123] H. Ishihara, F. Aral, and T. Fukuda, "Micro mechatronics and micro actuators," *IEEE/ASME Transactions on Mechatronics*, vol. 1, no. 1, pp. 68–79, 1996.

[124] M. Tabib-Azar, *Microactuators: Electrical, Magnetic, Thermal, Optical, Mechanical, Chemical and Smart Structures*. Springer, 1998.

[125] J. Pons, *Emerging Actuator Technologies: A Micromechatronic Approach*. John Wiley and Sons, 2005.

[126] R. S. Fearing, "Powering 3 dimensional microrobots - power density limitations," in *Tutorial on Micro Mechatronics and Micro Robotics, IEEE Int. Conf. on Robotics and Automation, ICRA '98*, 1998.

[127] K. Uchino and J. Giniewicz, *Micromechatronics*. CRC Press, 2003.

[128] N. Setter, *Piezoelectric Materials in Devices*. N. Setter, Ceramics Laboratory, EPFL, 2002.

[129] J.-M. Breguet, *Actionneurs "stick and slip" pour micro-manipulateurs*. Phd thesis, EPFL, 1998.

[130] A. Bergander, *Control, wear testing and integration of stick-slip micropositioning*. Phd thesis, EPFL, 2003.

[131] S. Devos, *Development of fast, stiff and high-resolution piezoelectric motors with integrated bearing-driving functionality.* Phd thesis, Katholieke Universiteit Leuven, 2006.

[132] K. Uchino, *Piezoelectric actuators and ultrasonic motors.* The Kluwer international series in electronic materials: science and technology, Boston: Kluwer Academic Publishers, 1997.

[133] T. Morita, "Miniature piezoelectric motors," *Sensors and Actuators, A: Physical*, vol. 103, no. 3, pp. 291–300, 2003.

[134] W. C. Tang, T.-C. H. Nguyen, M. W. Judy, and R. T. Howe, "Electrostatic-comb drive of lateral polysilicon resonators," *Sensors and Actuators, A: Physical*, vol. 21, no. 1-3, pp. 328–331, 1990.

[135] R. Legtenberg, A. W. Groeneveld, and M. Elwenspoek, "Comb-drive actuators for large displacements," *Journal of Micromechanics and Microengineering*, vol. 6, no. 3, pp. 320–329, 1996.

[136] Y. Sun, D. Piyabongkarn, A. Sezen, B. J. Nelson, R. Rajamani, R. Schoch, and D. P. Potasek, "A novel dual-axis electrostatic microactuation system for micromanipulation," in *Proc. IEEE/RSJ Int. Conf. on Intelligent Robots and Systems, IROS '02*, vol. 2, pp. 1796–1801, 2002.

[137] R. Yeh, S. Hollar, and K. S. J. Pister, "Single mask, large force, and large displacement electrostatic linear inchworm motors," *Journal of Microelectromechanical Systems*, vol. 11, no. 4, pp. 330–336, 2002.

[138] S. Gomez, R. Belen, M. Kiehlbauch, and E. Aydil, "Etching of high aspect ratio structures in Si using SF6/O 2 plasma," *Journal of Vacuum Science and Technology A: Vacuum, Surfaces and Films*, vol. 22, no. 3, pp. 606–615, 2004.

[139] B. J. Nelson, L. Dong, and F. Arai, "Micro/Nanorobots," in *Springer Handbook of Robotics* (B. Siciliano and O. Khatib, eds.), vol. Part B, Springer Berlin Heidelberg, 2008.

[140] P. Minotti and A. Ferreira, *Les micromachines.* Paris: Hermès, 1998.

[141] K. Ragulskis, R. Bansevicius, R. Barauskas, and G. Kulvietis, *Vibromotors for Precision Microrobots.* Hemisphere Publishing Corp., 1988.

[142] S. Fatikow and U. Rembold, *Microsystem Technology and Microrobotics.* Berlin Heidelberg: Springer-Verlag, 1997.

[143] T. Hayashi, "Research and development of micromechanisms," *Ultrasonics*, vol. 38, no. 1, pp. 6–14, 2000.

[144] Z. Pan and Z. Zhu, "Miniature pipe robots," *Industrial Robot*, vol. 30, no. 6, pp. 575–583, 2003.

[145] I. Kassim, L. Phee, W. S. Ng, F. Gong, P. Dario, and C. A. Mosse, "Locomotion techniques for robotic colonoscopy," *IEEE Engineering in Medicine and Biology Magazine*, vol. 25, no. 3, pp. 49–56, 2006.

[146] T. Hayashi, "Micro Mechanisms," *Journal of Robotics and Mechatronics*, vol. 3, no. 1, pp. 2–7, 1991.

[147] G. Winkler, "Analysing the vibrating conveyor," *International Journal of Mechanical Sciences*, vol. 20, no. 9, pp. 561–570, 1978.

[148] G. H. Lim, "On the conveying velocity of a vibratory feeder," *Computers & Structures*, vol. 62, no. 1, pp. 197–203, 1997.

[149] W. A. Marcos, "On The Design Of Oscillating Conveyers," *Journal of Engineering for Industry-Transactions of the ASME*, vol. 92 Ser B, no. 1, pp. 53–61, 1970.

[150] P. U. Frei, "An intelligent vibratory conveyor for the individual object transportation in two dimensions," in *Proc. IEEE/RSJ Int. Conf. on Intelligent Robots and Systems, IROS '02*, vol. 2, pp. 1832–1837 vol.2, 2002.

[151] Z. Hu, G. P. Maul, and D. Farson, "Piezo actuated vibratory feeding with vibration control," *International Journal of Production Research*, vol. 45, no. 5, pp. 1089–1100, 2007.

[152] D. Reznik, J. Canny, and K. Goldberg, "Analysis of part motion on a longitudinally vibrating plate," in *Proc. IEEE/RSJ Int. Conf. on Intelligent Robots and Systems, IROS '97*, vol. 1, pp. 421–427, 1997.

[153] A. Mitani, N. Sugano, and S. Hirai, "Microparts feeding by a saw-tooth surface," *IEEE/ASME Transactions on Mechatronics*, vol. 11, no. 6, pp. 671–681, 2006.

[154] K. F. Bohringer, B. R. Donald, and N. C. MacDonald, "Programmable Force Fields for Distributed Manipulation, with Applications to MEMS Actuator Arrays and Vibratory Parts Feeders," *International Journal of Robotics Research*, vol. 18, no. 2, pp. 168–200, 1999.

[155] T. Ebefors, J. U. Mattsson, E. Kalvesten, and G. Stemme, "Robust micro conveyer realized by arrayed polyimide joint actuators," *Journal of Micromechanics and Microengineering*, vol. 10, no. 3, pp. 337–349, 2000.

[156] K. B. Yesin, K. Vollmers, and B. J. Nelson, "Actuation, sensing, and fabrication for in vivo magnetic microrobots," *Springer Tracts in Advanced Robotics*, vol. 21, pp. 321–330, 2006.

[157] F. Arai, M. Ogawa, T. Fukuda, K. Horio, T. Sone, K. Itoigawa, and A. Maeda, "High speed random separation of microobject in microchip by laser manipulator and dielectrophoresis," in *Proc. IEEE Micro Electro Mechanical Systems, MEMS '00*, pp. 727–732, 2000.

[158] M. Dauge, M. Gauthier, and E. Piat, "Modelling of a planar magnetic micropusher for biological cell manipulations," *Sensors and Actuators, A: Physical*, vol. 138, no. 1, pp. 239–247, 2007.

[159] M. B. Khamesee, N. Kato, Y. Nomura, and T. Nakamura, "Design and control of a microrobotic system using magnetic levitation," *IEEE/ASME Transactions on Mechatronics*, vol. 7, no. 1, pp. 1–14, 2002.

[160] W. Driesen, J. M. Breguet, and R. Clavel, "Classification of locomotion principles for micro robotics," in *Workshop "Arc et Senans 2006", atelier LEA*, 2006.

[161] A. M. Flynn, R. A. Brooks, I. Wells, W. M., and D. S. Barrett, "The world's largest one cubic inch robot," in *Proc. IEEE Micro Electro Mechanical Systems, MEMS '89*, pp. 98–101, 1989.

[162] G. Caprari, P. Balmer, R. Piguet, and R. Siegwart, "Autonomous micro robot 'Alice': A platform for scientific and commercial applications," in *Proc. IEEE Int. Symp. on Micromechatronics and Human Science, MHS '98*, pp. 231–235, 1998.

[163] G. Caprari and R. Siegwart, "Mobile micro-robots ready to use: Alice," in *Proc. IEEE/RSJ Int. Conf. on Intelligent Robots and Systems, IROS '05*, pp. 3295–3300, 2005.

[164] H. Wörn, H. Wörn, M. Szymanski, and J. Seyfried, "The I-SWARM project," in *Proc. IEEE Int. Symp. on Robot and Human Interactive Communication, ROMAN '06*, pp. 492–496, 2006.

[165] O. Tezuka, "pico." `http://poor-robot.com/pico/`, 2007.

[166] LAMI-EPFL, "The Microrobots Jemmy and Inchy." `http://diwww.epfl.ch/lami/mirobots/1cubes.html`, 1997.

[167] J.-D. Nicoud, "Microengineering: When is small too small? Nanoengineering: When is large too large?," in *Proc. IEEE Int. Symp. on Micro Machine and Human Science, MHS '95*, pp. 1–6, 1995.

[168] P. Dario, M. C. Carrozza, C. Stefanini, and S. D'Attanasio, "A mobile microrobot actuated by a new electromagnetic wobble micromotor," *IEEE/ASME Transactions on Mechatronics*, vol. 3, no. 1, pp. 9–16, 1998.

[169] Z. Li, J. Chen, and J. Feng, " Design of an omni-directional mobile microrobot (OMMR-I) for a micro-factory with 2 mm electromagnetic micromotors," *Robotica*, vol. 23, no. 1, pp. 45–49, 2005.

[170] J. Li, Z. Li, and J. Chen, "An omni-directional mobile millimeter-sized microrobot with 3-mm electromagnetic micromotors for a micro-factory," *Advanced Robotics*, vol. 21, no. 12, pp. 1369–1391, 2007.

[171] "Guinness World Record - The DENSO Micro-Car." `http://www.densocorp-na.com/corporate/gwr.html`, 1995.

[172] U. Rembold and S. Fatikow, "Autonomous Microrobots," *Journal of Intelligent and Robotic Systems*, vol. 19, no. 4, pp. 375–391, 1997.

[173] U. Simu and S. Johansson, "Fabrication of monolithic piezoelectric drive units for a miniature robot," *Journal of Micromechanics and Microengineering*, vol. 12, no. 5, pp. 582–589, 2002.

[174] U. Simu and S. Johansson, "Evaluation of a monolithic piezoelectric drive unit for a miniature robot," *Sensors and Actuators, A: Physical*, vol. 101, no. 1-2, pp. 175–184, 2002.

[175] U. Simu and S. Johansson, "Analysis of quasi-static and dynamic motion mechanisms for piezoelectric miniature robots," *Sensors and Actuators, A: Physical*, vol. 132, no. 2, pp. 632–642, 2006.

[176] U. Simu, *Piezoactuators for Miniature Robots*. Phd thesis, Uppsala Universitet, Uppsala, Sweden, 2002.

[177] W. Benecke and W. Riethmuller, "Applications of silicon microactuators based on bimorph structures," in *Proc. IEEE Micro Electro Mechanical Systems, MEMS '89*, pp. 116–120, 1989.

[178] T. Ebefors, J. Mattson, E. Kalvesten, and G. Stemme, "A walking silicon micro-robot," in *Proc. Int. Conf. on Solid-State Sensors and Actuators, Transducers '99*, pp. 1202–1205, 1999.

[179] P. E. Kladitis and V. M. Bright, "Prototype microrobots for micro-positioning and micro-unmanned vehicles," *Sensors and Actuators, A: Physical*, vol. 80, no. 2, pp. 132–137, 2000.

[180] M. H. Mohebbi, M. L. Terry, K. F. Bo?hringer, G. T. A. Kovacs, and J. W. Suh, "Omnidirectional walking microrobot realized by thermal microactuator arrays," in *Proc. ASME Int. Mechanical Engineering Congress and Exposition*, vol. 2, pp. 2741–2747, 2001.

[181] Y.-M. Chen, J. W. Suh, G. T. Kovacs, R. B. Darling, and K. F. Böhringer, "Modeling and Control of a 3-Degree-of-Freedom Walking Microrobot," in *Proc. Solid State Sensor, Actuator, and Microsystems Workshop, Hilton Head '06*, 2006.

[182] A. Bonvilain and N. Chaillet, "Microfabricated thermally actuated microrobot," in *Proc. IEEE Int. Conf. on Robotics and Automation, ICRA '03*, vol. 3, pp. 2960–2965, 2003.

[183] J. G. Smits, "Design considerations of a piezoelectric-on-silicon microrobot," *Sensors and Actuators, A: Physical*, vol. 35, no. 2, pp. 129–135, 1992.

[184] S. Baglio, S. Castorina, L. Fortuna, and N. Savalli, "Development of autonomous, mobile micro-electro-mechanical devices," in *Proc. IEEE Int. Symp. on Circuits and Systems, ISCAS '02*, vol. 4, pp. IV/285–IV/288, 2002.

[185] D. Ruffieux, M. A. Dubois, and N. F. de Rooij, "An AlN piezoelectric microactuator array," in *Proc. IEEE Micro Electro Mechanical Systems, MEMS '00*, pp. 662–667, 2000.

[186] S. Tadokoro, T. Murakami, S. Fuji, R. Kanno, M. Hattori, T. Takamori, and K. Oguro, "An elliptic friction drive element using an ICPF actuator," *IEEE Control Systems Magazine*, vol. 17, no. 3, pp. 60–68, 1997.

[187] B. Kim, J. Ryu, Y. Jeong, Y. Tak, B. Kim, and J. O. Park, "A ciliary based 8-legged walking micro robot using cast IPMC actuators," in *Proc. IEEE Int. Conf. on Robotics and Automation, ICRA '03*, vol. 3, pp. 2940–2945, 2003.

[188] M. Otis, R. Bernier, Y. Pasco, H. Me?nard, H. Semmaoui, M. Jarry, and R. Fontaine, "Development of an Hexapod BioMicRorobot with Nafion-Pt IPMC Microlegs," in *Proc. Ann. Int. Conf. of the IEEE Engineering in Medicine and Biology*, vol. 4, pp. 3423–3426, 2003.

[189] G. Alici and N. N. Huynh, "Performance quantification of conducting polymer actuators for real applications: A microgripping system," *IEEE/ASME Transactions on Mechatronics*, vol. 12, no. 1, pp. 73–84, 2007.

[190] T. Ebefors and J. Mattson, "The micro robotics project." `http://www.s3.kth.se/mst/research/gallery/microrobot.html`.

[191] A. Hubert, "Microrobotique : micromanipulation et microrobots autonomes," *J3eA, Journal sur l'enseignement des sciences et technologies de l'information et des systèmes,*, vol. 2, no. Hors-Série 2, 14, 2003.

[192] R. Yeh, E. J. J. Kruglick, and K. S. J. Pister, "Surface-micromachined components for articulated microrobots," *Journal of Microelectromechanical Systems*, vol. 5, no. 1, pp. 10–17, 1996.

[193] R. Yeh, S. Hollar, and K. S. J. Pister, "Design of low-power silicon articulated microrobots," *Journal of Micromechatronics*, vol. 1, no. 3, pp. 191–203, 2001.

[194] K. Suzuki, I. Shimoyama, H. Miura, and Y. Ezura, "Creation of an insect-based microrobot with an external skeleton and elastic joints," in *Proc. IEEE Micro Electro Mechanical Systems, MEMS '92*, pp. 190–195, 1992.

[195] W. Zhang, S. Guo, and K. Asaka, "Development of an underwater biomimetic microrobot with compact structure and flexible locomotion," *Microsystem Technologies*, vol. 13, no. 8-10, pp. 883–890, 2007.

[196] N. Snis, U. Simu, and S. Johansson, "Piezoelectric drive platform for cm3 sized autonomous robot," in *Proc. Int. Conf. on New Actuators, ACTUATOR '04*, pp. 106–109, 2004.

[197] N. Snis, U. Simu, and S. Johansson, "A piezoelectric disc-shaped motor using a quasi-static walking mechanism," *Journal of Micromechanics and Microengineering*, vol. 15, no. 12, pp. 2230–2234, 2005.

[198] S. Bergbreiter, "Design of a 2-DOF Low Power Microrobot [online]." `http://www-bsac.eecs.berkeley.edu/~sbergbre/publications/EE245.pdf`, 2000.

[199] T. Sashida, "Motor device utilizing ultrasonic oscillation. U.S. Patent 4,562,374." , 1985.

[200] H. Hirata and S. Ueha, "Design of a traveling wave type ultrasonic motor," *IEEE Transactions on Ultrasonics, Ferroelectrics, and Frequency Control*, vol. 42, no. 2, pp. 225–231, 1995.

[201] T. Sashida and T. Kenjo, *An Introduction to Ultrasonic Motors* . Oxford : Clarendon Press, 1993.

[202] K. Spanner, "Survey of the Various Operating Principles of Ultrasonic Piezomotors," in *Proc. Int. Conf. on New Actuators, ACTUATOR '06*, pp. 414–421, 2006.

[203] R. Bansevicius and V. Blechertas, "Ultrasonic motors for mass-consumer products," *ULTRAGARSAS*, vol. 61, no. 4, pp. 50–52, 2006.

[204] W. Seemann, "A linear ultrasonic traveling wave motor of the ring type," *Smart Materials and Structures*, vol. 5, no. 3, pp. 361–368, 1996.

[205] M. Kuribayashi, S. Ueha, and E. Mon, "Excitation conditions of flexural traveling waves for a reversible ultrasonic linear motor," *Journal of the Acoustical Society of America*, vol. 77, no. 4, pp. 1431–1435, 1985.

[206] B. Houben, W. Symens, M. Versteyhe, D. Reynaerts, and H. Van Brussel, "Design and construction of a linear piezo-electrically driven forced travelling wave motor," in *Proc. Int. Conf. on New Actuators, ACTUATOR '00*, pp. 447–450, 2000.

[207] S. Devos, D. Reynaerts, F. Al-Bender, and H. Van Brussel, "A piezo-electrical travelling wave XY-stage," in *Proc. Int. Conf. on New Actuators, ACTUATOR '02*, pp. 470–473, 2002.

[208] P. Minotti, P. Cusin, P. Le Moal, and A. Ferreira, "Micromachined traveling wave motors: Three dimensional mechanical optimization and miniaturization limits evaluation," *Japanese Journal of Applied Physics, Part 1: Regular Papers and Short Notes and Review Papers*, vol. 36, no. 11, pp. 7009–7018, 1997.

[209] A. Volkov, "Positioning apparatus and method. European Patent EP1880467." , 2008.

[210] T. Shigematsu, M. K. Kurosawa, and K. Asai, "Nano meter stepping drive of surface acoustic wave motor," in *Proc. IEEE Conf. on Nanotechnology, IEEE-Nano '01.*, pp. 495–500, 2001.

[211] "NanoMobile." `http://northumbria.ac.uk/business/nce/info4staff/ic/opportunities/tech2licence/prj_nm/`.

[212] K. Tani, "Friction models for a mobile machine using piezo vibration," in *Int. Workshop on Advanced Motion Control, AMC '96*, vol. 2, pp. 717–722, 1996.

[213] M. K. Kurosawa, "State-of-the-art surface acoustic wave linear motor and its future applications," *Ultrasonics*, vol. 38, no. 1-8, pp. 15–9, 2000.

[214] M. Kurosawa, M. Takahashi, and T. Higuchi, "Ultrasonic X-Y stage using 10 MHz surface acoustic wave," in *Proc. IEEE Ultrasonics Symposium*, vol. 1, pp. 535–538, 1994.

[215] T. Shigematsu and M. K. Kurosawa, "Miniaturized SAW motor with 100 MHz driving frequency," in *Proc. IEEE Micro Electro Mechanical Systems, MEMS '04*, pp. 482–485, 2004.

[216] M. Kurosawa, M. Takahashi, and T. Higuchi, "Nanometer Resolution 2-D In-Plane Saw Motor," in *Proc. IEEE Ultrasonics Symposium*, pp. 535–538, 1994.

[217] W. G. May, "Piezoelectric Electromechanical Translation Apparatus. U.S. Patent 3,902,084." , 1975.

[218] O. Fuchiwaki and H. Aoyama, "Piezo based micro robot for microscope instrument ," in *Proc. Int. Conf. on Mechatronics Technology, ICMT '02*, pp. 499–503, 2002.

[219] A. Codourey, W. Zesch, R. Buchi, and R. Siegwart, "A robot system for automated handling in micro-world," in *Proc. IEEE/RSJ Int. Conf. on Intelligent Robots and Systems, IROS '95*, vol. 3, pp. 185–190, 1995.

[220] T. Koyanagi, R. Fukui, A. Torii, and A. Ueda, "Miniature robots with three degrees of freedom," in *Proc. IEEE Int. Symp. on Micromechatronics and Human Science, MHS '00*, pp. 207–212, 2000.

[221] A. Torii, H. Kato, and A. Ueda, "A miniature actuator with electromagnetic elements," *Electrical Engineering in Japan (English translation of Denki Gakkai Ronbunshi)*, vol. 134, no. 4, pp. 70–75, 2001.

[222] S. Yan, F. Zhang, Z. Qin, and S. Wen, "A 3-DOFs mobile robot driven by a piezoelectric actuator," *Smart Materials and Structures*, vol. 15, no. 1, 2006.

[223] H. C. Chen, M. T. Li, and L. N. Sun, "A high precise mobile positioning microrobot with macro/micro drivers," in *Proc. IEEE Int. Conf. on Mechatronics, ICM '05*, vol. 2005, pp. 328–333, 2005.

[224] P. Cusin, T. Sawai, and S. Konishi, "Compact and precise positioner based on the Inchworm principle," *Journal of Micromechanics and Microengineering*, vol. 10, no. 4, pp. 516–521, 2000.

[225] S. Konishi, K. Ohno, and M. Munechika, "Parallel linear actuator system with high accuracy and large stroke," *Sensors and Actuators, A: Physical*, vol. 97-98, pp. 610–619, 2002.

[226] M. V. Shutov, D. L. Howard, E. E. Sandoz, J. M. Sirota, R. L. Smith, and S. D. Collins, "Electrostatic inchworm microsystem with long range translation," *Sensors and Actuators, A: Physical*, vol. 114, no. 2-3, pp. 379–386, 2004.

[227] N. Tas, J. Wissink, L. Sander, T. Lammerink, and M. Elwenspoek, "Modeling, design and testing of the electrostatic shuffle motor," *Sensors and Actuators, A: Physical*, vol. 70, no. 1-2, pp. 171–178, 1998.

[228] M. P. de Boer, D. L. Luck, W. R. Ashurst, R. Maboudian, A. D. Corwin, J. A. Walraven, and J. M. Redmond, "High-performance surface-micromachined inchworm actuator," *Journal of Microelectromechanical Systems*, vol. 13, no. 1, pp. 63–74, 2004.

[229] E. Sarajlic, E. Berenschot, H. Fujita, G. Krijnen, and M. Elwenspoek, "Bidirectional electrostatic linear shuffle motor with two degrees of freedom," in *Proc. IEEE Micro Electro Mechanical Systems, MEMS '05*, pp. 391–394, 2005.

[230] W. C. Tang, T.-C. H. Nguyen, and R. T. Howe, "Laterally driven polysilicon resonant microstructures," *Sensors and actuators*, vol. 20, no. 1-2, pp. 25–32, 1989.

[231] R. Yeh, E. J. J. Kruglick, and K. S. J. Pister, "Microelectromechanical components for articulated microrobots," in *Proc. Int. Conf. on Solid-State Sensors and Actuators (Transducers âĂŹ95), and Eurosensors IX*, vol. 2, pp. 346–349, 1995.

[232] M. Baltzer, T. Kraus, and E. Obermeier, "Linear stepping actuator in surface micromachining technology for low voltages and large displacements," in *Proc. Int. Conf. on Solid-State Sensors and Actuators, Transducers '97*, vol. 2, pp. 781–784, 1997.

[233] N. R. Tas, T. Sonnenberg, R. Molenaar, and M. Elwenspoek, "Design, fabrication and testing of laterally driven electrostatic motors employing walking motion and mechanical leverage," *Journal of Micromechanics and Microengineering*, vol. 13, no. 1, pp. 6–15, 2003.

[234] R. Toda and E. H. Yang, "A normally latched, large-stroke, inchworm microactuator," *Journal of Micromechanics and Microengineering*, vol. 17, no. 8, pp. 1715–1720, 2007.

[235] H. N. Kwon, S. H. Jeong, S. K. Lee, and J. H. Lee, "Design and characterization of a micromachined inchworm motor with thermoelastic linkage actuators," *Sensors and Actuators, A: Physical*, vol. 103, no. 1-2, pp. 143–149, 2003.

[236] C. Anthierens, C. Libersa, M. Touaibia, M. Betemps, M. Arsicault, and N. Chaillet, "Micro robots dedicated to small diameter canalization exploration," in *Proc. IEEE/RSJ Int. Conf. on Intelligent Robots and Systems, IROS '00*, vol. 1, pp. 480–485, 2000.

[237] M. C. Carrozza, L. Lencioni, B. Magnani, P. Dario, D. Reynaerts, M. G. Trivella, and A. Pietrabissa, "A microrobot for colonoscopy," in *Proc. IEEE Int. Symp. on Micro Machine and Human Science, MHS '96*, pp. 223–228, 1996.

[238] S. J. Phee, S. J. Phee, W. S. Ng, I. M. Chen, F. Seow-Choen, and B. L. Davies, "Locomotion and steering aspects in automation of colonoscopy. I. A literature review," *Engineering in Medicine and Biology Magazine, IEEE*, vol. 16, no. 6, pp. 85–96, 1997.

[239] C. Groux, W. Driesen, R. Rabe, and R. Clavel, "Actionneur linéaire basé sur le principe du inchworm inertiel," student project, EPFL, 2006.

[240] S. Pan, "Piezoelectric Motor. WO Patent 9319494." , 1993.

[241] M. Brown, T. Hubbard, and M. Kujath, "Development of a long-range untethered frictional microcrawler," *Journal of Micromechanics and Microengineering*, vol. 17, no. 5, pp. 1025–1033, 2007.

[242] Y. Lai, J. McDonald, M. Kujath, and T. Hubbard, "Force, deflection and power measurements of toggled microthermal actuators," *Journal of Micromechanics and Microengineering*, vol. 14, no. 1, pp. 49–56, 2004.

[243] B. Shay, T. Hubbard, and M. Kujath, "Planar frictional micro-conveyors with two degrees of freedom," *Journal of Micromechanics and Microengineering*, vol. 18, no. 6, p. 065009, 2008.

[244] K. Jung, J. C. Koo, J. D. Nam, Y. K. Lee, and H. R. Choi, "Artificial annelid robot driven by soft actuators," *Bioinspiration and Biomimetics*, vol. 2, no. 2, 2007.

[245] G. La Spina, M. Sfakiotakis, D. P. Tsakiris, A. Menciassi, and P. Dario, "Polychaete-like undulatory robotic locomotion in unstructured substrates," *IEEE Transactions on Robotics*, vol. 23, no. 6, pp. 1200–1212, 2007.

[246] A. J. Ijspeert, A. Crespi, D. Ryczko, and J. M. Cabelguen, "From swimming to walking with a salamander robot driven by a spinal cord model," *Science*, vol. 315, no. 5817, pp. 1416–1420, 2007.

[247] V. K. Varma and W. E. Dixon, "Design of a piezoelectric meso-scale mobile robot: A compliant amplification approach," in *Proc. IEEE Int. Conf. on Robotics and Automation, ICRA '02*, vol. 2, pp. 1137–1142, 2002.

[248] N. Snis, E. Edqvist, U. Simu, and S. Johansson, "Monolithic fabrication of multilayer P(VDF-TrFE) cantilevers," *Sensors and Actuators, A: Physical*, vol. In Press, Corrected Proof, 2008.

[249] N. Snis and S. Johansson, "Miniature piezoceramic locomotion unit with resonant drive," *Sumitted to Journal of Micromechanics and Microengineering*, 2008.

[250] E. Edqvist, N. Snis, and S. Johansson, "Gentle dry etching of P(VDF-TrFE) multilayer micro actuator structures by use of an inductive coupled plasma," *Journal of Micromechanics and Microengineering*, vol. 18, no. 1, p. 015007, 2008.

[251] E. Edqvist, N. Snis, M. Sjölund, T. Murase, A. Söderberg, and S. Johansson, "The assembly of millimetre sized mass producible autonomous robots," in *Proc. Int. Conf. on New Actuators, ACTUATOR '08*, pp. 304–307, 2008.

[252] N. Snis, *Actuators for autonomous microrobots.* Phd thesis, Uppsala University, 2008.

[253] A. Ferreira, P. Minotti, and P. Le Moal, "New Multidegree of Freedom Piezoelectric Micromotors for Micromanipulator Applications (unpublished)," in *Proc. IEEE Ultrasonics Symposium*, p. 417, 1995.

[254] A. Ferreira and J. G. Fontaine, "Dynamic modeling and control of a conveyance microrobotic system using active friction drive," *IEEE/ASME Transactions on Mechatronics*, vol. 8, no. 2, pp. 188–202, 2003.

[255] S. Dembele and K. Rochdi, "A three DOF linear ultrasonic motor for transport and micropositioning," *Sensors and Actuators, A: Physical*, vol. 125, no. 2, pp. 486–493, 2006.

[256] K. J. Son, V. Kartik, J. A. Wickert, and M. Sitti, "An ultrasonic standing-wave-actuated nano-positioning walking robot: Piezoelectric-metal composite beam modeling," *Journal of Vibration and Control*, vol. 12, no. 12, pp. 1293–1309, 2006.

[257] G. Bozovic, T. Cimprich, and R. Clavel, "Microrobot mobile a 3 ddl base sur le principe des actionneurs ultrasoniques (Student project)." `http://infoscience.epfl.ch/record/90821`, 2006.

[258] T. Cimprich, F. Kaegi, W. Driesen, A. Ferreira, and J. M. Breguet, "Ultrasonic monolithic piezoelectric multi DOF actuators for mobile microrobots," in *Proc. Int. Conf. on New Actuators, ACTUATOR '06*, pp. 114–117, 2006.

[259] S. Bergbreiter and K. S. J. Pister, "Design of an autonomous jumping microrobot," in *Proc. IEEE Int. Conf. on Robotics and Automation, ICRA '07*, pp. 447–453, 2007.

[260] H. A. Gaberson and P. L. Stone, "Vibratory Locomotion," *Journal of Engineering for Industry-Transactions of the ASME*, vol. 96 Ser B, no. 2, pp. 644–652, 1974.

[261] P. Vartholomeos and E. Papadopoulos, "Analysis, design and control of a planar microrobot driven by two centripetal-force actuators," in *Proc. IEEE Int. Conf. on Robotics and Automation, ICRA '06*, vol. 2006, pp. 649–654, 2006.

[262] P. Vartholomeos and E. Papadopoulos, "Analysis and design of a novel mini-platform employing vibration micro-motors," in *Proc. IEEE Int. Conf. on Robotics and Automation, ICRA '05*, vol. 2005, pp. 3627–3632, 2005.

[263] J. M. Breguet, W. Driesen, F. Kaegi, and T. Cimprich, "Applications of piezo-actuated micro-robots in micro-biology and material science," in *Proc. IEEE Int. Conf. on Mechatronics and Automation, ICMA '07*, pp. 57–62, 2007.

[264] N. N. Bolotnik, S. F. Jatsun, A. S. Jatsun, and A. A. Cherepanov, "Automatically controlled vibration-driven robots," in *Proc. IEEE Int. Conf. on Mechatronics, ICM '06*, pp. 438–441, 2006.

[265] A. T. Nguyen and S. Martel, "Embedded piezo-actuation system for automatic motion control of a fleet of miniature robots operating on a synchronized vibrating platform," in *Proc. World Congress on Intelligent Control and Automation, WCICA '06*, vol. 2, pp. 8412–8415, 2006.

[266] K. Vollmers, D. R. Frutiger, B. E. Kratochvil, and B. J. Nelson, "Wireless resonant magnetic microactuator for untethered mobile microrobots," *Applied Physics Letters*, vol. 92, no. 14, 2008.

[267] S. Floyd, C. Pawashe, and M. Sitti, "An Untethered Magnetically Actuated Micro-Robot Capable of Motion on Arbitrary Surfaces," in *Proc. IEEE Int. Conf. on Robotics and Automation, ICRA '08*, 2008.

[268] A. Gmiterko, M. Dovica, M. Kelemen, V. Fedák, and Z. Mlýnkova, "In-pipe bristled micromachine," in *Proc. Int. Workshop on Advanced Motion Control, AMC '02*, pp. 599–603, 2002.

[269] B. Kim, M. G. Lee, Y. P. Lee, Y. Kim, and G. Lee, "An earthworm-like micro robot using shape memory alloy actuator," *Sensors and Actuators, A: Physical*, vol. 125, no. 2, pp. 429–437, 2006.

[270] B. Kim, S. Lee, J. H. Park, and J. O. Park, "Inchworm-like microrobot for capsule endoscope," in *Proc. IEEE Int. Conf. on Robotics and Biomimetics, ROBIO '04*, pp. 458–463, 2004.

[271] J. M. Conrad, "Stiquito for robotics and embedded systems education," *Computer*, vol. 38, no. 6, pp. 77–81, 2005.

[272] L. Sun, P. Sun, X. Qin, and C. Wang, "Micro robot in small pipe with electromagnetic actuator," in *Proc. of IEEE Int. Symp. on Micromechatronics and Human Science, MHS '98*, pp. 243–248, 1998.

[273] R. Sahai, S. Avadhanula, R. Groff, E. Steltz, R. Wood, and R. S. Fearing, "Towards a 3g crawling robot through the integration of microrobot technologies," in *Proc. IEEE Int. Conf. on Robotics and Automation, ICRA '06*, vol. 2006, pp. 296–302, 2006.

[274] K. Uchino, "Micro walking machines using piezoelectric actuators," *Journal of Robotics and Mechatronics*, vol. 1, no. 2, pp. 124–127, 1989.

[275] K. Uchino, "New applications of photostrictive ferroics," *Materials Research Innovations*, vol. 1, no. 3, pp. 163–168, 1997.

[276] P. Poosanaas, K. Tonooka, and K. Uchino, "Photostrictive actuators," *Mechatronics*, vol. 10, no. 4-5, pp. 467–487, 2000.

[277] T. Ikehara, M. Tanaki, S. Shimada, and H. Matsuda, "Optically-driven actuator using photo-induced phase-transition material," in *Proc. IEEE Micro Electro Mechanical Systems, MEMS '01*, pp. 256–259, 2001.

[278] S. Maeda, Y. Hara, T. Sakai, R. Yoshida, and S. Hashimoto, "Self-walking gel," *Advanced Materials*, vol. 19, no. 21, pp. 3480–3484, 2007.

[279] B. Carey, "The World's Smallest Robot." `http://www.livescience.com/technology/050915_smallest_robot.html`, 2005.

[280] Y. Kanamori, H. Yahagi, and K. Hane, "A microtranslation table with scratch-drive actuators fabricated from silicon-on-insulator wafer," *Sensors and Actuators, A: Physical*, vol. 125, no. 2, pp. 451–457, 2006.

[281] J. S. Park, L. L. Chu, A. D. Oliver, and Y. B. Gianchandani, "Bent-beam electrothermal actuators-Part II: Linear and rotary microengines," *Journal of Microelectromechanical Systems*, vol. 10, no. 2, pp. 255–262, 2001.

[282] J. M. Maloney, D. S. Schreiber, and D. L. DeVoe, "Large-force electrothermal linear micromotors," *Journal of Micromechanics and Microengineering*, vol. 14, no. 2, pp. 226–234, 2004.

[283] P. H. Pham, D. V. Dao, S. Amaya, R. Kitada, and S. Sugiyama, "Straight movement of micro containers based on ratchet mechanisms and electrostatic comb-drive actuators," *Journal of Micromechanics and Microengineering*, vol. 16, no. 12, pp. 2532–2538, 2006.

[284] P. H. Pham, D. V. Dao, and S. Sugiyama, "A micro transportation system (MTS) with large movement of containers driven by electrostatic comb-drive actuators," *Journal of Micromechanics and Microengineering*, vol. 17, no. 10, pp. 2125–2131, 2007.

[285] W. Mansour, M. Massoud, W. Morcos, and C. Lauzier, "Mechanism of Conveyance with Bristled Tracks," *ASME Journal of Engineering for Industry*, vol. 97, no. 1, pp. 167–174, 1975.

[286] S. Okabe, Y. Yokoyama, and G. Boothroyd, "Analysis of vibratory feeding where the track has directional friction characteristics," *The International Journal of Advanced Manufacturing Technology*, vol. 3, no. 4, pp. 73–85, 1988.

[287] T. Sashida, "Supersonic vibration driven motor device. U.S. Patent 4,325,264." , 1982.

[288] G. A. Racine, R. Luthier, and N. F. de Rooij, "Hybrid ultrasonic micromachined motors," in *Proc. IEEE Micro Electro Mechanical Systems, MEMS '93*, pp. 128–132, 1993.

[289] M. A. Dubois and P. Muralt, "PZT thin film actuated elastic fin micromotor," *IEEE Transactions on Ultrasonics, Ferroelectrics, and Frequency Control*, vol. 45, no. 5, pp. 1169–77, 1998.

[290] M. J. Daneman, N. C. Tien, O. Solgaard, A. P. Pisano, K. Y. Lau, and R. S. Muller, "Linear microvibromotor for positioning optical components," *Journal of Microelectromechanical Systems*, vol. 5, no. 3, pp. 159–165, 1996.

[291] M. Pai and N. C. Tien, "Low voltage electrothermal vibromotor for silicon optical bench applications," *Sensors and Actuators, A: Physical*, vol. 83, no. 1, pp. 237–243, 2000.

[292] T. Fukuda, N. Mitsumoto, F. Arai, and H. Matsuura, "Design and experiments of micro mobile robot using electromagnetic actuator," in *Proc. IEEE Int. Symp. on Micro Machine and Human Science, MHS '92*, pp. 77–82, 1992.

[293] T. Fukuda, N. Mitsumoto, F. Arai, and H. Matsuura, "Micro Mobile Robot Using Electromagnetic Actuator," in *Proc. of Int. Advanced Robotics Program (IARP) Workshop on Micro Robotics and Systems*, pp. 45–50, 1993.

[294] T. Matsuoka, M. Asano, H. Fukushima, H. Okamoto, M. Uchida, and T. Matsui, "Mechanical analysis of micro mobile machine with piezoelectric element," in *Proc. IEEE/RSJ Int. Conf. on Intelligent Robots and Systems, IROS '93*, pp. 1685–1690, 1993.

[295] K. Ioi, "Mobile micro-robot using centrifugal forces," in *Proc. IEEE/ASME Int. Conf. on Advanced Intelligent Mechatronics, AIM '99*, pp. 736–741, 1999.

[296] K. Isaki, A. Niitsuma, M. Konyo, F. Takemura, and S. Tadokoro, "Development of an active flexible cable by ciliary vibration drive for scope camera," in *Proc. IEEE/RSJ Int. Conf. on Intelligent Robots and Systems, IROS '06*, pp. 3946–3951, 2006.

[297] T. Fukuda, H. Hosokai, H. Ohyama, H. Hashimoto, and F. Arai, "Giant magnetostrictive alloy (GMA) applications to micro mobile robot as a micro actuator without power supply cables," in *Proc. IEEE Micro Electro Mechanical Systems, MEMS '91*, pp. 210–215, 1991.

[298] H. Miura, T. Yasuda, Y. K. Fujisawa, and I. Shimoyama, "Insect-model based microrobot," in *Proc. Int. Conf. on Solid-State Sensors and Actuators (Transducers âĂŹ95), and Eurosensors IX*, vol. 2, pp. 392–395, 1995.

[299] T. Higuchi, "Application of electromagnetic impulsive force to precise positioning tools in robot system," in *Proc. Int. Symp. of Robotics Research, ISRR '84*, pp. 144–149, 1984.

[300] T. Higuchi, Y. Hojjat, and M. Watanabe, "Micro actuator using recoil of an ejected mass," in *Proc. IEEE Micro Robots and Teleoperators Workshop*, pp. 16–21, 1987.

[301] K. Ikuta, A. Kawahara, and S. Yamazumi, "Miniature cybernetic actuators using piezoelectric device," in *Proc. IEEE Micro Electro Mechanical Systems, MEMS '91*, pp. 131–136, 1991.

[302] T. Higuchi and Y. Yamagata, "Precise positioning mechanism utilizing rapid deformations of piezoelectric elements (2nd report) - motion characteristics with enhanced friction," *Seimitsu Kogaku Kaishi / Journal of the Japan Society for Precision Engineering*, vol. 58, no. 10, pp. 1759–1764, 1992.

[303] K. Ikuta, S. Aritomi, and T. Kabashima, "Tiny silent linear cybernetic actuator driven by piezoelectric device with electromagnetic clamp," in *Proc. IEEE Micro Electro Mechanical Systems, MEMS '92*, pp. 232–237, 1992.

[304] T. Higuchi, K. Furutani, Y. Yamagata, K.-i. Kudoh, and M. Ogawa, "Improvement of velocity of impact drive mechanism by controlling friction," *Seimitsu Kogaku Kaishi / Journal of the Japan Society for Precision Engineering*, vol. 58, no. 8, pp. 1327–1332, 1992.

[305] K. Besocke, "An easily operable scanning tunneling microscope," *Surface Science*, vol. 181, no. 1-2, pp. 145–153, 1987.

[306] D. W. Pohl, "Dynamic Piezoelectric Translation Devices," *Review of Scientific Instruments*, vol. 58, no. 1, pp. 54–57, 1987.

[307] R. Matsuda and R. Kaneko, "Micro-step XY-stage using piezoelectric tube actuator," in *Proc. IEEE Micro Electro Mechanical Systems, MEMS '91*, pp. 137–142, 1991.

[308] D. Peichel, D. Marcus, R. Rizq, A. Erdman, W. Robbins, and D. Polla, "Silicon fabricated submicrometer stepper motor for microsurgical procedures," *Journal of Microelectromechanical Systems*, vol. 11, no. 2, pp. 154–160, 2002.

[309] S. W. Lee, K. G. Ahn, and J. Ni, "Development of a piezoelectric multi-axis stage based on stick-and-clamping actuation technology," *Smart Materials and Structures*, vol. 16, no. 6, pp. 2354–2367, 2007.

[310] P. Niedermann and H. Choffat, "High precision piezoelectric actuator. European Patent EP0750356." , 1996.

[311] K. Ikuta, M. Nokata, and S. Aritomi, "Biomedical micro robots driven by miniature cybernetic actuator," in *Proc. IEEE Micro Electro Mechanical Systems, MEMS '94*, pp. 263–268, 1994.

[312] H. Nishikawa, T. Sasaya, T. Shibata, T. Kaneko, N. Mitumoto, S. Kawakita, and N. Kawahara, "In-pipe wireless micro locomotive system," in *Proc. IEEE Int. Symp. on Micromechatronics and Human Science, MHS '99*, pp. 141–147, 1999.

[313] T. Shibata, T. Sasaya, and N. Kawahara, "Development of in-pipe microrobot using microwave energy transmission," *Electronics and Communications in Japan, Part II: Electronics (English translation of Denshi Tsushin Gakkai Ronbunshi)*, vol. 84, no. 11, pp. 1–8, 2001.

[314] B. Magnussen, S. Fatikow, and U. Rembold, "Actuation in microsystems: problem field overview and practical example of the piezoelectric robot for handling of microobjects," in *Proc. IEEE Symp. on Emerging Technologies & Factory Automation, ETFA '95*, vol. 3, pp. 21–27, 1995.

[315] S. Fatikow, "Automated micromanipulation desktop-station based on mobile piezoelectric microrobots," in *Proc. of SPIE - Microrobotics: Components and Applications*, vol. 2906, pp. 66–77, 1996.

[316] A. Bergander, W. Driesen, T. Varidel, and J.-M. Breguet, "Monolithic piezoelectric push-pull actuators for inertial drives," in *Proc. IEEE Int. Symp. on Micromechatronics and Human Science, MHS '03*, pp. 309 – 316, 2003.

[317] L. Juhas, A. Vujanic, N. Adamovic, L. Nagy, and B. Borovac, "Development of platform for micro-positioning actuated by piezo-legs," in *Proc. IEEE Int. Conf. on Robotics and Automation, ICRA '00*, vol. 4, pp. 3647–3653, 2000.

[318] S. Martel, "Fundamental principles and issues of high-speed piezoactuated three-legged motion for miniature robots designed for nanometer-scale operations," *International Journal of Robotics Research*, vol. 24, no. 7, pp. 575–588, 2005.

[319] S.-I. Kawakita, "Development of Autonomous Mobile Microrobot [online]," technical report, DENSO Corporation, 1999.

[320] "Micromechatronics and Microrobotics Group - The Microrobot Prototypes." `http://i60p4.ira.uka.de/tiki/tiki-index.php?page=Microrobots`.

[321] "Laboratoire de Nanorobotique - Research." `http://wiki.polymtl.ca/nano/index.php/Research`.

[322] T. Berghaus and P. Klaede, " Adjusting device for microscopic movements. GB Patent 2246236." , 1992.

[323] J.-M. Breguet and P. Renaud, "A 4-degrees-of-freedom microrobot with nanometer resolution," *Robotica*, vol. 14, pp. 199–203, 1996.

[324] A. Sulzmann, J. M. Breguet, J. Carlier, and J. Jacot, "Virtual Reality and high accurate vision feedback as key information for micro robot telemanipulation," in *Proc. of SPIE - Microrobotics: Components and Applications*, vol. 2906, pp. 38–57, 1996.

[325] R. Perez, J. M. Breguet, H. Bleuler, and R. Clavel, "Monolithic piezo-actuators: modelling, validation in the laboratory and optimisation of working conditions," in *Proc. Int. Conf. on New Actuators, ACUTATOR '00*, pp. 49–52, 2000.

[326] W. Zesch, R. Buechi, A. Codourey, and R. Y. Siegwart, "Inertial drives for micro- and nanorobots: two novel mechanisms," in *Proc. of SPIE - Microrobotics and Micromechanical Systems*, vol. 2593, pp. 80–88, 1995.

[327] J.-M. Breguet and R. Clavel, "Stick and slip actuators: Design, control, performances and applications," in *Proc. IEEE Int. Symp. on Micromechatronics and Human Science, MHS '98*, pp. 89–95, 1998.

[328] Y. Nomura and H. Aoyama, "Development of inertia driven micro robot with nano tilting stage for SEM operation," *Microsystem Technologies*, vol. 13, no. 8-10, pp. 1347–1352, 2007.

[329] A. Bergander, C. Canales, G. Boetsch, T. Maeder, G. Corradini, and J. M. Breguet, "A modular actuator system for miniature positioning systems," in *Proc. Int. Conf. on New Actuators, ACTUATOR '08*, 2008.

[330] W. Driesen, T. Varidel, and J. M. Breguet, "D2-09 : Improved microrobot prototype," internal deliverable of the micron project, EPFL, 2005.

[331] M. Mita, M. Arai, S. Tensaka, D. Kobayashi, and H. Fujita, "A micromachined impact microactuator driven by electrostatic force," *Journal of Microelectromechanical Systems*, vol. 12, no. 1, pp. 37–41, 2003.

[332] M. Mita, H. Toshiyoshi, and H. Fujita, "An electrostatic inertia-driven micro rover," in *Proc. IEEE Micro Electro Mechanical Systems, MEMS '05*, pp. 395–398, 2005.

[333] F. Altpeter, *Friction modeling, identification and compensation.* Phd thesis, EPFL, 1999.

[334] C. de Coulomb, *Théorie des machines simples, en ayant égard au frottement de leurs parties et à la roideur des cordages.* Bachelier Libbrairie, Quai des Augustins, Paris, 1781.

[335] C. Canudas de Wit, H. Olsson, K. Aström, and P. Lischinsky, "A new model for control of systems with friction," *IEEE Transactions on Automatic Control*, vol. 40, no. 3, pp. 419–425, 1995.

[336] R. Rabe, *Compact test platform for in-situ indentation and scratching inside a scanning electron microscope (SEM).* Phd thesis, EPFL, 2006.

[337] K. Johnson, *Contact mechanics.* Cambridge: Cambridge University Press, 1985.

[338] R. Clavel, *Composants de la microtechnique*. Lausanne: EPFL, 1999.

[339] R. Mindlin, "Compliance of elastic bodies in contact," *Journal of applied mechanics*, vol. 16, pp. 259–268, 1949.

[340] S. I. U. C. Center for Advanced Friction Studies, "Friction Center Coefficient Database." `http://frictioncenter.siu.edu/databaseSearch.html`, 2007.

[341] B. Fracheboud, W. Driesen, and R. Clavel, "Micro-moteur XY basé sur le principe du friction drive," student project, EPFL, 2003.

[342] D. Campolo, M. Sitti, and R. S. Fearing, "Efficient charge recovery method for driving piezoelectric actuators with quasi-square waves," *IEEE Transactions on Ultrasonics, Ferroelectrics, and Frequency Control*, vol. 50, no. 3, pp. 237–244, 2003.

[343] D. Meeker, "FEMM 4.0, Finite Element Method Magnetics and Electrosatics." `http://femm.foster-miller.net`, 2004.

[344] R. Dunsch and J. M. Breguet, "Unified mechanical approach to piezoelectric bender modeling," *Sensors and Actuators, A: Physical*, vol. 134, no. 2, pp. 436–446, 2007.

[345] N. Wyrsch, S. Dunand, and C. Ballif, "Micro Photovoltaic Modules for Micro Systems," in *Proc. Material Research Society Symp., MRS Spring Meeting*, vol. 1066, p. A10.4, 2008.

[346] C. Groux, W. Driesen, and R. Clavel, *Dispositif de plusieurs micro robots mobiles contrôlés par un projecteur*. Master thesis, EPFL, 2007.

[347] K. Noguchi, H. Fujita, M. Suzuki, and N. Yoshimura, "The measurements of friction on micromechatronics elements," in *Proc. IEEE Micro Electro Mechanical Systems, MEMS '91*, pp. 148–153, 1991.

[348] *Extrait de normes pour écoles et professions de la mécanique*. Winterthur: Schweizerische Normen-Vereinigung, societe suisse des constructeurs de machines ed., 2002.